UNIVERSITY OF THE SOUTHERN QUEENSLAND

NUMERICAL INVESTIGATION OF TRANSCRANIAL DIRECT CURRENT STIMULATION ON CORTICAL MODULATION

A dissertation submitted by

Syed Salman Shahid

For the award of

Doctor of Philosophy

June 2013

Abstract

Transcranial direct current stimulation (tDCS) is a non-invasive and sub-convulsive functional stimulation technique with applications in both clinical therapy and neuroscience research. The technique provides researchers and clinicians with a unique tool capable of modulating the neural excitability in both the central and peripheral nervous system. On a clinical level, the procedure has been used quite extensively for its potential therapeutic applications in a number of neurological disorders. Despite the advantages of being safe, low cost and easy to administer, our limited understanding on interaction mechanisms between the stimulation parameters and biological materials has impeded the development and optimisation of tDCS based therapies.

The focus of this thesis is to develop a realistic finite element based human head model to address the problems involved in the forward modelling of transcranial direct current stimulation. The study explores the effects of model complexities and anisotropic material properties on field estimations. The sensitivity of electric field and current density on accurate modelling of cortical and non-cortical structures, and the influence of heterogeneously defined anisotropic electric conductivity on field parameters were analysed in an incremental manner. Using the averaged and the subject specific Magnetic Resonance Imaging (MRI) and Diffusion Tensor Imaging (DTI) data, the head models with detailed anatomical features and realistic tissue conductive properties, were developed and employed to specifically address the role of stimulation parameters, such as: morphological variations, structural details, tissue behaviour, inter-subject variations, electrode montages and neural fibre pathways for defining the site and strength of modulation/stimulation.

This thesis demonstrates the importance of human head modelling in elucidating the complex electric field and current density profiles instigated by the non-invasive

electric stimulation. The results of this study strongly support the initial hypothesis that model complexity and accurate conductivity estimation play a crucial role in determining the accurate predictions of field variables. The study also highlighted the inadequacy of scalar field maps to decipher the complex brain current flow patterns and axonal/neural polarization. With the proposed refinements, model based strategies can be employed to optimally select the required stimulation strength and electrode montage specific to individual dose requirements. Therefore, the work conducted in this study will bridge the gap between the current clinical practices and the subject specific treatments by providing accurate physiologically representative simulation.

Certification of Dissertation

I certify that the ideas, experimental work, results, analyses, software and conclusions reported in this dissertation are entirely my own effort, except where otherwise acknowledged. I also certify that the work is original and has not been previously submitted for any other award, except where otherwise acknowledged.

---------- ----------

Signature of Candidate Date

ENDORSEMENT

---------- ----------

Signature of Supervisors Date

---------- ----------

Acknowledgement

My time at the USQ has been a great learning experience. I am extremely grateful to a number of people for their guidance and assistance.

Firstly I would like to express my gratitude to my Supervisor A/Professor Peng (Paul) Wen for his support, encouragement and patience. I am also grateful for his invaluable suggestions, discussion and confidence in my work.

I would like to thank Dr. Tony Ahfock for his unparalleled encouragement, guidance and support, and A/Professor John Leis for his guidance at the beginning of my PhD program. I would also like to acknowledge the technical and administrative support of the Faculty of Engineering and Surveying. Last but certainly not the least, my special gratitude goes to my parents, who have always been there for me and have shown consistent interest in my welfare.

List of related publications

The following papers, associated with the research contained in this dissertation, have been published or submitted for publication.

JOURNAL PAPERS

Shahid, S, Wen, P and Ahfock, T 2013, 'Numerical investigation of white matter anisotropic conductivity in defining current distribution under tDCS', Journal of Computer Methods and Programs in Biomedicine, vol. 109, no. 1, pp. 48-64.

Shahid, S, Wen, P and Ahfock, T 2012, 'Effects of model complexity and tissue anisotropic conductivity on cortical modulation during tDCS', IET Science, Measurement & Technology, vol. 6, no. 6, pp. 464 – 473

Shahid, S, Wen, P, Ahfock, T and Leis, J 2011, 'Effects of head geometry, coil position and CSF displacement on field distribution under transcranial magnetic stimulation', Journal of Medical Imaging and Health Informatics, vol. 1, no. 3, pp. 271-277

PEER-REVIEWED CONFERENCE PAPERS

Shahid, S, Wen, P and Ahfock, T 2011, 'Effect of fat and muscle tissue conductivity on cortical currents - a tDCS study*',* In: CME 2011: IEEE/ICME International Conference on Complex Medical Engineering, 22-25 May 2011, Harbin, China.

Shahid, S, Wen, P, Ahfock, T and Leis, J 2011, 'Effects of head geometry and coil position on field distribution under transcranial magnetic stimulation', In: MECBME 2011: Connecting Professionals in Biomedical Sciences and Technology, 21-24 Feb 2011, Sharjah, UAE.

Shahid, S and Wen, P 2010, 'Analytic and numeric evaluation of EEG forward problem using spherical volume conductor models', In: CME 2010: IEEE/ICME International Conference on Complex Medical Engineering, 13-15 Jul 2010, Gold Coast, Australia.

JOURNAL MANUSCRIPTS UNDER REVIEW/SUBMITTED

Shahid, S, Wen, P and Ahfock, T, 'Assessment of electric field distribution in cortical and sub-cortical regions under the influence of tDCS', under review at the Journal of Bioelectromagnetics, submitted on 19-10-2012 (under review).

Contents

List of Tables

List of Figures

1. INTRODUCTION

1.1. Background

Stimulation of the human nervous system is an important area of Bioelectromagnetic research, not only because of its clinical applications, but also because of the profound effect it has made in the field of cognitive neuroscience. To understand the dynamic response of the nervous system to external stimuli, many brain stimulation techniques have been proposed during the course of the last ten years. Some techniques have evolved quite significantly to target specific regions of the brain, eventually interfering with brain functions. Some of these have been developed into effective therapeutic interventions as well. In terms of fundamental principles of brain function, many of these techniques share the same underlying philosophy. However, it is often very difficult to identify the primary mechanism of action and distinguish them from epiphenomena, which are not directly related to a specific type of mechanism or its reaction by the brain. To understand brain response to external stimulation it is necessary to consider the response of tissues in terms of their electromagnetic and geometric properties. Electrical conductivity plays a pivotal role when the frequency of interest is between DC to 10 kHz. Beyond this range biological tissues exhibit strong dispersive behaviour.

This study focuses on a transcranially applied, non-invasive and non-convulsive technique called Transcranial Direct Current Stimulation (tDCS). Just like the Transcranial Magnetic Stimulation (TMS), the excitable tissue is stimulated with an electric current induced by an external mechanism. In case of TMS an externally applied

time varying magnetic field, using coils, is applied over the head. In tDCS, direct current is applied to the volume conductor via scalp electrodes hence, in both cases, the excitable tissue is stimulated by an induced electric current.

The tDCS, as a therapeutic intervention, has been the subject of clinical interest for many years, however most studies are based on clinical observations and empirical experiences. Current studies lack the theoretical depth to explain the electromagnetic behaviour of the human head in general and the excitable region in particular. Although there are some analytical and numerical models which explain the basic behaviour of electric field and current density in a volume conductor, more abstract phenomena, such as the effect of geometric variation, heterogeneous and anisotropic conductivity of different tissues and neuronal morphology limit their scope.

The induced electric field and current density are considered directly responsible to elicit the acute modification of membrane polarization (the direct-effect) and indirectly for the occurrence and duration of the long term effect (the after-effect). Variability in behavioural feedback depends on these induced field parameters. However, the strength and distribution pattern of induced electric field and current density is highly susceptible to changes in stimulation dose intensity, anatomical variations and subject-specific anatomical differences. Such information would be immensely valuable for understanding the resulting functional behaviour. Since in vivo and in vitro measurements of induced electric field are difficult to contemplate, interaction between stimulating field and target region is not well understood. However, this gap can be bridged by analysing the field behaviour in more realistic head models, which exhibit true anatomical features and conductivity behaviour.

1.2. Aim and objectives

The aim of this study is to systematically evaluate the contributions of model complexities and stimulation parameters in the forward solutions of transcranial direct current stimulation. Thus, following are the main objectives of the study:

1. Develop a framework capable of constructing, subject specific, morphologically accurate high-resolution finite element head models for the forward solution of tDCS and TES
2. Develop a scheme to incorporate tissue anisotropic dielectric behaviour in the finite element head models
3. Estimate the sensitivity of field parameters due to tissue conductivity variations using multiple anisotropic conductivity profiles
4. Estimate the sensitivity of field parameters due to subject specific morphological and conductivity variations
5. Provide a systemic comparison on the effects of variations in stimulation dose parameters (electrode location and electrode size) in shaping the cortical and deep brain electric fields
6. Investigate the role of white matter fibre architecture in defining the neural/axonal modulation/stimulation

1.3. Overview of the proposed strategy

The proposed study investigates the behaviour of induced electric field and current density distribution by employing anatomically accurate and structurally detailed human head models. The proposed models exhibit realistic inhomogeneous and anisotropic electrical conductivities. Using the averaged and individual Magnetic Resonance Imaging (MRI) and Diffusion Tensor Imaging (DTI) data, the influence of cortical variations, structural details and directional conductivity on induced electric fields have been examined. The role of model complexity, electrode size, electrode configuration, anisotropic conductivity distribution/variation and neural fibre pathways in defining the site and strength of modulation has also been explored. Due to the ability of the finite element method (FEM) to handle material anisotropic behaviour and complex geometries without discretization errors, the electric field and current density distribution are assessed and mapped using the finite element approach.

So far, most of the research conducted in this field is based on empirical experiences. As a result, a part of this study has been devoted to providing a solid understanding of the underlying bio-physical and neural stimulation/modulation mechanisms. In-

formation such as the spatial distribution of induced electric field and current density inside a head model provides a better understanding of the bio-physiological behaviour of the human head and the response of neural structures based on their intrinsic properties. The study has not used any live or deceased biological samples to validate the approach. Instead it has employed mathematical models and Maxwell equations for cross-validation.

1.4. Scope

The use of over-simplified spherical head models (Datta et al. 2008; Faria, Leal & Miranda 2009; Miranda, Faria & Hallett 2009; Miranda, Lomarev & Hallett 2006), underestimates the contribution of regional morphology, tissue inhomogeneity and anisotropy in the assessment of the spatial distribution of the induced electric field or current density. Geometrically simplified low resolution head models (Im et al. 2008; Im et al. 2012; Wagner et al. 2007), do not consider the role of complex geometries, non-cortical regions (subcutaneous fat and muscles of mastication) and deep brain regions in defining the distribution of field variables (*E/J*). Studies such as Hyun et al. (2009; 2010), Lee et al. (2009) and Oostendorp et al. (2008) employed white matter (WM) and skull anisotropic conductivity in field estimates. However, in these studies, model complexity was limited to five anatomical regions i.e. scalp, skull, cerebrospinal fluid (CSF), grey matter (GM) and white matter (WM). Additionally, the estimates were attributed to specific electrode montages, therefore, it is not possible to generalize the effect of tissue anisotropic conductivity on field parameters. Models developed by Parazzini et al. (2011) and Parazzini, Fiocchi and Ravazzani (2012), were anatomically intricate, however, their estimates are based on isotropic conductivity values. These estimates were also based on Virtual Family models (Christ et al. 2010), therefore, their formulation could not be effective in a clinical environment, especially in subject specific cases where regional brain variations/atrophy would change local field parameters.

Some recent studies have employed high-resolution head models for field assessment (Datta et al. 2009; Salvador, R. et al. 2010). Similarly, the study by Sadler et al.

(2010), employed isotropic electrical conductivities to estimate the field parameters across the cortical and sub-cortical regions. In one of the most recent studies, the analgesic effects of a weak electric field on chronic migraine were analysed using clinical and computational data (DaSilva et al. 2012). Similarly, another study by Parazzini, Fiocchi and Ravazzani (2012) analysed the efficacy of tDCS in the treatment of tinnitus using voxel based head models. Both studies employed isotropic computational models to estimate the spatial distribution of the induced electric field in the particular regions of interest. Using in vivo measurements on monkeys, Logothetis, Kayser and Oeltermann (2007) suggested that the GM was tangentially isotropic. However, studies such as (Hoeltzell & Dykes 1979; Komlosh et al. 2007) reported (regional) anisotropic behaviour in the cortex. Since the site and strength of E-field and its associated current density is coupled with conductivity variations, this may account for the variability in stimulation thresholds with oriented magnetic stimulations (Kammer, Vorwerg & Herrnberger 2007). Wolters et al. (2006), suggested the use of anisotropic estimation by employing Diffusion tensor imaging (DTI) in sub-cortical regions and GM to achieve more realistic assessments on Electroencephalography (EEG) and Magnetoencephalography (MEG) source localization.

Datta et al. (2009) reported the capability of high definition montage to modulate limited regions by confining the induced electric field in close proximity to the stimulating electrode. Studies such as (Borckardt et al. 2011; Minhas et al. 2010) proposed the use of the High-Definition tDCS (HD-tDCS) approach in the treatment of neuropsychiatric disorders due to its ability to deliver a targeted dosage. However, the foundation of these studies is based on the assumption of the brain being isotropic. Such a simplification can easily lead to an inaccurate assessment of dosage delivery and other field parameters. Several EEG, Deep Brain Stimulation (DBS), Electroconvulsive Therapy (ECT) and Electrical Impedance Tomography (EIT) studies have reported significant variations in field parameters by including WM anisotropic conductivity (Abascal et al. 2008; Chaturvedi et al. 2010; De Lucia et al. 2007; Deng, Lisanby & Peterchev 2011; Gullmar et al. 2006; Güllmar, Haueisen & Reichenbach 2010; Hallez, Staelens & Lemahieu 2009; Hallez et al. 2008; Hallez 2007; Haueisen et al. 1997; Haueisen et al. 2002; Kim et al. 2001; Opitz et al. 2011;

Rullmann et al. 2009; Thielscher, Opitz & Windhoff 2011; Wolters 2003; Wolters et al. 2005; Wolters et al. 2006). These models provide some understanding of the underlying mechanism of stimulation/propagation, however, it is not possible to extract tDCS specific information from these models, such as the impact of electrode configurations, strength of stimulation and possible modulation mechanisms.

The spatial distribution of an induced electric field is highly sensitive to electrode configurations and dielectric properties of underlying tissues. It is imperative to understand that the neural response to external electromagnetic stimulation is not only dependent on the strength of the induced fields, but also on the electrophysiological parameters, morphology and orientation of neurons with respect to the induced electric field. An In vitro study by Bikson et al. (2004) reported the dependence of neural polarization on the extracellular electric field. The study cited the influential role of neural orientation in defining the induced fields to be excitatory or inhibitory in nature. Similarly, Kabakov et al. (2012) reported the significance of neural pathway orientation in determining the effects (excitatory or inhibitory) of tDCS. Axonal projections were reported to determine the orientation specific field parameters with dendritic orientation affecting mostly the magnitude of excitation.

Current (forward) models only describe the spatial distributions of induced electric field. These scalar projections are not adequate to elucidate the mechanism of current flow and neural polarization in a volume conductor. Based on the study by Miranda et al. (2007), the component of the induced electric field parallel to the fibre pathways (E_P) can be used to identify the possible sites and strength of excitation along fibre tracts, therefore, ignoring the contribution of E_P, can lead to inaccurate predictions on the site and strength of excitation. E_P becomes quite significant in a scenario of pathological abnormalities of brain tissue such as stroke or brain atrophy. A Study by Korgaonkar et al (2011) reported depression related pathological modifications in the specific WM regions. The study reported (on average) a 7.8% drop in the fractional anisotropy maps (FA) over WM regions associated with the limbic system, dorsolateral prefrontal cortex, thalamic projection fibres, corpus callosum and other associated fibres in patients with severe depression. Such types of abnormalities are detectable by DTI scans and can be traced along particular fibre tracts. Consequently,

the current flow and neural polarization associated with such pathological modifications can easily be assessed and, if required, mitigated in the planning stage of subject specific treatment.

In vitro, three neural interaction mechanisms were examined by Amassian et al. (1994) and Maccabee et al. (1993). Similarly, Nilsson (1992) investigated this interaction using mathematical models. These studies concluded that the excitation of axons, depending upon their morphology, is elicited either by the induced electric field or by its gradient. More recent studies (Miranda et al. 2007; Silva, Basser & Miranda 2008) support the hypothesis that, in central nervous system, stimulation occurs at the peak of electric field rather than at the peak of its gradient. In a recent model based study, Salvador et al. (2011) reported the electrophysiological response of various cortical neurons in a uniform electric field. Even though these stimulation mechanisms can explain the interaction between the induced electric field and the excitable neurons, it is very difficult to accurately estimate the strength of dosage required to stimulate/modulate the targeted excitable population.

1.5. Thesis overview

The dissertation consists of nine chapters. The framework for the development of a realistic human head model is the pivotal part of this study. Chapters 5–8 illustrate various aspects of the human head model design and their implications/contribution in the accurate assessment of induced field parameters.

Chapter 2 presents an extensive overview of the physiology of human brain, neural structure and their role in shaping the electromagnetic stimuli. It also provides a broader coverage on the significance of electromagnetic stimulation and the mechanisms involved in stimuli dose delivery. Clinical implications of transcranial direct current stimulation, the importance of prognostic modelling and most importantly, an in-depth coverage on the development of forward head model design have been provided to familiarise the readers with current trends in forward solutions.

The chapter also provides the mathematical framework for the forward head model design. The application of Maxwell's equations and their quasi-static approximations in the formulation of a source free volume conductor model has been presented. With the use of appropriate boundary conditions, two different possible external sources have been proposed. The general structure for finite element formulation and the definitions of the statistical measures to quantify the accuracy and justify the addition of modelling complexities are presented. These statistical indices are used throughout Chapters 5–8 for the assessment of incremental complexities in the forward head model problem.

Chapter 3 describes the methods and techniques used to construct the realistic finite head models. The chapter starts with the application of the multi-modal imaging protocols required to construct an accurate depiction of the human head. A brief introduction to image registration, segmentation and finite element mesh generation are provided. The tools used to achieve spatial registration, multimodal image segmentation and tetrahedral mesh generation are also presented.

Chapter4 lists the isotropic electric properties of different tissues used in the thesis. The steps involved in the processing of diffusion tensor imaging, extraction and translation of diffusion tensor to conductivity tensors and, incorporation of anisotropic conductivity in non-cortical regions (skull, muscle of mastication and eye-muscles) have been presented. The last part of the chapter describes the materials and methods to track induce electric field and stimulation mechanisms along white matter fibre pathways.

Chapter 5 investigates the influence of the subcutaneous fat and muscle of mastication tissue on cortical current distribution. Using the combination of simulations, comparison with isotropic baseline models, high-end visualization and statistical matrices, the importance of model complexity and anisotropic behaviour of non-cortical tissues are explored.

Chapter 6 extends the methodology used in Chapter 5 to carry out the comparison between the artificial (eigenvalue decomposition) and DTI based anisotropic estimates. Using multi-compartmental tissue models, the strengths and weaknesses of

WM conductivity translation algorithms are analysed. The estimates take field parameters of the isotropic models as a baseline to compare variations in current density magnitude and distribution patterns associated with more complex models. The chapter also highlights the role of individual/subject specific anatomical variations on field distributions and the implications for considering individualised dose parameters on predictive modelling.

Chapter 7 highlights the role of grey matter and sub-cortical anisotropic conductivity on the site and strength of an induced electric field. The head models used in this chapter employ directional conductivity estimates from the measured diffusion tensor data. The chapter presents the effects of electrode position and inter-electrode distance on the possible site and strength of stimulation. Using three different brain conductivity profiles, the role of tissue heterogeneity on field sensitivity is also explored. Field assessments are presented using statistical indices, scalar field maps and electric field vector orientation plots.

Chapter 8 describes the field distributions characterised by High-Definition electrode montages and compares the field parameters in terms of strength and distribution with the conventional tDCS montage. The volume conductor models used in this chapter consider the skull, muscle of mastication and eye-muscles as anisotropic regions. The brain's directional conductivity is introduced using the Equivalent Isotropic Trace scheme. Statistical indices are used for intra-montage analysis and region of interest based ranking is used for inter-montage variations. The Last part of the chapter highlights the importance of white matter anisotropy in shaping the current flow along the selected fibre tracts by predicting significant variations from basic (scalar) current flow maps.

Chapter 9 is the conclusion chapter, which summarises the major outcomes of this study. The chapter also presents the current limitations, possible mitigation plans, as well as future directions.

2. ELECTROMAGNETIC STIMULATION OF HUMAN BRAIN

2.1. Classification of electromagnetic stimulation

Brain stimulation methods can be classified on the basis of their regional/focal influence on a particular neuro-anatomic structure. Examples of these are Deep Brain Stimulation (DBS) and Vagus Nerve Stimulation (VNS) or global effects (non-focal) such as Electroconvulsive Therapy (ECT) and Transcranial Direct Current Stimulation (tDCS). Dose (intensity) and level of invasiveness (surgical exposure) is another classifying factor, ranging from non-invasive treatments such as tDCS and Transcranial Magnetic Stimulation (TMS) to more convulsive approaches such as ECT and Magnetic Seizure Therapy (MST). These approaches initiate seizures and deliver high intensity dosages thus requiring general anaesthesia. DBS and VNS are characterized as more invasive as these procedures involve surgically implanted electrodes or neuro-stimulators. Duration of treatment is another classifying parameter. For instance, in tDCS or ECT based treatment, the treatment normally extends over a period of several weeks, whereas VNS is a long-term strategy suitable for chronic disorders. The side effects of brain stimulation also significantly differ from pharmacological, psychotherapy or physical therapies. Electric current has no metabolite or other residue, therefore the side effects are generally determined by endogenous or behavioural feedback.

2.2. Significance of electromagnetic stimulation

The use of electrical stimulation in the treatment of neurological disorders offers many distinct advantages over pharmacological approaches. The rapid propagation of an induced electric field and the endogenous or adaptive feedback of the brain make it possible to modify the stimulation parameters (dosage and location) based on patient or treatment specifications. Electromagnetic based therapies can also be used to target specific regions and deep brain structures.

The field of brain stimulation has seen significant growth in the last decade. These strategies not only complement conventional therapies and rehabilitations, but also pose as an alternative to ablative surgery. Brain stimulation techniques, such as ECT, are well-established treatments for chronic depression and schizophrenia. Similarly, DBS is widely applied for the focal stimulation of deep brain regions associated with Parkinson's disease. These treatment options being expensive and invasive cannot be administered in a normal clinical environment. TMS and tDCS being non-invasive and easy to administer have seen much attention in recent years.

TMS is a convulsive neuro-stimulation technique, based on Faraday's law of electromagnetic induction. In this technique, an externally applied time varying magnetic field is applied over the target region using very high current impulses. The magnetic field generates a time varying electric field inside the cortex which generates eddy currents. These induced currents are the primary source of cellular (membrane) excitation. Substantial research has been devoted to TMS for its application in physiology and cognitive investigations. TMS is a neuro-stimulation technique which acts at a supra-threshold level, on the other hand, tDCS is a cost effective neuro-modulation technique. Since, tDCS is a sub-threshold procedure, as it generates a modulatory change in the electrical environment of neurons rather than a discrete stimulation. Therefore, its action is similar to the local application of pharmacological agent.

2.3. Introduction to transcranial direct current stimulation

Transcranial direct current stimulation is a non-invasive, painless and sub-convulsive electrotherapy technique. The procedure modulates cortical excitability by a weak direct current via scalp electrodes (Antal et al. 2004; Antal et al. 2011; Fregni et al. 2005; Nitsche 2002; Nitsche & Paulus 2000; Nitsche et al. 2009; Wagner et al. 2007; Williams, Imamura & Fregni 2009). The procedure has been used quite extensively for its potential therapeutic applications in neuro-rehabilitation, depression, chronic pain, focal epilepsy, electroanalgesia, stroke, Alchemize disease and tinnitus (Boggio et al. 2007; Ferrucci et al. 2008; FregniBoggio, et al. 2006; Fregni, Freedman & Pascual-Leone 2007; FregniMarcondes, et al. 2006; Fregni & Pascual-Leone 2007; FregniThome-Souza, et al. 2006; Mignon et al. 1996; Nitsche et al. 2009; Schlaug, Renga & Nair 2008; Vanneste et al. 2010; Webster, Celnik & Cohen 2006; Williams, Imamura & Fregni 2009). tDCS acts at a sub-threshold level, i.e. it does not activate resting neurons, rather it modulates the activation rate of neurons by acting at the level of membrane potential (Sparing & Mottaghy 2008).

2.3.1. Mechanism of dosage delivery

In conventional tDCS, two relatively large sponge pads enclosed in conductive rubber are usually used. In a clinical environment, electric current is delivered via large (20–30 cm^2) sponge pads soaked in a saline solution. The region of electrode in contact with the skin defines the functional parameters of an electrode. At the point of electrode skin contact, the distribution of current density is not uniform. Due to the edge-effect, high current density zones are formed near electrode edges (Minhas, Datta & Bikson 2011; Miranda, Faria & Hallett 2009; Miranda, Lomarev & Hallett 2006). Therefore, electrodes with a large surface area are preferred over small EEG like electrodes. Large electrodes minimize the build-up of high skin currents at the point of contact and distribute the impact of much higher current zones across the rim of electrodes.

The relative position of electrodes is of high significance in shaping the cortical current density distribution patterns. In most of the cases, tDCS electrode montage is bicephalic, where both electrodes are placed at different locations on the scalp (Nitsche

& Paulus 2000). Other, schemes, such as one anode and two cathodes (Miranda, Lomarev & Hallett 2006) and two anodes and two cathodes have also been exploited (Ferrucci et al. 2008). One of the limitations of bi-cephalic montage is the difficulty in isolating the effect induced by the reference electrodes (cathodes) therefore, under certain circumstances, extra-cephalic reference electrode are favoured (Cogiamanian et al. 2007; Im et al. 2012). Using a model based approach, Miranda et al. (2006) reported field strength enhancement in the brain with an increase in distance between electrodes, however, Wagner et al. (2007) reported the greater influence by the relative locations of electrodes.

Model based studies, such as (Datta et al. 2009; Datta et al. 2008) demonstrated the effectiveness of multiple, small, electrodes to achieve focal/localized stimulation at the cost of stimulation strength. Similarly, a study by Nitsche et al. (2007) highlighted the influence of larger electrodes in rendering the stimulation to be ineffective. In theory, a combination of electrodes with different sizes can be used to generate more targeted stimulation. In practice however, the use of smaller electrodes can generate undesirable effects on the superficial regions of the head as there is no clear formulation relating the injected current strength to the electrode area (Miranda, Faria & Hallett 2009). Some recent studies proposed the use of multiple electrodes to optimize the stimulation area by varying location and strength across electrodes. The use of two point electrodes (Im et al. 2008) and multiple electrode schemes (Dmochowski et al. 2011; Park et al. 2011) demonstrated the application of numerical optimization to fine tune the site and strength of induced electric fields.

Our understanding regarding the underlying physiological mechanisms, involved in electromagnetic based stimulation is rather limited. It is believed that the exposure of electromagnetic fields can alter the neural membrane polarization (Peterchev et al. 2011). At a cellular level, the induced electric field generates potential difference across the ends of neurons, causing disturbance in potential across the membrane leading to a current flow across the gradient. This neural current regulates the membrane potential, leading to variations in spontaneous neural activity (Coben & Evans 2010, pp. 319-49).

2.3.2. Dosage and its relationship with excitability

The strength of an induced electromagnetic field is an important parameter that defines the threshold of stimulation. As a result, high field strengths can initiate action potential (neuro-stimulation) and modulate neural activity. A good example is TMS, which works at a supra-threshold level to achieve neuro-stimulation, modulation and secondary synaptic changes.

The electric field induced by tDCS is not strong enough to initiate neuro-stimulation. Primarily, such low strength fields cause local variations in ionic conductance, generating non-propagating electrotonic potential. Lack of sodium channels in dendrites and somata are the main reason for electrotonic conduction. These potentials are non-propagating as they rapidly (exponentially) decay along a stretch of membrane. Neurons with length considerably larger than their diameters use electrotonic potentials to trigger action potentials.

As identified by Tehovnik (1996), the action potential threshold ranges from 22 to 275 A/m^2 for various cortical neural populations. In the case of tDCS, a weak induced field along a stretch of neuron only regulates electrotonic potentials and changes the probability of neural membrane potential to reach the action potential threshold. Under such circumstances, action potential can be achieved by a spatial and temporal cohesive modulation of electrotonic potentials in a neural population.

Depending on the time of exposure, the effects of tDCS can outlast the stimulation period (the after-effect). These after-effects can be sustained for up to few hours (Nitsche et al. 2003; Nitsche & Paulus 2001). Unlike the direct-effect of tDCS which does not significantly alter the synaptic plasticity, pharmacological based studies (Liebetanz et al. 2002; Nitsche, M. et al. 2004; Nitsche, M. A. et al. 2004), suggest that the after-effect requires a combination of glutamatergic and membrane mechanisms, which are similar to the neuroplastic phenomena of long-term potentiation (LTP) and long-term depression (LTD).

Transcranial direct current stimulation can also interfere with cortical excitability via intra-cortical and corticospinal neurons (Ardolino et al. 2005; Nitsche et al. 2005). Studies on the peripheral nerve and spinal cord have also reported the involvement of

non-synaptic mechanisms in the after-effect of stimulation (Ardolino et al. 2005; Cogiamanian et al. 2008).

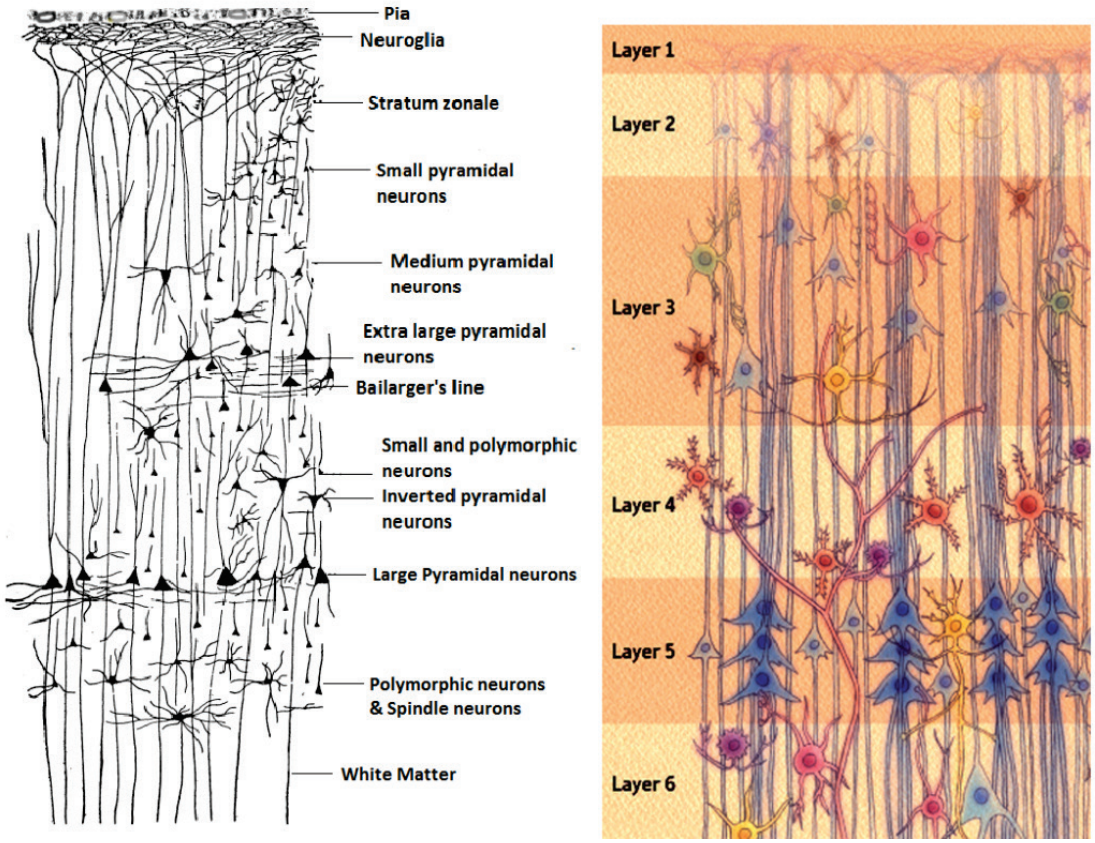

Figure 2.1: The layered structure of cerebral cortex. Source: http://chronopause.com.

Since tDCS regulates cortical activities in a polarity dependent manner, anodal tDCS generally enhance spontaneous neural activities, and cathodal tDCS is attributed to attenuation or inhabitation (Nitsche & Paulus 2000; Purpura & McMurtry 1965). Hyper or depolarization of neurons is attributed to their capacitive behaviour, however, the strength and direction of neural polarization also depends on the length, size and morphology of neurons. Similarly, orientation of axons, dendrites and soma with respect to the induced electric field, also play an equally important role. Bikson et al. (2004) hypothesized the linear relationship between the effect of an induced electric field on neurons and its magnitude. However, there are other factors which also contribute to the final output of the stimulation. The in vitro study by Radman et al.

(2009) suggests that, under an optimally oriented sub-threshold electric field, soma of pyramidal cells in layer V of rat cortical tissue were most sensitive to polarization. The same study also reported that neurons in cortical layer V and VI had the lowest action potential thresholds. Figure 2.1 illustrates the layered structure of cerebral cortex.

2.4. Scope of tDCS forward head modelling

Neurophysiological effects (after-effect) of tDCS are dependent on the strength and duration of stimulation. The orientation and strength of an induced electric field and current density define the polarity specific behaviour. Neurophysiological studies suggest that during the administration, the "direct-effect" of stimulation is attributed to the neural membrane (potential) modulation. The "after-effect" which can persist for a few minutes to hours (after the administration) involves NMDA-receptor dependent mechanisms.

The strength and distribution of induced electric field and current density play a crucial role in defining the rate and possible site of neural activation/modulation, yet very little is known about the factors which may influence the intensity and spatial distribution patterns of cortical currents. Low cost, portability and ease of application/administration make tDCS an ideal tool in cognitive neuroscience and neuropsychiatric therapy. Transcranial direct current stimulation has established itself as a safe, well tolerated therapeutic tool and, unlike pharmacological based treatments, this tool offers a non-invasive alternative which is customizable and reconfigurable to stimulate different regions of a brain.

In order to improve subject and target specific treatment along with robust interpretation of patient specific results, electrotherapy dosage and individual anatomical details play a significant role. The site and strength of modulation is determined by the dosage as it determines the strength of injected current along with the shape, size, number and position of electrodes. Individual anatomical details also pose a major challenge in identifying the proper site of modulation and dosage parameters.

2.4.1.The forward human head model

2.4.1.1. Analytical and simplified numerical head models

In order to find the optimal stimulation parameters such as the strength and spatial distribution of induced electric field and current density, a number of analytical and computational models have been developed. These models vary in anatomical and, physiological details and complexities. The spherical volume conductor models are an over-simplified depiction of the forward problem. Earlier studies described the volume conductor as a single homogeneous sphere (Ary, Klein & Fender 1981; Brody, Terry & Ideker 1973; Frank 1952; Wilson & Bayley 1950). Similarly, in TMS, Eaton (1992) proposed a single layer homogeneous model to calculate the E-field distribution in the volume conductor by a time-varying magnetic field.

Rush & Driscoll (1969; 1968) proposed the analytical solution of a 3-layer spherical volume conductor model. The authors used the 3-layer inhomogeneous volume conductor model, consisting of scalp, skull and brain to estimate the current density distribution due to two external (point) electrodes. They demonstrated that the estimates were in good agreement with experimental measurements. By using multiple electrode positions, the authors hypothesized that approximately 45% of the injected current could enter the brain. Using the same model, Saypol et al. (1991) performed a comparative study on the electric field distribution generated by external electric and magnetic sources. Using finite size electrodes, Stecker (2005) extended the work of Rush and Driscoll (1969; 1968) to examine the role of electrode size on field distribution. The four layer models illustrated the importance of including the CSF in forward computation (Ferdjallah, M., Bostick, F. X. & Barr, R. E. 1996; Neil Cuffin & Cohen 1979; Stok 1986). In the case of TMS, the CSF was shown to effectively shunt the induced current away from the spinal cord (Scivill, Barker & Freeston 1996). Using a square model with two dissimilar conductivities, Ren & Ueno (2000) showed that the conductive boundaries have an altering effect on the induced field distributions.

The first semi-analytical solution to deal with anisotropy in the EEG forward problem was proposed by De Munck (1988). The proposed model could simulate the ef-

fect of anisotropic conductivity in all except the inner-most layer. This model was further refined by Munck and Peters (1993) to incorporate anisotropy in even the inner-most layer. The procedure proposed by De Munck was further generalized by Zhou & Van Oosterom (1992). Using a semi-analytic procedure the authors computed the potential distribution for a 4-layer spherical model with isotropic and various anisotropic conductivity values. The authors concluded that the radial conductivity of the skull and the tangential conductivity of the brain greatly influence the potential distribution on the scalp. There are no analytical models available to represent anisotropy in tDCS or TMS however, using reciprocity, the transition from EEG or MEG field modelling to tDCS models is relatively seamless. The underlying physics involved in calculating these field parameters are similar. In the EEG/MEG forward problem, the sources (inside the head model) and the properties of the head model are known, whereas the field distribution inside the head is unknown. In tDCS/TMS, the known source (electrodes/coil) is outside the head model, the geometric and the material properties of the head model are known and the induced E-field inside the volume conductor is unknown. Compared to EEG or MEG source models, the source of tDCS is strong. Therefore, certain assumptions and boundary conditions need to be modified according to tDCS E-field modelling.

2.4.1.2. Numerical volume conductor models

Using a finite element model of the human head with 13 different tissue types, Haueisen et al. (1997) concluded that the tissue resistivity greatly affects the magnetic field close to the source. Therefore, skull directional conductivity must be examined for its contribution in the distortion of magnetic field distribution, especially when the geometry is not symmetrical. By using FEM, Mohr (2003) performed a comparison between various iterative solvers by calculating the bioelectric field in EEG forward models. Although, the main objective of the study was to assess the performance and accuracy of various solvers, the author also illustrated the effects of tissue inhomogeneity and anisotropy on the volume current distribution.

Using an inhomogeneous spherical head model, (Miranda, Lomarev & Hallett 2006) assessed the current density distribution under the influence of conventional electrode sizes. The current density was observed to be highly non-uniform at the scalp-

electrode interface and the strongest magnitude of current density was located on the scalp, confined by the rim of electrodes (the edge effect). Depending on the electrode configuration, the skull attenuated approximately 40–60% of the injected current. Low conductivity of the skull caused the field distribution to be significantly weaker in magnitude and uniform in distribution across the spherical brain region. The current flow was mostly radial under the electrodes and between electrodes it was observed to be tangential. Studies such as (Datta et al. 2008; Faria 2010; Faria, Hallett & Miranda 2011; Faria, Leal & Miranda 2009) employed inhomogeneous finite element spherical volume conductor models to analyse the role of multiple electrode schemes on the focality and distribution of induced fields (*E/J*). These studies reported improvement in the focality of stimulation under multiple small electrode configurations at the cost of field strength. Increasing the inter-electrode distance resulted in decreased shunting of the current through the scalp and vice versa. Electrodes with different sizes generated asymmetric current distributions causing relatively localized fields under small electrodes.

In Transcranial Electric Stimulation (TES), the relatively lower conductivity of the skull plays a crucial role in defining the magnitude and distribution of field parameters. In some studies, the skull has been considered as a single anisotropic region (Hyun et al. 2009; Hyun et al. 2010; Oostendorp et al. 2008; Wolters 2003; Wolters et al. 2006) whereas, in most of the studies the skull has been considered as a single homogeneous and isotropic region (Datta et al. 2009; Im et al. 2008; Miranda, Faria & Hallett 2009; Miranda, Lomarev & Hallett 2006; Sadleir et al. 2010; Wagner et al. 2007). The human skull, in fact, is composed of three distinguishable regions, spongoasa enclosed in compacta bone, and the idea of skull being anisotropic is associated with its layered composition. A recent study by Sadleir et al. (2007) reported such a scheme to be sub-optimal, however, a most recent study suggests that both the anisotropic and isotropic approximations are valid as the optimal conductivity values are largely dictated by the equivalent radial conductivity of the three-layered skull (Rampersad, Stegeman & Oostendorp 2011, 2012).

Using the finite element approach, Ramon et al. (2004; 2006) investigated the effects of head model complexity on the distribution of volume currents. The authors constructed four models with increasing complexity (from 5 tissue to 11 tissue types)

and assessed the influence of complexity on EEG source localization. The study concluded that the model complexity and the inclusion of CSF play a significant role in the volume current distribution. Even though, in tDCS, the effect of model complexity has not yet been assessed directly, studies such as Datta et al. (2009) and (Datta, Bikson & Fregni 2010) used MRI derived high-resolution individual head models to assess the field distribution in the presence of refined cortical geometry and skull defects. Sadleir. et al. (2010) employed 10 different tissue types and analysed the field distribution in the specific regions of interest. Studies such as DaSilva et al. (2012), Parazzini, Fiocchi and Ravazzani (2012) and Parazzini et al. (2011) used multiple cortical and sub-cortical regions in field assessment. So far, there are no studies in TES or tDCS dealing directly with the importance of model complexity in field estimation.

Extending the work of Haueisen et al. (2002), Wolters (2003) proposed a technique to introduce white matter anisotropy in the FE models. Using the assumption proposed by Basser, Mattiello & LeBihan (1994b) that effective electrical conductivity tensor shares the eigenvectors with the effective diffusion tensor of water and that, there exists a linear relationship between the electrical conductivity tensor and the effective diffusion tensor in brain white matter (WM) (Tuch et al. 1963; Tuch et al. 1999), the author illustrated the significance of WM anisotropy on the accuracy of source localization in both EEG and MEG. Using a similar approach, studies such as Hyun et al. (2009, 2010) and Oostendorp et al. (2008) employed skull and WM anisotropy for tDCS forward modelling. These studies used point electrodes rather that actual size electrode pads. Such an assumption causes the current density, at the point of contact, to be unrealistically high, which may impede accurate estimates of current density. Additionally, their model complexity is limited to five regions i.e. scalp, skull, CSF, grey matter and white matter. These studies also highlighted the combined effect of skull and WM anisotropy, therefore, it is not possible to estimate the individual effects of skull and WM anisotropy. Since, the root causes of skull and WM anisotropy are different, they have altogether different effects on the field parameters.

Hallez et al. (2005) proposed the finite difference model based on reciprocity (Rush & Driscoll 1969) to solve the EEG forward problem. The proposed model was spher-

ical with 5 layers and included skull and WM anisotropy. By comparing the results with the analytical model (Munck & Peters 1993), the authors concluded that the exclusion of skull and WM anisotropy lead to dipole localization errors of 13 and 11%, respectively. However, for their models to exhibit anisotropy, the grid size should be less than 1mm which when introducing real geometry, greatly increase the computational cost. This is another reason that the proposed study aimed to use the FEM.

Employing a 5-layer anatomically accurate head model, Wolters et al. (2006) examined the influence of structural and electrical anisotropy in both the skull and the WM based on EEG and MEG source reconstruction. Using FEM and making use of both the Wang Constraint (Wang, Y., Haynor, D. & Kim, Y. 2001) and Volume Constraint (Wolters 2003), the authors provided an insight into the effects of the skull and WM anisotropy based on field distribution maps, isopotential surfaces, return current flow and statistical error estimates. They found that the WM anisotropy channels the flow of return currents in directions parallel to WM fibre tracts.

When extracting anisotropic conductivities from DTI, the data also show diffusion trends in grey matter (GM). Wolters et al. (2006) suggested the use of anisotropic estimation, by employing DTI, in sub-cortical and GM to achieve more realistic assessment on EEG and MEG source localization. Hallez et al. (2007) investigated GM anisotropic behaviour on EEG source localization. Due to the low fractional anisotropy, the authors concluded that the effect of GM anisotropy had negligible effects on source localization. Bangera et al. (2010) used the experimental data gathered by employing deep brain electrodes to consenting subjects. The authors used the exact location of electrodes to create dipolar at known locations in the brain and at the same time recorded the EEG signal. Using the coordinates of dipolar sources, dipoles were introduced in different FE models of increasing complexity and DTI data was used to introduce WM anisotropy. The study found that the return currents do not align completely with fibre directions but are channelled in a general direction of a fibre with more alignment than the isotropic scenario.

Güllmar, Haueisen & Reichenbach (2010) investigated the influence of WM directional conductivity on EEG/MEG forward and inverse solution. They used a detailed high-resolution head model and introduced anisotropic conductivity to WM by using

DTI data. By using 25000 dipoles as source over the entire neocortex they concluded that if a high-resolution FE model were to be used in EEG/MEG source localization, the influence of WM anisotropy had to be considered. Using an Electroconvulsive therapy based computational model, Lee et al. (2010, 2011) demonstrated the implication of WM anisotropy (using fixed anisotropy ratio) in conjunction with various electrode configurations.

In this dissertation, the notion of the forward head model has first been explored in terms of the EEG forward problem, and is then extended to tDCS paradigm. In case of tDCS, the effects of geometry, source and material properties (inhomogeneous and anisotropic conductivity) on current density/electric field distribution are not identical to that of the EEG forward problem. The effect of charge accumulation in TES further complicates the overall current distribution in a volume conductor model. Additionally, modality specific information, such as the role of electrode montage and strength of stimulation on field parameters is not easy to comprehend using the EEG based forward models.

2.5. Mathematical formulation of forward head model

The field of bioelectromagnetism can be classified on the basis of Principle of Reciprocity and Maxwell's equations. "*Based on the principle of reciprocity, the sensitivity distribution in the detection of bioelectric signals, the energy distribution in electric stimulation and the sensitivity distribution of electric impedance measurement are the same*" (Malmivuo & Plonsey 1995). The statement is also valid for the associated bioelectromagnetic and biomagnetic procedures. Maxwell's equations, on the other hand, describe the electromagnetic behaviour or the interaction of electric and magnetic fields on each other. On the basis of field specific behaviour, bioelectromagnetism can be classified on the foundation of either bioelectric, biomagnetic or bioelectromagnetic paradigms.

In the field of tDCS, the biological material (tissue) can be considered as conductive medium therefore, it is possible to generalize the formulation of Maxwell's equation for bioelectromagnetics problem (Malmivuo & Plonsey 1995).

2.5.1.Maxwell's equations

The Maxwell's equations for time varying electromagnetic field in differential and integral forms are given by:

$$\nabla \cdot D = \rho_v \Rightarrow \oint_s D.ds = \int_v \rho_v \cdot dv = Q_{enclosed} \tag{2.1}$$

Gauss's Law for electric field

$$\nabla \cdot B = 0 \Rightarrow \oint_s B \cdot ds = 0 \tag{2.2}$$

Gauss's Law for magnetic field (non-existence of magnetic monopole)

$$\nabla \times E = -\frac{\partial B}{\partial t} \Rightarrow \int_l E \cdot dl = -\frac{\partial}{\partial t}\int B \cdot ds = V \tag{2.3}$$

Faraday's Law

$$\nabla \times H = J + \frac{\partial D}{\partial t} \Rightarrow \int H \cdot dl = \int (J + \frac{\partial D}{\partial t}) \cdot ds = I_{Total} \tag{2.4}$$

Ampere's Law

where D is the electric flux density or electric displacement (C/m^2), ρ_v is the volume charge density. Q is the charge; B is the magnetic flux density (*Tesla* or $Weber/m^2$); E is the electric field intensity (V/m); V is the potential difference, H is the magnetic flux density (A/m); J is the conduction current density (A/m^2) and $\partial D/\partial t$ is the displacement current density (A/m^2).

By taking divergence of eq. (2.4) (divergence of a curl of a vector field vanishes), the equation of continuity can be obtained by eq. (2.1) and is given by:

$$\nabla \cdot J = -\frac{\partial \rho_v}{\partial t} \tag{2.5}$$

Since eq. (2.1–2.5) are indefinite, it is necessary to relate these field quantities using experimental observations. For example, when an electric field is applied to a conductor, conduction current occurs due to the drift motion of electrons. The conductor atoms remain neutral ($\rho_v=0$) and the whole conductor remains at rest. The average drift velocity of electrons is directly proportional to the applied field. Therefore, for a conductor, the constitutive relation between the induced electric field and the current density is given by:

$$J = \sigma E \tag{2.6}$$

And, for a dielectric, the constitutive relationship between the electric flux density, magnetic flux density and their corresponding fields are given by:

$$D = \varepsilon E \tag{2.7}$$

$$B = \mu H \tag{2.8}$$

where, σ, ε and μ are the conductivity (*S/m*), permittivity (*F/m*) and permeability (*H/m*) of a medium, respectively and for anisotropic materials, these parameters are defined in terms of tensors. Transcranial direct current stimulation technique involves the injection of external current via scalp electrodes. Therefore, the total amount of current density is given by:

$$J = J_{conduction} + J_{source} \tag{2.9}$$

where $J_{conduction}=\sigma E$ is the ohmic current and J_{source} represents the current source.

2.5.2. Quasi-static approximation

In the frequency range of DC – 10 kHz, several approximations can be considered to simplify the field solution (Ferdjallah, M., Bostick, F. & Barr, R. 1996; Heller & van Hulsteyn 1992; Plonsey & Heppner 1967; Webster & Hughes 1991). Since, in this frequency range, the wavelength is several orders of magnitude larger than the di-

mensions of a biological medium, therefore the phase of the electric field can be assumed to have a constant value within, and in, the vicinity of a material (propagation effects). Additionally, the eddy currents generated by the magnetic field due to the induced electric field are negligible (inductive effects: $\varepsilon << \sigma/\omega$) and finally, tissue capacitive effects are also considered insignificant. The expression ($\sigma + j\omega\varepsilon$) defines the complex material properties of the biological medium. For capacitive effects (ε) to be ineffective, $j\omega\varepsilon/\sigma << 1$. Therefore, for tDCS and TMS, tissue capacitive effects can be ignored and the only dominant factor is the material conductive/resistive property (σ). In other words, biological material exhibit strong resistive behaviour in the frequency range of DC – 10 kHz. As a consequence of quasi-static approximation, it is possible to decouple the electric and magnetic fields by ignoring the time varying electric flux density (D) and the magnetic flux density (B) from equations (2.3) and (2.4), respectively.

Under the quasi-static assumption, the field and its sources vary slowly, therefore their time derivatives can be ignored, i.e.

$$\nabla \cdot J = 0 \tag{2.10}$$

Equation (2.10) indicates that the total current density must be solenoidal and the electric field is divergence free, i.e.

$$\nabla \cdot D = 0 \tag{2.11}$$

$$\nabla \cdot B = 0 \tag{2.12}$$

$$\nabla \times E = 0 \tag{2.13}$$

$$\nabla \times H = J \quad as \frac{\partial D}{\partial t} = 0 \tag{2.14}$$

i.e. the displacement current is negligible compared to the conduction current. In bioelectromagnetism, the current density (J) is the summation of ohmic current (σE), the external source current (J_{source}) and the impressed current (J_s).

$$J = \sigma E + J_s + J_{source} \tag{2.15}$$

The impressed current is a non-conservative current caused by the bioelectric activity of nerve and muscle cells due to the conversion of energy from chemical to electrical form (Malmivuo & Plonsey 1995). The basic building block of this non-conservative current is the electric current dipoles therefore, the impressed current density is equivalent to the volume dipole moment density of a source. In the case of tDCS the source current is not ionic in nature rather it is externally applied, therefore, the term J_s is considered zero ($J_s=0$).

By taking the divergence across both sides of eq. (2.6):

$$\nabla \cdot J = \nabla \cdot \sigma E \tag{2.16}$$

Under the quasi-static assumption, the induced electric field is governed by the following equation:

$$E = -\nabla V \tag{2.17}$$

where V is the potential difference.

By using eq. (2.17) in eq. (2.16)

$$\begin{gathered} \nabla \cdot J = \nabla \cdot \sigma(-\nabla V) \\ or \\ \nabla \cdot \begin{bmatrix} \sigma_{xx} & \sigma_{xy} & \sigma_{xz} \\ \sigma_{yx} & \sigma_{yy} & \sigma_{yz} \\ \sigma_{zx} & \sigma_{zy} & \sigma_{zz} \end{bmatrix} \begin{bmatrix} \partial V/\partial x \\ \partial V/\partial y \\ \partial V/\partial z \end{bmatrix} = 0 \qquad \text{in } \Omega \end{gathered} \tag{2.18}$$

Under steady state and appropriate boundary conditions, eq. (2.18) (the Laplace's equation) has a unique solution. Therefore, expressions (2.17) and (2.6) can be used to estimate the electric field and the current density, respectively.

2.5.3. Boundary conditions

Maxwell's equations cannot be solved without the specification of the required boundary conditions at the material interfaces. In tDCS these boundary conditions describe the forward problem by defining the relationship between the external stimulation and the estimated potential gradients in a volume conductor model. Equation (2.18) describes the field distribution in the head model domain Ω due to an external stimulus (Figure 2.2). The boundary condition (2.19) expresses the continuity of the normal component of the current density between regions of different conductivity.

$$\begin{gathered} \left(n \cdot J_1\right)\big|_{\Gamma_i} = \left(n \cdot J_2\right)\big|_{\Gamma_i} \\ \text{or} \\ \left[n.(\sigma \nabla V_1)\right]\big|_{\Gamma_i} = \left[n.(\sigma \nabla V_2)\right]\big|_{\Gamma_i} \end{gathered} \tag{2.19}$$

The boundary condition (2.19) is only applicable across the inner boundaries (Γ_i) of a volume conductor. On the head surface i.e. the exposed boundaries (Γ_e) are considered electrically insulated and are represented by Neumann boundary conditions:

$$\begin{gathered} (n \cdot J)\big|_{\Gamma_e} = 0 \\ \text{or} \\ \left[n.(\sigma \nabla V)\right]\big|_{\Gamma_e} = 0 \end{gathered} \tag{2.20}$$

The exposed surface of cathode (Γ_s) is assigned the Dirichlet boundary (*V=0 volts*) condition, whereas, the exposed surface of anode (Γ_s) can be assigned with either the Dirichlet ($V=V_0$ *volts*) or the Neumann ($n \cdot J = J_n$ *A/m*^{2}) boundary conditions. Where V_0 is the fixed electrode voltage and J_n is the surface current density normal to the electrode surface.

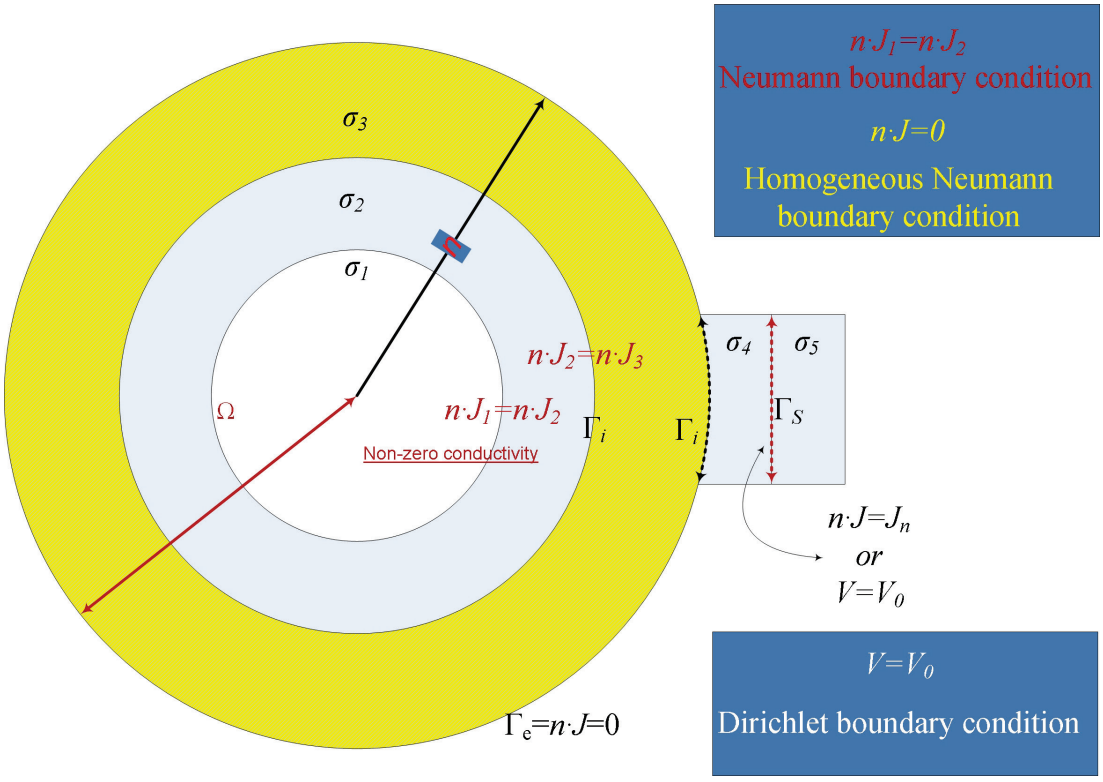

Figure 2.2: The general bioelectric problem. The domain Ω is divided into a number of subdomains, classified by their individual electrical conductivities.

2.6. Numerical modelling formulation for tDCS

The finite element method is one of the most successful computational methods for electromagnetic simulations. The method is well suited for solving the boundary value problems (BVP) that arise in bioelectromagnetism. The method is flexible as it accommodates geometrical adaptability and material generality for modelling arbitrary shapers (geometries) and materials of any composition. Beside FEM, there exist several numerical techniques capable of addressing various aspects of electromagnetic modelling with their specific advantages and limitations (Sadiku 2000).

In the past, the boundary element method (BEM) has been used quite extensively in head modelling and EEG source localization (Cuffin et al. 2001; Hamalainen & Sarvas 1989; Scheler et al. 2007; Yvert et al. 1997). The BEM solves the BVP by converting the equations into a set of integral equations defined over surfaces of piecewise homogeneous isotropic compartments. The method can handle complex geome-

tries and calculations are only performed on the compartmental boundaries. As a result, the computational cost is low but at the same time material composition has to be isotropic.

The finite difference method is another numerical technique capable of addressing arbitrary shapes and complex material compositions. Unlike BEM, FDM is easily implementable, however this technique uses a regular grid (mesh) and any boundary must be interpolated as a staircase slope. Consequently, field variables outside the grid must be interpolated. In the case of head modelling, the complex and detailed anatomical features require a very refined grid which can lead to undesirably high computational cost.

2.6.1.Finite element method based formulation

In FEM, the volume conductor model (domain) is classified in terms of sub-domains with unknown functions represented by a simple interpolation function with known coefficients. The entire system is then approximated by a finite number of unknown coefficients. The linear system of algebraic equations can be formulated by either Variational Approach (Rayleigh–Ritz method) or Weighted Residual (Galerkin) method and the field variable (V) is determined by solving a linear system of equations using some efficient solvers (Bastos & Sadowski 2003; Jin 2002).

The elliptical (governing) equation with the state variable $V(x,y,z)$ over the domain Ω is given by:

$$-\nabla \cdot \left(\sigma \nabla V\right) + aV = f \quad in \ \ \Omega \tag{2.21}$$

Where σ is the conductivity, "a" is a constant and f is the source term. Since the elliptical equation is the general form of the Poisson and Laplace equation and by setting a=0, equation (2.21) becomes the Poisson's equation whereas, by setting f=0, Laplace's equation is obtained. By assuming the generalized Neumann boundary condition over the entire domain and projecting eq. (2.21) on the subspace of the state variable, it is possible to find the solution (u) of the elliptical differential equation (2.21) over the domain Ω:

$$\int_{\Omega}\left[-\left(\nabla\cdot\left(\sigma\nabla V\right)\right)\cdot\psi+a\cdot V\cdot\psi\right]dv=\int_{\Omega}f\cdot\psi dv \tag{2.22}$$

applying Green's theorem

$$\int_{\Omega}\left(\psi\nabla V^{2}V+\nabla\psi\nabla V\right)dv=\oint_{\Gamma=d\Omega}\psi\frac{\partial V}{\partial n}ds \tag{2.23}$$

$$\therefore\int_{\Omega}\left[\left(\sigma\nabla V\right)\cdot\left(\nabla\psi\right)+a\cdot V\cdot\psi\right]dv-\oint_{\Gamma=d\Omega}\sigma\cdot\psi\frac{\partial V}{\partial n}ds=\int_{\Omega}f\cdot\psi dv \tag{2.24}$$

The generalized Neumann boundary condition is given by:

$$\sigma\frac{\partial V}{\partial n}+qV=g \tag{2.25}$$

by substituting $q=g=0$

$$\sigma\frac{\partial V}{\partial n}=0 \tag{2.26}$$

Equation (2.26) is only valid when the subspace $x\rightarrow X$ and then the solution for ψ will approximate the subspace. By assuming Neumann boundary condition (2.25) on the exposed boundary, except for the location of electrodes, equation (2.24) takes the form:

$$\int_{\Omega}\left[\left(\sigma\nabla V\right)\cdot\left(\nabla\psi\right)+a\cdot V\cdot\psi\right]dv-\oint_{\Gamma=d\Omega}(g-q)\cdot\psi ds=\int_{\Omega}f\cdot\psi dv$$

$$or$$

$$\int_{\Omega}\left[\left(\sigma\nabla V\right)\cdot\left(\nabla\psi\right)+a\cdot V\cdot\psi\right]dv \qquad (2.27)$$

$$-\int_{\Omega}f\cdot\psi dv-\oint_{\Gamma=d\Omega}(g-q)\cdot\psi ds=0\quad for\ all\ \psi$$

Equation (2.27) is called the variational or weak form of a differential equation and is obtained by substituting the unknown function (V) with a test function (ψ) in the governing equation and multiplying it by a weighted function. In order to translate the weak form of the differential equation to the finite-dimensional subspace xN, it is imperative to define this subspace as xN [illegible] with V and x in it. As equation (2.27) is valid for all ψ, it is helpful to define N basis functions that span ψ i.e. $V_i \in \psi N$ Hence

$$\psi(l)=u(l)=\sum_{j=1}^{N}U_jV_j(l) \qquad (2.28)$$

The expression (2.27) is known as the Galerkin's method and can further be extended using V and ψ:

$$\sum_{j=1}^{N}\left(\int_{\Omega}\left[\left(\sigma\nabla V_j\right)\cdot\nabla V_i+aV_jV_i\right]dv+\oint_{\Gamma=d\Omega}qV_jV_ids\right)U_j$$

$$=\int_{\Omega}fV_idv+\oint_{\Gamma=d\Omega}gV_ids \qquad (2.29)$$

$$for\ i=1\cdots\cdots N$$

where $\int_{\Omega}\left(\sigma\nabla V_j\right)\cdot\nabla V_idv=K_{i,j}$, $\int_{\Omega}aV_jV_idv=M_{i,j}$, $\oint_{\Gamma=d\Omega}qV_jV_ids$ $=Q_{i,j}$, $\int_{\Omega}fV_idv=F_{i,j}$ and $\oint_{\Gamma=d\Omega}gV_ids=G_i$

In matrix form equation (2.29) can be written as:

$$\begin{gathered}(K+M+Q)U=F+G \\ or \\ KU=F\end{gathered} \tag{2.30}$$

where U is the solution matrix (potential at the nodes of a mesh), which can be obtained by solving the set of linear equations in (2.30). The boundary conditions are satisfied implicitly and automatically in the solution process.

2.7. Assessment criteria for model comparison

To estimate the field parameters, such as the strength and distribution of induced electric field and current density associated with different proposed models, the following statistical indices have been used:

Correlation coefficient (CC)

$$CC=\frac{\sum_{i=1}^{n}\left(\left(X_i^{BASELINE}-\overline{X}^{BASELINE}\right)\left(X_i^{VAR}-\overline{X}^{VAR}\right)\right)}{\left(\sqrt{\sum_{i=1}^{n}\left(X_i^{BASELINE}-\overline{X}^{BASELINE}\right)^2}\right)\left(\sqrt{\sum_{i=1}^{n}\left(X_i^{VAR}-\overline{X}^{VAR}\right)^2}\right)}$$

$$where \tag{2.31}$$

$$\overline{X}=\frac{\sum_{i=1}^{n}X_i}{n}$$

where $X^{BASELINE}$ is the baseline parameters, such as the electric field or current density of the isotropic head model, and X^{VAR} represents the same field parameters for different head models considered in the comparison. The Correlation coefficient is a statistical technique used to identify the degree of relationship among the variables. The range of CC varies from -1 (negative relation) to 1 (positive correlation) with 0 identifying that there is no relationship between the variables.

Magnification factor (MAG)

MAG is the measure of magnitude variation among the variables. The errors are given in terms of a scaling ratio with MAG =1 corresponding to a perfect match in the magnitude of base line and variable parameter (Meijs et al. 2002).

$$MAG = \frac{\sqrt{\sum_{i=1}^{n}\left(X_i^{BASELINE}\right)^2}}{\sqrt{\sum_{i=1}^{n}\left(X_i^{VAR}\right)^2}} \tag{2.32}$$

Relative difference measure (RDM)

RDM is the measure of topographic variation (Meijs et al. 2002). The minimum error corresponds to 0 and the maximum topographic error corresponds to an RDM of 1. RDM is insensitive to the scaling variations among the data sets been compared, making it an ideal choice for comparison of distribution differences among field parameters.

$$RDM = \sqrt{\sum_{i=1}^{n}\left(\frac{X_i^{BASELINE}}{\sqrt{\sum_{i=1}^{n}\left(X_i^{BASELINE}\right)^2}} - \frac{X_i^{VAR}}{\sqrt{\sum_{i=1}^{n}\left(X_i^{VAR}\right)^2}}\right)^2} \tag{2.33}$$

Residual error (RE)

$$RE = \sqrt{\frac{\sum_{i=1}^{n}\left(X_i^{BASELINE} - X_i^{VAR}\right)^2}{\sum_{i=1}^{n}\left(X_i^{VAR}\right)^2}} \tag{2.34}$$

2.8. Chapter summary

The chapter provided an in-depth literature survey on the electromagnetic based stimulation mechanisms. The tissue-stimuli interaction at macroscopic scale (tissue level) and microscopic scale (cell level), role of predictive modelling in devising the stimulation parameters and in-depth coverage on various aspects of the forward model development were provided. The chapter also provided the mathematical groundwork for the forward head modelling and numerical modelling formulation for passive volume conductor models of TES.

3. HUMAN HEAD MODEL DEVELOPMENT

3.1. Realistic human head model construction

The construction of a realistic, anatomically accurate head model is a complex task. The procedure involves the assimilation of various clinically available modalities to represent the true structural details and material composition of a human head. In bioelectric field modelling, it is imperative to consider those imaging modalities which can be used to distinguish between different tissues. Magnetic Resonance Imaging (MRI) can provide detailed contrast among soft tissues, such as grey matter and white matter, whereas Computed Tomography (CT) is more suitable for identifying hard tissue such as bone. MRI is completely safe for humans as it measures the hydrogen density within the targeted region. The proton (H^+) density varies significantly between soft tissues and as a result it is easy to distinguish cortical tissue like grey matter from white matter. Hard tissue does not contain sufficient protons (H^+) and, as a result, it is difficult to isolate the skull region by using just a single MRI scan type. CT scans are not advisable for routine physiological examination in healthy humans as CT measures the absorption of ionizing radiation (X-rays) along their path through the body. Hard tissue such as bone absorbs a relatively large proportion of radiation. As a result, it is easy to identify skull, diploe inside a skull and sinuses with CT.

In MRI, the contrast between different tissues depends on their proton density. A strong spin echo signal corresponds to a high proton density in the tissue and the image intensity also depends on the relaxation time T1 and T2. The image contrast of a

T1-weighted MRI is greatly affected by the longitudinal relaxation time (T1) in a non-linear manner and also by proton density (Tofts 2005, pp. 111-41). Similarly, in a T2-weighted MRI, image contrast is mainly influenced by the Transverse relaxation time (T2). Since T1-weighted MRI uses short echo time (TE) and repetition time (TR), T1 scans show a high level of contrast between soft tissue and better differentiation between solid and fluid filled tissue. In contrast, a T2-weighted MRI uses longer TE and TR as T2 determines the signal decay after excitation therefore, the image has a high signal intensity for CSF and other fluids (Tofts 2005, pp. 142-201).

Proton Diffusion-Weighted MRI (PD-MRI) scans ideally have no contrast from either T1 or T2 decay, however suitable corrections for T2 and occasionally T1 losses are made due to practical constraints. In PD-weighted images the contrast in signal strength is due to the amount of available spins. The scan uses a spin echo or gradient echo sequence with short TE (to minimize T2 losses) and long TR (to minimize T1 losses) (Tofts 2005, pp. 85-109). Due to the special characteristic of PD-weighted MRI, these images can be used for the identification of the inner skull layer. In this study, T1-weighted MRI (to identify soft tissues) with co-registered T2-weighted MRI (to identify fluid/CSF) and co-registered PD-weighted MRI (to segment inner skull surface) were employed to improve the modelling of CSF/ventricular, skull and non-cortical regions, such as sub-cutaneous fat and muscle of mastication.

The steps involved in the construction of a high-resolution finite element head model are presented in Figure 3.1. Steps such as image registration, image segmentation, electrode design, 3D model construction and tetrahedral mesh generation are presented in this chapter. Methodology involving boundary condition assignment and selection of appropriate governing equation were discussed in Chapter 2. The schemes to incorporate isotropic and anisotropic material properties in a volume conductor model are discussed in Chapter 4.

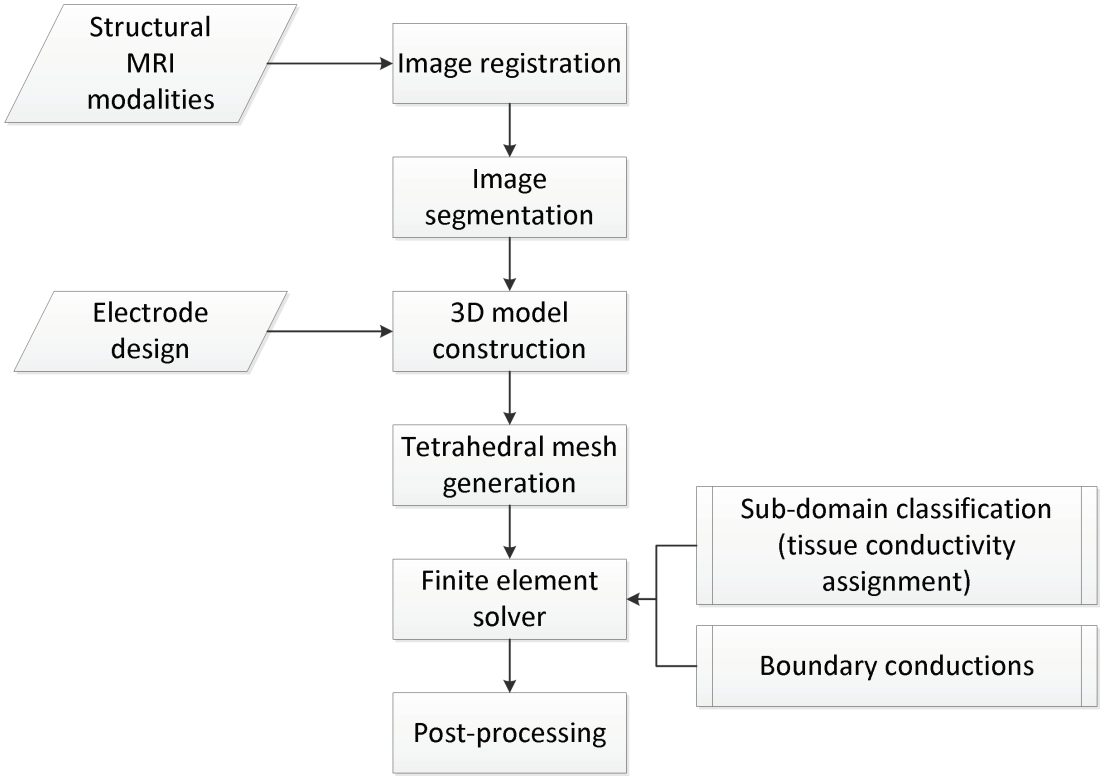

Figure 3.1: Isotropic finite element head model construction workflow.

3.1.1. Scalar imaging modalities

In this study, the head models were derived from simulated datasets and subject specific datasets. The simulated datasets were obtained from the BrainWeb (*BrainWeb: Simulated Brain Database. McConnell Brain Imaging Center Montreal Neurological Institude. McGill University n.d.*). These datasets are based on realistic MRI data volumes generated by an MRI simulator (Aubert-Broche, Evans & Collins 2006). Each dataset contains a co-registered volume of 181×217×181 slices with 1mm isotropic voxel resolution. The T1-weighted simulated scan was generated using SFLASH with (Repetition time) TR=18ms, flip angle $=30^0$ and (Echo time) TE=10ms. The T2-weighted scan was obtained using dual echo spin echo, late echo (DSE_LATE) with TR=3300ms, flip angle=90^0 and TE=35 for dual echo spin echo and 120ms for late echo. The PD-MRI used dual echo spin echo, early echo with TR=3300ms, flip angle 90^0, and TE=35 and 120ms. These simulated datasets provide

the detailed cortical structure which is attributed to the average of 27 co-registered scans (Aubert-Broche, Evans & Collins 2006).

To address the issue related to individual anatomical variations and their effect on dose delivery and site of stimulation, the T1 MRI scan of an individual subject (MNI_0591) was obtained from the ICBM subject database (*ICBM:International Consortium for Brain Mapping n.d.*). The scan was obtained using a GR pulse sequence on Siemens 1.5T MRI scanner. The scan has $1mm^3$ voxel resolution and 256×256×175 slices. The slice thickness is 1.0mm. TR=22ms and TE=9.199ms. Additional details about the subject and scan parameters can be accessed from the LONI ICBM database (*ICBM:International Consortium for Brain Mapping n.d.*).

Another dataset (H0351.2001) of an individual 24 year old African American consisting of T1 and T2 weighted scans, was obtained from the Allen Institute for Brain Science (*Allen Institute for Brain Science n.d.*). Each volume has $1mm^3$ iso-voxel resolution and consists of 185×180×192 slices. Acquisition parameters such as an acquisition plane, TE and TR were not provided by the repository.

3.1.2. Spatial image registration

Registration of multi-modal datasets is a fundamental step for extracting relevant information for the next major step in head model construction, the image segmentation. The outcome of registration is a coordinate transformation matrix that correlates the location (coordinates) from one image to the coordinates of that particular location in the other image. In short, image registration ensures that a particular set of coordinates in a source image represents the same feature or the structure in a reference or target image. The process of image registration can be classified in the following four steps: 1) Registration basis, 2) Geometric transformation, 3) Similarity measures and 4) Optimisation (Brown 1992).

Registration basis: The level of noise or distortion in modalities strongly biases the selection parameters for registration. With high levels of distortion, registration strongly favours the anatomical space over the raw intensities as it restricts the space search and ignores non-significant information. A stereotactic frame or point-like markers can be used to facilitate the registration process. Registration methods based

on such demarcation/control points are known as extrinsic methods, whereas methods based on anatomic details (image intensity) are called intrinsic methods (Beutel & Sonka 2000, pp. 449-51).

Geometric transformation: This transfer involves coordinate mapping from the source image (I_1) to the reference/target image (I_2) by a transformation T. In general image registration is given by:

$$I_2(x, y) = i[I_1\{S(x, y)\}] \tag{3.1}$$

where S is the spatial coordinate transformation required to map the spatial coordinates of $I_1(x,y)$ to I_2 in terms of (x',y') i.e. :

$$x', y' = S(x, y) \tag{3.2}$$

and i is the intensity transformation, which is particularly important when modality (image) contains various low frequency distortions in its intensity due to different field inhomogeneities. Using eq. (3.1) and ignoring intensity transformation, T=S represents the spatial transformation. A number of transformations such as rigid, affine (linear) and non-linear transformation are available. Rigid and affine transformations are best suited for intra-subject registration. In this study, intra-subject registration was applied to subject-specific modalities. Rigid transformation can be defined by 6 degree of freedom (DOF) i.e. three translation and three rotation, whereas, affine transformation can be defined by twelve DOF i.e. three translation, three rotation, three scaling and three skews/shears. Affine transformation can also be used in subject to standard registration e.g. Talairach space (Friston 2006, pp. 49-62). Non-linear registration can be described when the DOF are more than twelve. Inter-subject registration requires image mapping from different subjects with significant anatomical variations, hence higher order transformations are necessary to accommodate for local deformations due to anatomical differences. Non-linear registration is also useful in intra-subject registration to address non-linear distortions in images and mapping soft tissue regions across images.

Similarly measures: Similarity measure is used to compare performance of different transformation parameters and provides an index (cost function) that can be used to

quantify the dissimilarity between two modalities (images). The measure is used to optimise the transformation to achieve minimum cost by measuring the registration errors, or by quantifying the dissimilarities between two images (Jenkinson et al. 2002). Similarity measures are classified either as a landmark measure or as image intensity-based cost functions. Least squares, normalized correlation, correlation co-efficient, mutual information and normalized mutual information are some of the most commonly used intensity-based cost functions applied to medical modalities.

Optimization: to minimise the similarity measure, based on a cost function, an optimization scheme can be selected to search the parameter space, with dimensionality defined by the number of DOF of transformation. Derivative based optimization algorithms are more efficient and faster. A common issue in optimization-based problems is the failure of an algorithm to identify the global minimum, i.e. the returned transformation is attributed to a local minimum of the cost function instead of the required global minimum. To address this issue, Jenkinson et al. (2002) highlighted the use of image smoothing techniques to eliminate discontinuity in images and adaption of global-local (hybrid) optimization schemes. Sonka, Fitzpatrick and Masters (2002, pp. 447-513) provide a comprehensive review of optimization schemes and their implication in intra- and inter-subject registration.

Image intensity is defined on a regular grid using discrete values however, calculation of similarity measures for a given value of geometric mapping, in general, requires image interpolation to determine the intensity values at intermediate grid points. Linear interpolation technique is the most common type of scheme employed for fast interpolation. Linear interpolation has a low pass filtering effect on a target image, leading to loss of high frequency information and, at a same time, a reduction in noise level.

In this project, it was necessary to have a robust and automated registration scheme which would provide a fast, accurate and robust mechanism to align images of the same, and different MRI modalities. To address this issue Automated Image Registration (AIR) (Woods et al. 1998), FMRIB Linear Image Registration Library (FLIRT) and FMRIB Non-linear Image Registration Library (FNIRT) (Jenkinson et

al. 2002; Smith et al. 2004) were explored to identify the scheme best suited for the requirements of intra- and inter-subject image registration.

3.1.3. Spatial coregistration/transformation of scalar volumes

The scalar volumes obtained from the BrainWeb (*BrainWeb: Simulated Brain Database. McConnell Brain Imaging Center Montreal Neurological Institude. McGill University n.d.*) are 1mm isotropic, high-resolution scans created by registering 27 scans (T1-weighted gradient echo acquisitions with TR/TE/FA = 18ms/10ms/30 deg) of a single subject in stereotaxic space. Each volume contains 181×217×181 slices extending from the top of scalp to the base of foramen magnum. Each scalar volume (T1, T2 and PD-MRI) was co-registered using the FMRIB Linear Registration Library (FLIRT) (Jenkinson et al. 2002). The T1 and T2 weighted MRI scans of the subject (H0351.2001) were also linearly registered using the FLIRT.

3.2. Multimodal image segmentation

Tissue segmentation is required to classify different tissue types based on their intensity or morphological features. Tissue classification is a major prerequisite for defining the material properties of the elements in finite element head models. In this study, segmentation was performed in a semi-automated fashion using multiple libraries of 'FSL' and 'Simpleware' package. The process is multi-step, beginning with skull stripping and ending with the classification of sub-cortical structures.

Depending on the requirements of subsequent studies, the head models were segmented into five (scalp, skull, CSF, GM and WM) to twenty anatomically distinguishable regions. The T1-weighted MRI datasets were used to identify the GM, WM, subcutaneous fat, eye-muscles, muscles of mastication, eye (sclera), eye-lens, skull, SCF and the scalp. In each model, these regions were classified using the commercially available medical image processing software 'Simpleware'. The skull and CSF have very low signal intensity in T1-weighted MRI, therefore, it was quite difficult to distinguish these regions from each other using only the T1 images. To

address this issue, subject to the availability of scans, T2-weighted MRI sets were used to trace the CSF voxels, and inner skull boundaries were segmented using the PD-MRI volumes.

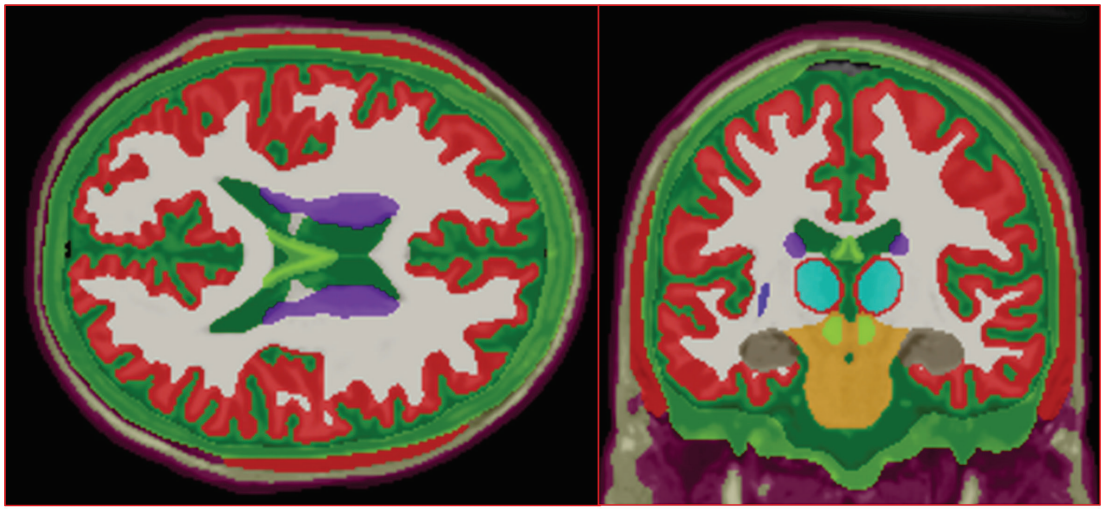

(a) (b)

Figure 3.2: Masks of twenty segmented tissues of the head model using T1, T2 and PD-MRI volumes of the simulated datasets (a) axial slice and (b) coronal slice.

Using the FSL libraries such as BET and FAST (Smith et al. 2004), additional masks (scalp, skull, CSF, GM and WM) were obtained in an automated manner. Similarly, using FSL (FISRT), masks of sub-cortical structures such as the hippocampus, thalamus, putamen etc. were also generated. The complete list of sub-cortical regions used in finite element models is illustrated in Table 4.1. Figure 3.2 illustrates the masks of twenty segmented tissues which were classified using T1, T2 and PD-MRI of the simulated datasets. In order to obtain the sagittal sinus, superior orbital and inferior orbital fissure, the masks obtained from the FSL were compared with the masks generated by the 'Simpleware'. The tissue classification was further assisted by making the cross comparison with the brain atlas (Woolsey, Hanaway & Gado 2008).

3.3. Electrode modelling

The location and dimensions of electrodes are two important parameters which define the likely site and strength of stimulation (Faria, Leal & Miranda 2009; Miranda, Lomarev & Hallett 2006). In this thesis, electrodes of two different configurations were analysed to understand the role of the electrode position and dimensions in defining the site of stimulation. The first type of electrode configuration is conventional bi-cephalic. In this configuration, each square electrode had an area of 25cm^2 and, depending on the location of electrodes on the scalp, their thickness varied from 2 to 5mm. Montages C3-Fp2, F3-Fp2, P3-Fp2 and C3-C4 were selected based on recent reports by Alexandre et al. (2011) and Utz et al. (2010). Locations of anodes (F3, P3 and C3) and cathodes (Fp2 and C4) were derived from the EEG 10-20 system. In this study the electrode size of 25cm^2 was selected as there is evidence of several human clinical trials of tDCS using this particular electrode size (Hummel et al. 2005; Iyer et al. 2005). Figure 3.3 shows the location of these conventional configurations on the head models.

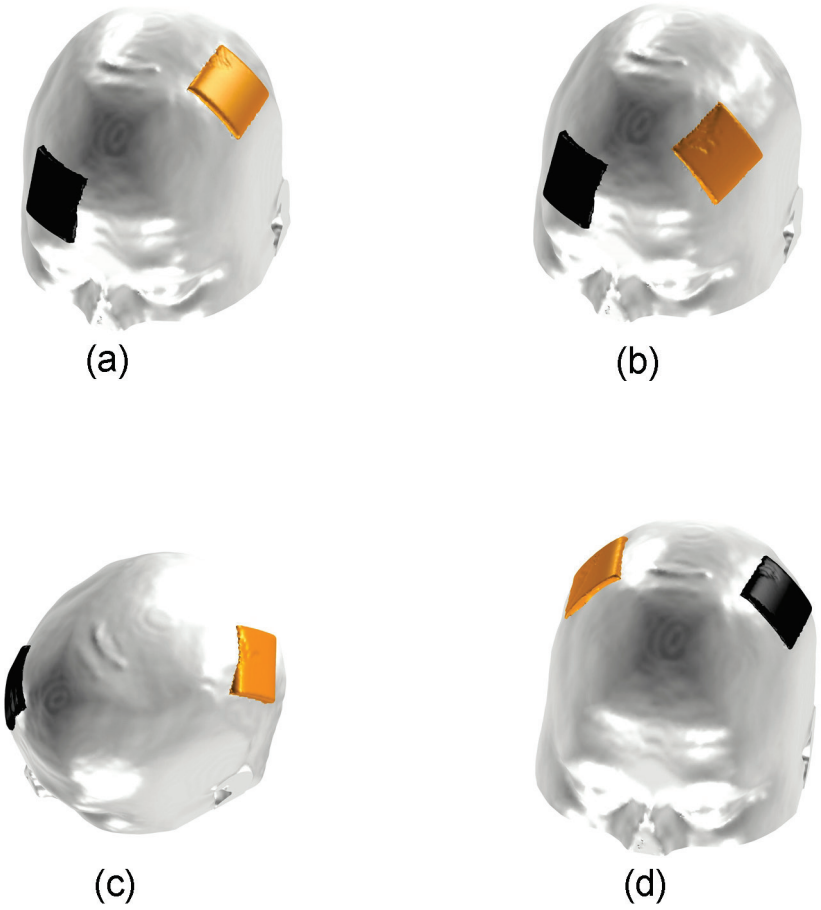

Figure 3.3: Four conventional bi-cephalic electrode montages. (a) C3-Fp2 electrode configuration, (b) F3-Fp2 electrode configuration, (c) P3-Fp2 electrode configuration and (d) C3-C4 electrode configuration.

The second type of montage is based on High-Definition electrode setup (Datta et al. 2009). In HD-montages, the 4x1 electrode configuration was selected, with the anode placed and C3 or C1 and surrounded by four cathodes. For the 4x1 HD montage with anode at C3, the cathodes were placed at C1, FC3, CP3 and C5. For 4x1 HD montage with anode at C1, the cathodes were placed at Cz, C3, FC1 and CP1. The electrode locations were derived for the International 10-10 EEG electrode system. Each HD electrode was modelled as a cylinder with a height of 2mm and a radius of 6mm. The electrodes were modelled in ScanCAD (Simpleware, Exeter, UK) and imported in ScanIP (Simpleware, Exeter, UK) for mesh generation.

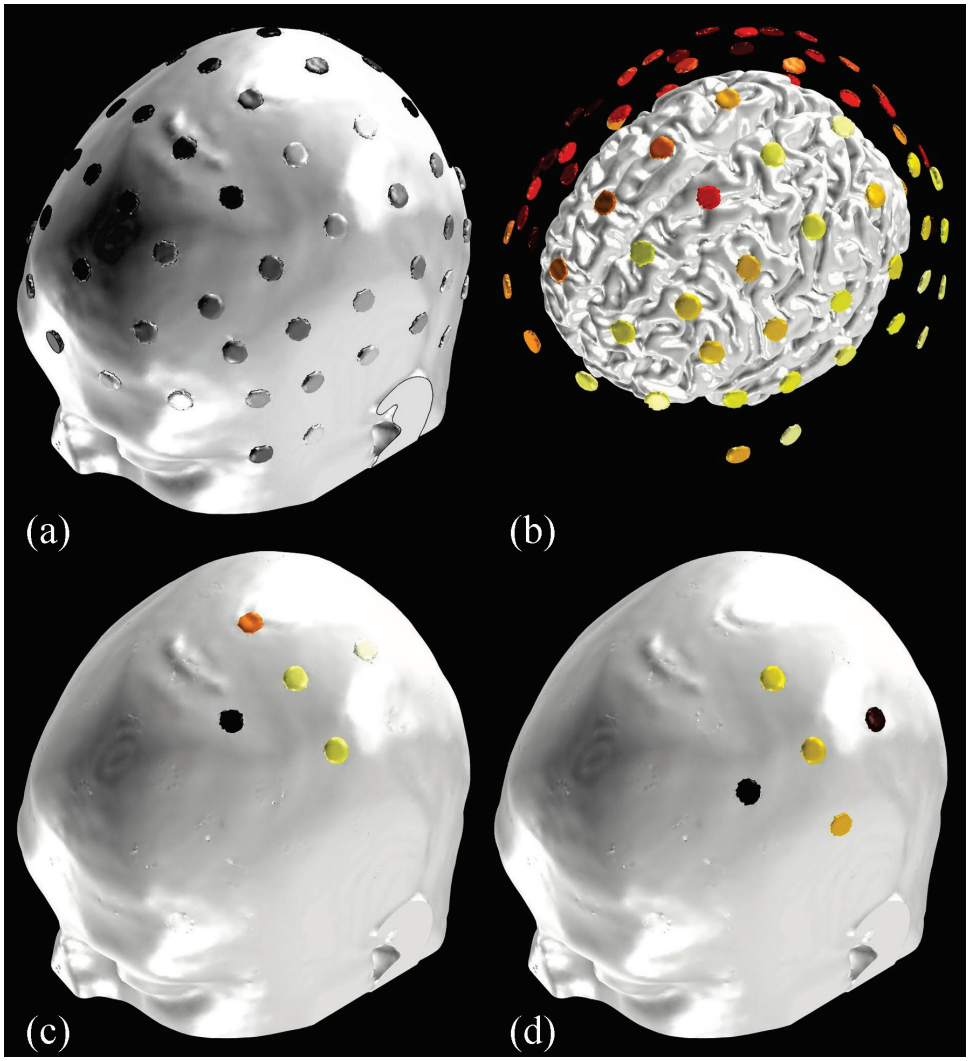

Figure 3.4: High–definition electrode configuration derived from the International 10–10 EEG electrode system. (a) 64 electrode positions derived from the 10–10 EEG electrode system. (b) 64 electrodes covering the brain, (c) HD montage with anode at C3 and cathode positioned at C1, FC3, CP3 and C5, and (d) HD montage with anode at C1 and four cathodes placed at Cz, C3, FC1 and CP1.

3.4. Mesh generation

Given the intricacy and detailed features of a human head, it is imperative to model the complexities using a balanced approach. A major step in human forward head modelling is the field calculations. The accuracy and speed of computational problems is highly dependent on the type of discretisation used. In this study, tetrahedral elements were selected to represent the discretised volume conductor model. The highly convoluted cortical geometry is best represented by tetrahedral mesh without

(unnecessarily) increasing the computational cost. With 'Simpleware' and using the masks obtained from tissue segmentation, the surface mesh was used to determine the triangular approximation of the interface between tissue types. These surface meshes were converted into a volumetric tetrahedron grid using the advancing front method, which filled each region, defined by the surface data, with tetrahedral elements. The minimum edge length of 0.5 mm, maximum edge length of 2 mm and the maximum error of 0.125 mm were selected to optimise the surface mesh generator. Similarly, the maximum target grid size with smooth adaptation was selected to be $2\times2\times2$ mm^3. The minimum element quality of 0.7 was selected with off surface meshing. The number of elements across a layer was selected to be 1.2 so that at least one element edge length would fit across the layers (necessary to improve calculation accuracy across thin regions < 1mm) (*Simpleware Reference Guide* 2010). Figure 3.5 illustrates the tetrahedral volumetric mesh generated by using the simulated datasets.

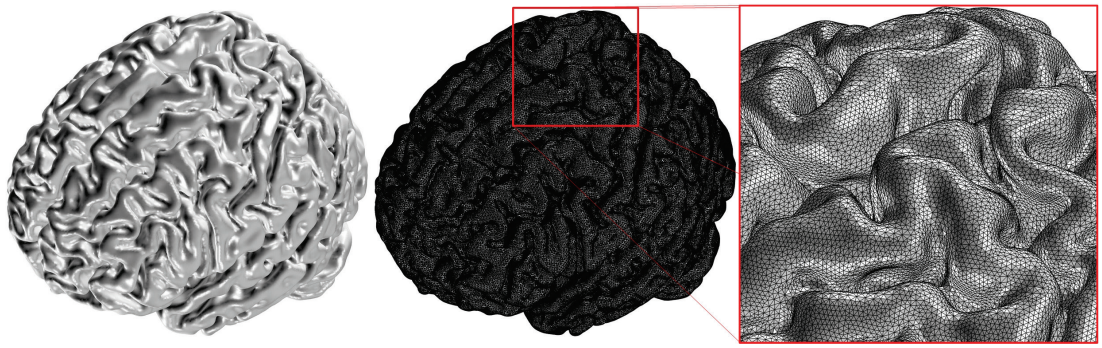

Figure 3.5: Tetrahedral volumetric mesh with approximately 2 million tetrahedral elements. (a) Three dimensional representation of human brain, (b) Tetrahedral volumetric mesh over the brain region and (c) Region of interest highlighting the mesh quality.

Other meshing options, such as hexahedral mesh, were also explored. Studies such as (Güllmar, Haueisen & Reichenbach 2010) used hexahedral mesh with one hexahedron per voxel, allowing a straight forward volumetric mesh from the MRI. Using an irregular hexahedral, the geometric accuracy was further improved. However, due to the homogeneous grid size across the volume conductor, it was estimated that very high node numbers would be required to accurately represent the cortical foldings.

However, a large node number would lead to a very high computational cost. Another approach is adaptive hexahedral mesh (Parazzini et al. 2011), which depending on the structure, would populate appropriate numbers of node points. But, due to time constraints, the adaptive hexahedral mesh approach was not pursued. On average, the finite element head models used in this thesis were composed of around 2 million tetrahedral elements. The adaptive mesh generation algorithm was optimised to generate high density across thin layers (0.5 mm) and around cortical foldings.

3.5. Chapter summary

The chapter presented the methodology/schemes to develop anatomically accurate and high-resolution human head models for the forward solution of TES. Multimodal imaging volumes were used to construct the multi-compartmental head models. The proposed scheme was used on subject specific and averaged scalar MRI scans to identify and construct head models with five to twenty anatomical regions. The methods and tools available to perform spatial registration, tissue segmentation and mesh generation were discussed. The procedure to incorporate various bi-cephalic and high-definition electrode montages was also discussed in the chapter.

4. ELECTRICAL PROPERTIES OF HUMAN HEAD TISSUES

4.1. Isotropic electrical conductivities of head tissues

As illustrated in Chapter 2, the electromagnetic characteristic of a biological medium can be expressed by Maxwell's equations. Biological tissues are, in general, highly dispersive in nature and have three main relaxation regions, namely, α (low frequency), β (medium frequency) and γ (high frequency). However, between the frequency range of 0 to 10 kHz, material (tissue) capacitive, inductive, propagation and time varying effects can be ignored. Therefore, the quasi-static approximation of Maxwell's equations can be used (Malmivuo & Plonsey 1995; Nunez & Srinivasan 2006). Under this approximation, biological tissues exhibit strong resistive (electrical) behaviour.

Under quasi-static approximation, the induced electric field (E) inside a volume conductor model can be calculated by:

$$E = -\nabla V \tag{4.1}$$

where V is the potential difference and, using the Ohm's law, the current density (J) associated with electric field (E) can be obtained as:

$$J = \sigma E \tag{4.2}$$

where σ is the electric conductivity of a medium and for anisotropic materials such as human skull, muscles or brain, the electric conductivity can be represented by a symmetric 3×3 tensor:

$$\underline{\sigma} = \begin{bmatrix} \sigma_{xx} & \sigma_{xy} & \sigma_{xz} \\ & \sigma_{yy} & \sigma_{yz} \\ & & \sigma_{zz} \end{bmatrix} \tag{4.3}$$

Depending upon the model complexity, the average isotropic electric conductivities of the different tissues used in this thesis, are illustrated in Table 4.1.

Table 4-1: Isotropic conductivity assignment

Tissue/material type	Conductivity (S/m)	Reference
Scalp	0.43	Holdefer, Sadleir and Russell (2006)
CSF	1.79	Baumann et al. (1997)
Subcutaneous fat	0.025	Gabriel, Gabriel and Corthout (1996)
Eye-muscles/muscles of mastication	0.16	Gabriel, Gabriel and Corthout (1996)
Eye	0.5	Gabriel, Gabriel and Corthout (1996)
Eye-lens	0.31	Gabriel, Lau and Gabriel (1996)
Skull	0.015	Oostendorp, Delbeke and Stegeman (2002)
GM	0.32	Goncalve et al. (2003)
WM	0.15	Nicholson (1965)
Hindbrain(cerebellum, pons, medulla, brainstem)	0.25	Average brain conductivity Geddes and Baker (1967)
Red nucleus	0.25	Average brain conductivity Geddes and Baker (1967)
Thalamus	0.32	Goncalve et al. (2003)

Hippocampus	0.32	Goncalve et al. (2003)
Fornix crura	0.32	Goncalve et al. (2003)
Caudate nucleus	0.32	Goncalve et al. (2003)
Globus pallidus par externa	0.32	Goncalve et al. (2003)
Globus pallidus par interna	0.32	Goncalve et al. (2003)
Putamen	0.32	Goncalve et al. (2003)
Superior sagittal sinus	1.79	Conductivity of CSF Baumann et al. (1997)
Electrode pads	0.14	Datta et al. (2009)
Conductive gel	0.43	Conductivity of scalp

4.2. Modelling the anisotropic conductivity for non-cortical structures

Human skull directional conductivity behaviour is attributed to low conductivity in the radial direction (σ_R) and is much higher in its tangential direction (σ_T). This anisotropic behaviour is linked to a series connection of high, low and high resistivity of inner compacta, spongiosa and outer compacta, respectively (Figure 4.1). According to DeMunck (1988), Marin et al. (1998), Munck and Peters (1993), and Van den Broek et al. (1998), the human skull exhibits anisotropic conductivity with a ratio of 1:10 i.e. $\sigma_T=10\sigma_R$. Where, σ_T represents the conductivity in tangential direction and σ_R stands for conductivity in the radial direction. Certain factors, such as the variation in thickness of spongiosa and compacta layers, inhomogeneous skull resistivity and inter- and intra-subject variability, may lead to erroneous estimates. Therefore, two conductivity constraints were considered:

$$\sigma_R \sigma_T = \sigma_{ISO}^2 \tag{4.4}$$

The product of radial and tangential conductivity must be constant and equal to the square of its isotropic conductivity, the Wang Constraint (Wang, Haynor, & Kim 2001) or the Volume Constraint (Wolters 2003):

$$\frac{4}{3}\pi\sigma_R\sigma_T^2 = \frac{4}{3}\pi\sigma_{ISO}^3 \tag{4.5}$$

The Volume Constraint restricts the volume of a conductivity tensor to its isotropic value. In other words, the Volume Constraint restricts the eigenvalues to retain their geometric mean. In the literature the expression of anisotropic conductivity is usually given in local coordinates:

$$\sigma_{SKULL} = \begin{bmatrix} \sigma_R & 0 & 0 \\ 0 & \sigma_T & 0 \\ 0 & 0 & \sigma_T \end{bmatrix} \tag{4.6}$$

where σ_{SKULL} is a second rank symmetric tensor $(\sigma_{SKULL}^T = \sigma_{SKULL})$ and a positive definite. In order to incorporate skull anisotropy in a FE model, it is however, necessary to translate eq. (4.6) into a global coordinate system. To achieve this task the following Jacobian transformation was used (Ida & Bastos 1997; Jiansheng & Zhanghong 2003; Zhang, Zhu & He 2004):

$$J_{uk} = \sum_{i=1}^{3} \frac{\partial u_k / \partial v_i}{\left(\sum_{j=1}^{3} \left(\partial v_j / \partial v_i \right)^2 \right)^{1/2}} \; J_{v_i} \quad k = (1,2,3) \tag{4.7}$$

Where *u=[x,y,z]* and *v=[x',y',z']* are global and local coordinates, respectively. The rotational transfer matrix *A* obtained from this transformation must be orthogonal i.e. $A^{-1} = A^T$, where *T* stands for transpose. Once the transfer matrix was obtained, the conductivity tensor in a global Cartesian coordinates system is obtained by (Wang, Haynor, & Kim 2001):

$$\sigma_{(x,y,z)} = A\sigma_{(diag)}A^T \tag{4.8}$$

Using the same methodology, directional conductivity in the muscles of mastication and eye muscles were introduced. However, the longitudinal eigenvalues (σ_L) were chosen to be 5 times higher than their respective transverse eigenvalues (σ_{Trans}) i.e. $\sigma_L = 5\sigma_{Trans}$ (Wang, Haynor, & Kim 2001):

$$\sigma_{muscle} = A \begin{bmatrix} \sigma_L & & \\ & \sigma_{Trans} & \\ & & \sigma_{Trans} \end{bmatrix} A^T \tag{4.9}$$

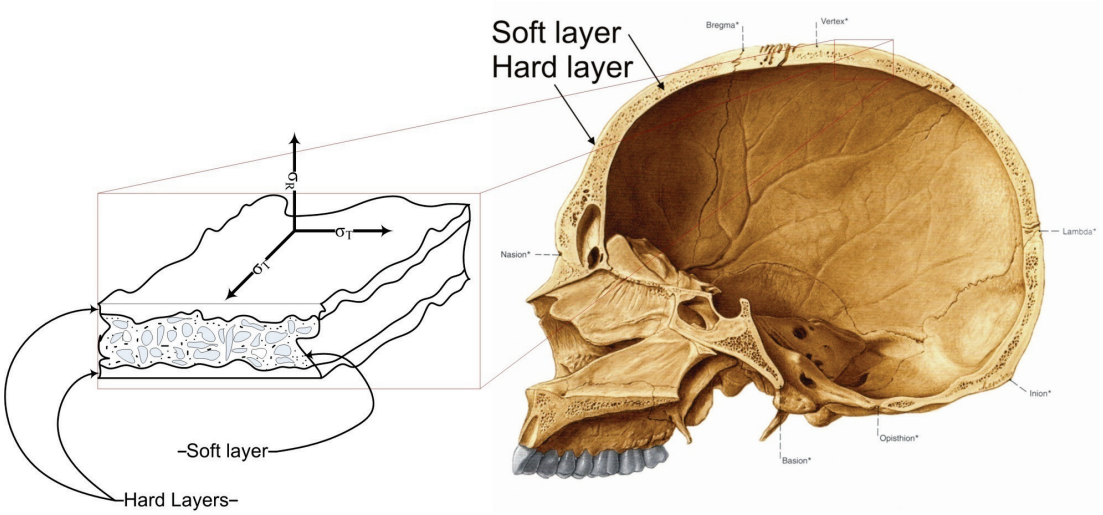

Figure 4.1: The three layer composition of human skull, the soft bone (spongiosa) enclosed by the hard bone (compacta). Source: (Hallez, Staelens & Lemahieu 2009; Hallez et al. 2008).

4.3. Modelling the anisotropic conductivity of the brain

The human central nervous system is composed of more than 10^{10} neurons and these cells are primarily composed of axons and dendrites. The group of axons which bundle together and wrapped in Perineurium (a connecting tissue) is termed Fasciculi and the combination of different groups of Fasciculi with blood vessels form the nerve fibre. The white matter of the brain is composed of the part of those Fasciculi which contain white fatty myelinated Schwann cells. The conductivity along the nerve fibre direction σ_L in WM has been measured to be around 10 times higher than in transverse direction σ_{Trans} (Geddes & Baker 1967).

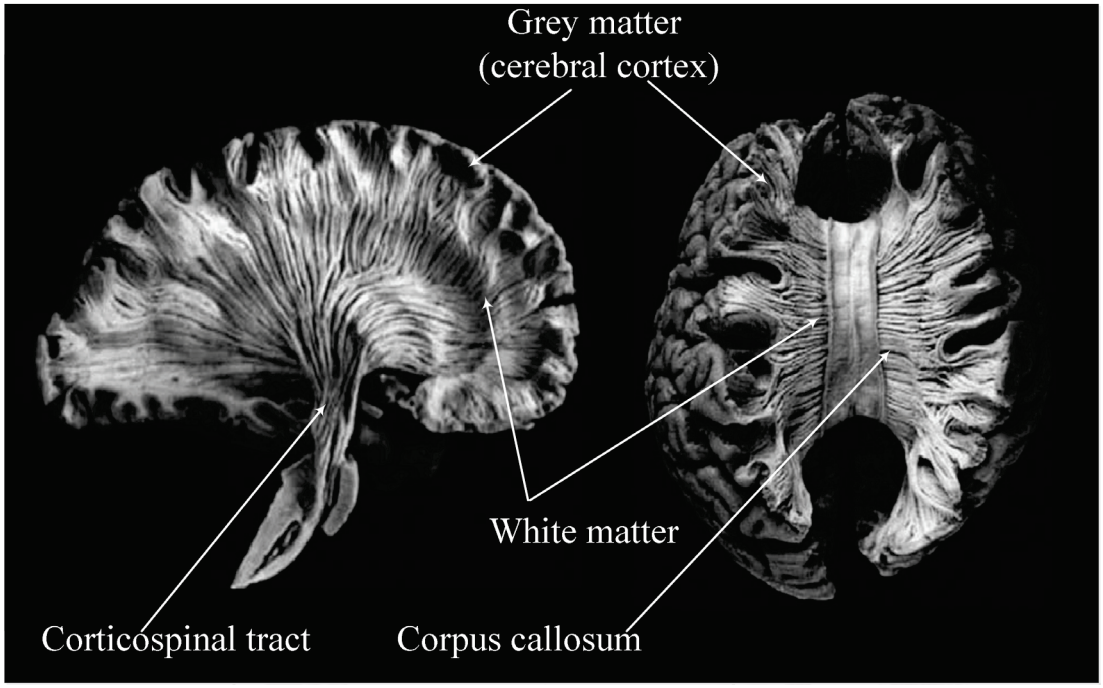

Figure 4.2: The complex fibre architecture (WM fibre bundles) of the human brain. Source: (http://www.vh.org/Providers/Textbooks/BrainAnatomy).

Scalar MRI volumes do not provide directional information about nerve fibre in a voxel. DT-MRI, on the other hand, has been shown to provide sufficient vector information necessary to articulate fibre structures of major white matter tracts of a brain. This orientation information can be used to estimate the directional conductivity of the human brain. Basser, Mattiello and LeBihan (1994b) proposed the possibility of mapping the diffusion tensor to the conductivity tensor by assuming that the effective electrical conductivity tensor shares the same eigenvectors as the effective diffusion tensor, even though they would have different eigenvalues (Figure 4.11). Tuch et al. (2001) proposed a method to quantitatively estimate the relationship between the conductivity tensor of the tissue and the water diffusion tensor. The relationship between these two quantities is linked by the observation that, even though no physical relation coexists between these two phenomena in free space, they are linked under the boundary condition imposed by the tissue geometry. Although a linear conductivity to diffusivity relationship may appear as a valid approximation, direct measurement of the WM conductivity suggests an observable deviation from such an approximation (Nicholson 1965; Wolters 2003).

4.3.1. Estimating brain anisotropic conductivity from measured diffusion tensor data

Brain is primarily composed of two main cell types, neurons which take part in signal transmission and processing, and glial cells whose functions are mainly described in terms of support and nutrition. Glial cells are the most abundant type of cells present in the brain. Neuronal bodies mostly dominate the grey matter tissue. The cortical region is composed of more than 10^{10} neurons. Around 90% of all the neurons in the brain are situated in the grey matter (Pakkenberg & Gundersen 1997).

A typical neuron has a central body called soma, a large number of branches called dendrites and a uniquely long branch called axon. Axons serve as a connection to remote neurons. In white matter, axons are myelinated. The myelin sheath is composed of a special type of glia cells with alternating layers of lipid and protein. The myelin sheaths are periodically interrupted along the axon in the nodes of Ranvier which causes the faster and uninterrupted propagation of action potential. In young adults, white matter constitutes approximately 35% of brain volume (Tang et al. 1997). Depending on the trajectories of axons, their diameters range from 1μm to 15 μm. Axons with similar trajectories form fasiculi or fibre bundles.

An MRI can be used to measure local chemical and physical properties of water. Properties such as molecular diffusion and flow (perfusion) can be assessed at voxel scale. Normally the MRI registers motion effects which can be quantified by the Apparent Diffusion Coefficient (*ADC*) and is composed of both the diffusion and perfusion effects. Compared to diffusion, perfusion-based echo attenuation is always stronger and as a result, it is possible to separate both effects on quantitative basis.

Like any fluid, water has a characteristic intrinsic self-diffusion (Brownian) constant, *D*, which highlights the movements of molecules in their microenvironment (Crank 1998). In a time scale of few milliseconds to seconds, the MRI can be made sensitive to the dynamic movement of water molecules in the range of 10^{-8} – 10^{-4} meters. These displacements (Brownian-movements) are well within the range of cellular dimensions. As a result, MRI diffusion measurements (DT-MRI) can provide a

unique understanding about the microstructure, morphology and physical characteristics of a biological tissue.

At body temperature, the Brownian-movements of water molecules are in the range of 10^{-8} – 10^{-6} m in 50 – 100 ms and this displacement is sufficient for a single water molecule to confront multiple axonal membranes (Tofts 2005, pp. 203-56). Myelinated axons have a lipid bilayer which strongly restricts molecular diffusion along its transverse direction and hence, a strong but not the only source of directional diffusion. Studies, such as Beaulieu and Allen (2005), Gulani et al. (2001), McNab (2008) and Wimberger et al. (1995) suggested some degree of anisotropy. It has also been reported that single axons or well aligned micro tubules within axons have a minimal effect on anisotropic diffusion (Beaulieu & Allen 1994). In white matter regions, where axons are bundled together to form fibre bundles, the combined effect of non-porous myelin sheaths and axonal membranes make a strong diffusion projection (Beaulieu 2002; Pierpaoli et al. 1996).

4.3.1.1. Diffusion tensor calculation

According to Fick's first law, the flux (j) is proportional to the rate of change of (gradient) of concentration (∇u) i.e.

$$j = -D\nabla u \tag{4.10}$$

where D is the diffusion coefficient. In an anisotropic medium, the flux does not follow the gradient directly Rather, its path is defined by the material directional properties i.e.

$$j = -\underline{D}\nabla u \tag{4.11}$$

According to the standard model of diffusion, with the passage of time, the concentration of solute in a solvent changes as the function of the divergence of the flux (Landini, Positano & Santarelli 2005, pp. 429-30):

$$\frac{\partial u}{\partial t} = \nabla \cdot \underline{D}(\nabla u) \tag{4.12}$$

In diffusion MRI, the Diffusion-Weighted Images (DWI) are acquired by employing direction sensitizing gradient pulses (Stejskal & Tanner 1965) which use two strong static magnetic field gradient pulses with 180^0 phase shift to control the diffusion gradient. The dependence of the observed echo signal intensity S is calculated from (Stejskal & Tanner 1965; Westin et al. 2002):

$$S = S_0 e^{-bD} \text{ or } S/S_0 = e^{-bD} \tag{4.13}$$

where S_0 is the signal obtained without diffusion weighting, D or ADC is the Apparent Diffusion Constant and b is the diffusion weighting factor. For a rectangular gradient b is defined by (Le Bihan et al. 1986):

$$b = \gamma^2 \delta^2 \left(\Delta - \delta/3\right) G^2 \tag{4.14}$$

where γ is the gyromagnetic ratio, δ is the duration of the diffusion gradient pulse, G is the strength of the diffusion gradients and Δ is the time interval between the diffusion gradient pulses. Using the logarithm to obtain D from eq. (4.13):

$$D = \frac{\ln\left(S/S_0\right)}{b} \text{ or } -bD = \ln\left(S/S_0\right) \tag{4.15}$$

In the presence of an anisotropic medium, the strength of diffusion would be direction dependent. Under the assumption that the probability of molecular displacement follows a multivariate Gaussian distribution over the observed diffusion time, the diffusion process can be illustrated by a 3×3 tensor matrix, proportional to the variance of the Gaussian distribution (Stejskal & Tanner 1965). In three-dimensional representation:

$$\ln\left(\frac{S}{S_0}\right) = -\sum_{i=1}^{3}\sum_{j=1}^{3} b_{ij} D_{ij} \tag{4.16}$$

$$\ln\left(\frac{S}{S_0}\right) = -\left(b_{xx}D_{xx} + 2b_{xy}D_{xy} + 2b_{xz}D_{xz} + b_{yy}D_{yy} + 2b_{yz}D_{yz} + b_{zz}D_{zz}\right) \tag{4.17}$$

or in matrix notation:

$$\ln\left(\frac{S}{S_0}\right) = -trace(b\underline{D}) \tag{4.18}$$

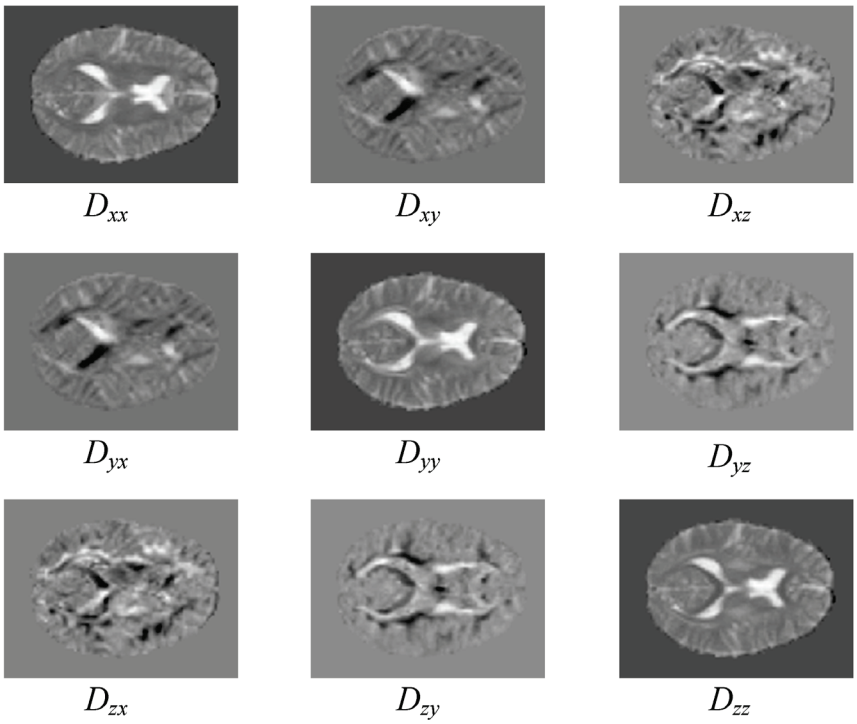

Figure 4.3: Nine coefficients of a diffusion tensor field. The diagonal components of the tensor are dominant indicating the positive definiteness of the diffusion tensor.

Basser, Mattiello and LeBihan (1994a; 1994b) proposed the use of multivariate linear regression to calculate D from a non-diffusion-weighted image (b_0) and a minimum set of six or more diffusion weighted images acquired along non-collinear directions. Assuming the diffusion tensor D is a second rank tensor, the diffusion tensor can be characterised as (Figure 4.3):

$$\underline{D} = \begin{pmatrix} D_{xx} & D_{xy} & D_{xz} \\ D_{yx} & D_{yy} & D_{yz} \\ D_{zx} & D_{zy} & D_{zz} \end{pmatrix} \tag{4.19}$$

where *xyz* represents the scanner frame of reference with *z* being the direction of the static magnetic field.

4.3.1.2. Diffusion anisotropy by tensor parameters

$\underline{D}$ is symmetric and positive definite i.e. $D_{xy}=D_{yx}$, $D_{xz}=D_{zx}$ and $D_{yz}=D_{zx}$ (Figure 4.3). If the medium is isotropic then $D_{xx}=D_{yy}=D_{zz}$ and off diagonal terms would be zero. The DWIs are acquired in the scanner's frame of reference, which can hinder the extraction of meaningful information. Since $\underline{D}$ has been considered a second rank tensor, therefore, using the property of tensors, $\underline{D}$ can be diagonalized using the eigenvalue decomposition i.e.

$$\begin{pmatrix} D_{xx} & D_{xy} & D_{xz} \\ D_{yx} & D_{yy} & D_{yz} \\ D_{zx} & D_{zy} & D_{zz} \end{pmatrix} = \begin{pmatrix} v_{x1} & v_{x2} & v_{x3} \\ v_{y1} & v_{y2} & v_{y3} \\ v_{z1} & v_{z2} & v_{z3} \end{pmatrix} \begin{pmatrix} \lambda_1 & & \\ & \lambda_2 & \\ & & \lambda_3 \end{pmatrix} \begin{pmatrix} v_{x1} & v_{x2} & v_{x3} \\ v_{y1} & v_{y2} & v_{y3} \\ v_{z1} & v_{z2} & v_{z3} \end{pmatrix}^T \quad (4.20)$$

$$or$$

$$D = V \cdot \Lambda \cdot V^T$$

The eigenvalue decomposition provides three eigenvalues ($\lambda_1, \lambda_2, \lambda_3$) with their three corresponding eigenvectors ($\boldsymbol{v_1, v_2, v_3}$) representing three main diffusion directions. The eigenvector corresponding to the largest eigenvalue points in the direction of the largest diffusion coefficient (principal diffusion direction) also known as the Principal Diffusion Vector (PDV). For a real positive definite symmetric tensor, the eigenvalues are always real (positive and non-zero) and the eigenvectors are orthogonal to each other (Figure 4.4). Under the assumption that, in DTI, the water self-diffusion is characterised by a multivariate Gaussian distribution, the diffusion tensor $\underline{D}$ can be considered as a covariance matrix, describing the translational displacement of the diffusing molecules. Therefore, Diffusion field ($\underline{D}$) can be represented by an ellipsoid, highlighting the probabilistic behaviour of molecular diffusion at a voxel scale (Le Bihan et al. 2001; Shimony et al. 1999).

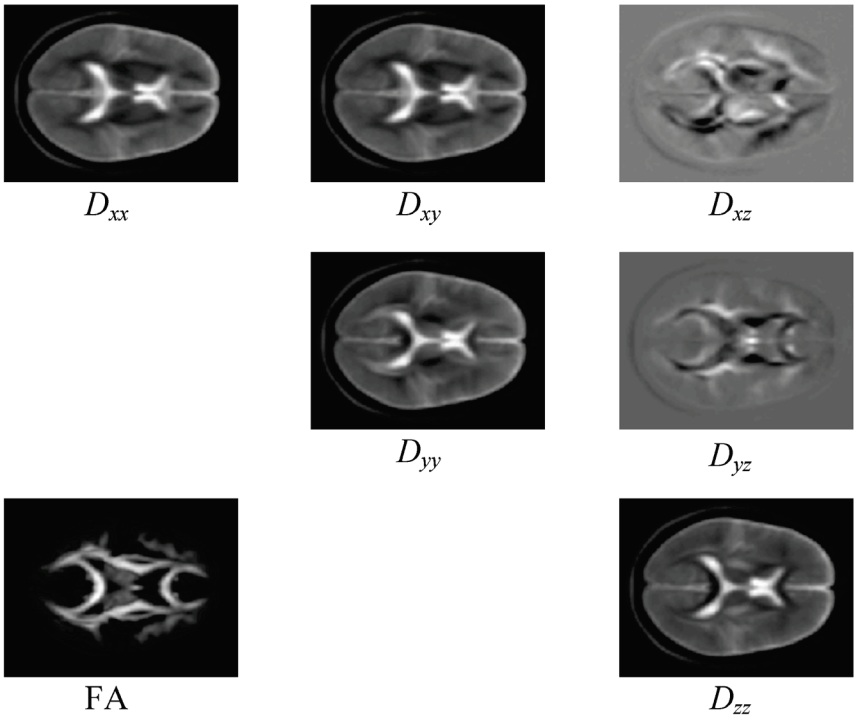

Figure 4.4: Quantitative diffusion and fractional anisotropy (*FA*) maps. Out of nine, only six (three diagonal and three off diagonal) coefficients are required to represent the complete tensor field information (second rank and symmetric tensor approximation).

In the ellipsoidal representation, the ellipsoid's axes are defined by the three eigenvalues and its orientation by the corresponding eigenvectors. Using the symmetric properties of the ellipsoid, the diffusion tensor can be classified in terms of basic geometric measures (Westin et al. 1997) (Figure 4.5 and Figure 4.6):

a) Linear case, C_L ($\lambda_1 >> \lambda_2 \approx \lambda_3$): The diffusion is mainly in the direction corresponding to the principal diffusion vector:

$$C_L = \frac{\lambda_1 - \lambda_2}{\lambda_1 + \lambda_2 + \lambda_3} \tag{4.21}$$

b) Planer case, C_P ($\lambda_1 \approx \lambda_2 >> \lambda_3$): The diffusion resembles a flat disc, restricted to a plane spanned by the two eigenvectors corresponding to the two largest eigenvalues:

$$C_P = \frac{2(\lambda_2 - \lambda_3)}{\lambda_1 + \lambda_2 + \lambda_3} \tag{4.22}$$

c) Spherical case, C_S ($\lambda_1 \approx \lambda_2 \approx \lambda_3$): All eigenvalues are of approximately the same size. The diffusion coefficients are almost the same in all directions:

$$C_S = \frac{3\lambda_3}{\lambda_1 + \lambda_2 + \lambda_3} \tag{4.23}$$

It can be shown that indices (4.21, 4.22 and 4.23) fall in the range of 0 to 1 and their sum is unity:

$$C_L + C_P + C_S = 1 \tag{4.24}$$

Various scalar measures of anisotropy have been proposed (Basser 1995; Basser & Pierpaoli 1996; Conturo et al. 1996; Pierpaoli & Basser 1996). Among the most widely used anisotropy indices, Fractional anisotropy (*FA*) and Relative anisotropy (*RA*) are the most widely acceptable measures and are based on the normalized variance of the eigenvalues (Basser 1995).

$$FA = \sqrt{\frac{3}{2}}\left(\sqrt{\frac{(\lambda_1 - \lambda_M)^2 + (\lambda_2 - \lambda_M)^2 + (\lambda_3 - \lambda_M)^2}{(\lambda_1^{\,2} + \lambda_2^{\,2} + \lambda_3^{\,2})}}\right) \tag{4.25}$$

where $\lambda_M = \dfrac{\lambda_1 + \lambda_2 + \lambda_3}{3}$

$$RA = \frac{\sqrt{(\lambda_1 - \lambda_2)^2 + (\lambda_2 - \lambda_3)^2 + (\lambda_3 - \lambda_1)^2}}{\lambda_1 + \lambda_2 + \lambda_3} \tag{4.26}$$

Other widely accepted anisotropy measures are the Volume ratio (*VR*) (Basser 1995; Basser & Pierpaoli 1996) and the Volume fraction (*VF*) (Pierpaoli & Basser 1996).

$$VR = \frac{\lambda_1 \lambda_2 \lambda_3}{\lambda_M} \tag{4.27}$$

and

$$VF = 1 - VR \tag{4.28}$$

FA and *VF* are rotationally and scale invariant anisotropy indices, and range from 0 (isotropic) to 1 (anisotropic) for positive eigenvalues.

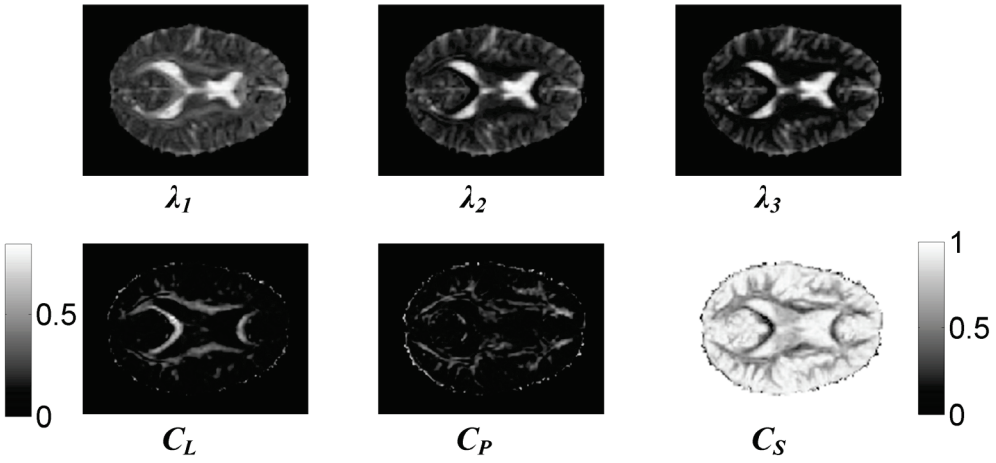

Figure 4.5: Scalar measures derived from the diffusion tensor of the subject specific data (UCLA_0591). Eigenvalues (λ_1, λ_2, λ_3) (from high to low) and the linear, planer and spherical geometric measures illustrating the diffusion classification, the sum of which is unity.

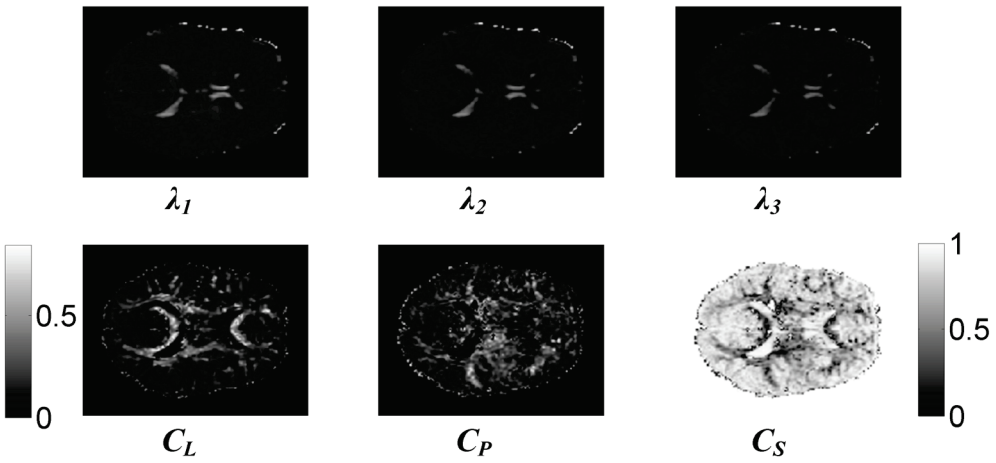

Figure 4.6: Scalar measures derived from the diffusion tensor of the subject specific data (H0351.2001). Eigenvalues (λ_1, λ_2, λ_3) (from high to low) and the linear, planer and spherical geometric measures illustrating the diffusion classification, the sum of which is unity.

4.3.1.3. Artefacts in DT-MRI

Motion sensitivity: A typical set of diffusion-weighted gradients generates a 360^0 phase shift for spins moving at a velocity in the order of 1mm/sec. At this scale, the head movements and cardiac pulsations cause the bulk of unavoidable tissue motion. During acquisition, subject motion can cause ghosting or artefactual spatial redistribution of DW signal intensities. Generally, head motion can be classified as a rigid-body motion (global translation and rotation). Therefore, geometric distortions can be rectified by applying a uniform phase transformation to the entire image (Anderson & Gore 1994; Miller & Pauly 2003) or by using navigator echoes in DWI pulse sequence (Ordidge et al. 1994; Wang et al. 2005). Physiological motion artefacts such as eye movements and pulsation of CSF can be addressed by employing the fast echo-planar (EPI) acquisition sequences and cardiac gating schemes (Pierpaoli et al. 2003; Skare & Andersson 2001).

Eddy currents: Large and rapidly switching (alternating) diffusion gradients generated by the (RF) gradient coils during DW measurements induce eddy currents in the electrically conductive structures of the primary coils. These eddy currents generate additional undesirable, rapid and slowly decaying magnetic fields. Residual magnetic fields caused by the eddy currents produce image translation and geometric distortions. These eddy currents change with each diffusion encoding gradient direction, and therefore, effectively change the actual *b-value* from the prescribed one. Second, the slow decaying residual magnetic field (gradient) causes geometric distortion to DWI during the sampling.

To rectify the artefacts due to eddy currents, online (during acquisition) correction schemes such as bipolar diffusion-encoding gradients, self-shielding gradient coils, pre-compensated gradient waveforms and an improved feedback mechanism to the gradient amplifiers are employed in modern scanners (Alexander, Tsuruda & Parker 1997; Papadakis et al. 2000). Post-processing techniques, such as co-registration to a common template or b_0 image were proposed to compensate for geometric distortions (Bastin 1999; Jones, Horsfield & Simmons 1999; Mangin et al. 2002; Nielsen, Ghugre & Panigrahy 2004; Poupon et al. 1998; Rohde et al. 2004).

Image noise: Noise in DWI can introduce significant corruption to bias the eigenvalues. At a low SNR, which is attributed to higher diffusion weighting and reduction in acquisition, it is often difficult to acquire reliable estimates. Noise corruption in images can lead to an overestimation of anisotropy making the isotropic medium anisotropic and the anisotropic medium more anisotropic (Pierpaoli & Basser 1996). Noise is also attributed to estimation errors (eigenvalue sorting) and biasness in derived anisotropy indices (Basser & Pajevic 1999, 2000; Bastin, Armitage & Marshall 1998; Chen & Hsu 2005). Post-processing noise removal filtering and regularization techniques based on regression or positive definiteness constraints on eigenvalues have been proposed (Ahrens et al. 1998; Barmpoutis & Vemuri 2010; Barmpoutis et al. 2007; Chefd'hotel et al. 2002; Coulon, Alexander & Arridge 2004; Fillard et al. 2007; Wang et al. 2004).

Magnetic field inhomogeneities and susceptibility artefacts: Magnetic field inhomogeneities most commonly occur at the tissue-air interface (frontal lobe above the sinuses). Due to an abrupt change in magnetic susceptibility (μ), the change in magnetic field causes additional magnetic field gradients (Clark, Barker & Tofts 1999; Farzaneh, Riederer & Pelc 1990). Susceptibility variations cause geometric distortions and by introducing additional local gradients which make the *b-value* spatially dependent. At high field strengths (3 Tesla or higher) the influence of magnetic field inhomogeneities become more significant. EPI-based sequences are highly sensitive to susceptibility at high field strengths and Bammer et al. (2001) proposed the sensitivity encoding (SENSE) approach to address these susceptibility artefacts.

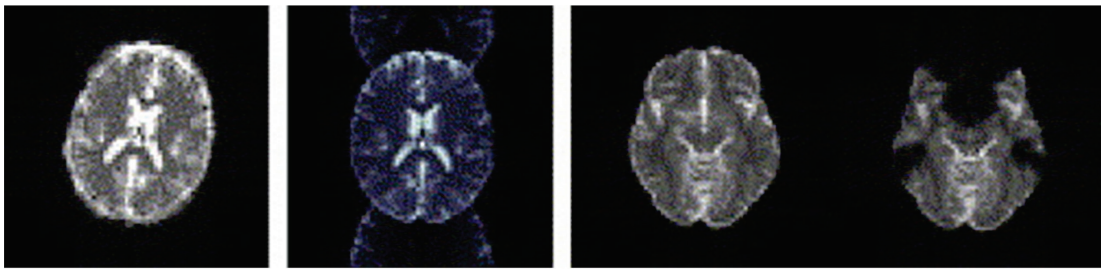

Figure 4.7: Different type of artefacts in DT-MRI.

4.3.1.4. DW imaging modalities

In this study, the anisotropic conductivity distribution of the brain was estimated from the measured diffusion tensor data. For the subject specific case (NMI_0591), the DWIs were obtained from the ICBM subject database (*ICBM:International Consortium for Brain Mapping n.d.*). The scan was obtained using an SE/EP pulse sequence with 90^0 flip angle on Siemens 1.5 T MRI scanner. The sequence had TE=94 ms and TR=8000 ms. Each data volume contained 96×96×60 matrix of isotropic voxels with 2.5 mm resolution. The dataset has 31 non-zero gradient directions with the *b-value* of 1000 s/mm^2. Additional details about the subject and scans can be obtained from the LONI ICBM database.

Another DTI dataset of an individual (H0351.2001) was obtained from the Allen Institute for Brain Science (*Allen Institute for Brain Science n.d.*). The acquisition parameters such as acquisition plane, flip angle, sequence type, TE and TR are not provided with the data. Each data volume consists of 128×128×68 matrix of isotropic voxels with 2 mm resolution. The dataset has 66 gradient directions and the *b*-value of 1000 s/mm^2.

The ICBM DTI-81 atlas was used to estimate the conductivity distribution in simulated scalar datasets. The ICBM DTI-81 atlas is a stereotaxic probabilistic white matter atlas co-registered to the anatomical template (ICBM-152). The atlas is based on probabilistic tensor maps obtained from 81 normal subjects. Scans were obtained on 1.5 T Siemens MRI scanners. The data was acquired using a single-shot echo-planer sequence with sensitivity encoding and a parallel imaging factor of 2.0. For additional details about the atlas, its acquisition parameters and co-registration with anatomical template refer to Mori et al. (2008) and Oishi et al. (2008).

4.3.1.5. DTI data processing

Before image registration, the subject specific DWI volumes were corrected for distortion and misalignment due to eddy currents and head movements. FDT (FMRIB Diffusion Toolbox) of FMRIB (Behrens et al. 2003) was employed to perform the distortion and misalignment corrections. The procedure used the b_0 image of the DWI data to perform the affine transformation with the rest of the images in the da-

taset. Diffusion tensors were calculated by performing the linear least-square fit of the tensor coefficients (Basser, Mattiello & LeBihan 1994a). Since the linear estimation does not guarantee the positive definiteness of the measured diffusion tensor, the DTIfit (of FMRIB Diffusion Toolbox) was not employed to calculate the diffusion parameters. Rather, the scheme (Fillard et al. 2007) was implemented in Matlab to replace the null or negative eigenvalues with the log-Euclidean average of the corresponding positive neighbours. The maximum likelihood scheme based on log-Euclidean average does not introduce outliers unlike the Cholesky decomposition (Wang et al. 2004). The processed tensor matrices were diagonalized using the eigenvalue decomposition (since the tensor is symmetric, the singular value decomposition would also yield the same results) to obtain three eigenvalues and their corresponding eigenvectors (voxel wise). Using the eigenvalues, the scalar anisotropy indices such as *FA* and *RA* were determined. Figure 4.8 shows the effect of noise on eigenvalues and fractional anisotropy index.

Scalar image registration requires a spatial transformation matrix that correlates the source image to the target image in a way that the features in both images become aligned. Since, DT-MRI contains directional information which is affected by the spatial transformation, registration of DT-MRI is a two-step procedure. The initial step involves the spatial registration of T2 (b_0 image of the DW data) or the *FA* map with either the (subject) high resolution T1-weighted volume (intra-subject registration) using FMRIB linear image registration library (FLIRT) or the standard template (inter-subject registration) using the FMRIB non-linear registration library (FNIRT).

One of the main requirements for non-linear registration (FNIRT) is to normalise the data with the provided standard. FSL (FNIRT) uses 'MNI152T1' as a spatial reference. The non-linear registration (FNIRT) requires a large number of parameters to work well for matching T1-weighted structural data to the 'MNI152T1-weighted' standard brain. These parameters are provided in its configuration file 'T1_2_MNI152_2mm.cng'. Similarly, for matching DWI, it uses the 'FMRIB58FA' standard brain and its associated 'FA_2_FMRIB58_1mm.cnf' configuration file. Depending upon the requirement for subject-specific study, linear affine transformation (FLIRT) was used, and for registration of DTI-81 atlas to simulated datasets, the non-linear registration (FNIRT) was employed.

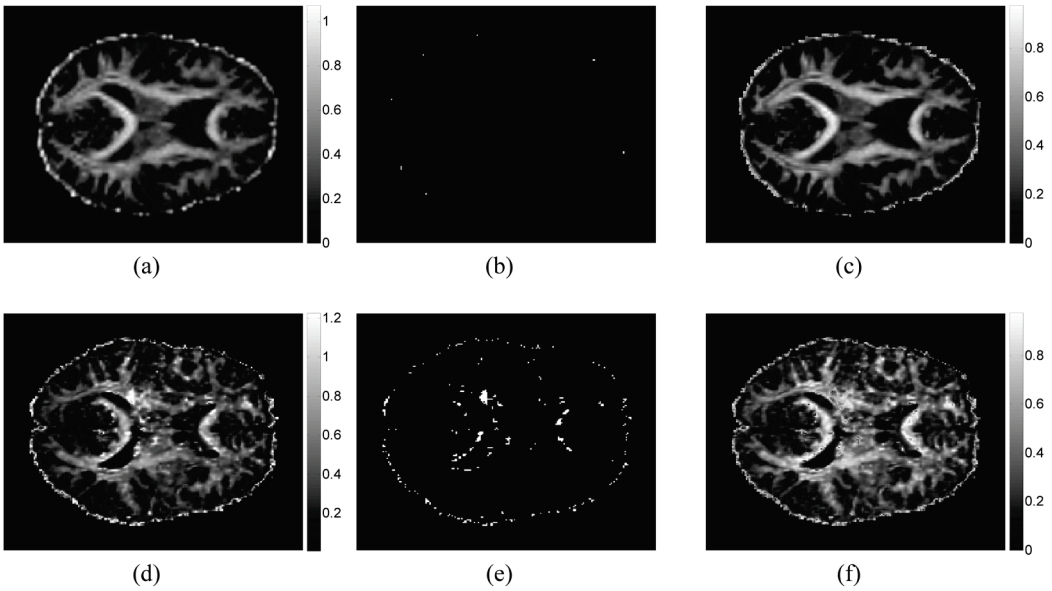

Figure 4.8: Effect of negative eigenvalues on the fractional anisotropy (*FA*) maps of UCLA-0591 and H0351.2001 data. (a) and (d) show the *FA* maps of individual subjects without noise compensation. (b) and (e) illustrate the regions affected by the noise artefacts in terms of *FA* values higher than 1. (c) and (f) *FA* maps after imposing the positive definiteness (the noise compensation).

The second step involves the local tensor orientation correction which is required to preserve the actual directions of diffusion vectors (Alexander et al. 2001). One way to address this issue is to apply the transformation matrix obtained from either the FLIRT or FNIRT to the diffusion tensor dataset (vecreg). If the linear transformation matrix is given by:

$$\underline{A} = \begin{pmatrix} a_{11} & a_{12} & a_{13} \\ a_{21} & a_{22} & a_{23} \\ a_{31} & a_{32} & a_{33} \end{pmatrix} \tag{4.29}$$

then the rotational part R is calculated as

$$R = A\sqrt{A^T A} \tag{4.30}$$

and finally by using singular value decomposition (SVD), the tensor at each voxel can be calculated by:

$$D' = RDR^T \tag{4.31}$$

where R^T is the transpose of R.

The above transformation does not alter the size and shapes of the tenor, i.e. the eigenvalues are insensitive to this transformation and it only affects the orientation (eigenvectors) of a tensor (Figure 4.9).

Alexander et al. (2001) proposed the 'Preservation of Principal Direction' (PPD) scheme to address the issue of spatial variation in tensor orientation due to the non-rigid parts of the affine transformation "$\underline{A}$" eq. (4.29). However, it has been shown that for intra-subject alignment (vectorly) due to the near rigid nature of the transformation matrix between different images, the reorientation effects of the non-rigid part of the transformation were insignificant (Alexander et al. 2001). In this study, the PPD algorithm was implemented in Matlab to address the reorientation effects of the non-rigid transformation among the simulated datasets and the diffusion tensors of the DTI-81 atlas.

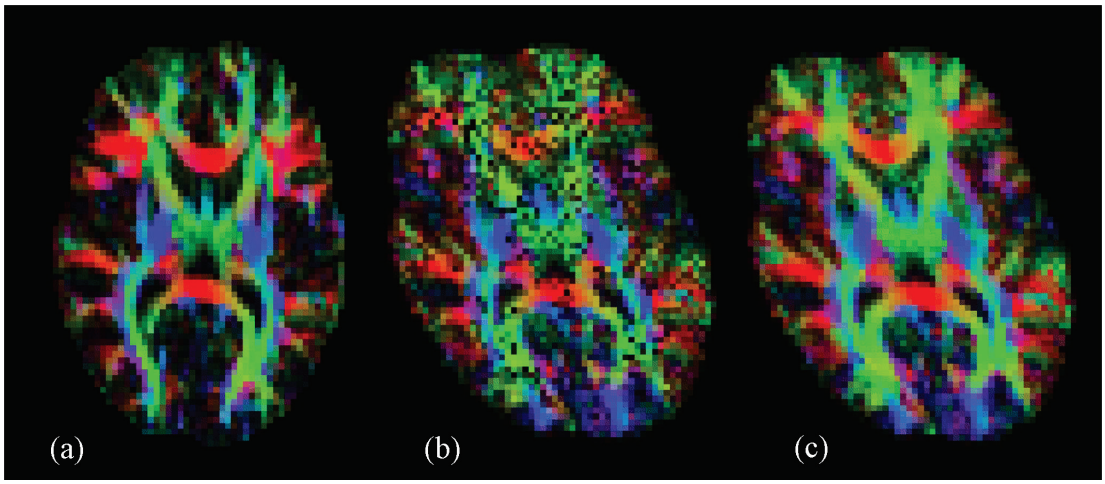

Figure 4.9: (a) DWI with local tensor information, (b) Spatially co-registered DWI, (c) Spatially co-registered DWI after orientation correction.

4.3.1.6. Translation of diffusion tensor to conductivity tensor

To determine the anisotropic electrical conductivity of the WM, this research considered two approaches. In the first procedure, it was assumed that nerve fibres emanate radially from the centre of the WM. Although this procedure is an oversimplified version of WM conductivity estimation, it is useful as it can be used to analyse the

current density pattern and its variation along pre-assigned (simulated) neural pathways. In addition, the model based on this type of conductivity was also selected to compare the behaviour of J distribution with isotropic and DTI driven models. The later was carried out to find correlation (if any) between the DTI-based models and the radial model. This procedure is termed as the Artificial Anisotropy Method. Assuming the difference of 1:10 between longitudinal (σ_L) and transverse (σ_{Trans}) conductivity i.e. $\sigma_L = 10\sigma_{Trans}$, the conductivity tensor can be obtained from eq. (4.9) using either the Wang Constraint, eq. (4.4) or the Volume Constraint, eq. (4.5).

A more realistic approach used in this study was to derive the WM anisotropic conductivity distribution from the DT-MRI. There are a number of algorithms, based on the relationship between conductivity and the diffusion tensor. In this study, three DTI oriented procedures were considered to estimate the anisotropic conductivity distribution of the WM.

The linear conductivity to diffusivity relationship based on the Effective Medium Approach (Tuch et al. 1999) (Figure 4.10) poses certain limitations such as, unlike EEG forward analysis the conductivity of the large intracellular volume cannot be ignored under TES and TMS (Miranda et al. 2001). Furthermore, at intra-tissue level this relationship is not well correlated although a well-defined linearity has been analysed on inter-tissue level (Kim et al. 2001). Using the procedure proposed by Miranda et al. (2001) and used by Kim et al. (2001) on 2D and Abascal et al. (2008) on 3D Electrical Impedance Tomography (EIT), the diffusion tensors in the WM volume were scaled by the ratio of their isotropic conductivity trace to the trace of the measured diffusion tensor, i.e.

$$\underline{\underline{\sigma}} = \frac{3\sigma_{ISO}}{trace(D)} D \tag{4.32}$$

where $3\sigma_{ISO}$ is the isotropic conductivity tensor trace and $\boldsymbol{D}$ is the measured diffusion tensor. This procedure estimates the anisotropic conductivity distribution based on the inherent variability of diffusion tensor and, at the same time, contains the numeric factor to constrain the trace of the conductivity tensor. This procedure is termed the Equivalent Isotropic Trace Approach.

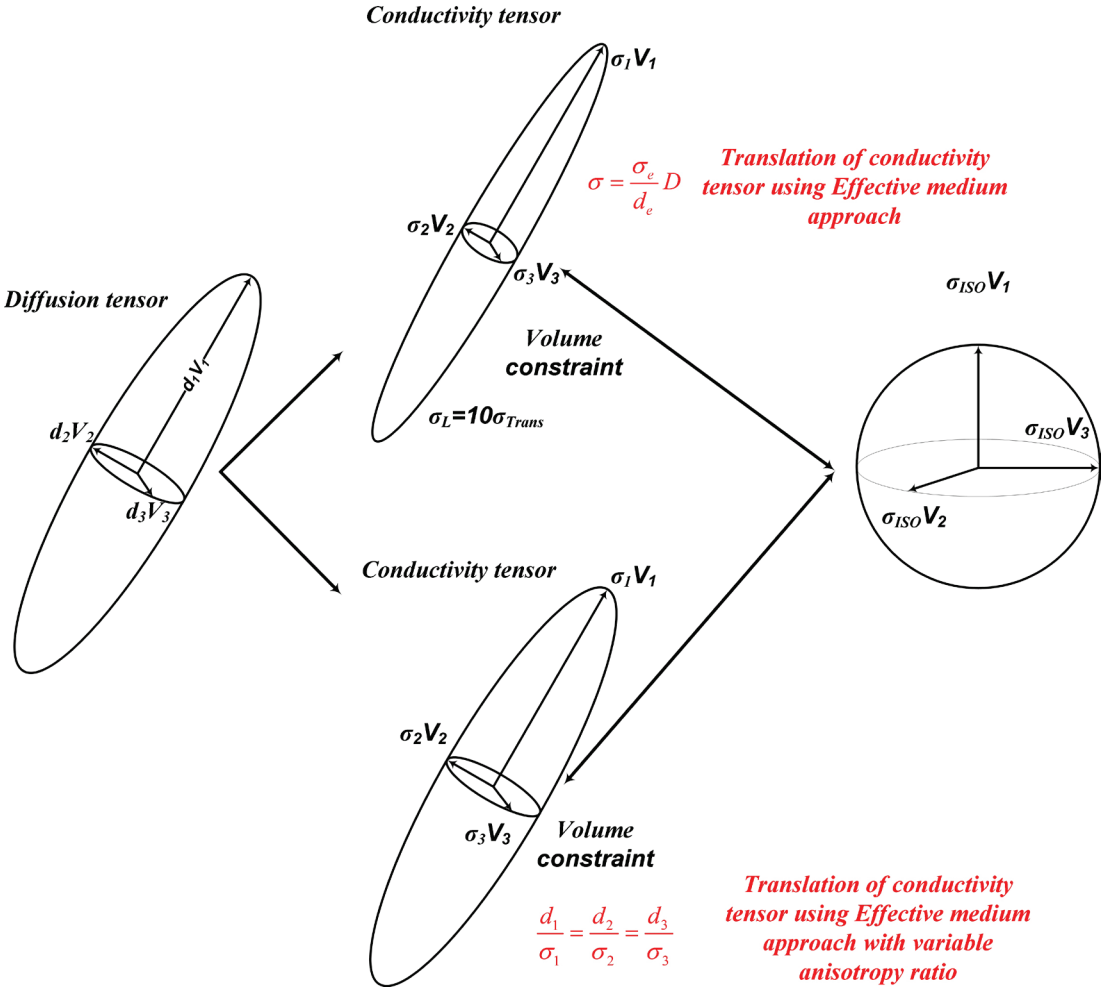

Figure 4.10: Translation of diffusion tensor to conductivity tensor using the Effective Medium Approach and its derivative.

For the subsequent two algorithms, it was assumed that the conductivity tensor and the measured diffusion tensor share the same eigenvectors (Basser, Mattiello & LeBihan 1994b). The second DTI oriented technique was based on the fixed anisotropic ratio among σ_L and σ_{Trans}. As proposed by Wolters et al. (2006). The fixed ratio of $\sigma_L = 10\sigma_{Trans}$ along with the Volume Constraint is somewhat more suitable for analysing the effects of variation in anisotropic conductivity orientation, as this method retains the original orientations of the diffusion tensor (eigenvectors) and, at the same time provides a fixed or pre-assigned change in the volume/magnitude of a conductivity tensor (eigenvalues). This procedure is known as Fixed Anisotropic Approach.

The Proportional Anisotropic Ratio method was proposed by Hallez et al. (2008). The procedure estimates the anisotropic conductivity distribution at a voxel level by retaining the principal directions of a diffusion tensor (eigenvectors) and constrains the magnitude of a conductivity tensor by its isotropic value (Figure 4.10). In this procedure, Volume Constraint (eq. 4.5), provides the scaling factor between the conductivity and the measured diffusion tensor. The linear relationship between the unknown eigenvalues of the conductivity tensor (σ_1, σ_2, σ_3) and the measured diffusion tensor (λ_1, λ_2, λ_3) in the brain is given by:

$$\frac{\lambda_1}{\sigma_1} = \frac{\lambda_2}{\sigma_2} = \frac{\lambda_3}{\sigma_3} \tag{4.33}$$

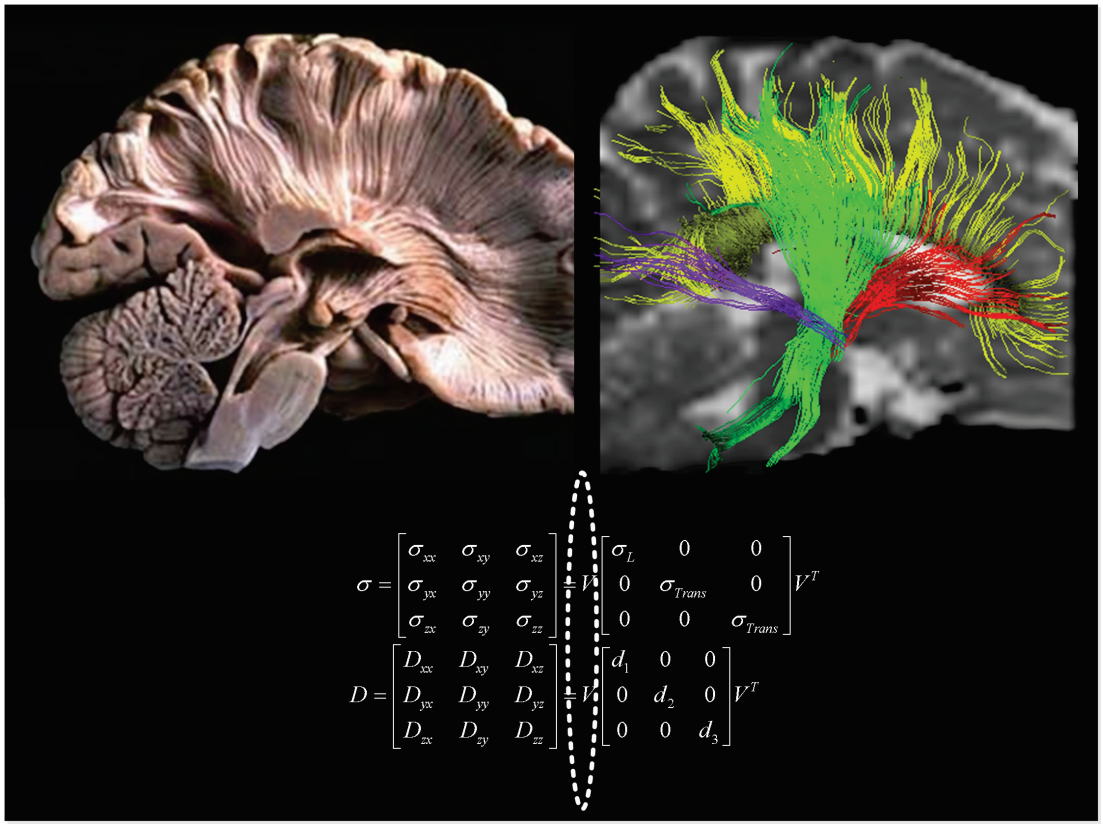

Figure 4.11: The linear relationship between the conductivity tensor and measured diffusion tensor based on the Effective Medium Approach.

4.4. Induced electric field tracking and assessment of stimulation mechanisms along fibre pathways

The DT-MRI data contains enough spatial information to trace the architecture of highly organised and coherent tissues, such as the white matter and skeletal muscle. Since diffusion in brain can be hypothesised to have a multimodal Gaussian behaviour, it can be characterised by a second rank symmetric tensor model. On voxel scale, this tensor framework can be used to estimate the direction of principal eigenvectors. Such directional information can be used to produce voxel wise fibre orientation maps or continuous tractography maps. Streamline techniques which have been employed for vector field visualisation can be adopted for white matter fibre visualisation. Several streamline-tractography algorithms were developed to trace the fibre architecture of human brain (Conturo et al. 1999; Lazar, Hasan & Alexander 2001; Lazar et al. 2003; Mariana Lazar & Khader Hasan 2000; Poupon et al. 2000; Weinstein, Kindlmann & Lundberg 1999).

Fibre architecture can be used to investigate the orientation specificity of different tDCS montages. With the help of this additional information, it is possible to analyse the role of fibre pathways in regulating the neural activity. Based on the study conducted by Miranda et al. (2007) three possible neural modulation mechanisms were investigated. For a long unmyelinated fibre, the passive response of an axon to the induced E-field can be obtained from the Cable equation (Basser & Roth 1991; Basser & Roth 1990).

$$\lambda^2 \frac{\partial^2 V}{\partial l^2} - \tau \frac{\partial V}{\partial t} - V = \lambda^2 \frac{\partial E_P}{\partial l} \tag{4.34}$$

where τ is the time constant and λ is the space constant. In this study the value of λ is considered 1mm (Silva, Basser & Miranda 2008). At a steady state, change in membrane potential $V = (V_{membrane} - V_{resting})$ due to a sub-threshold stimulus is given by:

$$V(l) = -\lambda^2 \frac{\partial E_P}{\partial l} \tag{4.35}$$

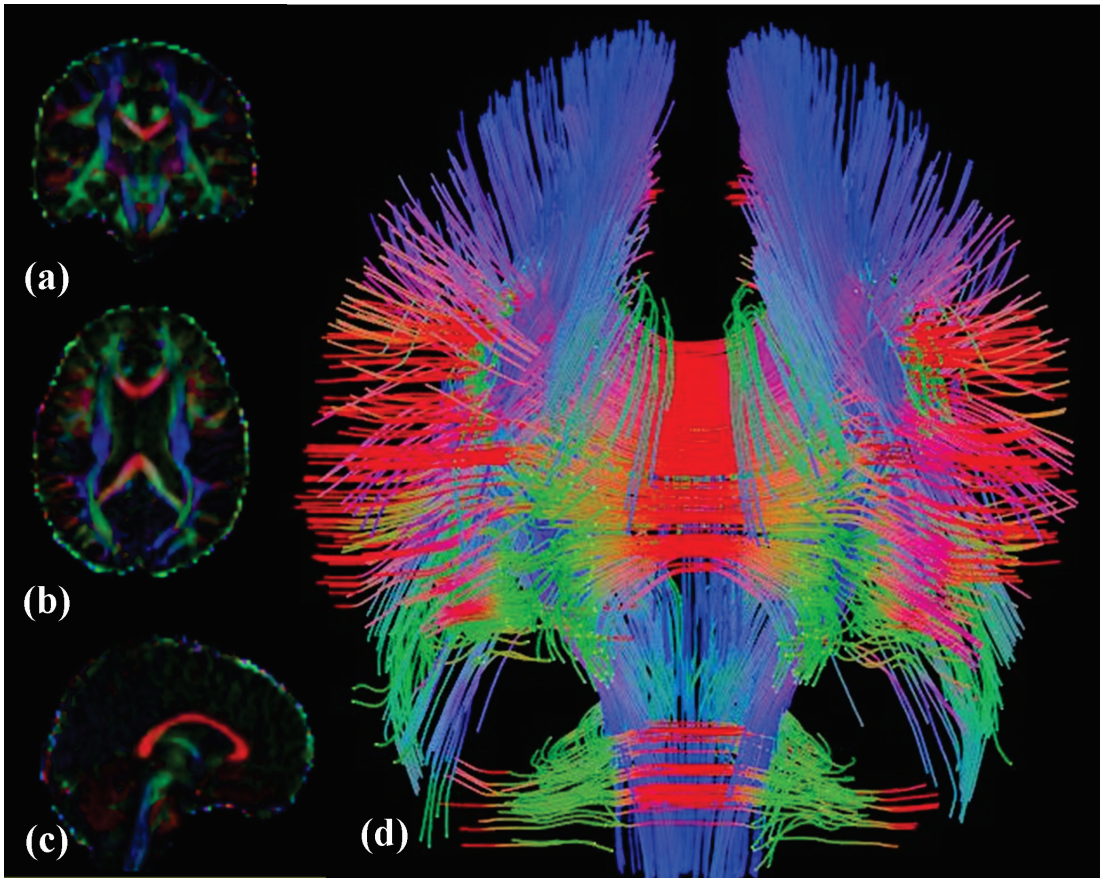

Figure 4.12: The directionally encoded colour *FA* maps (a) Coronal, (b) Axial, (c) Sagittal plane and (d) Major White matter fibre tracts. The directionally encoded colour *FA* maps incorporate major eigenvector information for each voxel. The fibre orientation is encoded by (RGB) colour scheme i.e. Red (right – left), Green (anterior – posterior) and Blue (superior – inferior). Subject specific DWI data (MNI_0591) was used to obtain these maps.

E_P is the component of the induced electric field which is locally parallel to the fibre segment (Δl) having a total length l (mm). In other words, it is the gradient of E_P, which defines the potential sites of modulation along a fibre path. Another possible candidate for neural modulation is λE_P itself. For instance, in a high E-field region, for a fibre of length $l >> \lambda$, possible site for hyper- or de-polarization would be in the vicinity of fibre termination or a sharp bend. Another possible scenario would involve axons crossing internal boundaries, such as the GM-WM boundary or WM-sub-cortical boundary. Change in tissue conductivity gives rise to a discontinuity in the normal component of the induced E-field. This discontinuity caused by the tissue heterogeneity can lead to a change in the membrane potential:

$$V(l) = -\lambda \frac{\Delta E_P}{2} e^{-\frac{|l|}{\lambda}} \tag{4.36}$$

In this research, these mechanisms of neural modulation were compared on fibres of five different regions, namely, left corticospinal tract (L-CST), right corticospinal tract (R-CST), genu of corpus callosum (G-CC), splenium of corpus callosum (S-CC), middle section of corpus callosum (M-CC) and modified fibres of L-CST. These fibres were generated by the orientation corrected and co-registered principal eigenvectors and the *FA* maps. Using the regions of interest as proposed by Wakana et al. (2007), these parameters were used to perform the fibre tracking using the deterministic approach, FACT (Fibre assignment by continuous tracking) implemented in the DTI studio (Jiang et al. 2006). In this streamline based algorithm, all those voxels in the dataset exhibiting *FA* values above a preselected threshold would be 'seeded' and each line propagates along the principle eigenvector. At a boundary between two voxels, the algorithm checks the orientation of the corresponding principal eigenvector and *FA* value. If the *FA* value was less than the prescribed threshold or if the curvature angle was greater than the prescribed value, the streamline was truncated. Since the principal eigenvector is bidirectional, by taking the dot product between each consecutive vector, the direction of propagation is determined, and tracking is implemented in both forward and backward directions. Compared to other tracking algorithms (Lazar & Alexander 2003), the 'FACT' has demonstrated good computational speed and accuracy over curved tracts.

Five ROIs were created to perform the fibre tracking with the *FA* threshold of 0.2 and the angle limit of 45^o. As a special case, selected fibres across L-CST were tracked using the *FA* of 0.1 and the angle limit of 90^o. The motive behind this approach was to analyse the role of fibre crossing at the GM-WM interface along with the impact of sharp bends on membrane de- or hyper-polarization. The artificial bends were introduced by assuming that these fibres tend to be projected normal to the local WM boundary. To ensure smooth transition along the fibre path, spline interpolation was applied. Fibres were assigned their respective E_P values using the Cubic interpolation and 3D visualization was performed in the Paraview (Squillacote 2007). Figure 4.13 shows the spread of the activating function (E_P) under the influence of bi-cephalic montage (C3–Fp2).

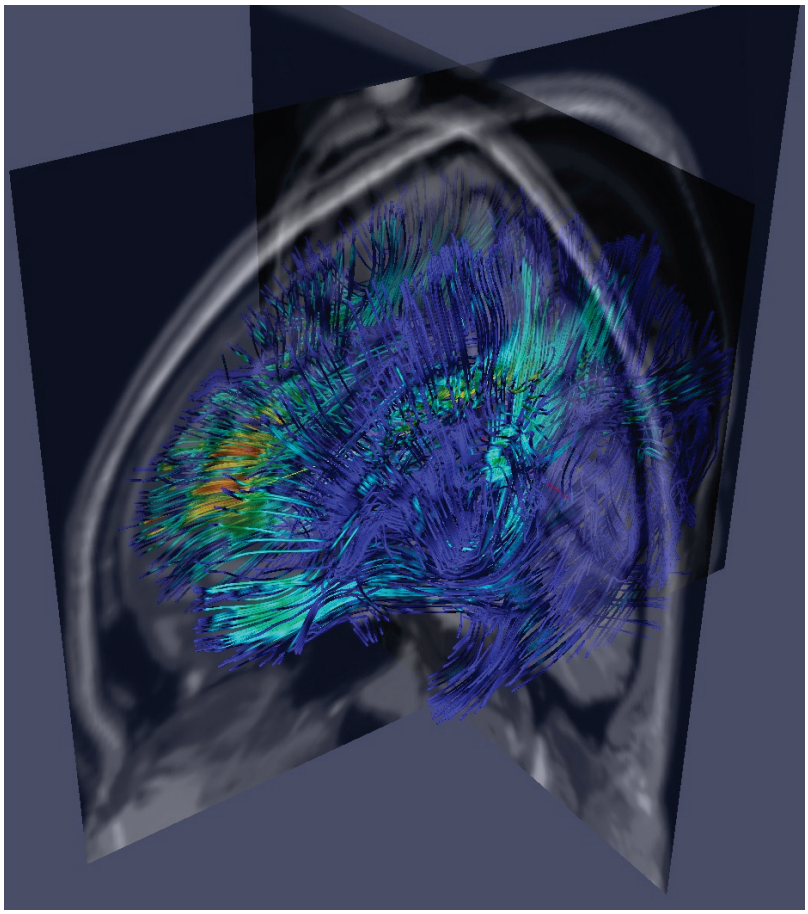

Figure 4.13: Projection of the activating function (E_P) along the fibre tracts. The electric field was induced using a conventional 5x5 cm^2 electrode pads place at C3 (anode) and Fp2 (cathode).

4.5. Chapter summary

The chapter listed the average isotropic electrical conductivity values of different regions (tissues) of human head used in this thesis. The chapter provided an in-depth coverage on modelling the anisotropic conductivity of non-cortical structures. The application of eigenvalue decomposition with fixed eigenvalues was employed to introduce fixed ratio anisotropic conductivity in human skull, mastication muscles and eye muscles.

The second part of the chapter deals with the framework to introduce anisotropic conductivity in human brain. The schemes to use artificial anisotropy and DTI based conductivity estimation were formulated. The steps involved in the processing of

DWI, diffusion tensor extraction and the translation of diffusion tensor to conductivity tensors were presented. The schemes to utilise the white matter fibre architecture to track induced electric field and three mechanisms of stimulation were also proposed.

5. ROLE OF MODEL COMPLEXITY ON FIELD ASSESSMENT

5.1. Introduction

The aim of this chapter is to investigate the influence of non-cortical tissues, such as muscle of mastication and subcutaneous fat, on the induced cortical electric field. The assessment was carried out using high-resolution anatomically accurate human head models derived from the T1, T2 and PD-MRI volumes of the simulated datasets. Two conventional electrode configurations (C3–Fp2 and C3–C4) with realistic dimensions (5x5cm^2) were used to perform the comparison between the commonly used five-layer isotropic head model and the proposed nine-layer head model.

Using eigenvalue decomposition, the anisotropic conductivity was introduced in the skull, mastication muscle and the white matter. The nine layer isotropic model was compared with four anisotropic models with varying degrees of anisotropy to assess the shunting effects of the anisotropic skull and muscle of mastication on cortical current density. The use of artificial white matter anisotropy provided the upper bounds (maximum) of field variations expected from a fixed anisotropy ratio and predefined fibre orientation. Hence, the inclusion of artificial white matter anisotropy warranted the use of realistic white matter conductivity distribution in forward models of tDCS.

In this chapter, the results are presented in two sections. The first section focuses on the influence of model complexity on cortical field distribution, and the second section is dedicated to analysing the role of the skull, muscle of mastication and (artificial) white matter anisotropy in shaping the brain current density distribution.

5.2. Material and methods

5.2.1. Head model design

The baseline MRI based head model comprises of nine different tissues. The MRI data sets were obtained from the BrainWeb (*BrainWeb: Simulated Brain Database. McConnell Brain Imaging Center Montreal Neurological Institude n.d.*). Each dataset contains 181x217x181 slices with 1 mm isotropic voxel resolution. Additional details about the datasets are provided in Chapter 3, Section 3.1.1. The T1-weighted MRI volume was used to segment the WM, GM, subcutaneous fat, eye-muscles, mastication muscles, eye (sclera) and scalp tissue. CSF voxels were identified with the co-registered T2-weighted MRI volume. Similarly, inner skull boundaries were segmented using PD-MRI volume. The tissue classification was further assisted by a cross-comparison against the brain atlas (Woolsey, Hanaway & Gado 2008) and the tissue classification study (Ramon, Schimpf & Haueisen 2006). The detailed image registration and segmentation framework is provided in Chapter 3, Section 3.1.3 and 3.2, respectively. The entire segmentation procedure, 3D model construction and volumetric mesh generation was carried out in a commercially available package "Simpleware" in a semiautomatic manner. Two electrode configurations containing two electrodes each of 25 cm^2 area were also modelled in the same package. The volumetric mesh model contained nine regions corresponding to nine different segmented tissues and comprised of around five million tetrahedral elements.

5.2.2. Tissue conductivity

In order to address the issue of model complexity, each layer in the model was assigned with its respective average isotropic electrical conductivity. For a nine layer model, electrodes were assigned the conductivity of 1.4 S/m (Datta et al. 2009), scalp

the conductivity of 0.43 (Holdefer, Sadleir & Russell 2006), CSF of 1.79 (Baumann et al. 1997), subcutaneous fat, eye muscle, muscle of mastication and eye of 0.025, 0.16, 0.16 and 0.5, respectively (Gabriel, Gabriel & Corthout 1996). Similarly, the skull was assigned the conductivity of 0.015 (Oostendorp, Delbeke & Stegeman 2002), whereas GM and WM were assigned the isotropic electrical conductivities of 0.32 and 0.15 S/m, (Goncalve et al. 2003; Nicholson 1965) respectively.

In addition, the five layer model was derived from the above-mentioned model by replacing the conductivity values of fat, muscle and eye tissue to that of scalp conductivity. Hence, the total number of elements in both models was identical. This particular approach was adopted to eliminate any variation in field calculations which might arise due to differences in mesh density. To address the issue related to anisotropic conductivity, the skull, muscle and WM were assigned the anisotropic electrical conductivities.

In terms of electrical conductivity, the human skull can be considered as a series connection of high, low and high resistor network representing the outer compacta, spongiosa and inner compacta, respectively. This series network (skull) exhibits low conductivity in a radial direction and a much higher electrical conductivity in its tangential direction (Wolters et al. 2006). In this part of the study the conductivity ratio of 10:1 ($10\sigma_R:\sigma_T$) was selected to represent the directional conductivity (Akhtari et al. 2002; De Munck 1988; Rush & Driscoll 1968). To restrict the anisotropic conductivity tensor magnitude to its isotropic value, the Wang Constraint was applied (Wang, Haynor & Kim 2001). Based on this constraint, the product of radial and tangential components of conductivity must be constant and equal to the square of its isotropic value (eq. 4.4).

To keep consistency in the conductivity assignment procedure, the same constraint was used while defining the muscle and WM anisotropy. In Cartesian coordinate system, anisotropy can be defined by eq. (4.3). However, in the literature, anisotropic conductivities are normally presented in the local coordinate system. Therefore, it is necessary to transform the local system to a global one using the transformation provided in eq. (4.9), (Jiansheng & Zhanghong 2003). Using the same approach, anisotropy in the muscle tissue was introduced, except, the longitudinal eigenvalues were

five times greater than the transverse eigenvalues i.e. ($\sigma_L=5\sigma_{Trans}$) (Wang, Haynor & Kim 2001). To introduce anisotropy into the WM, artificial anisotropy with a fixed ratio of 10:1 ($\sigma_L=10\sigma_{Trans}$) along with the Wang Constraint was introduced (Tuch et al. 2001). Although this procedure kept the direction of a tensor radially oriented, it was possible to regulate anisotropy ratios.

5.2.3. Electrode configurations and current density calculation

Two bi-cephalic electrode configurations were selected to estimate the effects of model complexity and tissue anisotropy on cortical current distribution (J). The first, C3 (anode) - Fp2 (cathode), configuration was chosen as the primary montage as (in clinical practice) this configuration has already shown its significance to modulate the primary motor cortex (Utz et al. 2010). The second configuration, where anode was placed at the approximate location of C3 and the cathode at C4, was considered not only to supplement the argument (in subsequent sections) but also to isolate any ambiguity that may arise due to a particular electrode configuration. Each electrode was modelled as a 5x5 cm^2 square block with an average thickness of 0.2 cm.

The exposed surface of the cathode was assigned the zero potential boundary condition ($V=0$). Similarly, the exposed boundary of the anode was assigned the Dirichlet boundary condition ($V=V_0$). In each case, the applied voltage had to be readjusted so that approximately $1mA$ of current would flow through the anode surface. The rest of the exposed boundaries were considered electrically insulated ($n\cdot\sigma\nabla V=0$) and continuity of the normal component of J, ($n\cdot J_1=n\cdot J_2$), was preserved across all the inner boundaries.

Since the considered volume conductor model was passive in nature, Laplace's equation ($\nabla\cdot\sigma\nabla V=0$) was used to estimate the induced E and Ohm's law ($J=\sigma E$) was employed to calculate the J distribution. Under quasi-static approximation, models were solved in a commercial finite element package "COMSOL".

5.3. Results and analysis

5.3.1. Influence of model complexity on field assessment – impact of non-cortical structures

To assess the effects of additional tissue layers on *J* magnitude and distribution, the behaviours of the nine layer model described in the previous section and the commonly used five layer model were compared with each other. Both models were analysed using the previously mentioned electrode configurations. The maximum *J* in both models, under both electrode configurations, was found around the rim of the electrodes. This non-uniform distribution was the result of the edge effect, as reported by Faria, Leal and Miranda (2009) and Miranda, Lomarev and Hallett (2006). It was observed that almost half of the current injected via scalp electrodes was shunted through the scalp and a major portion of the current, which penetrated to the lower layers, was displaced (shunted) by the highly conductive CSF. Hence, the CSF served as another region with high *J*.

Since five layer head models consider low conductive fat, muscle and relatively higher conductive eye tissue as the part of the scalp, any assessment based on such models is based on incomplete and inaccurate information. In order to validate this hypothesis, *J* was obtained for both models under both electrode configurations, on an arbitrary straight line as shown in Figure 5.1 (c). From Figure 5.1 (a) and Figure 5.1 (b) it can be seen that the *J* is higher in the nine layer model. This variation was more prominent in the scalp and CSF regions whereas regions of fat and muscle had substantially lower magnitude of *J*. Similarly, *J* in the regions of GM, WM and skull had a slightly elevated magnitude when compared to the five layer model. Figure 5.1 (d) provides a comparative view between the five and nine layer models in terms of tissue conductivity assignment.

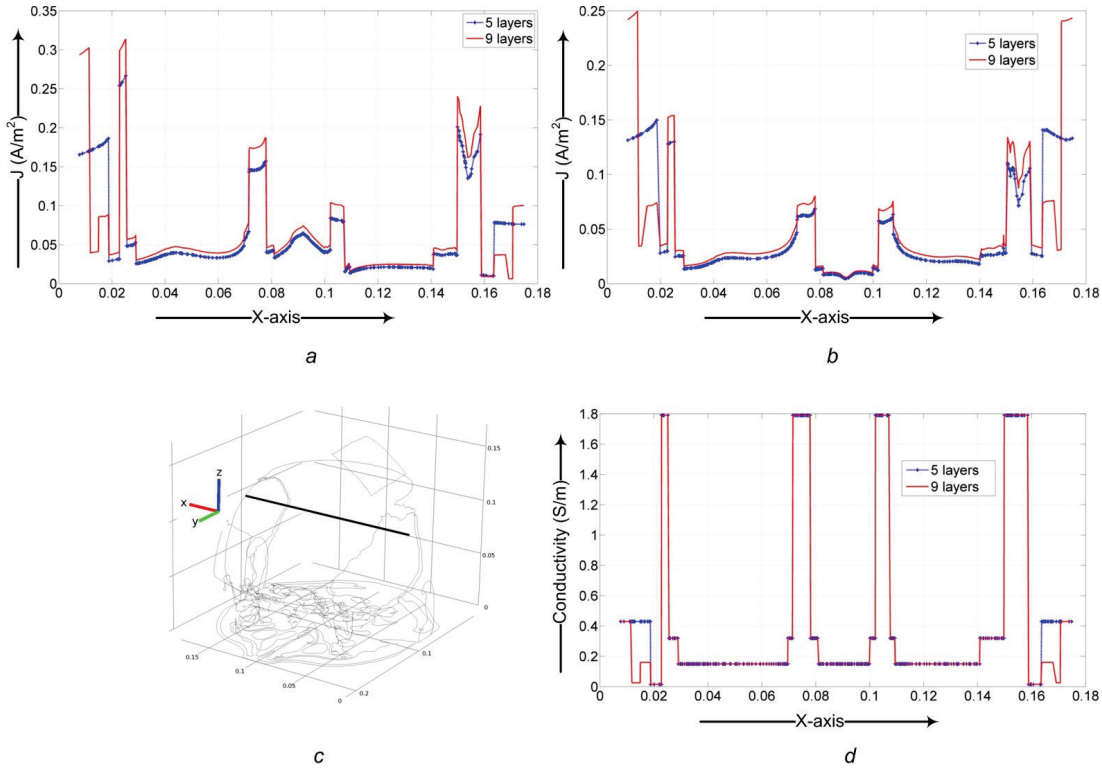

Figure 5.1: Current density variation across an arbitrary straight line, (a) 1D J distribution using C3-Fp2 electrode configuration, (b) 1D J distribution using C3-C4 electrode configuration, (c) an arbitrary straight line (parallel to the xy plane) starting from x=0 (left side of the head model) to x=0.18m (right side of the head model) and passing through various regions of the head model (d) Electrical conductivity variation across an arbitrary straight line.

Under the C3-Fp2 electrode configuration, the comparative analysis of volumetric data (five and nine layer models) suggested that there was the increase of 45.17% in J_{max} and approximately 29.60% increase in J_{median} at the scalp. It was also found that J exhibited an approximate log-normal distribution which concurs with the earlier findings of Sadleir et al. (2010). Table 5.1 illustrates the comparison of J_{median} across different layers using both electrode configurations.

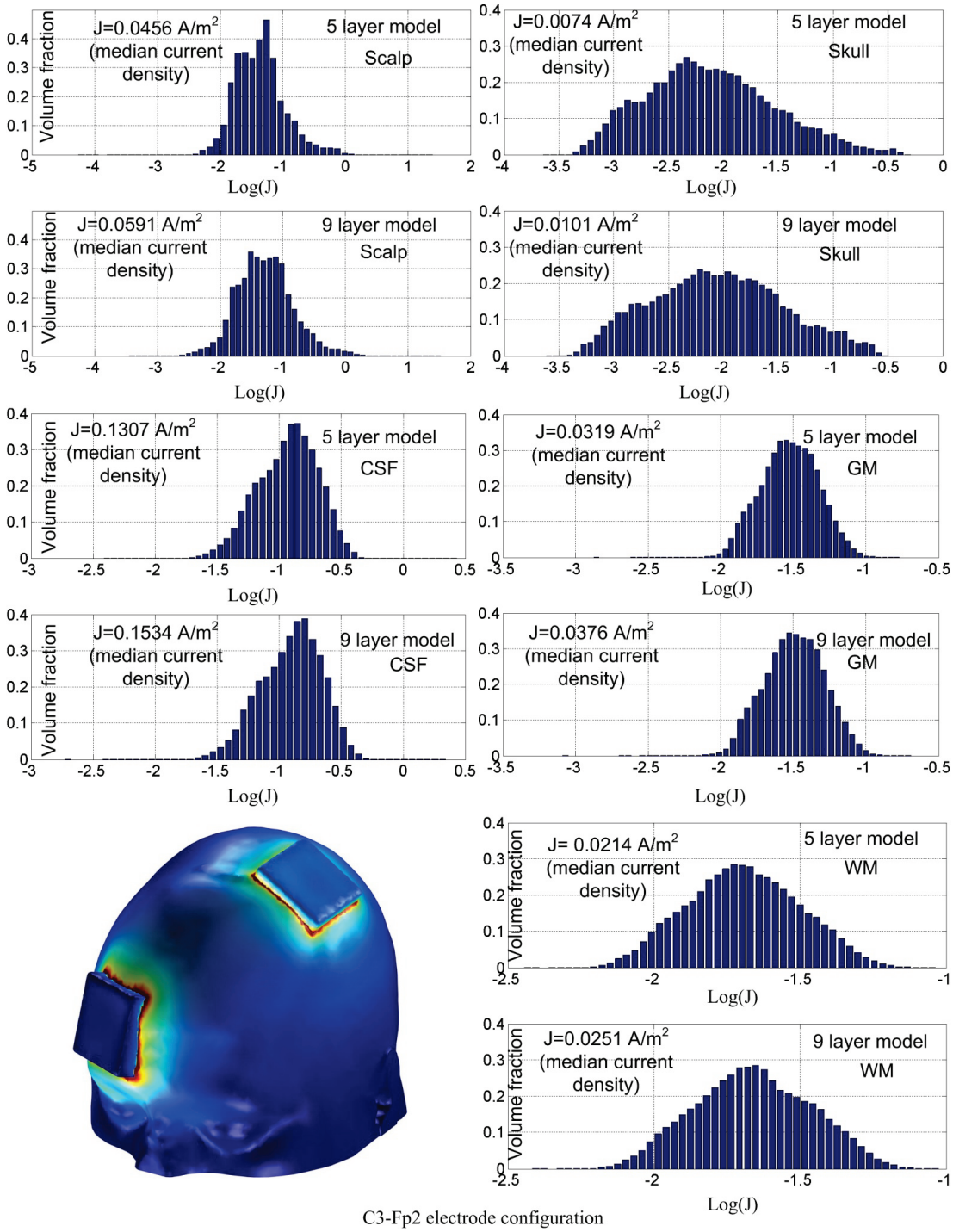

Figure 5.2: Comparative analysis of current density distribution between 5 and 9-layer head models, C3- Fp2 electrode configuration.

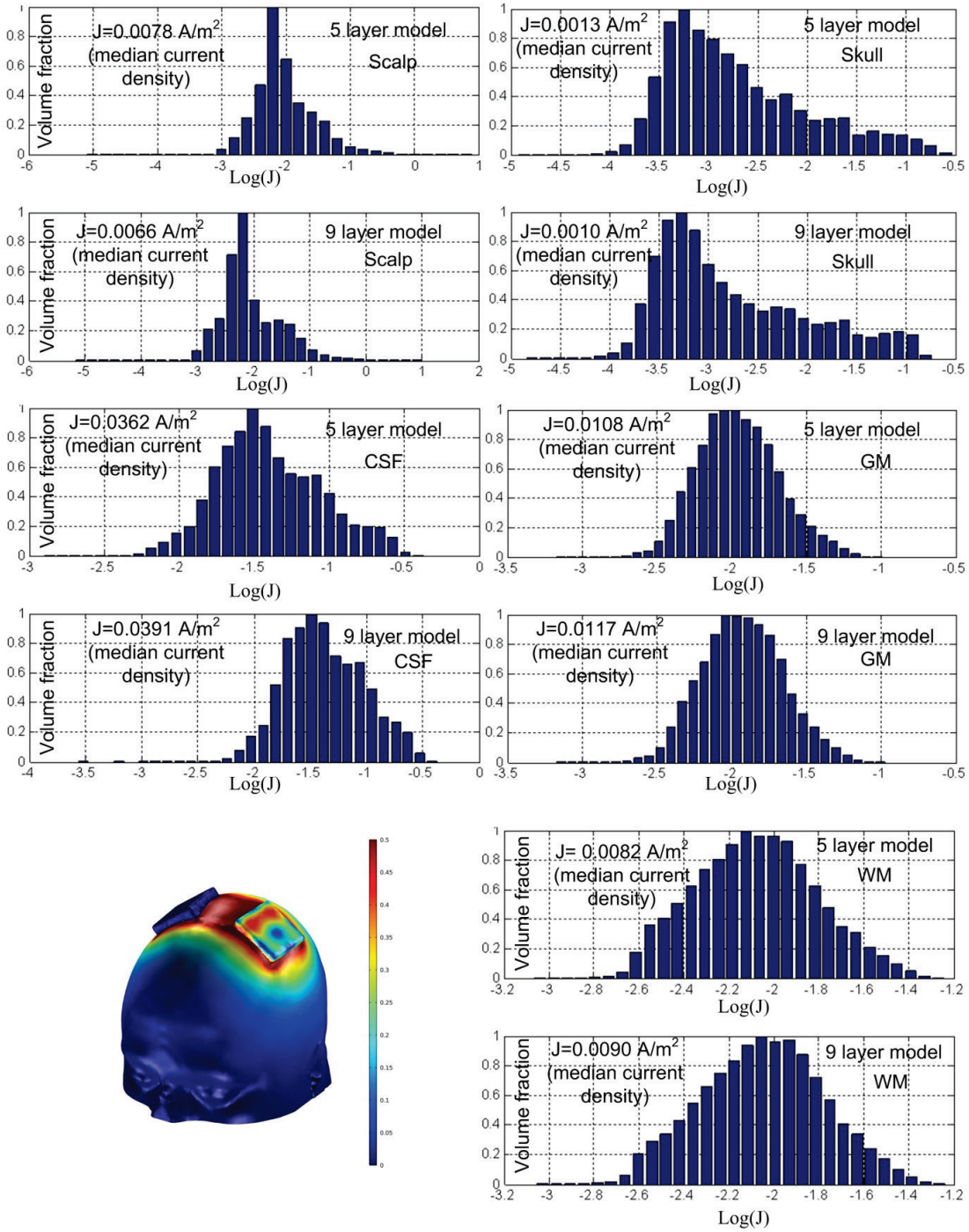

Figure 5.3: Comparative analysis of current density distribution between 5 and 9-layer head models, C3–C4 electrode configuration.

Table 5-1: Comparison of J_{median} across different layers

Tissue type	(C3-Fp2) -% change in J_{median}	(C3-C4) -% change in J_{median}
Scalp	↑29.60	↓6.01
Skull	↑36.48	↓ 13.63
CSF	↑14.79	↑19.19
GM	↑15.16	↑20.65
WM	↑17.29	↑20.57

From Table 5.1 and Figure 5.2, it can be seen that under the C3-Fp2 electrode configuration, the inclusion of additional layers led to an increase in *J* across different tissue regions. Considering the large distance between the anode and the cathode, a reduction in the effective volume of the preferential path (scalp) of current led to an increase in *J* across the scalp and the cortex. However, from the C3-C4 configuration (Figure 5.3 and Table 5.1) it can be observed that there was 6.01 % drop of J_{median} across the scalp and 13.63% drop across the skull. This observation implied that the position of stimulating electrodes also played an equally important role in defining the J distribution, as hypothesised by Miranda, Lomarev and Hallett (2006) and Wagner et al. (2007). Since decreasing the distance between electrodes led to a drop in current flow into the brain it was observed that, compared to C3-C4, the C3-Fp2 electrode configuration had on average higher *J* across cortical structures (≈ 70% across GM and 48% across WM). The inclusion of fat and muscle regions in a model under C3-C4 configuration has further limited the flow of current across the scalp and skull. This behaviour is indicative of the complex nature of a resistive network pattern of the head model. It is also worth mentioning that deeper regions still experienced an increase in *J*. Hence, it can be deduced that the inclusion of additional layers, at the cost of scalp tissue, channels more current through the GM and WM.

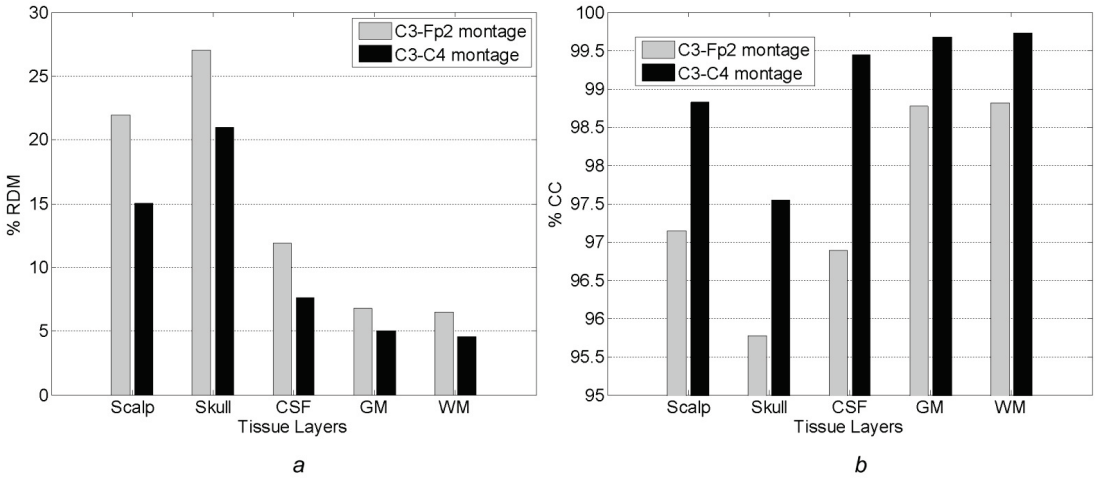

Figure 5.4: (a) Topographic variation in *J* as a function of model complexity and (b) Correlation coefficient as a function of model complexity.

From Figure 5.4 (a) and Figure 5.4 (b), it can be observed that maximum topographic errors, in both electrode configurations, were recorded across the skull region followed by the scalp tissue, whereas GMs recorded modest variations in J distribution. On the other hand, WM recorded slightly less variation than GM. Similarly, CC depicted the strongest mismatch across the skull region followed by the scalp and CSF layers. In order to assess these distribution variations quantitatively, the distribution patterns of active regions, under both electrode configurations, were assessed in terms of the percentage of *J* magnitude, which was more than 50% of J_{max} for the tissue volume with lowest J_{max}. From Table 5.2, it can be seen that GMs in nine layer models had a more widespread pattern of active regions. A similar pattern was also observed across the WMs of nine layer models under both electrode configurations.

Table 5-2: Concentration of active regions across GM and WM

Electrode configuration	**C3-Fp2**		**C3-C4**	
Model type	5-layers	9-layers	5-layers	9-layers
		GM		
Active region (%)	0.5821	2.3703	1.0599	1.7742
		WM		
Active region (%)	3.1543	8.4705	2.6186	4.1232

From Figure 5.4 it can also be noticed that, although the indices have different values for both electrode configurations, these indices project an almost identical trend from scalp to WM. This observation indicates that, under different electrode configurations, the *J* exhibits quite a similar variation in its distribution as it progresses through different regions of the head.

5.3.2. Influence of tissue anisotropy (artificial) on field estimates

The effects of anisotropy on current density distribution (*J*) were analysed using five models (nine layered) with previously mentioned electrode configurations. Table 5.3 illustrates the type of models used in the comparison, along with their respective tissue conductivities.

Table 5-3: Conductivity assignment for model comparison (conductivities are in *S/m*)

Models	Scalp	Fat	Muscle/eye-muscle	Skull	CSF	GM	WM	Eyes
M1	0.43	0.025	0.16	0.015	1.79	0.32	0.15	0.5
M2	0.43	0.025	$\sigma_L=5\sigma_{Trans}$ $\begin{bmatrix}0.0715 & & \\ & 0.3577 & \\ & & 0.3577\end{bmatrix}$	0.015	1.79	0.32	0.15	0.5
M3	0.43	0.025	0.16	$\sigma_T=10\sigma_R$ $\begin{bmatrix}0.0047 & & \\ & 0.0473 & \\ & & 0.0473\end{bmatrix}$	1.79	0.32	0.15	0.5
M4	0.43	0.025	0.16	0.015	1.79	0.32	$\sigma_L=10\sigma_{Trans}$ $\begin{bmatrix}0.4743 & & \\ & 0.0474 & \\ & & 0.0474\end{bmatrix}$	0.5
M5	0.43	0.025	$\sigma_L=5\sigma_{Trans}$ $\begin{bmatrix}0.0715 & & \\ & 0.3577 & \\ & & 0.3577\end{bmatrix}$	$\sigma_T=10\sigma_R$ $\begin{bmatrix}0.0047 & & \\ & 0.0473 & \\ & & 0.0473\end{bmatrix}$	1.79	0.32	$\sigma_L=10\sigma_{Trans}$ $\begin{bmatrix}0.4743 & & \\ & 0.0474 & \\ & & 0.0474\end{bmatrix}$	0.5

Using 1-D *J* analysis across these five models, from Figure 5.5, it can be observed that anisotropic conductivity played a significant role in shaping *J* amplitude, not only across the anisotropic layer, but also across the adjoining isotropic regions. Under the C3-Fp2 configuration, it can be seen that model M5 displayed an increase in *J* magnitude across the scalp region. This increase in magnitude at the scalp tissue was attributed to the shunting effect generated by the anisotropic skull and muscle conductivities. This anisotropic behaviour channelled more current across the scalp and, as a result, less current was depicted across the cortex. Through the low conductive fat and skull regions, *J* was quite suppressed, whereas, at the GM, *J* of M5 was lower than that of M1, but greater than that of M3. This behaviour further indicated the shunting effect caused by anisotropic conductivities of muscle and skull tissues. Even though the magnitude of *J* through the CSF region was quite high (in all models), *J* of M3 was the lowest across that region, again suggesting the shunting effect caused by the skull tissue. Across the WM, M4 recorded a substantial increase in *J* which was attributed to higher radial conductivity across the anisotropic WM tissue. The effect of WM anisotropy can be detected across other regions of model M5 in terms of an overall increase in J magnitude.

Under the C3-C4 configuration, which provided more symmetric electrode assignment, *J* almost behaved in a similar fashion. Using the same 1-D approach, comparison between M1 and M5 (C3-Fp2/C3-C4) recorded an RDM of (33.50%/39.67%) and CC of (87.09%/84.27%), which indicated that, at the location of analysis, tissue anisotropy had a strong influence on *J* strength and the distribution pattern.

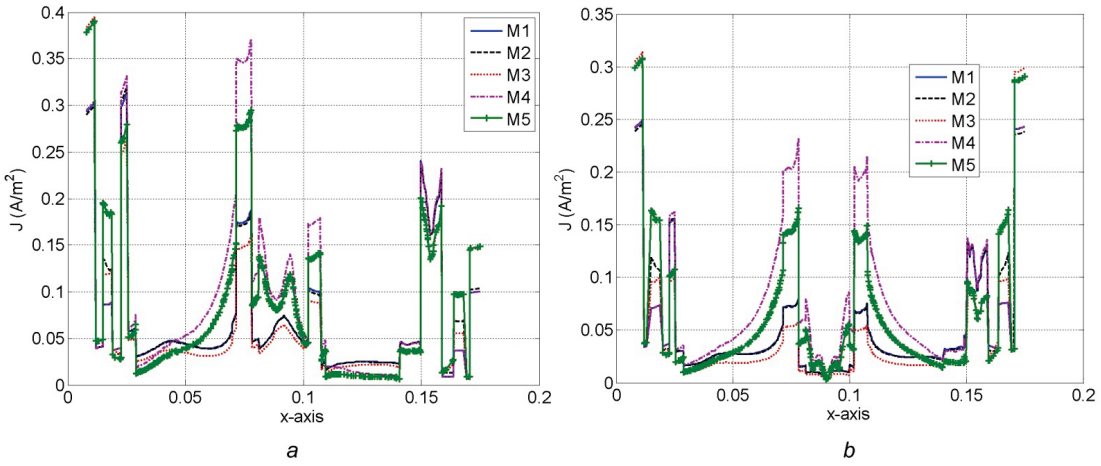

Figure 5.5: 1D *J* distribution pattern across a straight line passing through five (conductivity wise) different head models, (a) 1D *J* distribution using C3-Fp2 electrode configuration, (b) 1D *J* distribution using C3-C4 electrode configuration.

From Figure 5.6, it can be observed that the inclusion of anisotropy had a profound effect on the *J* distribution right across the scalp region. At the same time, comparison between M1 and M5 recorded an increase of almost 11 % in the median value of *J* (C3- Fp2 configuration), whereas, C3-C4 configuration recorded an increase of 55 % in J_{median}, which, in addition to anisotropy, can be attributed to the close proximity of electrodes.

Using the distribution pattern and median values of *J* in Figure 5.6, it can be observed that in model M2, where the longitudinal conductivity in muscle regions was five times than that of its transverse value, there was an increase in J_{median} (1.86%) across the scalp. The conductivity tensor caused additional current to flow along the longitudinal direction of the muscle tissue, leading to the additional flow of current through the scalp and less current through the cortex.

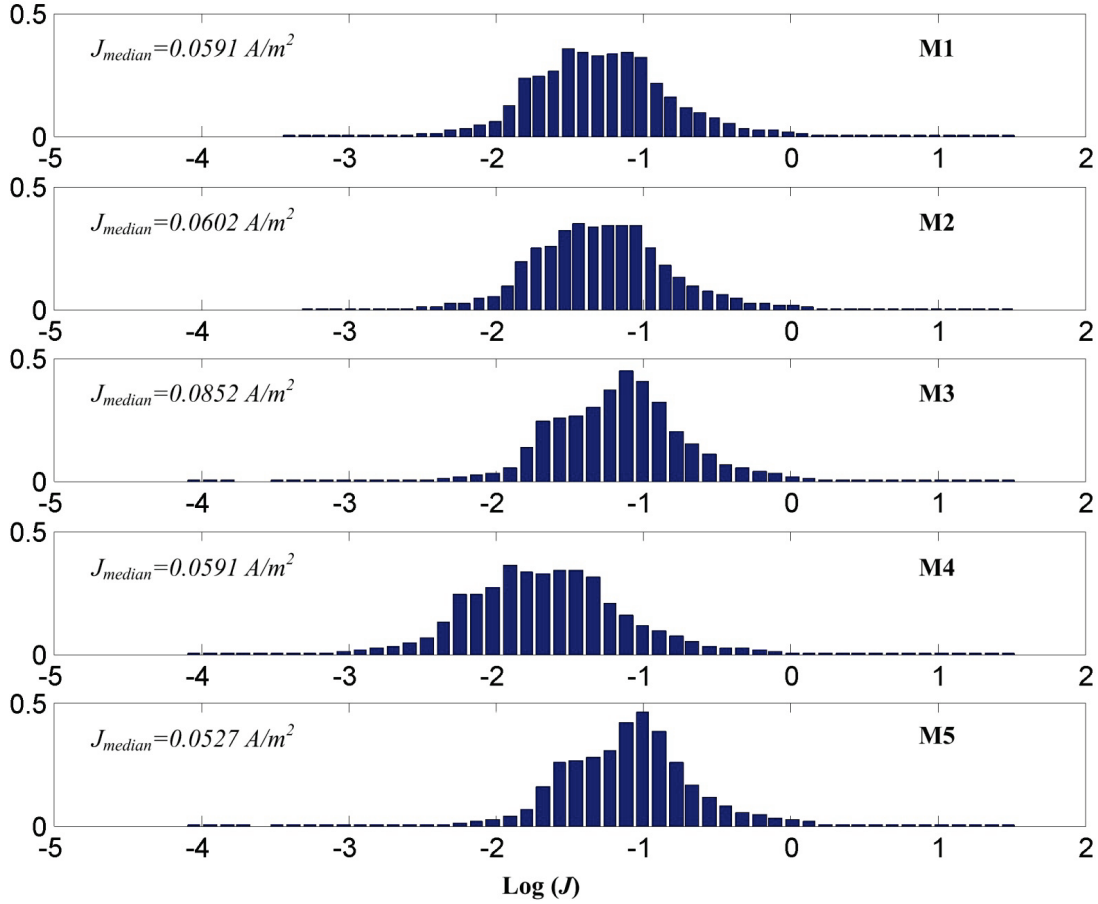

Figure 5.6: Current density distribution across the scalps of M1, M2, M3, M4 and M5 under C3-Fp2 electrode configuration.

The anisotropic skull (M3), with its radial conductivity being 10 times less than the tangential one, restricted current from flowing to deeper regions, causing a shift in the distribution pattern and leading to an increase in J_{median} (44%) across the scalp. On the other hand, the 10 times higher longitudinal conductivity of the WM, with respect to its transverse conductivity, caused the distribution to move left along the x-axis, depicting the change in distribution pattern across the scalp. However, its overall effect on the scalp was not strong. This variation in the distribution pattern can be attributed to the reorientation of current flow in the radial direction of the conductivity tensor and less current in its tangential orientation.

Under C3-Fp2 electrode configuration, the behaviour of J across the GM and WM is illustrated in Figure 5.7(a) and Figure 5.7(b), respectively. From this figure, it can be observed that anisotropic conductivity caused the cortical currents to be more scat-

tered across the GM and WM leading to a more dispersed, diffused pattern of hotspots. These cortical regions of maximum J were more prominent in deeper regions of sulci, mostly scattered across the top of the left parietal, left frontal and the right prefrontal lobes (not shown in Figure 5.7a).

The comparison between M1 and M5 indicated a drop of 15 % in J_{median} across the GM of M5, whereas, J_{max} in M5 was almost (34%) higher than that of M1. This behaviour indicated a more dispersed pattern of active regions, with some regions exhibiting higher values of J due to the reorientation of current flow caused by the directional conductivity of the WM. By comparing M1 with M4, it can be observed that J_{max} across the GM had a substantial increase of 85%, while J_{mean} was ≈ 1% less than that of M1. These facts further support the hypothesis that there was a substantial drop in J magnitude but, some regions had higher/lower values of J due to the directional conductivity of WM. Overall, this behaviour was further suppressed by the shunting effect caused by the skull and muscle anisotropic conductivities. Similar behaviour was also observed across the white matters of models M1 to M5.

Comparing the histogram (M1 and M5) (Figure 5.7) along with RDM, indicated a strong change in the distribution pattern of approximately 26 % across the GM (Table 5.4) and almost 47% across the WM (Table 5.5). Similarly, CC recorded the strongest mismatch across the GM and WM in M1-M5 comparison.

Under the same definition of active regions, Table 5.6 provides a comparative analysis of the effects of anisotropic tissue conductivity on cortical current distribution. It can be observed that the inclusion of the anisotropic skull and muscle tissue led to a drop in the concentration of hotspots. This behaviour was substantially aggravated due to the skull anisotropy. On the other hand WM anisotropy led to a significant proliferation in hotspot distribution.

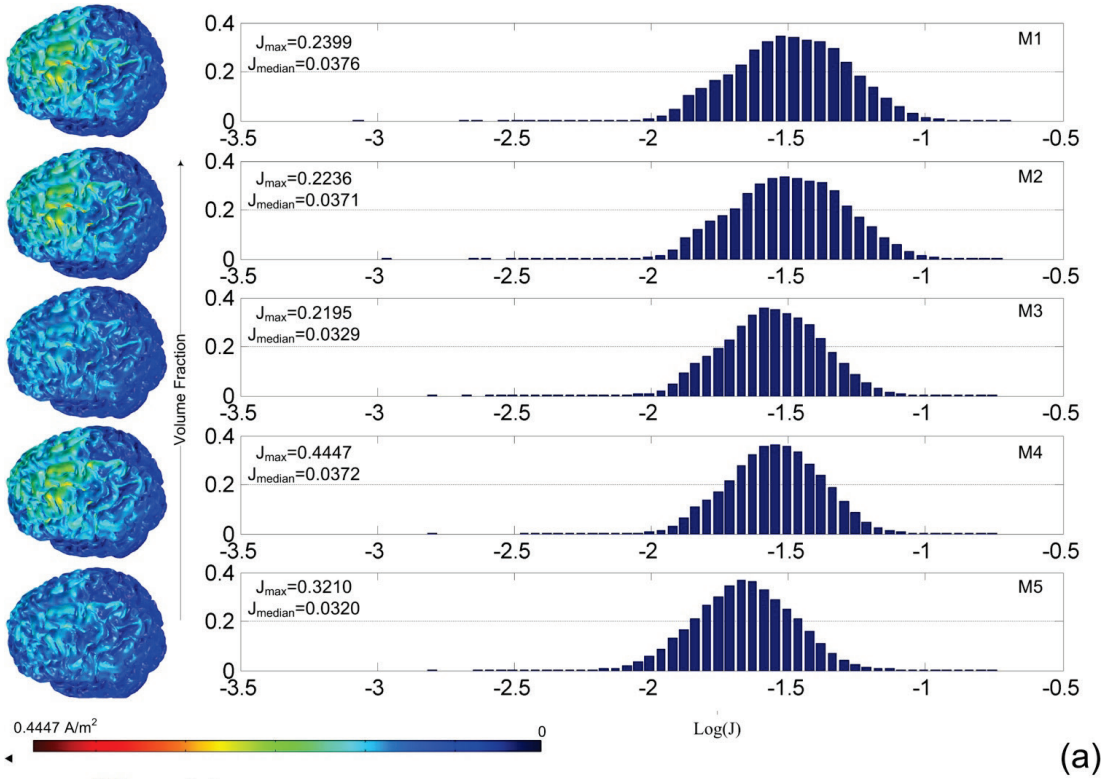

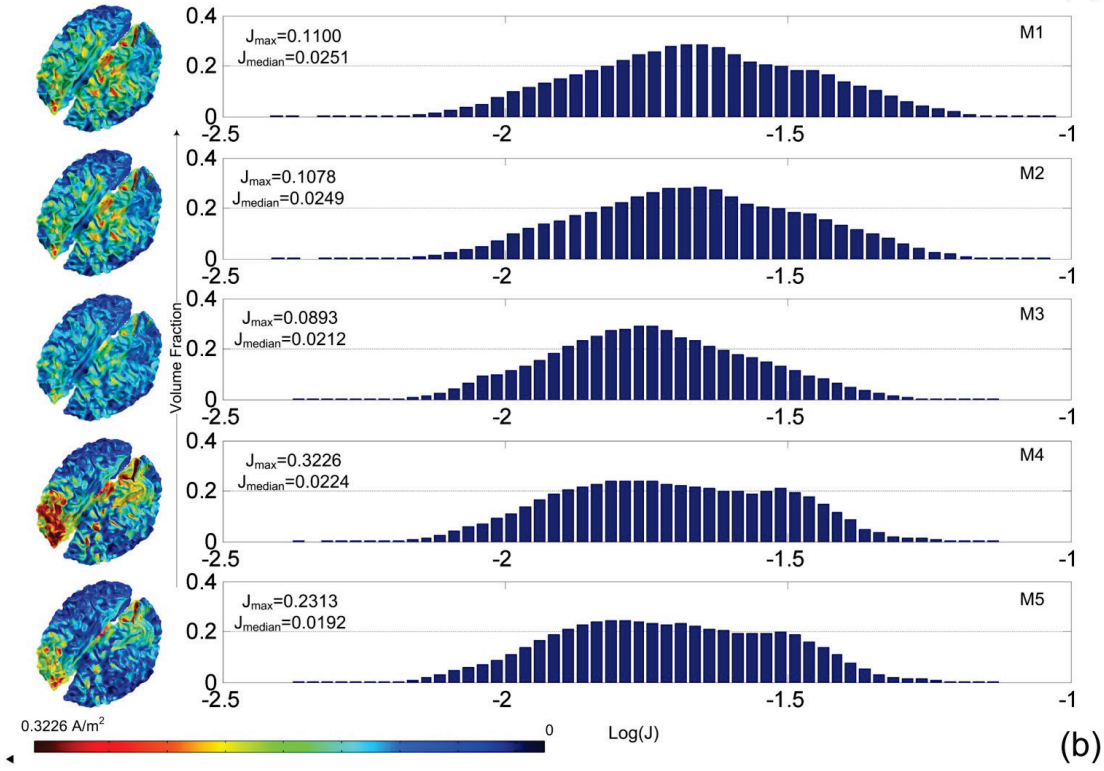

Figure 5.7: (a) Current density distribution across GMs and (b) Current density distribution across WMs, under C3-Fp2 electrode configuration.

Table 5-4: Statistical variations across GM under C3-Fp2 electrode configuration

RDM	CC
(M1-M2)	
0.0218	0.9988
(M1-M3)	
0.1117	0.9703
(M1-M4)	
0.2436	0.8629
(M1-M5)	
0.2656	0.8108

]

Table 5-5: Statistical variations across WM under C3-Fp2 electrode configuration

RDM	CC
(M1-M2)	
0.0192	0.9990
(M1-M3)	
0.1015	0.9731
(M1-M4)	
0.4695	0.7505
(M1-M5)	
0.4762	0.7054

The orientation of cortical currents plays a crucial role in cortical modulation (facilation or inhibition/suppression) (Wagner et al. 2007). A number of factors may influence this current orientation, such as, electrode configuration, morphological variations in skull and cortex, skull to cortex distance, CSF conductivity, inherent heterogeneity between GM and WM, and directional conductivity of the skull, muscles and WM. Figure 5.8 provides a comparative view of current orientation among M1 (isotropic) and M5 (anisotropic) head models under C3-Fp2 electrode configuration. Using this posterior view of a coronal slice, it can be observed that overall current was flowing from the anode towards the cathode. However, in M5, there were regions where the current was flowing in orientations quite different from the M1 flow.

These were the regions of anisotropic conductivity in M5 and the directions of current in those regions were primarily dictated by the local conductivity tensor. Furthermore, these current lines were not completely aligned with principal eigenvectors, rather, they tend to trace the general pattern defined by those values. Chapters 6 and 7 investigate this behaviour in more details. Using the conductivity assignment drawn from the actual DTI data, Chapters 6, 7 and 8 provide better estimates of cortical current orientation, especially in the deeper regions of the brain.

Table 5-6: Concentration of active regions across GM and WM

Model	M1	M2	M3	M4	M5
GM-C3-Fp2 electrode configuration					
Active region %	0.6390	0.5561	0.0790	1.5017	0.4423
WM-C3-Fp2 electrode configuration					
Active region %	11.9870	11.2571	3.9410	25.8441	17.9834
GM-C3-C4 electrode configuration					
Active region %	3.5268	3.4632	0.9817	4.3269	1.4057
WM-C3-C4 electrode configuration					
Active region %	6.4484	6.3274	1.9599	14.3133	6.7456

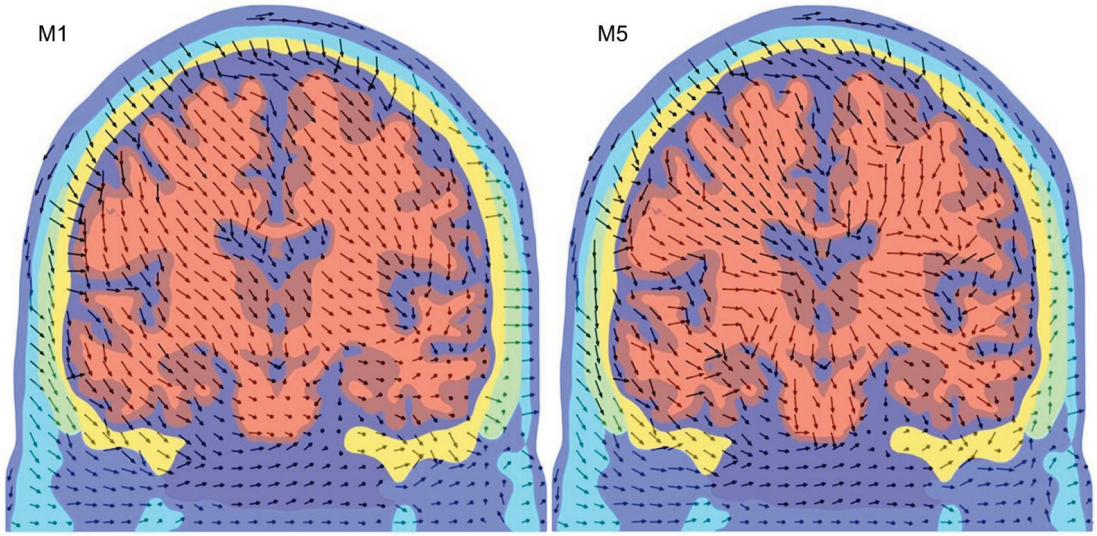

Figure 5.8: Current density distribution pattern, isotropic (M1) vs. anisotropic (M5) distribution pattern under C3-Fp2 electrode configuration.

5.4. Conclusion

In this chapter, a high resolution anatomically accurate human head model and its derivatives were employed to assess the variation in J across different regions of the human head. The inclusion of additional tissues and their effects on cortical current intensity and distribution were quantified using statistical measures such as the Relative Difference Measure and Correlation Coefficient. The commonly used five layer isotropic head model was compared to the proposed nine layer models under two different electrode configurations. It was observed that the inclusion of these layers in a model had a profound effect on the scalp and cortical currents. Under the C3-Fp2 electrode montage, an approximately 30% increase in J_{median} was observed across the scalp and 17% across the GM and WM. Reduction in the effective volume of the preferential path (scalp) of current caused additional current to flow through the cortex. Incorporation of these layers, especially the low conductive subcutaneous fat tissue favoured deeper penetration of the current. As a result, there was an increase in the current density across the cortex.

The maximum J of 0.3210 A/m^2 was recorded for model M5, across the cortex, under C3-Fp2 electrode configuration. Based on the study conducted by Radman et al. (2009) inactive neurons require around 79–120 mV/mm of induced E for activation.

Whereas, the maximum E corresponding to J_{max} (found in M5) was around 1 mV/mm in GM and minimum directional conductivity of WM produced 4.88 mV/mm of E in the WM. These values were approximately 79 and 16 times less than the threshold values, respectively. Hence, under current clinical protocols, tDCS must be treated as a neuro-modulatory procedure. In terms of the safety of operation this maximum cortical J was approximately 440 times less than the prescribed threshold (142.9 A/m^2) (Liebetanz et al. 2009).

Anisotropic electrical conductivity has a major role in shaping the current distribution across the head model. This chapter has demonstrated that the anisotropy caused a wider and more diffused distribution pattern of J across the cortex and played a pivotal role in defining J intensities. Hence, anisotropic conductivity would cause a significant effect on neural modulation, not only around the superficial layers of the cortex, but also in the deep regions of the brain such as the corpus callosum. Anisotropic muscle conductivity displayed a mild shunting effect, causing more current to flow through the superficial tissue layers of the head, thus leading to a slight drop in cortical currents. Similarly, the skull anisotropic conductivity generated a strong shunting effect, restricting the flow of current from deeper parts of the head and led to the displacement in stimulation areas. WM anisotropic conductivity had a strong effect on cortical current orientation, thus changing the distribution pattern of J across the GM and WM.

6. ROLE OF REALISTIC WHITE MATTER ANISOTROPIC CONDUCTIVITY ON FIELD ESTIMATES

6.1. Introduction

Tissue heterogeneity and white matter fibre architecture pose a major challenge in interpreting electric fields and current distributions. These field parameters (E/J) are considered directly responsible for eliciting the acute modification of membrane polarization (the direct-effect) and indirectly for the occurrence and duration of the after-effect. To understand the role of field parameters on the site and strength of stimulation, it is imperative to assess and quantify these variables under realistic conditions. This chapter provides an insight into the changes in the strength and distribution patterns of induced current density across the human brain due to the inclusion of realistic WM anisotropic conductivity patterns.

In the previous chapter artificial WM anisotropy was used as a test case to validate the need for more realistic WM anisotropy estimations in the forward solutions of tDCS. At this stage of the study, simulated datasets and subject-specific datasets were used to construct anatomically accurate human head models. A bi-cephalic conventional montage (C3–Fp2) with each square electrode having an area of 25cm^2 was used to inject *1mA* of direct current into the volume conductor models. Each

model (averaged and individual) was segmented into nine regions, and WM anisotropy was introduced using the artificial (Chapter 4) and measured DTI datasets.

Using the averaged and subject-specific head models, the limitations of anisotropic estimation algorithms along with the impact of heterogeneously defined anisotropic distribution, were investigated across the GM, WM and specific regions of interest. The Chapter also highlights the role of subject-specific anatomical variations on field estimates and emphasise on the need to consider subject-specific dose parameters in forward models of tDCS.

6.2. Material and methods

6.2.1. Isotropic volume conductor model construction

The simulated datasets (T1, T2 and PD-MRI) were used to construct the high resolution finite element head model with nine tissue types. This averaged model had already been used in Chapter 5. Additional details about this model are provided in Chapter 3, Section 3.1.1 and Chapter 5, Section 5.2.1. In order to analyse the influence of anatomical variations on conductivity tensor distribution estimations, the T1-weighted MRI of an individual subject (MNI_0591) was obtained from the ICBM Subject Database. The subject-specific structural data consisted of T1-weighted MRI with $1mm^3$ voxel resolution and 256x256x176 slices. Additional details about the subject's scan can be accessed from the LONI ICBM database (*ICBM:International Consortium for Brain Mapping* n.d.). The scalar MRI of the individual subject was truncated along the z-axis to match the features available in its DTI dataset. Using the FSL (Smith et al. 2004), masks of scalp, skull, CSF, GM and WM were generated from the T1-weighted scan of the subject. Segmentation of subcutaneous fat, eye-muscles, muscles of mastication and eyes were performed manually using Simpleware. In both cases (averaged and subject-specific), the tissue classification was further assisted by a cross comparison against the brain atlas (Woolsey, Hanaway & Gado 2008) and the tissue classification study (Ramon, Schimpf & Haueisen 2006).

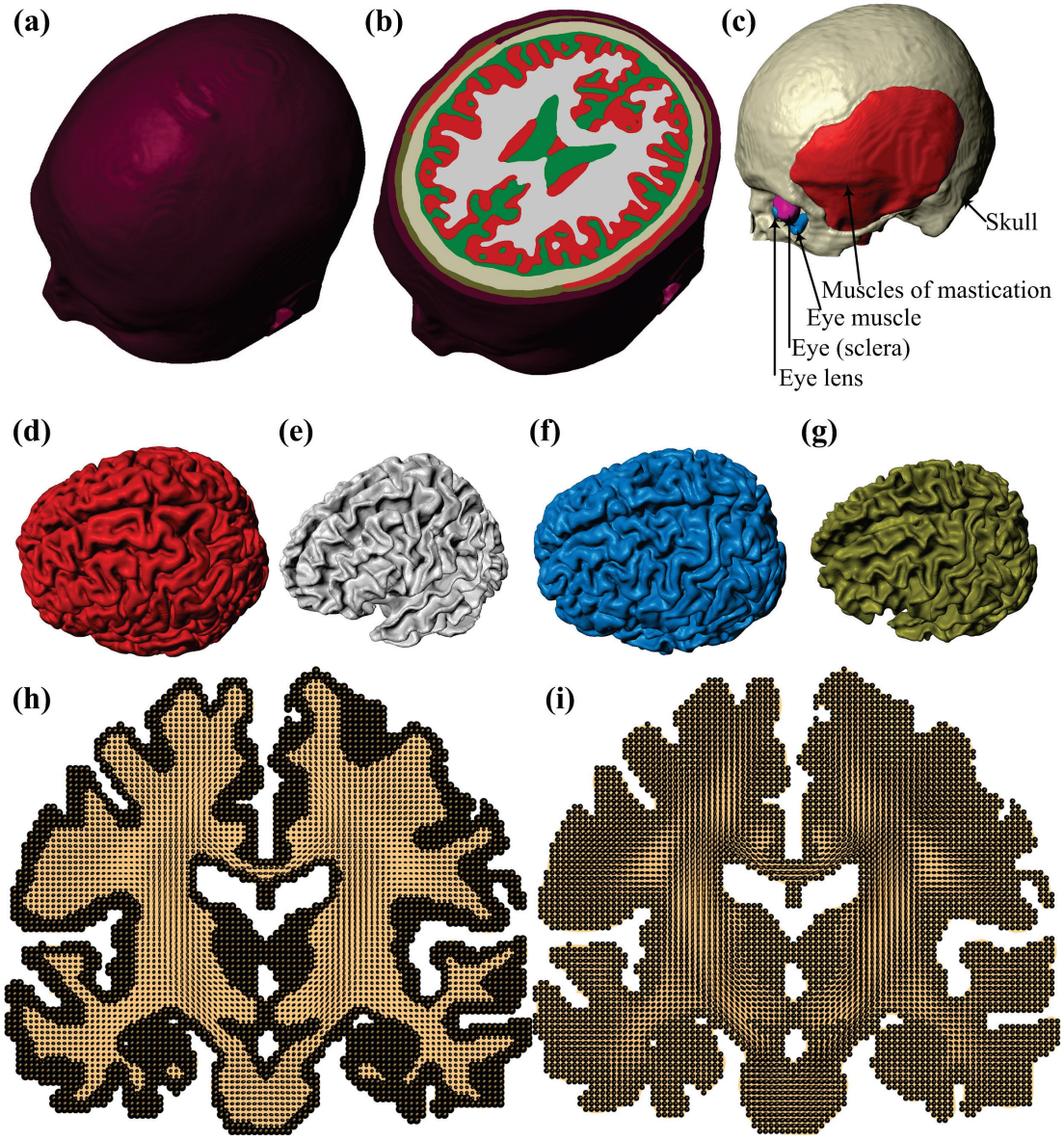

Figure 6.1: Cortical and non-cortical regions segmented from the averaged and subject specific MRI datasets. (a) Volumetric head model highlighting the scalp region of the averaged head model. (b) 3D cutaway view of the averaged head model, illustrating various cortical and non-cortical regions. (c) The skull, muscles of mastication, eye muscles, eye (sclera) and eye-lens obtained from the averaged MRI datasets. (d) GM of the averaged head model. (e) WM of the averaged head model. (f) GM obtained from the individual (MNI_0591) MRI dataset. (g) 3D WM volumetric model representation based on subject specific dataset. (h) Coronal slice of the averaged head model illustrating conductivity tensor representation in the form of ellipsoids. The distribution is produced using (A3) Equivalent Isotropic Trace algorithm. (i) Normalized conductivity tensors representation across the coronal slice of the averaged model.

The entire segmentation procedure, 3D model construction and volumetric mesh generation was carried out in a commercially available package (Simpleware) in a semiautomatic manner. In this chapter the 3D model based on the simulated scans is termed the 'averaged model' and in the rest of the chapter the model and its derivatives will be represented by the letter "A", whereas, in the case of the individual models, notation "I" is used. Single electrode configuration, containing two square electrodes each of 25 cm^2 area was also modelled in the same package. The volumetric mesh models contained nine regions corresponding to nine different segmented tissues (excluding the electrodes) and comprised of around two million tetrahedral elements. The mesh generation algorithm was optimized to obtain greater mesh density across the thin layers (0.5 mm) and around cortical structures. Figure 6.1(a–g) provides an overview of the 3D models used in this chapter.

6.2.2. Incorporation of WM anisotropic conductivity

The Diffusion Tensor Imaging (DTI) volume of the subject (MNI_0591) was obtained from the LONI ICBM database (*ICBM:International Consortium for Brain Mapping .n.d*). Each data volume consisted of a 96x96x60 matrix of isotropic voxels with a resolution of 2.5 mm. The dataset has 31 gradient directions with a *b-value* of 1000 s/mm^2. In order to correct the distortion and misalignment caused by eddy currents and head movement, the FDT (FMRIB Diffusion Toolbox) of FMRIB software library (Behrens et al. 2003) was used. Local diffusion tensor information was obtained by performing the linear least-square fit to the tensor coefficients (Basser, Mattiello & LeBihan 1994a). To ensure the positive definiteness of the measured diffusion tensor, the scheme proposed by Fillard et al. (2007) was used to replace the null or negative eigenvalues with the log-Euclidean average of the corresponding positive neighbours. Additional parameters such as the fractional anisotropy (*FA*) at each voxel, principal diffusion direction and diffusion tensor were also extracted using the eigenvalue decomposition. Using the same library (FSL FLIRT), the affine spatial registration of diffusion weighted images to the high-resolution scalar volume data (T1-MNI_0591) was carried out. However, this registration did not perform the

necessary local tensor orientation correction which is required to retain the actual orientation of vectors (Alexander et al. 2001). To address this issue, the affine transformation matrix obtained from the above operation was employed in the '***vecrec***' (FDT) to perform the necessary orientation correction. This rotation procedure only affects the eigenvectors of a tensor, while preserving the integrity of its eigenvalues.

For the averaged model case, the DTI atlas (ICBM-DTI 81) was used. The ICBM-DTI-81 *FA* map was used to register with 'FMRIB58FA' standard template using the FSL (FNIRT). The transformation matrix was used to spatially co-register the atlas tensor maps and by using the PPD algorithm (Alexander et al. 2001), the reorientation effects of the non-rigid transformation among the simulated datasets and the diffusion tensor map of the DTI-81 atlas were resolved. Section 4.4.5 of Chapter 4 provides an in-depth coverage on the procedure (used in this chapter) to derive the local tensor information.

6.2.3. Tissue electric conductivity assignment

The models used in this part of the study are composed of nine anatomical regions and their conductivity assignments are similar to the nine-layer models used in the previous chapter. Since the notion behind this study was to investigate the effect of WM anisotropic conductivity, the skull and the muscle were assigned their average isotropic electrical conductivity values. In this chapter, the field assessments were performed at a mesoscopic scale, therefore the convoluted fibre architecture in GM would make the resulting current distribution pattern almost isotropic as reported by the in vivo study of Logothetis, Kayser and Oeltermann (2007). Hence, GM was also assigned with its averaged isotropic conductivity value.

To determine the anisotropic electrical conductivity of the WM, two approaches were considered. In the first procedure, it was assumed that nerve fibres emanate radially from the centre of the WM (Chapter 5). Although this procedure is an over-simplified version of WM conductivity estimation, it is useful as it can be used to analyse the current density pattern and its variation along the pre-assigned (simulated) neural pathways. The more realistic approach used in this chapter is to derive the

WM anisotropic conductivity distribution from the DT-MRI. There are a number of algorithms based on the relationship between conductivity tensor and diffusion tensor. In this study, three DTI oriented procedures were considered to estimate the anisotropic conductivity distribution of the WM. Section 4.4.6 of Chapter 4 provides the details in relation to the procedures used for modelling directional conductivity of the WM.

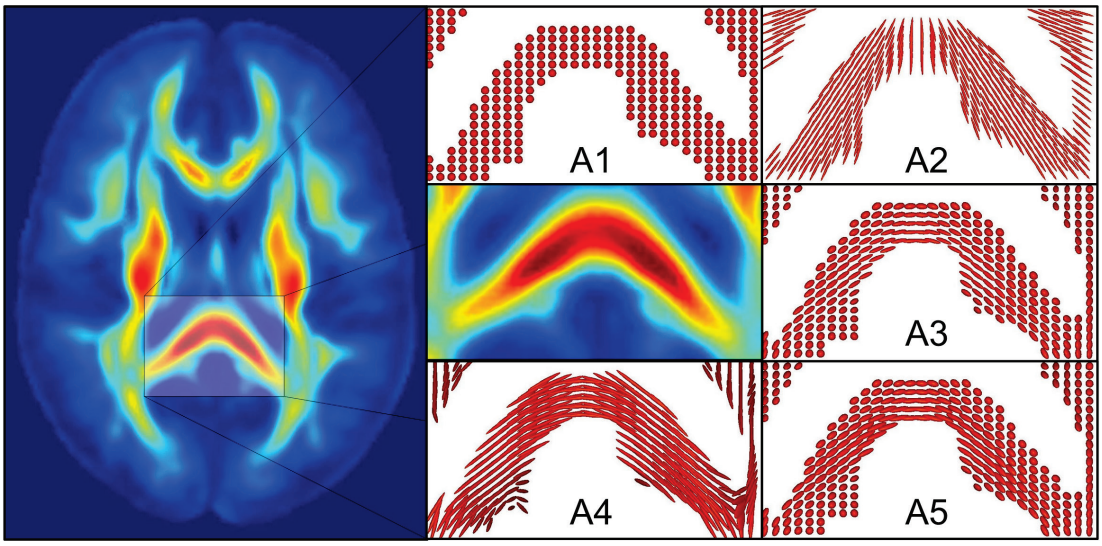

Figure 6.2: Dorsal view of an axial slice of *FA* (fractional anisotropy) map obtained from the measured diffusion tensor data. Regions of high anisotropy are depicted in red and yellow colours, whereas, the contrast of blue colour indicates regions of low anisotropy. ROI illustrates conductivity tensor ellipsoids. Their shape and orientation is dictated by the procedure employed. A1, Isotropic head model; A2, artificial anisotropy (radial) based head model; A3, head model based on Equivalent Isotropic Trace algorithm; A4, model based on fixed (eigenvalues) anisotropic algorithm and A5, model based on Proportional Anisotropic Ratio algorithm.

6.2.4. Electrode configuration and current density calculation

A single bi-cephalic conventional montage (C3–Fp2) was selected to assess the effects of WM anisotropy on cortical current distribution. The electrode positions C3 (anode) and Fp2 (cathode) were derived from the International 10–20 system. This particular electrode configuration was selected because of its significance in clinical practice to modulate the primary motor cortex (Utz et al. 2010). Each electrode was modelled as a 5cm x 5cm square pad with an average thickness of 0.2 cm.

An inward current density of $0.4\ A/m^2$, corresponding to $1mA$ of current, was assigned to the exposed surface of the anode, i.e. $n \cdot J = 0.4\ A/m^2$ (Numann Boundary condition). On the other hand, the exposed surface of the cathode was assigned the Dirichlet boundary condition, i.e. $V=0$. The rest of the exposed boundaries were considered electrically insulated ($n \cdot J=0$) and the continuity of the normal component of current density ($n \cdot J_1 = n \cdot J_2$) was preserved across all the inner boundaries.

In this chapter, the volume conductor model was considered electrically passive. The effect of initial electrical state of neurons on current density distribution was neglected. Therefore, the Laplace's equation $\nabla \cdot \sigma \nabla V = 0$ was used to estimate the induced electric field (E), and Ohm's law ($J=\sigma E$) was employed to calculate the current density distribution. Under the assumption of negligible displacement current (quasi-static approximation), models were solved in a commercial finite element package "Comsol". A linear iterative solver "Conjugate Gradient" preconditioned by "Algebraic Multigrid" was used in all simulations.

6.2.5. Sensitivity analysis

To study the robustness of conductivity distribution, the topographic variations in the current density of the averaged models were compared to their respective subject-specific models. Since the direct cross-model comparison was not feasible (mismatch in node coordinates), each anisotropic model was compared with their respective isotropic models and then the trend was compared with the results of the individual head models.

6.3. Results and analysis

6.3.1. Volume/domain analysis

To analyse the effects of WM anisotropic conductivity, the current density (J_1) of the isotropic head model (A1) was compared with that of models A2 (artificial anisotropy), A3 (Equivalent Isotropic Trace), A4 (fixed Anisotropic Ratio) and A5 (Propor-

tional Anisotropic Ratio), respectively, across the GM and WM. Figure 6.3 describes the distribution pattern of the magnitude of current density across the GM and WM for all the five averaged models. The regions between C3 and Fp2 (electrode locations) showed clusters of high current density (hotspots). This behaviour was observable across all the five models and was more prominent across the WM regions. Across the grey matter of all five models, hotspots were more prominent in the deeper regions of cortical sulci or the walls of gyri. The locations of hotspots were almost identical across all models with observable changes in their magnitudes. In MNI coordinates, the approximate location of J_{max} for models A1, A3 and A5 was (40, 34, 14), whereas, for models A2 and A4, these spots corresponded to (-14, 2, 50) and (13, 63, 4), respectively.

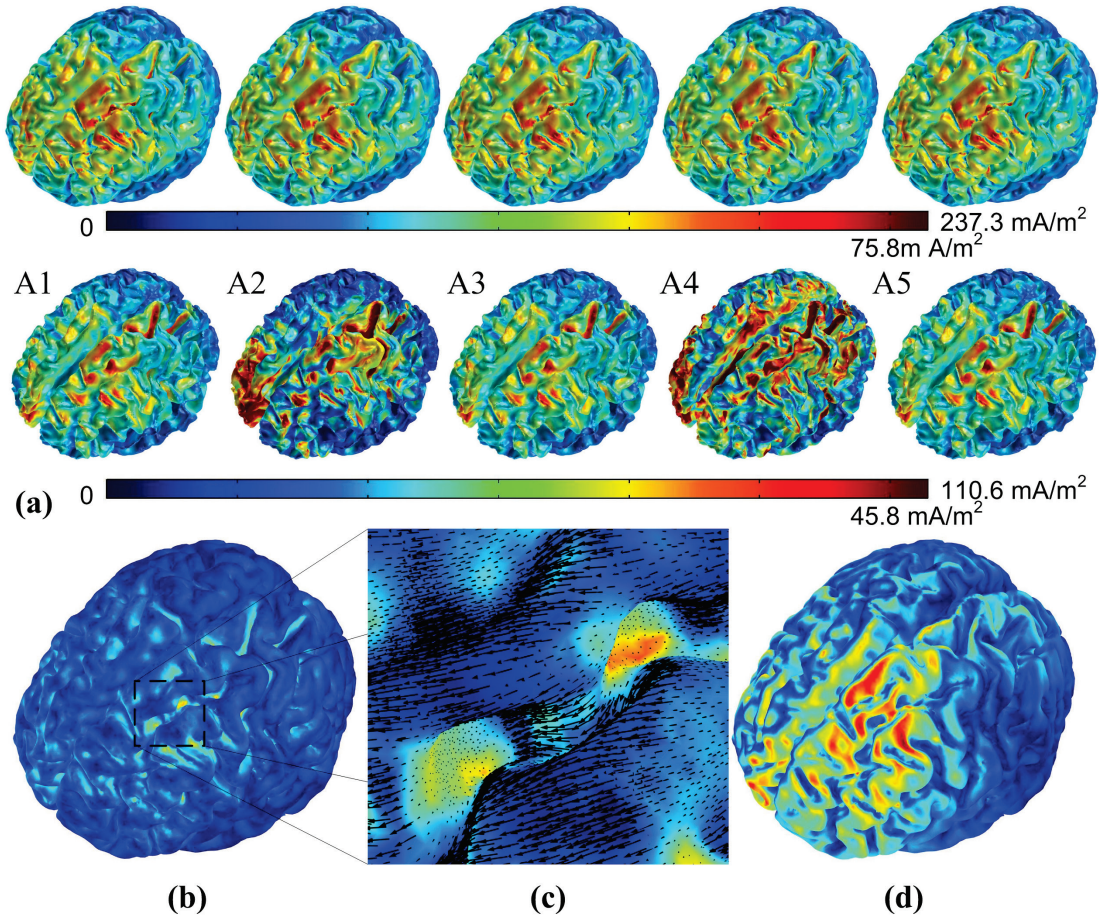

Figure 6.3: (a) Distribution of current density (magnitude) across the GM and WM of all the five models. (b) Distribution pattern of the magnitude of the normal component of current density across the cortex of model A3. (c) Selected region highlighting the strength of the normal component of current density and black arrows indicate the direction of the induced

current density vector. (d) Tangential component of current density across the cortex of A3. A1, Isotropic head model; A2, artificial anisotropy (radial) based head model; A3, head model based on Equivalent Isotropic Trace algorithm; A4, model based on fixed (eigenvalues) anisotropic algorithm and A5, model based on Proportional Anisotropic Ratio algorithm.

These hotspots were formed in those regions of the GM and WM where the direction of induced current is perpendicular to the local boundary. Figure 6.3(b) shows the distribution pattern of the magnitude of the normal component of the current density across the interface of the CSF-GM of model A3. Whereas, Figure 6.3(d) illustrates the distribution pattern of the magnitude of the tangential component of the induced current density. From Figure 6.3(c), it can be seen that current density (black arrows) across active regions were perpendicular to the boundary of the CSF-GM (black dots). Since the normal component of the induced current density was continuous across internal boundaries, internal regions which were locally perpendicular to the incident current would have no or negligible tangential component, thus causing the higher proportion of current to pass straight through those areas. Formation and location of hotspots were directly related to the direction of current flow. However, the flow itself depends on a number of factors such as the position, shape, size and configuration of the stimulating electrodes. In addition, the high conductivity of CSF along with the inherent heterogeneity between the GM and WM also played an equally important role. The influence of anatomical variations (gyral geometry and cortical folding) in the field assessment was also significant when dealing with subject-specific strategies.

The effect of anisotropy along with the degree of variation due to different anisotropic approaches, was scrutinized by using the percentage differences between the isotropic and anisotropic models. Figure 6.4 illustrates the non-absolute percentage difference between J_I and current density magnitudes corresponding to the grey matter of models A2, A3, A4 and A5, respectively. The pattern in Figure 6.4(b) is close to normal distribution and, with respect to models A3 and A5, most of the differences in J magnitude are less ± 10%. For this reason in comparisons of A3–A1 and A5–A1, the projection scale has been fixed between -10 (blue) to 10 (red) (Figure

6.4a) .On the other hand, models A2 and A4 displayed a more substantial difference across both ends (the projection scale for comparisons A2–A1 and A4–A1 is fixed between -50 (blue) to 50(red)). The differences were projected on the cortex to identify the regions affected by the inclusion of anisotropy. Additionally, variations caused by different anisotropic procedures could also been identified. Anisotropy, in general, caused the field strength to increase across the crowns and lips of gyri directly underneath and between the electrodes. On the other hand, field strength had dropped in the cortical sulci across all the models.

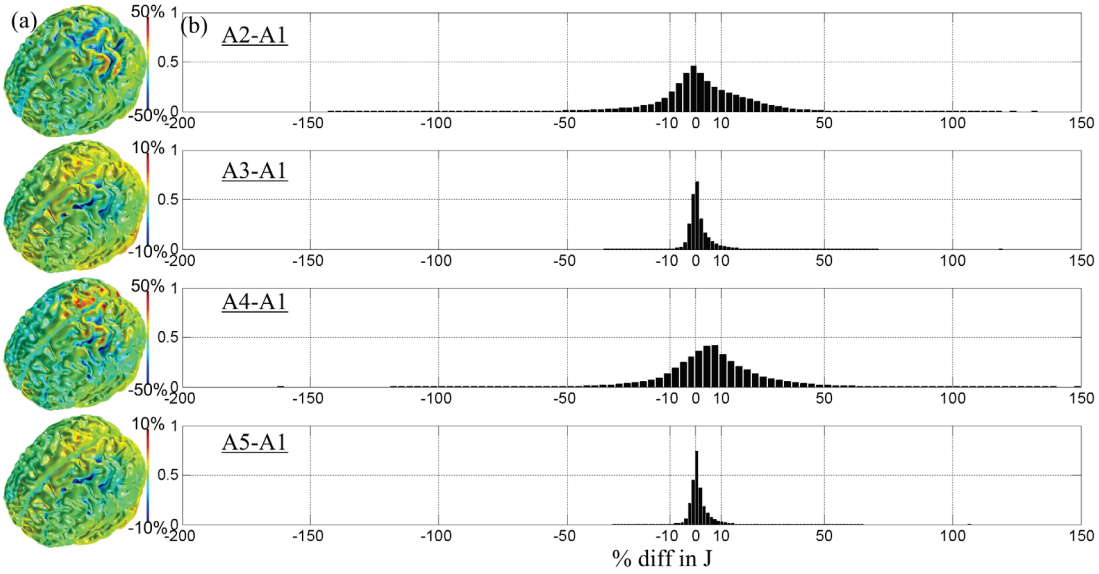

Figure 6.4: Variation of current density distribution in terms of percentage differences across the GM of (A2-A1), (A3-A1), (A4-A1) and (A5-A1). (a) Projection of % difference in J over the cortex. Regions where the strength of J has increased is shown in red and yellow colours. Whereas regions where the magnitude of J has dropped is indicated by a contrast of blue colour (b) histogram analysis highlighting the spread of difference distribution. A1, Isotropic head model; A2, artificial anisotropy (radial) based head model; A3, head model based on Equivalent Isotropic Trace algorithm; A4, model based on fixed (eigenvalues) anisotropic algorithm and A5, model based on Proportional Anisotropic Ratio algorithm.

In terms of WM, the distributions of (A3–A1) and (A5–A1) were similar to their respective GM distributions. However, the difference envelope was slightly broader than ±10%. This indicates a greater influence of anisotropy across the WM volumes. The responses of (A2–A1) and (A4–A1) were rather more flat with difference distribution being significantly high. Across WM regions where the current was aligned

with nerve fibres, showed approximately 20% increase in local field strength, e.g. regions containing the corticospinal tracts showed high magnitude, whereas regions of corpus callosum and cingulum indicated a drop of roughly the same percentage (Figure 6.5a). Locally, variations of ± 100% were recorded for the models with fixed anisotropy, whereas, ± 20% was observed for the variable anisotropic models.

Across the GM, the maximum topographic error was recorded for the comparison of (A2–A1), whereas, (A5–A1) had the minimum RDM, as shown in Table 6.1. In the WM, the maximum topographic error was observed for the comparison of (A4–A1), closely followed by (A2–A1), whereas, around a 10% error was recorded for (A3–A1) and (A5–A1). The results obtained from model A4 were in a close agreement with the study of Lee et al. (2009). Similarly, magnitude variations in *J/E* between the fixed anisotropic ratio model A4 and variable anisotropic ratio model A5 showed a trend similar to that reported by Hyun et al. (2009).

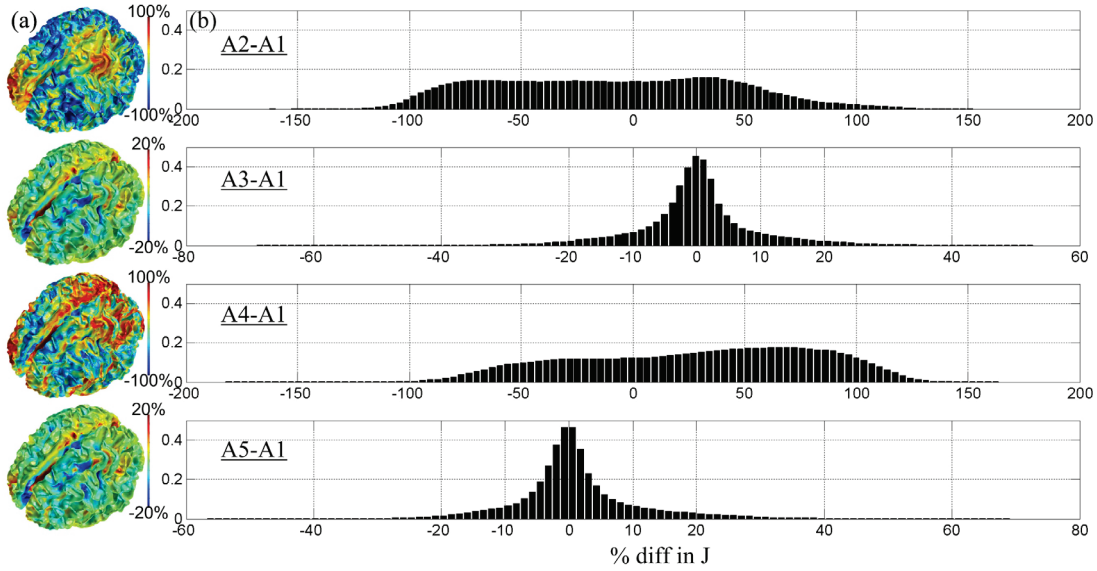

Figure 6.5: Variation of current density distribution in terms of percentage differences across WM of (A2-A1), (A3-A1), (A4-A1) and (A5-A1). (a) Projection of % difference across the white matters. For A3-A1 and A5-A1 the scale is fixed between ±20%. For comparison A2-A1 and A4-A1 the scale is set between ±150% (b) histogram analyses depicting the spread of difference distribution. A1, Isotropic head model; A2, artificial anisotropy (radial) based head model; A3, head model based on Equivalent Isotropic Trace algorithm; A4, model

based on fixed (eigenvalues) anisotropic algorithm and A5, model based on Proportional Anisotropic Ratio algorithm.

These statistical indices indicated variations in the topography of the current distribution across the grey and white matter. Changes in the topography of *J* were directly related to the eigenvalues and eigenvectors of a conductivity tensor. Eigenvectors tend to align current along their principal axis, however, the degree of alignment is determined by their respective eigenvalues. For this reason, models based on the fixed anisotropic ratio showed a higher degree of topographic variations than models based on the variable anisotropic ratio (A3, I3, A5 and I5).

Table 6-1: Percentage RDM and CC across GM, WM, M1, Contralateral M1 and Supplementary motor area of averaged models. A1: Isotropic head model, A2: artificial anisotropy (radial) based head model, A3: head model based on Equivalent Isotropic Trace algorithm, A4: Model based on fixed (eigenvalues) anisotropic algorithm and A5: model based on Proportional Anisotropic Ratio algorithm

Regions	A2-A1	A3-A1	A4-A1	A5-A1
		% RDM		
GM	18.79	3.47	15.04	3.15
WM	46.48	10.68	48.29	11.28
Motor cortex (M1)	24.65	5.14	18.95	4.70
Contralateral M1	15.02	3.23	14.03	2.92
Left SMA	8.86	2.52	8.36	2.34
		% CC		
GM	91.55	99.69	94.42	99.75
WM	75.44	96.29	48.92	95.87
Motor cortex (M1)	67.57	98.26	84.58	98.34
Contralateral M1	88.94	99.23	89.03	99.37
Left SMA	93.68	99.25	95	99.35

From Table 6.2, it can be seen that the comparison of models (A2–A1) recorded an 89% increase of J_{max} in the GM, whereas, (A4–A1) recorded a 23% increase. On the other hand, (A3–A1) and (A5–A1) showed a drop of around 0.6% in J_{max}. In the WM

domain, the increase of 2.2%, 4.4% and 50% were observed in the median values of the current density of models A3, A5 and A4, respectively.

Table 6-2: Maximum and median values of current density for GM, WM, M1, Contralateral M1 and Supplementary motor area of averaged models. A1: Isotropic head model, A2: artificial anisotropy (radial) based head model, A3: head model based on Equivalent Isotropic Trace algorithm, A4: Model based on fixed (eigenvalues) anisotropic algorithm and A5: model based on Proportional Anisotropic Ratio algorithm

Regions	A1	A2	A3	A4	A5
			J_{max} (mA/m^2)		
GM	125.2	237.3	124.4	155.0	124.5
WM	45.9	108.8	45.8	110.6	45.7
motor cortex (M1)	102.0	193.7	96.7	101.8	96.5
Contralateral M1	64.9	90.3	64.7	75.3	64.4
Left SMA	74.2	96.6	77.4	93.1	76.9
			J_{median} (mA/m^2)		
GM	20.1	19.5	19.4	17.8	19.4
WM	13.5	11.2	13.8	20.3	14.1
motor cortex (M1)	32.1	32.3	30.8	27.4	30.9
Contralateral M1	26.2	25.2	25.7	23.4	25.7
Left SMA	45.6	45.6	45.6	42.7	45.4

From Tables 6.1 and 6.2, it can be observed that the WM anisotropy had a more significant effect on the J distribution of WM than the GM. In isotropic layers, the changes in the topography and strength were the by-product of J variations of the anisotropic WM. Since the models considered had no active regions, enhancement of current strength in one region had to be compensated by an equal drop in other regions. For example, in models A3, A4 and A5 the strength of current density (J_{median}) in the WM was increased, whereas, in the GM, J_{median} of the corresponding models dropped. The degree of this enhancement was directly related to the magnitude and orientation of the conductivity tensor.

These small variations in J_{max} and J_{median}, across the grey and white matter of models A3 and A5, indicated the variations across the entire selected domains and did not highlight the significance of local variations. For this reason, the volume of interest analysis is carried out in the next section.

6.3.2. Volume of interest (VOI) analysis

To assess the impact of anisotropy on regions of high *FA,* two volumes of interest across the corpus callosum were selected. The first volume encompasses the portion of genu of corpus callosum, and the second region is around the splenium of corpus callosum, as shown in Figure 6.6. The Figure also shows the *J* distribution across (dorsal view) the axial slice of model A4. Insets A and B clearly describe the current distribution pattern across the sections of the corpus callosum.

By comparing the % RDM values of Table 6.3 to Table 6.1, it can be seen that (A2–A1) and (A4–A1) were close to their previous values, which is indicative of the influence of constant magnitude (eigenvalues) of the conductivity tensor employed in models A2 and A4. On the other hand, a significant increase was observed in the comparisons of (A3–A1) and (A5–A1), especially in the case of the splenium of corpus callosum. As shown in Figure 6.7, this region had a high value of *FA*, which was attributed to the parallel alignment of nerve fibres. Compared to A1 of Table 6.4 the modest increase in J_{max} *(A3=5.3% and A5=3.1%)* and J_{median} *(A3=9.2% and A5=10%)* were also observed for A3 and A5 models.

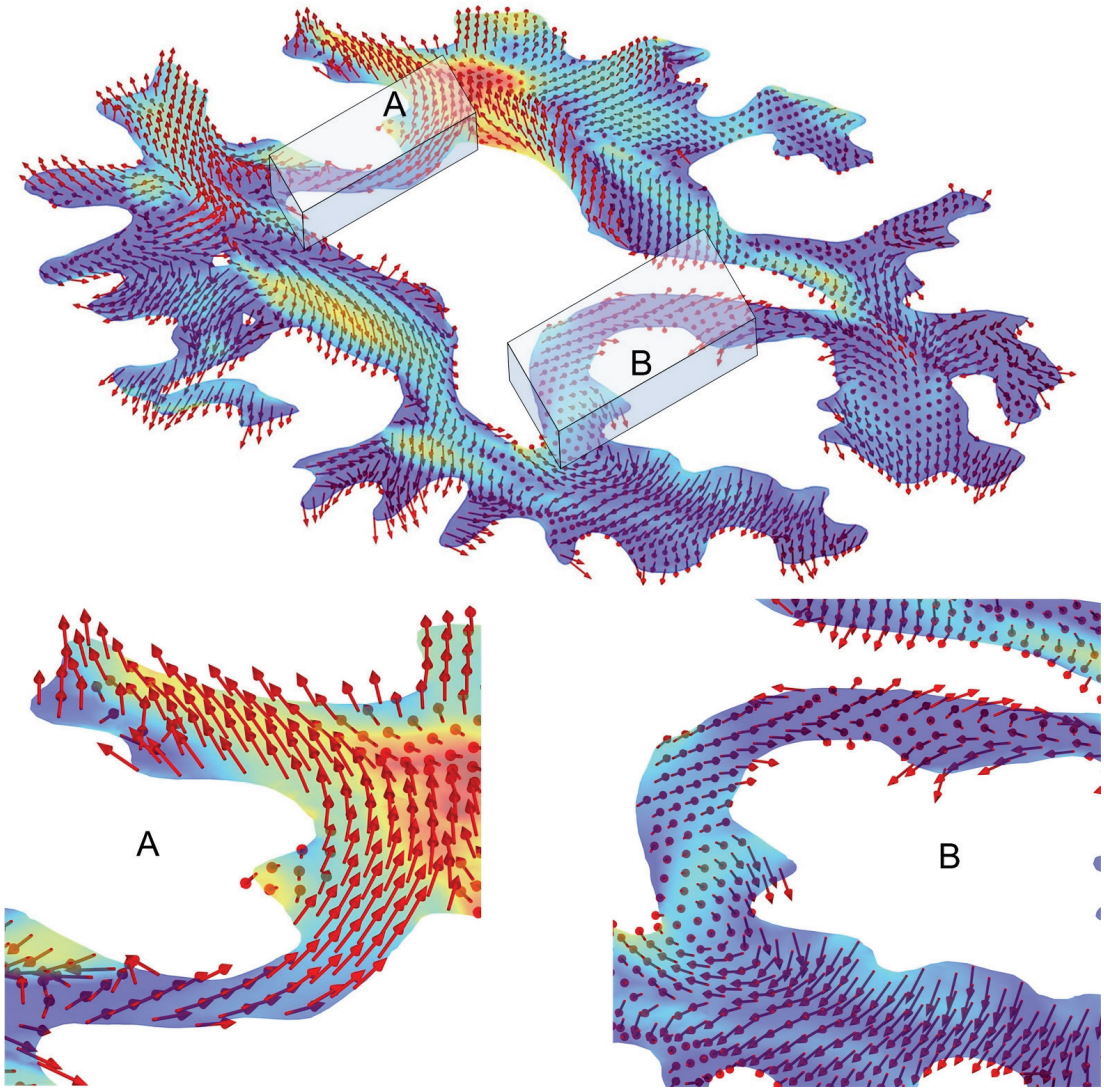

Figure 6.6: Current distribution pattern across an axial slice of model A4 (Fixed anisotropic ratio), along with the regions of interest.

Table 6-3: Percentage RDM for two regions of interests

ROI	A2-A1	A3-A1	A4-A1	A5-A1
% RDM (Genu of corpus callosum)	48.74	14.81	44.93	14.42
% RDM (Splenium of corpus Callosum)	47.90	19.44	52.28	19.50

Table 6-4: Maximum and median values of current density (mA/m^2) across ROI of averaged models under consideration. A1: Isotropic head model, A2: artificial anisotropy (radial) based head model, A3: head model based on Equivalent Isotropic Trace algorithm, A4: Model based on fixed (eigenvalues) anisotropic algorithm and A5: model based on Proportional Anisotropic Ratio algorithm

ROI	A1	A2	A3	A4	A5
J_{max}(Genu of corpus callosum)	27.2	68.5	27.4	91.3	27.7
J_{median}(Genu of corpus callosum)	15.8	22.9	16.1	28.3	15.9
J_{max}(Splenium of corpus callosum)	31.8	99.8	33.5	64.0	32.8
J_{median}(Splenium of corpus callosum)	10.8	11.9	11.8	19.4	11.9

In the isotropic model A1, the current distribution was dictated by the location of electrodes, structure, shape, conductivity of a volume conductor and the boundary condition, i.e. ($n \cdot J_1 = n \cdot J_2$). This behaviour is represented in Figure 6.7 for splenium of corpus callosum. The effect of anisotropic conductivity was quite prominent in all of the models. Even though the primary driving factors of the current were the location of electrodes and the boundary conditions, the pattern of J distribution was more affected in models A4 and A2 due to the fixed anisotropic ratio among σ_L and σ_T. On the other hand, patterns generated by models A3 and A5 were relatively mild and similar to each other. However, the strength of J in both cases had increased.

In order to analyse the contribution of anisotropy (fibre pathways) in altering the J distribution in M1, Contralateral M1 and supplementary motor area (SMA), VOI analysis was carried out across these selected regions in the left hemisphere, except for Contralateral M1.

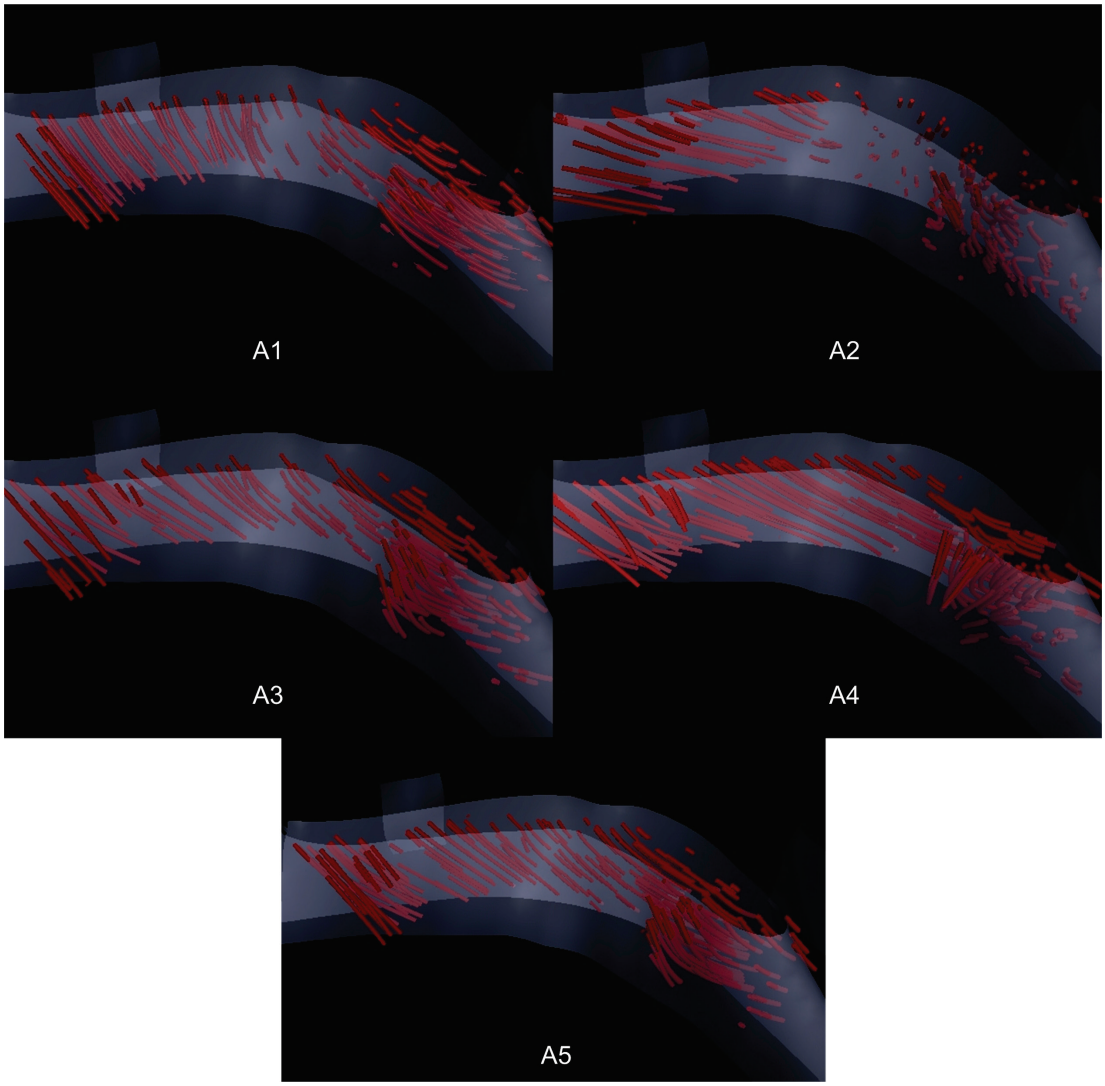

Figure 6.7: Current density patterns across the ROI (Splenium of corpus callosum) under various conductivity distribution schemes, using averaged models. A1, Isotropic head model; A2, artificial anisotropy (radial) based head model; A3, head model based on Equivalent Isotropic Trace algorithm; A4, model based on fixed (eigenvalues) anisotropic algorithm and A5, model based on Proportional Anisotropic Ratio algorithm.

From Figure 6.8, it can be seen that the trend in *J* variation is similar to that of the GM domain (Table 6.2). Hotspots were mostly confined between and in the proximity of electrodes therefore, SMA and M1 regions recorded (on average) high values of *J*. Models A2 and A4 shared the same conductivity ratio (eigenvalues) therefore, they showed strong topographic errors across the selected regions (Figure 6.8c and Table 6.1). The current flow was influenced by the orientation of the conductivity

tensor (eigenvectors), consequently large errors in CC were recorded for M1 in comparison (A2–A1) (approximately 67%) compared to 84% in (A4–A1). It can further be seen that, by including the anisotropy in the WM, the value of J_{max} was increased in M1, Contralateral M1 and SMA regions of A4 model. On the other hand, the median value of J (with respect to model A1) recorded a 14% drop in M1 and a 10 % drop in the Contralateral M1 regions of model A4. Interestingly the WM of A4 recorded a 50% increase in its J_{median} (Table 6.2). These observations signify the importance of J redistribution in the entire head model, which was primarily governed by the degree of anisotropy of the WM. The extent of this variation was highly correlated with the type of algorithm used in WM conductivity estimation.

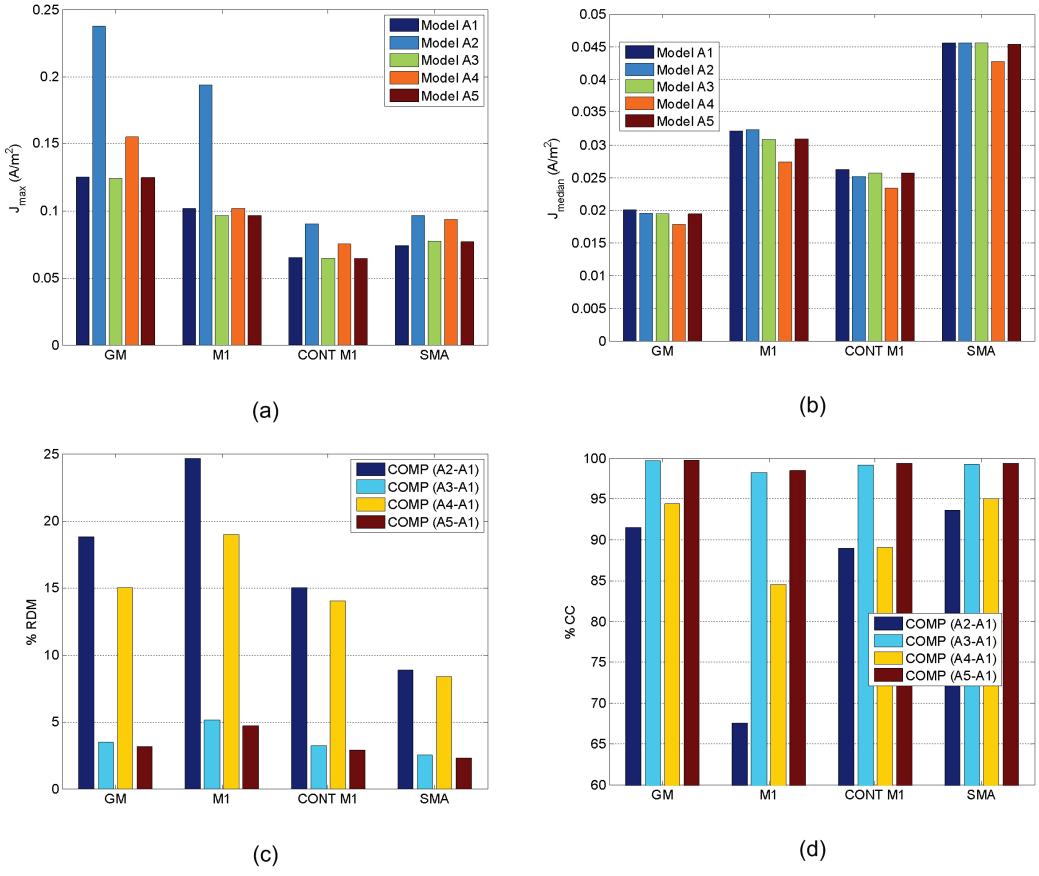

Figure 6.8: Comparison of (a) maximum and (b) median values of the current density (J) across the GM, M1, Contralateral M1 and SMA of the averaged models. (c) Topographic variation assessment across selected regions of various models using isotropic model A1 as a comparison reference. The degree of topographic variations has been measured using the relative difference measure (RDM). (d) Correlation coefficient, highlighting the type of relationship between J_{ISO} and J_{ANISO} across the ROIs in selected models. A1: Isotropic head mod-

el, A2: artificial anisotropy (radial) based head model, A3: head model based on Equivalent Isotropic Trace algorithm, A4: Model based on fixed (eigenvalues) anisotropic algorithm and A5: model based on Proportional Anisotropic Ratio algorithm.

Figure 6.9 describes the % difference of *J* across the coronal slices by comparing A1 with A2, A3, A4 and A5, respectively. In the case of the fixed anisotropy, (A2–A1) and (A4–A1), large differences in *J* magnitudes were observed across the corpus callosum, corticospinal tract and cingulum. Even though models A2 and A4 employed fixed anisotropic ratio, both had different patterns of the distribution errors indicating a strong influence of conductivity tensor orientation (eigenvectors) on the *J* distribution.

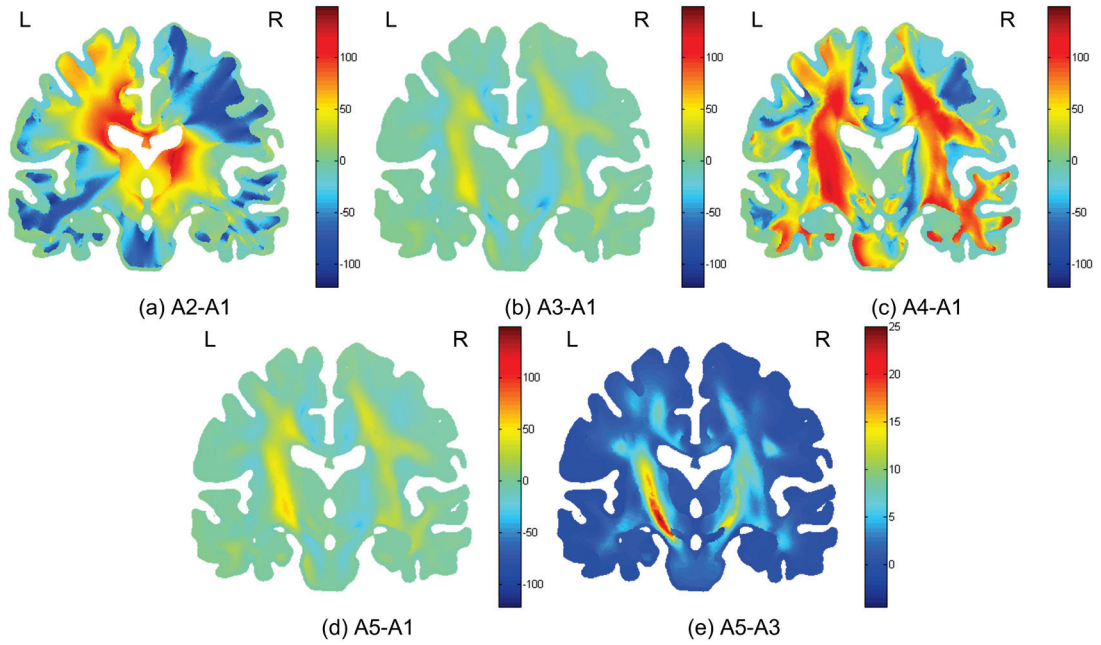

Figure 6.9: Visualization of percentage difference in current density across an arbitrary coronal slices of averaged models under discussion. A1: Isotropic head model, A2: artificial anisotropy (radial) based head model, A3: head model based on Equivalent Isotropic Trace algorithm, A4: Model based on fixed (eigenvalues) anisotropic algorithm and A5: model based on Proportional Anisotropic Ratio algorithm. A1, Isotropic head model; A2, artificial anisotropy (radial) based head model; A3, head model based on Equivalent Isotropic Trace algorithm; A4, model based on fixed (eigenvalues) anisotropic algorithm and A5, model based on Proportional Anisotropic Ratio algorithm.

Compared to Figure 6.9(a and c) the % differences in Figure 6.9(b and d) were not that high, i.e. the maximum differences were approximately 57 % and 55%, and average differences were around 5.4% and 5.3 %, respectively. However, locally the worst affected areas were around the corticospinal tract, corpus callosum and the cingulum. Overall, under the C3-Fp2 electrode configuration, the general current flow was from top to the bottom of the corpus callosum. As the current lines passed through the corticospinal tracts of models A3 and A5, they deviated from their isotropically defined path and tended to realigned themselves along the main fibre direction (principal eigenvectors). As a result, the strength of current density across the corticospinal tracts was enhanced. On the other hand, current lines were almost orthogonal to the cingulum and the corpus callosum, and as a result an observable drop in J strength was seen for models A3, A4 and A5 across these regions.

Well-aligned fibres offer high conductivity along their lateral, and low conductivity along their transverse directions. When the induced current is incident on these fibres, due to an increase in local conductivity, the direction of current density vectors across that particular region tends to realign themselves with the principal direction of eigenvectors and as a result, their strength along the fibre direction increases. Since the magnitude of a conductivity tensor is dictated by its eigenvalues and, in the fixed anisotropic ratio models the magnitude of conductivity across the entire domain was constant ($\sigma_L=10\sigma_T$), variations of up to ± 150% were observed (Figure 6.4b and Figure 6.5b). On the other hand, in the variable anisotropic ratio models, the magnitude of the local conductivity tensor was dependent on the strength of the local diffusion tensor (eigenvalues). Regions of high FA had the highest ratio among their lateral to transverse eigenvalues. Hence, the variable anisotropic ratio provided heterogeneously defined anisotropic conductivity distribution.

By comparing the two variable anisotropic methods with each other, the maximum difference of 27 % was observed across the corticospinal tracts and the average localized variation of approximately 5% was observed across the WM. Although these differences were moderate, they highlighted the differences due to different scaling factors. In model A5, σ_L was considered 10 times of σ_T and then the Volume Constraint was applied to restrict the volume of the local conductivity tensor to the vol-

ume of its isotropic conductivity tensor. Therefore, this method was not only sensitive to the average iso-conductivity value, but, also to the scaling ratio ($\sigma_L = 10\sigma_T$). Any change in the scaling ratio would yield a different conductivity distribution. On the other hand, the Equivalent Isotropic Trace method was only sensitive to the average iso-conductivity value and the variable scaling factor was derived by the ratio of iso-conductivity trace to diffusivity trace.

6.3.3. Role of anatomical variation in field distribution

To quantify the influence of anatomical variability on the strength and distribution patterns of the current density, subject-specific models (I) were compared with the averaged/normalized head models (A). The assessment was conducted on the DTI based models only. Comparing Figure 6.3 with Figure 6.10, the shift in the locations of hotspots can easily be identified, although in both cases these high J regions were confined between the anode and the cathode. As expected, the strength of J also showed considerable variations. These differences were attributed to the anatomical variations between the averaged and the subject specific head models. Such changes include, but are not limited to the difference in cortical folding and changes in the volume of each sub-domain (regions). From Figure 6.11(a–d), the trend in J_{max} and J_{median} of the subject-specific models was comparable to that of the averaged head models. Similarly, the Correlation Coefficient and RDM showed similar variations in the trend.

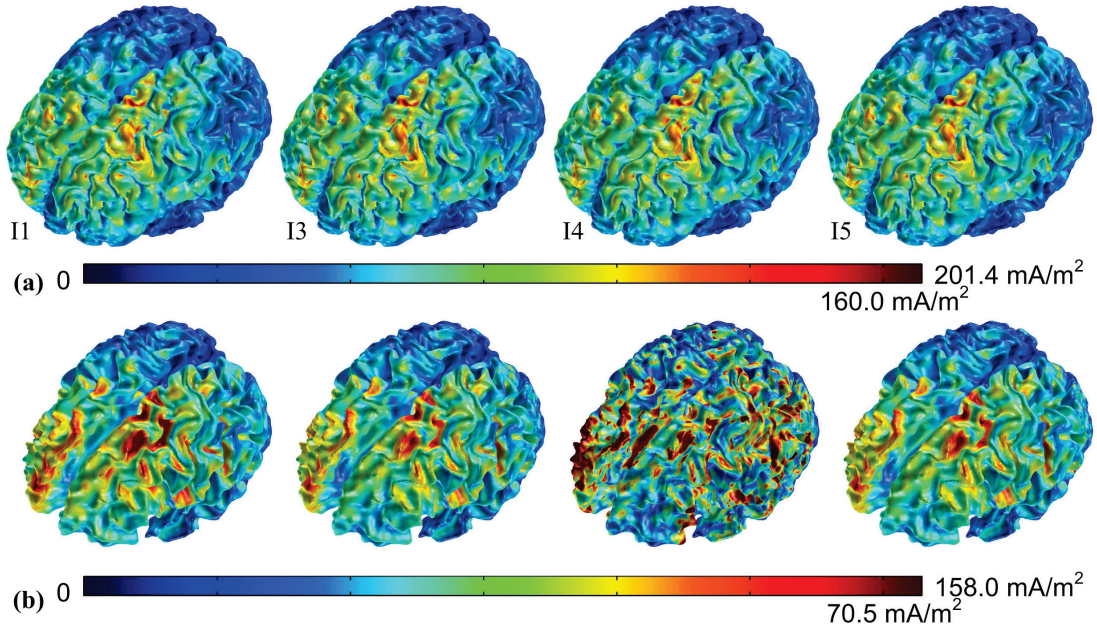

Figure 6.10: Current density distribution (magnitude) across (a) GM, (b) WM, of subject specific head models. I1, Isotropic head mode; I2, artificial anisotropy (radial) based head model (not included in sensitivity analysis); I3, head model based on Equivalent Isotropic Trace algorithm; I4, model based on fixed (eigenvalues) anisotropic algorithm; and I5, model based on Proportional Anisotropic Ratio algorithm.

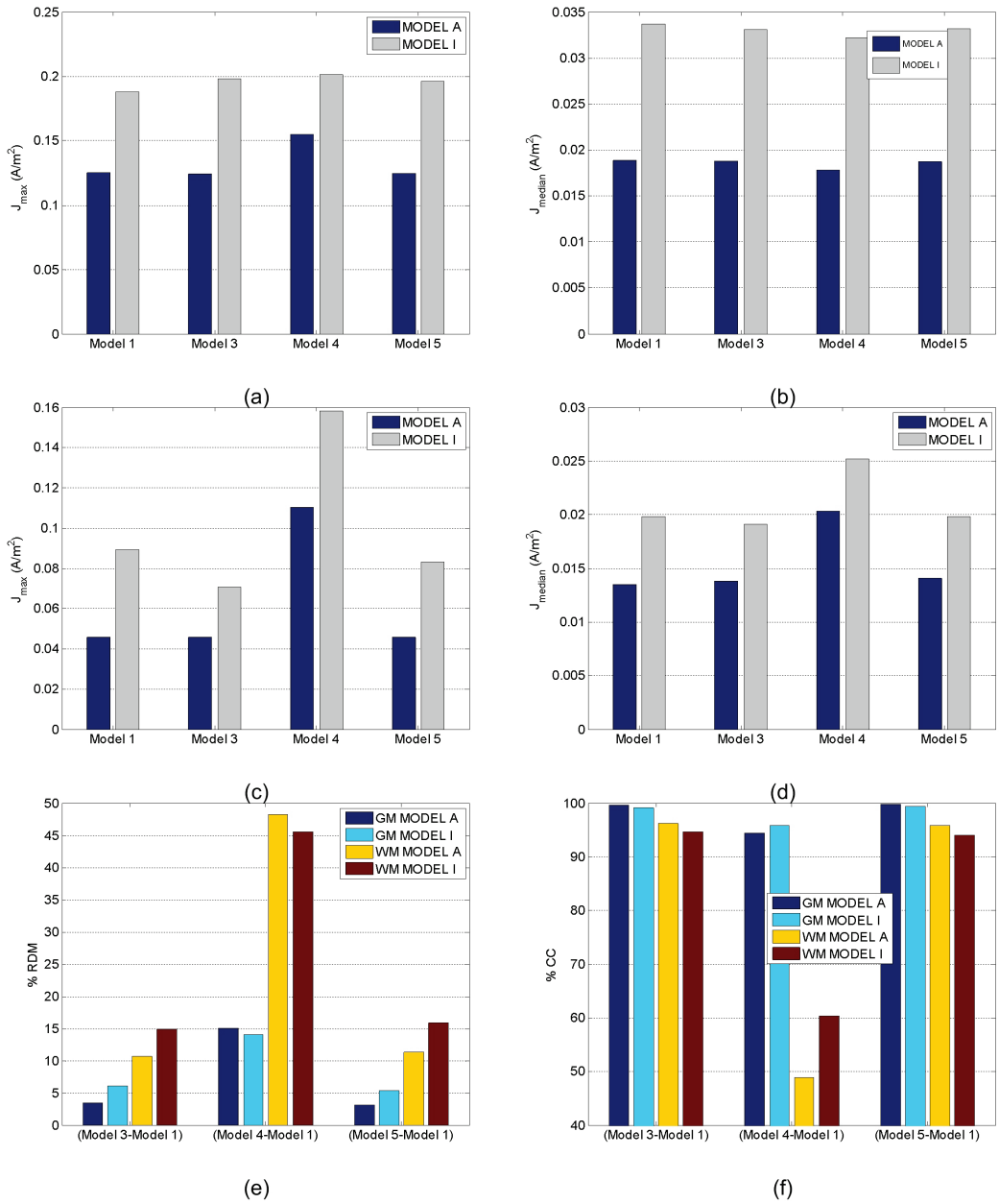

Figure 6.11: Comparison of J_{max} and J_{median} among the averaged (A) and subject specific (I) head models. Change in (a) maximum and (b) median values of current density across the gray matters. Variations in the strength of (c) maximum and (d) median values of current density across the individual and subject specific white matters (e) topographic variations in current density distribution across DTI based (averaged and subject specific) models with respect to their isotropic models. (f) Correlation among the magnitude of J across various head models.

6.4. Discussion

In this chapter, high resolution anatomically accurate human head models and their derivatives were employed to investigate the variations in the current density magnitude and distribution patterns across the GM and WM. The nine layered isotropic model (A1) was compared with models having the WM anisotropic conductivity introduced by two different approaches. Since the field distributions of models A1/I1 were similar to the models used in the earlier studies (Bikson 2011; Datta et al. 2011; Datta et al. 2009; Parazzini et al. 2011; Salvador et al. 2010), these isotropic models were used for comparison with different anisotropic models of this study. The assessment was carried out using the % difference between the magnitude of the current density of model A1 and the model with artificial anisotropy (A2), heterogeneously defined anisotropy (A3), model based on the fixed anisotropic ratio (A4) and the model having variable anisotropic ratio (A5), respectively. Histogram and statistical measures such as RDM were also employed to better understand the distortion in J distribution caused by the WM anisotropic conductivity. Since these estimates were not validated via clinical/experimental studies, caution must be practiced while interpreting these results.

The model A2, which incorporated artificial anisotropy, caused the maximum degree of variation, when compared to model A1. Similarly, model A4 which was based on the fixed anisotropic ratio also recorded significant differences in current density magnitude and distribution pattern across the volume conductor. WM anisotropy of the model A2 was based on the local coordinate transformation, which defined radially oriented electrical conductivity distribution. The Volume Constraint was employed using the fixed anisotropic ratio of $\sigma_L=10\sigma_T$ to retain the volume of the anisotropic tensor equivalent to its isotropic volume. On the other hand, A4 was derived from the measured diffusion tensor using the fixed anisotropic ratio algorithm. One of the objectives of this study was to compare the behaviour of A2 to A4 in order to find any similarity in J response between the artificial and the fixed ratio models. It had been observed that both models when compared to A1 displayed different distribution patterns and magnitude variations across the GM and WM. This, of course,

was attributed to the pattern in which their eigenvectors were arranged. Hence, artificial anisotropy procedure cannot be used to substitute the DTI driven procedures, as eigenvectors of the conductivity tensor play an important role in defining/channelling current flow.

Comparison between the three DTI driven procedures also showed different degrees of current alignment, especially across high *FA* regions. It was observed that current passing through anisotropic regions would tend to realign (reorient) itself more along the fibre direction (principal eigenvectors) than of isotropic case. However, this reorientation was further affected by the influence of shape, structure and the heterogeneous conductivity of a volume conductor. Specifically, the conductivity of the CSF, which by the virtue of its highly conductive nature, generated a strong current distribution effect. Other contributing factors were the location and size of electrodes and the imposing boundary conditions.

Since the principal eigenvector of a conductivity tensor defined the direction of the main axis and eigenvalues determined the magnitude of this axis, significant differences were observed for the GM of model A4 (±50 %) compared to A3 and A5, for which errors were in the range of ±10%. The procedures used in A3 and A5 relied on the more realistic approaches to address the magnitude of anisotropic variations across the WM volume. The algorithms employed in A3/I3 and A5/I5 provided biologically plausible estimations as they did not overestimate the conductivity distribution. Consequently, there was a considerable drop in the distribution errors along with maximum and average differences of *J* magnitude when compared to the WM of A4 (A4 ≈ 150%, A3 and A5 ≈ 20%). Although, the two variable anisotropic methods used in models A3 and A5 provided realistic estimations of the electrical conductivity across the WM, which method is more accurate is a debatable issue. To answer this, and the question of model validation, it would be imperative to conduct the comparison using clinical/experimental data. The procedure used in Bangera et al. (2010) for the experimental validation of EEG forward modelling can be adopted. Alternatively, the subject-specific data obtained from EIT (Yan, Xu & Li 2010) or EEG source localization procedures can be used to validate the accuracy of these two methods. Functional MRI or Arterial Spin Labelling (ASL) schemes, in conjunction

with tDCS, can be used to identify the primary regions of stimulation/modulation. With improvement in medical imaging, inconsistencies in such studies can be improved, making these concurrent procedures more effective in identifying the site and strength of stimulation. With high spatial resolution, such schemes can be used to validate a predictive modelling paradigm (Antal et al. 2011; Kwon et al. 2008; Zheng, Alsop & Schlaug 2011).

The method used in model A5 assumed the linear relationship between conductivity and diffusion tensors across different tissue types. However, this linear relationship is not strong at the intra-tissue level. Hence, linear mapping at voxel to voxel level between measured diffusion tensor and conductivity is still subject to further research (Kim et al. 2001). On the other hand, in model A3, the anisotropic conductivity distribution was based on the inherent variability of the diffusion tensor and, at the same time, constrained by the isotropic trace. In terms of computational resources and processing time, the method used in A5 is more expensive, as this procedure requires the computation of eigenvalues and eigenvectors at each interpolation point in the WM domain. On the other hand, the algorithm in A3 only requires the trace calculation of diffusion tensor at each voxel/interpolation point. Hence, from a predictive modelling (clinical) point of view, the Equivalent Isotropic Trace method poses a significant advantage of low pre-processing time without compromising the quality of conductivity distribution. Therefore, more accurate/realistic, subject, montage, treatment, and atrophy specific models can be developed rapidly without compromising the quality of the assessment.

The % difference among model A1 and anisotropic models gave an insight into the extent of variations in J distribution across the GM, WM, and highly anisotropic regions such as the corpus callosum, corticospinal tracts and cingulum. In accordance with Hyun et al. (2009), it was observed that the degree of current distribution was highly co-related with *FA*. However, their study did not identify the formation of hotspots across the GM and WM. Similarly, the study conducted by Parazzini et al. (2011) did not highlight these formations either. Several factors such as the inhomogeneity between the GM and the WM conductivity, selection of conductivity values, low-resolution simplified models and geometrical inaccuracies can contribute to the

absence of these active regions. Hence this phenomenon can be considered as a good indicator for the correctness of anatomical structures of the cortex (Datta et al. 2009; Salvador et al. 2010).

From models A3 and A5, the strong effect of WM anisotropic conductivity on field distribution were observed in the local WM regions and to a lesser extent, in the surrounding GM. The diffusion tensor map obtained from the raw DTI data was approximated as a second rank symmetric tensor therefore, it was not possible to accurately estimate the actual extent of anisotropy in the regions of fibre crossings. Because of this limitation, such locally anisotropic regions appeared isotropic with low *FA* intensity. Such a limitation could be attributed to the low magnitude and topographic errors in A/I3 and A/I5 models. In future studies, it would be imperative to identify the regions of fibre crossing using some advance DTI processing algorithms such as Kun et al. (2008) or by using the Diffusion Spectrum Imaging (DSI) scheme (Wedeen et al. 2012; Wedeen et al. 2008). Such improvements would lead to more accurate estimates of conductivity distribution across regions of low *FA* and in GM.

The sensitivity analysis of *J* magnitude and the distribution pattern showed considerable changes. For example, inter-isotropic head model comparison showed on average 50% difference in J_{max} and 75% in J_{median} across the GM. Similarly, for the WM, these magnitude variations accounted for 68% and 37% for J_{max} and J_{median}, respectively. Considering inter-subject anatomical variations, such changes were expected. However, the inter-subject trend in magnitude and topographic variations remained similar, thus, confirming the robustness of the conductivity estimation schemes.

6.5. Conclusion

This chapter investigated the impact of white matter directional conductivity on brain current density under the influence of transcranial direct current stimulation. The study employed different conductivity profiles to represent conductivity distribution in the white matter of the brain. The conductivity profiles were derived from the arti-

ficial and measured diffusion tensor imaging datasets. The finite element method was used to estimate the current density distribution across the head models (averaged and subject-specific). Strengths and weaknesses of artificial and realistic conductivity profiles were compared by analysing the variation in current density magnitude and distribution patterns, with respect to the isotropic models. Results indicated that anisotropy profoundly influenced the strength of current density (up to ≈ 50% in WM) as it caused current flow to deviate from its isotropically defined path along with diffused distribution patterns across the GM and WM. The extent of this variation was highly correlated with the degree of the anisotropy of the regions. Regions of high anisotropy and the models of fixed anisotropic ratio displayed higher and wider degree of variations, respectively, across various structures (topographic variations up to 48%). In contrast, models which were correlated with the magnitude of the local diffusion tensor, behaved in a less exacerbated manner (≈ 10% topographic changes in WM). Anisotropy increased the current density strength across the cortical gyri under and between the stimulating electrodes, whereas a significant drop was recorded in deeper regions of the brain (maximum % difference ≈ ±10). In addition, it was observed that (under the tDCS paradigm) the Equivalent Isotropic Trace algorithm was more suited for incorporating directional conductivity than other considered approaches, as this algorithm is computationally less expensive and insensitive to the limiting factor imposed by the Volume Constraint. The chapter also quantified inter-subject variations in field parameters (E/J) due to individual structural variations and validated the robustness of conductivity estimation methodologies via inter-model comparison.

7. EFFECT OF GREY MATTER AND SUB-CORTICAL ANISOTROPY ON FIELD ASSESSMENT

7.1. Introduction

The primary objective of this chapter is to address the role of regional anisotropic conductivity of GM and deep brain regions in shaping the strength and distribution of an induced electric field across multiple regions of interest. In this chapter the head model is composed of nineteen anatomical regions and the directional conductivity of GM, WM and the sub-cortical regions was derived from the measured diffusion tensor data. The Equivalent Isotropic Trace algorithm was used to translate the diffusion tensor to conductivity tensor. Inhomogeneity among anisotropic regions was implemented by adjusting the scaling factor in eq. (4.32). The sensitivity in simulation results due to variations in GM and sub-cortical regional conductivities, was introduced by assigning WM conductivity value to GM and the sub-cortical regions in model I3. Four conventional bi-cephalic electrode montages were used to estimate the influence of brain anisotropy.

The field assessment utilised the variations in the magnitude of the induced electric field and the divergence in its orientation to estimate the contribution of the three selected conductivity profiles. The chapter outlines the significance of considering re-

finements in a volume conductor construction by quantitatively assessing the contribution of GM and sub-cortical anisotropy on brain electric fields. The highly dependent nature of induced electric field on tissue conductivity was analysed to highlight the uncertainty in the reported values of tissue dielectric properties at low frequencies, and the effects of these uncertainties on field estimations. Additionally, the use of four conventional electrode configurations emphasized the montage dependent behaviour of brain anisotropy in shaping the site and strength of the induced electric field.

7.2. Material and methods

7.2.1. Isotropic head model construction

Scalar MRI volume sets (T1, T2 and PD-weighted MRI) were obtained from the BrainWeb (Cocosco et al. 1997). Initially 10 regions were identified such as GM, WM, subcutaneous fat, eye (sclera), eye-muscles, eye-lens, mastication muscles, skull, CSF and scalp. These regions were identified and segmented using the commercially available software "Simpleware". Using the FSL (BET and FAST) (Smith et al. 2004), additional masks of scalp, skull, CSF, GM and WM were generated. Similarly, using the FSL (FIRST) mask of sub-cortical structures such as the hippocampus, thalamus and putamen were generated. A complete list of sub-cortical regions used in this study is provided in Table 7.1. In the final step, the masks of the scalp, skull and CSF (obtained from the FSL) were compared with the masks generated by Simpleware to introduce superior orbital and inferior orbital fissure. Tissue classification was further assisted by a cross comparison with the brain atlas (Woolsey, Hanaway & Gado 2008).

The three dimensional model construction and tetrahedral mesh generation was conducted in the Simpleware software. In the same package, regions such as the pons, medulla, brainstem and cerebellum were combined to form the hindbrain. Two square electrodes of approximately 25 cm^2 area each were also modelled in the same package. In the base model, electrodes were placed at the approximate location of C3

and Fp2. These locations were derived from the international 10-20 EEG system. This electrode configuration was chosen based on its significance in modulating the primary motor cortex (Utz et al. 2010). In total, nineteen anatomical regions were classified and the base model consisted of more than two million tetrahedral elements. The DTI atlas (ICBM-DT-81) was used to obtain the co-registered fractional anisotropy (*FA*), principal diffusion direction and diffusion tensor maps. Section 4.4.5 of Chapter 4 provides detailed information regarding the procedure to extract the local tensor information. The co-registered maps (spatial and vector directions) can be seen in Figure 7.1 (b and h).

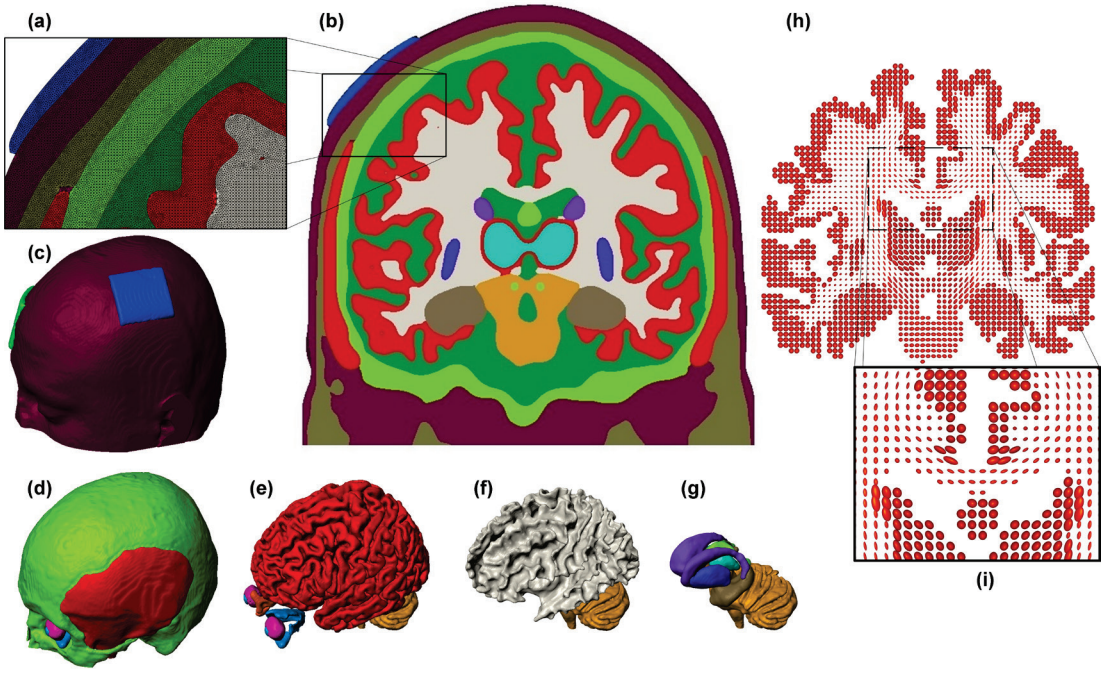

Figure 7.1: (a) The volumetric tetrahedral mesh across various regions of the head model, (b) Arbitrary coronal slice illustrating various segmented regions of the head model, (c), C3-Fp2 electrode configuration, (d) volumetric representation of skull and muscles of mastication, (e) Volumetric depiction of GM, hindbrain, eyes, eye-lens, and eye muscles, (f) white matter and hindbrain, (g) sub-cortical structures such as hippocampus, caudate nucleus, putamen, thalamus, fornix, globus pallidus par externa, globus pallidus par interna and red nucleus, (h) coronal slice representing the anisotropic conductivity distribution across GM, WM and sub-cortical regions in the form of ellipsoids, (i) Zoomed out region from (h) illustrating variation in the magnitude and degree of alignment among conductivity tensors across the GM, WM and sub-cortical regions.

7.2.2. Conductivity assignment

The average isotropic conductivity values of different tissues are listed in Table 7.1. Three additional models were derived from the base model (I1) by assigning different conductivity values to the cortical and sub-cortical regions. Model I1 has all the 19 regions and each region was assigned its respective isotropic conductivity value (σ_{ISO}). In model I2, only the WM had the directional conductivity. Model I3 had all the cortical and sub-cortical structures being anisotropic however, the average isotropic value was kept at 0.15 S/m (the conductivity of WM). In model I4, the reference isotropic conductivities (σ_{ISO}) were the same as that of I1 (inhomogeneous) however, the cortical and sub-cortical regions were assigned the heterogeneously defined anisotropic conductivities ($\underline{\sigma}$). The details of conductivity assignment are described in Table 7.1. In this study, model I3 was considered to determine the variability of simulation results with respect to the GM and sub-cortical regions' conductivities.

Table 7-1: Conductivity Assignment

Materials	Conductivity (S/m)				Reference
	I1	I2	I3	I4	
Scalp	0.43	0.43	0.43	0.43	Holdefer, Sadleir and Russell (2006)
CSF	1.79	1.79	1.79	1.79	Baumann et al. (1997)
Subcutaneous fat	0.025	0.025	0.025	0.025	Gabriel, Gabriel and Corthout (1996)
Eye-muscles/muscles of mastication	0.16	0.16	0.16	0.16	Gabriel, Gabriel and Corthout (1996)
Eye	0.5	0.5	0.5	0.5	Gabriel, Gabriel and Corthout (1996)
Eye-lens	0.31	0.31	0.31	0.31	Gabriel (1996)
Skull	0.015	0.015	0.015	0.015	Oostendorp, Delbeke and Stegeman (2002)

GM	0.32	0.32	Aniso	Aniso	Goncalve et al. (2003)
WM	0.15	Aniso	Aniso	Aniso	Nicholson (1965)
Hindbrain	0.25	0.25	Aniso	aniso	Average brain conductivity Geddes and Baker (1967)
Thalamus	0.32	0.32	Aniso	Aniso	Goncalve et al. (2003)
Hippocampus	0.32	0.32	Aniso	Aniso	Goncalve et al. (2003)
Fornix crura	0.32	0.32	Aniso	Aniso	Goncalve et al. (2003)
Caudate nucleus	0.32	0.32	Aniso	Aniso	Goncalve et al. (2003)
Globus pallidus par externa	0.32	0.32	Aniso	Aniso	Goncalve et al. (2003)
Globus pallidus par interna	0.32	0.32	Aniso	Aniso	Goncalve et al. (2003)
Putamen	0.32	0.32	Aniso	Aniso	Goncalve et al. (2003)
Red nucleus	0.25	0.25	Aniso	aniso	Average brain conductivity Geddes and Baker (1967)
Sponge Pads	0.14	0.14	0.14	0.14	Datta et al. (2009)

7.2.3. Translation of diffusion tensor to conductivity tensor and electrode configurations

In this chapter the Equivalent Isotropic Trace algorithm (eq. 4.32) was used to translate the local diffusion tensor information to the conductivity tensor. As mentioned in Chapter 6, the Equivalent Isotropic Trace Approach estimates the conductivity distribution on the basis of the inherent variability in diffusion tensor and, at the same, time restricts the magnitude of a conductivity tensor by a variable scaling factor (ratio of isotropic conductivity trace to diffusion tensor trace). Therefore, unlike the Effective Medium Approach (Tuch et al. 1999) or its derivative (Hallez, Staelens & Lemahieu 2009; Hallez et al. 2008), where only the principal eigenvector and its associated eigenvalue is used, the Equivalent Isotropic Trace algorithm utilizes the complete diffusion tensor information to define the conductivity distribution. The use

of complete diffusion tensor information, rather than the main eigenvector, has been demonstrated to generate much smoother fibre tract reconstruction along with an improvement in fibre propagation in regions of low anisotropy such as the GM and fibre crossing regions (Lazar et al. 2003; Tensaouti, Lotterie & Berry 2009). Figure 7.1 (h & i) show the ellipsoidal representation of the conductivity tensor of model I4. It can be seen that the volume of WM ellipsoids are variable and smaller than that of the GM and sub-cortical structures. This behaviour is indicative of the role of the average isotropic conductivity (σ_{ISO}) values used in eq. (4.32).

To assess the role of electrode location on the strength and distribution of the induced E-field, three additional bi-cephalic electrode configurations were used. These additional montages (F3-Fp2, P3-Fp2 and C3-C4) were selected based on recent reports by Utz et al. (2010) and Alexandre F et al. (2011). In each case, the area of each square electrode was fixed at 25cm^2. Locations of anodes (F3, P3 and C3) and cathodes (Fp2, Fp2, and C4) were derived from the EEG 10-20 system. Figure 3.3 and Column 1 of Figure 7.7 illustrate the location of these configurations on the head models.

In this chapter, the exposed surface of cathodes were assigned zero volts ($V=0$), (Dirichlet boundary condition). Similarly, the exposed boundaries of the anodes were assigned the Dirichlet boundary condition ($V=V_0$). In each case, the applied voltage (V_0) was readjusted so that approximately $1mA$ of current flowed through the anode surface. The rest of the exposed boundaries were considered electrically insulated ($n\cdot\sigma\nabla V=0$), and the continuity of the normal component of J, ($n\cdot J_1=n\cdot J_2$) was preserved across all the inner boundaries.

The effects of the initial electrical state of neurons on the J and E distribution, and the role of functional connectivity, neural connections and neural activation dynamics in the presence of an external stimulation were ignored. Hence, Laplace's equation was used to determine the induced E-field. Under the assumption of quasi-static approximation, i.e. displacement current has a negligible role to play (Jin 2002), models were solved in a commercial finite element package Comsol Multiphysics 4.1 (Comsol Inc, Burlington, MA, USA).

7.3. Results and analysis

7.3.1. Impact of brain anisotropy

To estimate the distribution of the E-field across the cortical and sub-cortical regions, model I1 was compared with models I2, I3 and I4, respectively. In each case the anode was located at C3, and the cathode was positioned at Fp2. Compared to model I1, it was observed that the anisotropy caused variations in the strength of E-field hotspots across the cortex. Across the GM, these hotspots were more prominent in the deeper regions of the cortical sulci or the walls of gyri, and were dispersed across the left parietal, left frontal and right prefrontal lobs. The formation of active zones away from regions directly under the electrodes, was attributed to the location of electrodes, convoluted geometry of the cortex and a highly conductive CSF layer, which also acted as a region of high current density.

Comparing model I1 with other three models, it was observed that the highest magnitude of E-field was recorded in model I3, as show in Figure 7.2. This high E strength could be attributed to the lower average isotropic value (σ_{ISO} = 0.15 S/m) assigned to the GM, WM and sub-cortical structures. In terms of directional conductivity, the only variable between models I3 and I4 was the scaling factor. Since this factor defined the amplitude of the conductivity tensor, and in the case of model I3, there was a significant drop in the average conductivity values right across the GM. Consequently, this drop substantially increased the magnitude of the E-field in model I3. The E-field distribution across the selected regions of interest (ROI) and sub-cortical regions also displayed the similar trend (Figure 7.2b, Figure 7.2c and Figure 7.4). The location of E_{max} corresponding to each model was traced using the MNI coordinates with noticeable changes in their locus. The approximate location of E_{max} for models I1, I2, I3 and I4 corresponded to (16, 29, 2), (-15, 13, 46), (40, 29, 16) and (22, 49, 3), respectively.

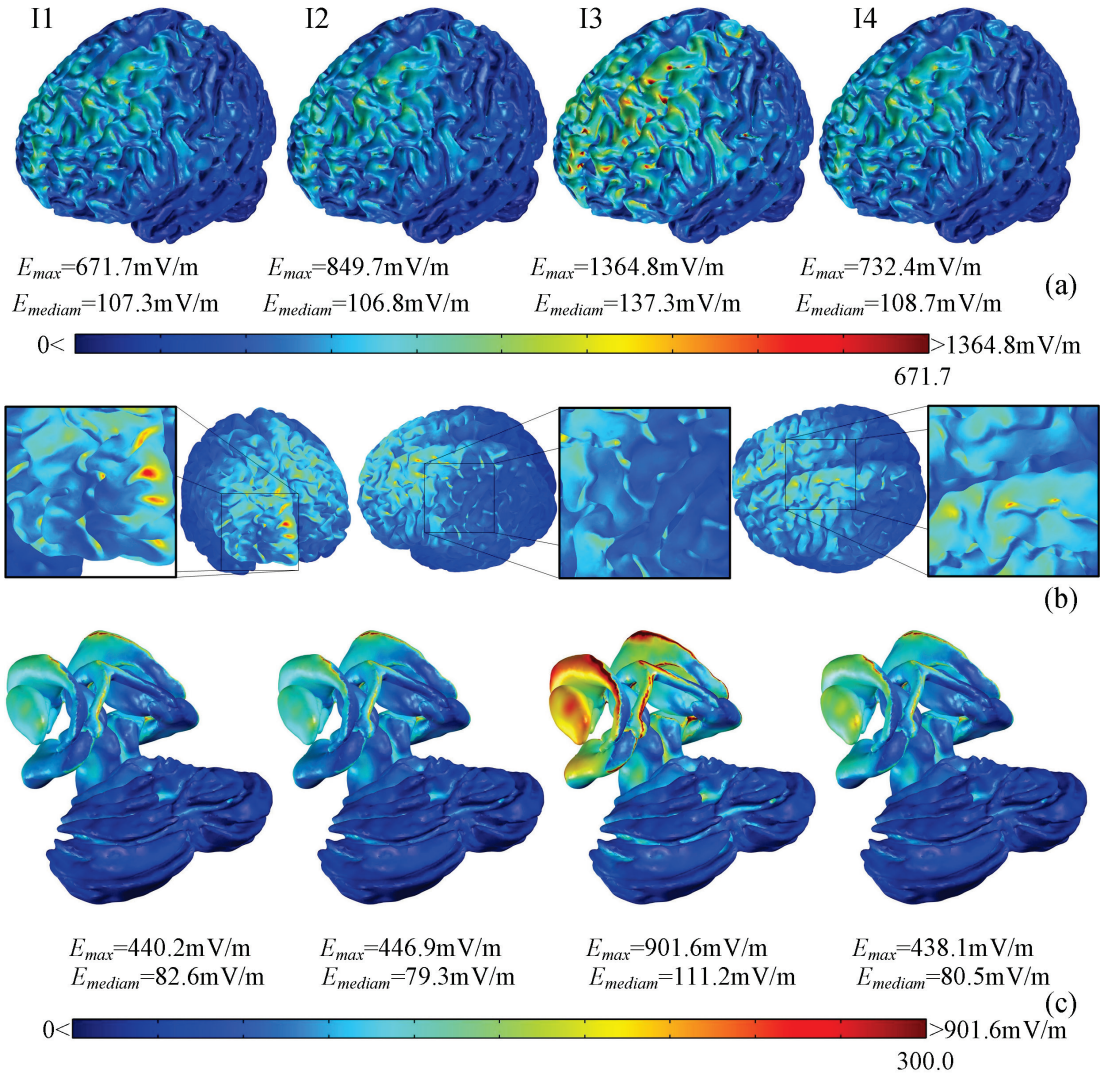

Figure 7.2: Induced Electric field distribution across (a) brain of models I1, I2, I3 and I4, (b) E-field distribution across the selected regions of model I4, highlighting the complex distribution pattern (from left to right) in the vicinity of cathode (Fp2), anode (C3) and SMA, respectively. (c) Induced electric field distribution across the selected sub-cortical structures of models I1, I2 I3 and I4, respectively.

To further investigate the influence of directional conductivity on the magnitude of the E-field distribution, the % differences between $|E_{I1}|$ and $|E_{I2}|$, $|E_{I3}|$ and $|E_{I4}|$ were estimated. Across the brain, the average difference of 44.07% was calculated for the comparison of models (I3-I1), whereas the comparisons I4-I1 and I2-I1 estimated the differences of 34.77% and 4.92%, respectively. Figure 7.3 highlights these distributions over the volume of the brain. In terms of the topographic errors,

the highest variation across the cortex was recorded for the comparison of models (I3-I1) (Figure 7.3c). For the comparison (I4-I1) the brain recorded the topographic error of approximately 40%, whereas, WM displayed the error of around 10%. Among the ROIs in model I4, the left SMA recorded the highest magnitude of E-field (E_{max}/E_{median}=503.7/233.3 *mV/m*) (Figure 7.4a and Figure7.4b). In terms of the % difference between (I4-I1), ROIs such as M1, Contralateral M1 and left SMA recorded 3.33/1.65, 5.72/1.17 and 7.88/6.00% variation in E_{max}/E_{median}, respectively.

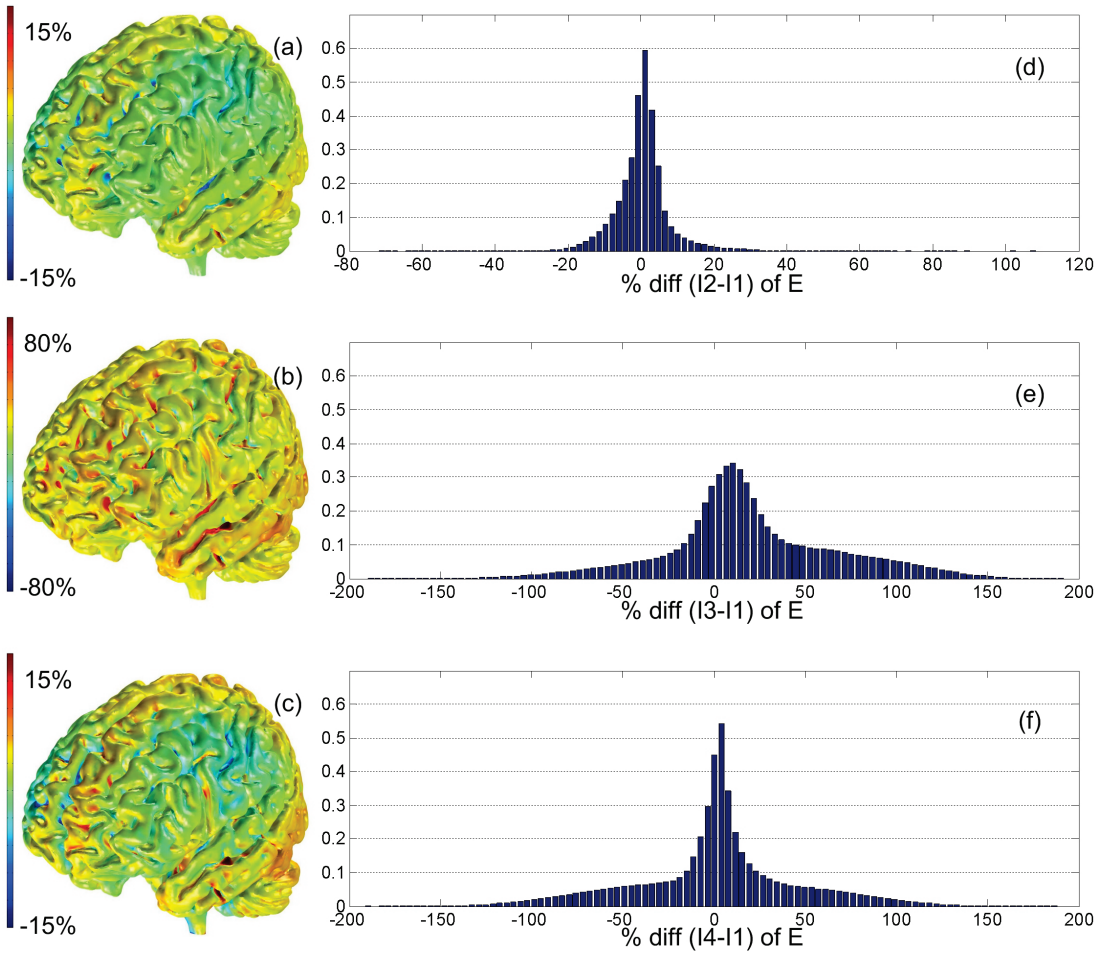

Figure 7.3: Projection of percentage differences on the brain volume (a) I2-I1, (b) I3-I1 and (c) I4-I1. Difference distribution plots; (d) I2-I1, (e) I3-I1 and (f) I4-I1.

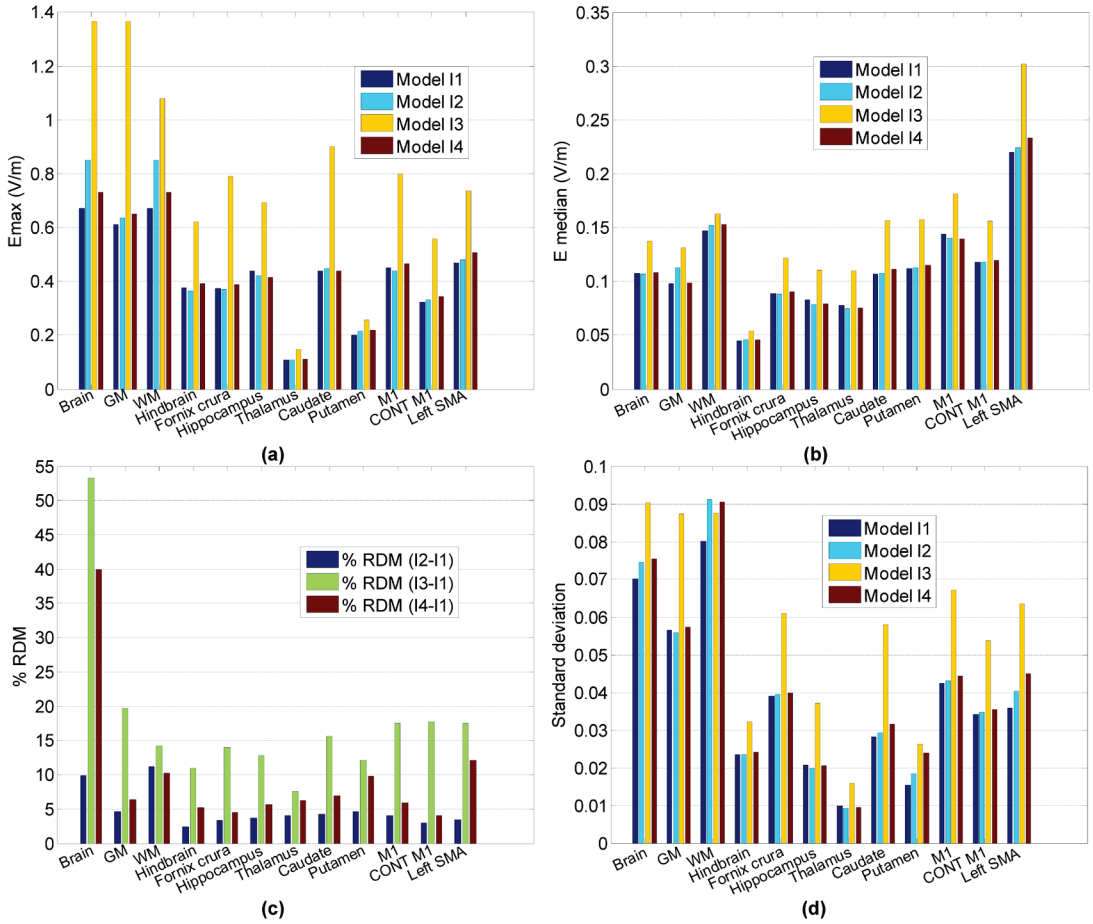

Figure 7.4: Comparison of E_{max} across selected regions of a brain using four (conductivity wise) different head models, (b) Comparison of E_{median} across selected regions of a brain using (conductivity wise) different head models, (c) Topographic assessment by comparing selected regions of each model with their respective isotropic counterparts and (d) standard deviation in E-field distributions across various regions of the selected head models.

Figure 7.5 shows the pattern of % difference in $|E|$ across a posterior view of a coronal slice by comparing the model I1 with models I2, I3 and I4, respectively. In the case of comparison (I2-I1), large variations in $|E|$ were observed across the corpus callosum, corticospinal tract (pyramidal tract) and cingulum (Figure 7.5a). Since CSF, by virtue of its highly conductive nature generated a strong current distribution effect, the transition of this strong induced current across the relatively less conductive GM caused the E-field strength (across the superficial layers of GM) to increase. This increase is shown in Figure 7.5. Similar patterns were observed across the GM-WM boundaries in the WM as well as across the sub-cortical interfaces. In-

clusion of anisotropy in the GM and sub-cortical regions of (I3 and I4) caused differences to propagate further across these regions. In the comparison (I3-I1), the large difference (ave ≈ 19%) was attributed to the low conductivity of the brain (0.15 S/m), whereas, in the comparison (I4-I1), these additional differences (ave ≈ 5 %) were due to the inhomogeneous anisotropy of the GM and sub-cortical regions. In model I3, the conductivity of the GM was 11.9 times lower than the conductivity of the CSF. On the other hand, in model I4 the conductivity of the GM was 5.59 times lower than that of the CSF.

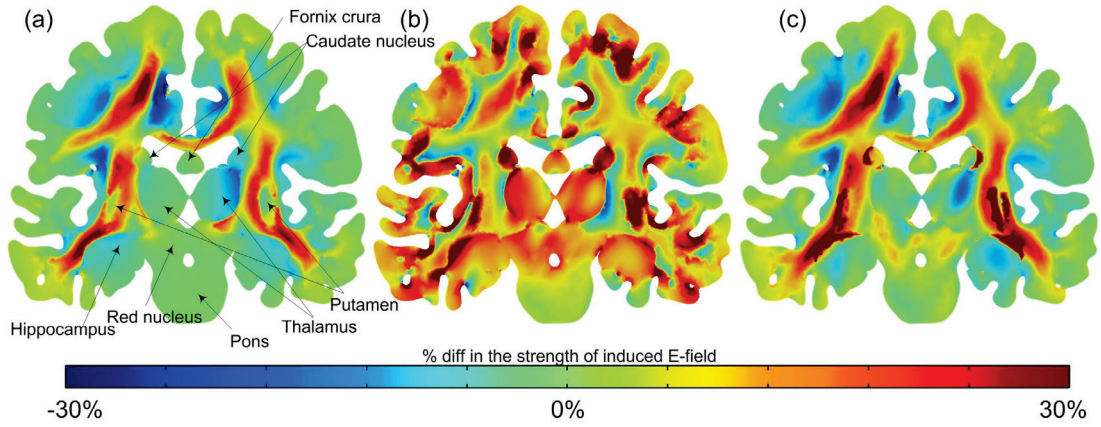

Figure 7.5: Percentage difference in the strength of induced electric field across the posterior view of a coronal slice (a) I2-I1, (b) I3-I1 & (c) I4-I1.

The inclusion of anisotropy in a model effectively changed the principal direction of local conductivity tensor and these variations had an inverse impact on the induced E-field. Figure 7.6 illustrates the posterior view of a coronal slice of the GM, WM and the sub-cortical structures. In order to assess the relation between the induced E-field and the anisotropic conductivity, the cosine of the angle between the vector projection of E_{I4} with the principal eigenvector of conductivity tensor, and the induced E_{I4} vector were plotted (Figure 7.6b). The scale from 0 to 1 indicates the degree of alignment between these vectors. However, comparing the E-field vectors of model I1 with that of model I4 indicated that, within the WM the extent of variation in the direction of local E-fields was not significant. However, there were regions with a small degree of deviation, which were more prominent in the right hemisphere

around the boundary of GM-WM (Figure 7.6c). On the other hand, the strength of E-fields (E_{I1} and E_{I4}) across high *FA* regions, such as the corticospinal tracts, showed substantial differences (Figure 7.6d and Figure 7.5c). Regions where the directions of E-fields were noticeably different were around the interface of GM-WM, and to a lesser extent on the boundary interface of sub-cortical regions such as the thalamus, hippocampus, fornix crura, caudate nucleus and the hindbrain.

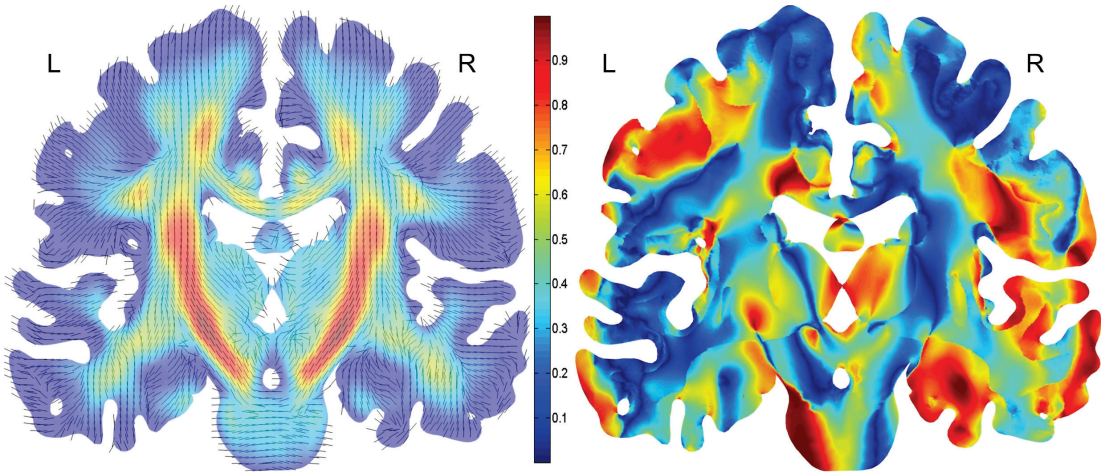

(a) Fractional Anisotropy map and principal fibre direction

(b) Cosine of the vector projection of $\boldsymbol{E_{I4}}$ on the principal eigenvector of conductivity tensor and $\boldsymbol{E_{I4}}$

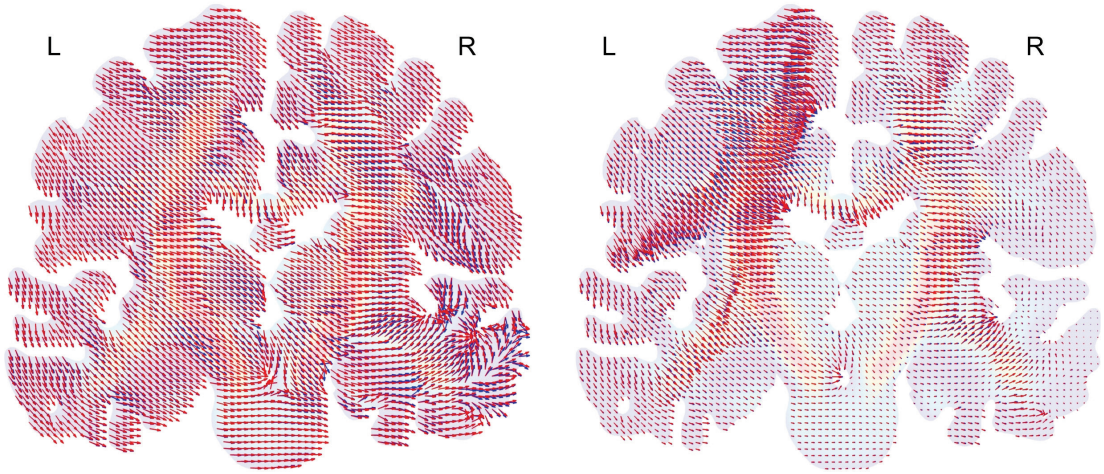

(c) Orientation variation among $\boldsymbol{E_{I1}}$(blue) and $\boldsymbol{E_{I4}}$ (red)

(d) Orientation and magnitude variation among $\boldsymbol{E_{I1}}$(blue) and $\boldsymbol{E_{I4}}$ (red)

Figure 7.6: Orientation analysis, posterior view of a coronal slice, containing GM, WM, and sub-cortical regions (a) fractional anisotropy (*FA*) map obtained from the measured diffusion tensor data. Regions of high anisotropy are shown in red and yellow colours, whereas, contrasts of blue colour indicate regions of low anisotropy. (b) Cosine of the parallel component of E_{I4} (vector projection of E_{I4} on the principal eigenvectors of the conductivity tensor) and E_{I4} vector. Regions of strong alignment are shown in red and yellow, whereas, contrasts of blue illustrate regions of strong orthogonallity (c) Projection of normalized E_{I1} (blue arrows)

and E_{I4} (red arrows) along the plane. (d) Projection of non-normalized E_{I1} (blue arrows) and E_{I4} (red arrows) vectors along the plane.

In the tDCS paradigm, the location of electrodes is the major factor in defining the global direction of current flow. In this scenario an anode was placed over the left motor cortex, causing a strong flow of current to pass radially through the left cortical hemisphere. As a result, the strength of E-field across the left hemispheric WM (pyramidal tracts) was higher than the right one (Figure 7.5 and Figure 7.6d).

By comparing the directions of the local conductivity tensor (Figure 7.6a) to the orientation of E-field (Figure 7.6c), it can be observed that the regions where the E-field vector was locally orthogonal (or close) to the principal eigenvectors of the conductivity tensor showed high field strengths, compared to the isotropic model I1. As an example, high *FA* regions indicated location of well-defined and highly parallel fibres of the pyramidal tracts, corpus callosum and the cingulum (Figure 7.6a). Locally, the E-field was highly transverse across the pyramidal tracts and the corpus callosum and was relatively parallel to the cingulum. As a result, the strength in the corticospinal tracts and corpus callosum was high, whereas, across the cingulum it dropped (Figure 7.6d and Figure 7.5). As expected the E-field distribution of model I3 was significantly different from models I2 and I1. In model I3, the WM as well as the GM and sub-cortical structures were anisotropic with a single low scaling factor. High field strength was recorded across the pyramidal tracts and its associated GM. The model I4 had a distinct spatial E-field distribution, compare to I3. This distribution was attributed to the degree of variability within the scaling factor. Because of this inhomogeneity in the conductivity distribution, the spatial distribution of E-field was less exacerbated compared to model I3.

7.3.2. Electrode montage variation

The influence of electrode montage variation on the strength and distribution of the induced E-field is illustrated in Figure 7.7. By using the four selected configurations, it was observed that these electrode montages resulted in the distinct field patterns

with noticeable variations in their strengths. From the third column of Figure 7.7, it can be observed that the hotspots across the cortex were mostly confined between and in the proximity of electrodes. Columns 2 and 4 highlight the complex field distribution and field variations caused by the electrode variations and the brain anisotropy, respectively. Similarly, Column 5 illustrates the field distribution across the selected sub-cortical regions.

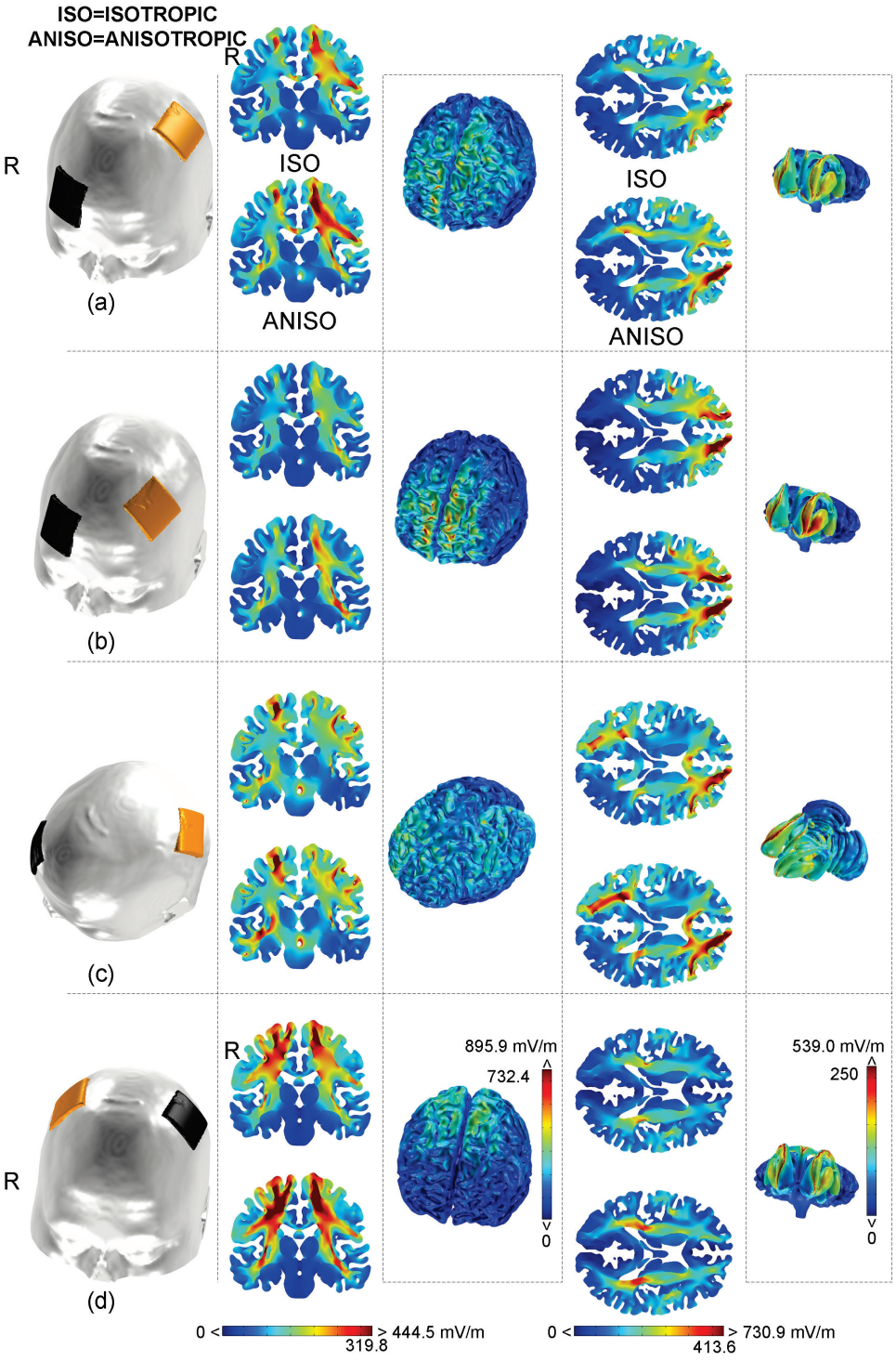

Figure 7.7: Role of electrode montage and anisotropy in shaping the induced E-field, (a) C3-Fp2 electrode montage, (b) F3-Fp2 montage, (c) P3-Fp2 montage and (d) C3-C4 montage.

Generally, it is expected that, with an increase in the distance between the electrodes, the strength of the E-field would be enhanced in the brain (Parazzini, Fiocchi & Ravazzani 2012). For example, montage P3-Fp2, resulted in a more scattered and diffused distribution with high field strength in the selected regions (GM, WM and hindbrain) whereas, the configuration F3-Fp2, displayed the lowest field strength in the GM and WM. However, the sub-cortical regions such as the caudate nucleus and the putamen (basal ganglia) showed field strengths comparable to the P3-Fp2 montage. Therefore, it appears that distance between the electrodes was not as important as their relative locations (Wagner et al. 2007). For example, in case of C3-Fp2 and C3-C4, comparable field strengths were observed in the GM and WM (E_{max}/E_{median}). However, sub-cortical regions showed distinct field distributions. In the P3-Fp2 montage, high field strengths were observed in the thalamus and hippocampus. In case of C3-C4, symmetric field distribution across the caudate nucleus and putamen can be seen (5th column, Figure 7.7d). In case of P3-Fp2 and F3-Fp2, left portions of these sub-cortical regions were subjected to high field strengths due to their proximity to the stimulating electrodes.

It was observed that the effect of anisotropy was montage-specific. For example the inclusion of brain anisotropy in the C3-C4 and F3-Fp2 montages increased the field strength (E_{max}/E_{median}) in the WM by 46/5.5 and 25/5.5%, respectively, whereas in the P3-Fp2 and C3-Fp2, the enhancements were 7/3.4 and 9/4.1%, respectively. On the other hand, the hippocampus showed a drop (E_{median}) of 6.5/6.6/1.9/5 %, (C3-C4)/(F3-Fp2)/(P3-Fp2)/(C3-Fp2). From the second and the fourth columns of Figure 7.7, it can be seen that the inclusion of the pyramidal tracts (anisotropy) in the models enhanced the field strength across these pathways. This field enhancement propagated further in the symmetric configuration and, as a result, the montage C3-C4 showed high magnitude and topographic variations across most of the selected domains (Figure 7.7b and Figure 7.7c). Across the considered montages, the approximate % drop between the E_{max}/E_{median} of the isotropic hippocampus and the isotropic GM was 28/16% for the C3-Fp2 and P3-Fp2 whereas, F3-Fp2 and C3-C4 recorded around a 53/4.4 and 61/15% drop, respectively. In the anisotropic case, montages C3-FP2, P3-Fp2, F3-Fp2 and C3-C4 recorded a drop 36/20, 32/20, 61/12 and

65/21%, respectively. Similarly, for the fornix, the drop (in E_{max}) across montages (*ISO/ANISO*) were 38/40, 32/30, 55/58 and 40/44 %, respectively.

Since electric currents follow the path of least resistance, in the presence of anisotropy, the current would tend to align itself more along the fibre pathways. However, the major contributor in defining the general flow of current would be the relative position of electrodes. The orthogonal current projections on fibre pathways caused the local E-field enhancement due to an abrupt drop in the local conductivity ($J=\sigma E$). In regions away from the electrodes, where the driving effect of electrodes was minimal, the current flow deviated easily from local drops in conductivity and, as a result, field variations in such regions were minimal, P3-Fp2 vs. C3-C4 montage (Figure 7.8c).

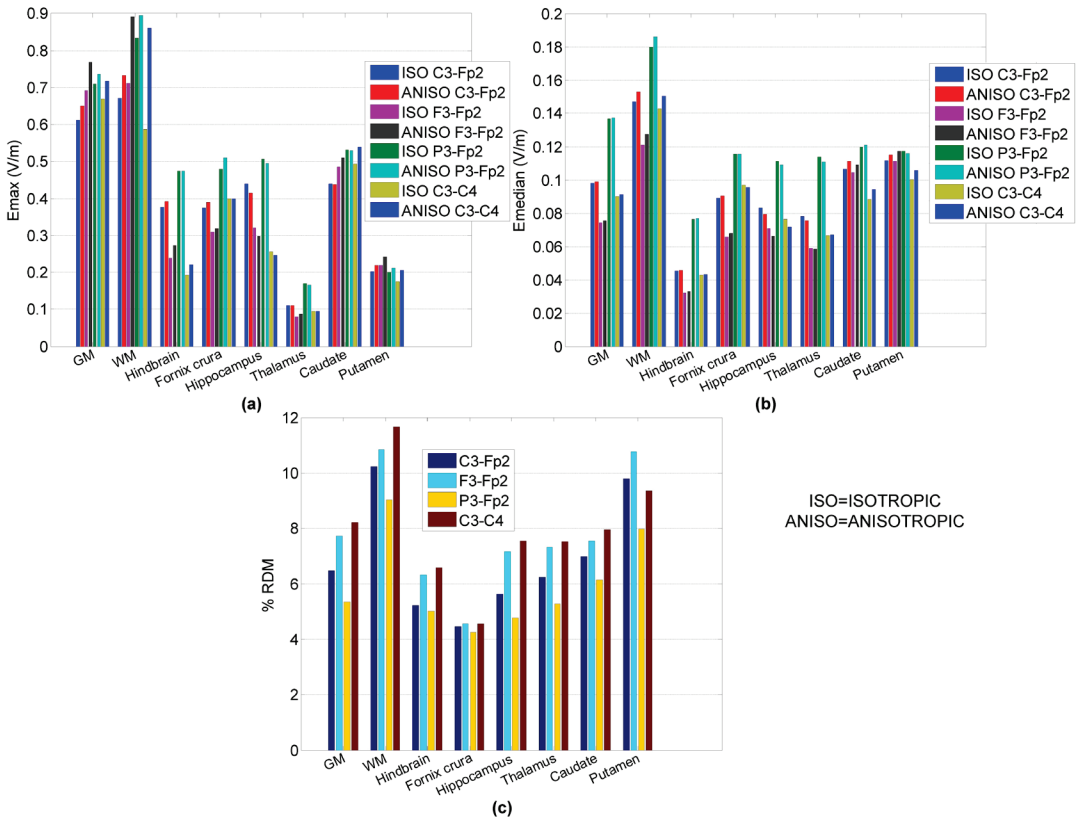

Figure 7.8: Comparison of various electrode montages across the selected regions based on (a) E_{max}, (b) E_{median} and (c) % RDM (topographic variation).

7.4. Discussion

In this study, a high-resolution finite element head model and its derivatives were employed to estimate the influence of tissue anisotropy on the amplitude and orientation of an induced electric field. These estimates were primarily made under the classical electrode configuration (C3-Fp2), which has been widely used in the clinical practice to modulate the primary motor cortex. It was observed that the impact of anisotropic conductivity under various electrode montages was not generalizable. Directional conductivity could facilitate field enhancement or attenuation. The degree of such a variation depended on the flow of current with respect to the orientation of fibre architecture. Therefore, each montage should be evaluated independently for its merits.

Under the general rule of thumb, increased cortical field strength would be expected by increasing the separation of scalp electrodes. However, a recent study by Bikson et al. (2010) emphasized on the role of relative electrode positions on neuro-modulation. Depending upon the specific montage, increasing electrode separation may decrease the strength of neuro-modulation at a specific region of interest. For example, in the putamen, E_{max}/E_{median} of F3-Fp2 was higher than that of the P3-Fp2. The site and strength of brain modulation is not a simple function of electrode locations or distance between electrodes, rather it is based on a complex relationship between electrode position and size, relative distance between electrodes, anatomical features and tissue properties.

The dependence of the E-field on directional conductivity was estimated by comparing the field distribution of the isotropic model I1 with three different anisotropic models (I2, I3 and I4), under the C3-Fp2 montage. Compared to the differences incurred by the anisotropic WM, the inclusion of anisotropy in the GM and sub-cortical regions (I2 vs. I4) increased the differences in the E-field from 5 to 34 % in the brain and 3 to 40% across the selected sub-cortical regions. These differences highlight the significance of GM and sub-cortical anisotropy in field estimation.

In agreement with (Parazzini et al. 2011), it was observed that the maximum amplitude would be located around the superficial layers of the cortex. However, non-negligible differences were observed between the GM and WM of isotropic model I1. This contradiction is due to the fact that the authors used almost identical tissue conductivity values for the GM and WM, whereas, in this study the conductivity assigned to GM was relatively higher than that assigned to the WM. In sub-cortical structures, a similar trend in terms of a drop in the strength of E-field was observed. Sub-cortical regions showed noticeable strength in the E-field. An important issue in predictive modelling is the accurate representation of the dielectric properties of cortical tissues. Due to the lack of consensus in the values reported in the literature, it remains a challenge. These uncertainties in dielectric values will have a strong influence on the strength and distribution of induced E-field. For example, comparison between models of (I3-I1) and (I4-I1) showed substantial differences in the strength and distribution patterns of the E-field. These variations were attributed to the differences in the GM and the sub-cortical conductivities of models I3 and I4.

WM is composed of highly parallelized fibre bundles that are detectable at a macroscopic scale (voxel level), therefore, their diffusion profile can satisfactorily be represented by a symmetric second rank diffusion tensor. The GM, in contrast, is composed of multiple cell types, axons projections and dendritic fibres. At a sub-voxel level (microscopic scale), these axons and dendritic fibres project in specific directions, however, such orientations are not detectable at a voxel scale (≈1- 2 mm^3). Therefore, under Pulsed Gradient Spin Echo based sequences, the regions associated with fibre crossings (WM) and the GM appear close to isotropic.

The study by Logothetis, Kayser and Oeltermann (2007) emphasized on the homogeneity of conductivity in the GM of a monkey. However, studies by Hoeltzell and Dykes (1979) and Goto et al. (2010) showed the evidence of anisotropy in the somatosensory cortex of a cat and somatosensory barrel cortex of Wistar rats, respectively. It is possible that some of these variations were species dependent. However, the study by Logothetis, Kayser and Oeltermann (2007) had some limitations as highlighted by Goto et al. (2010). With homogeneous conductivity in the GM, the spatial proliferation of the Local Field Potential (LFP) must be directionally independent,

whereas, Goto et al. (2010) reported directional dependency of conductivity distribution with vertical component of conductivity been twice as that of the horizontal component of the conductivity. Studies such as Kajikawa and Schroeder (2011) and Wang. et al. (2005), reported LEPs corresponding to the vertical volume conduction of the layer IV to reach the cortical surface. These studies highlight the existence of anisotropy at micro-meso scale.

Despite the obvious limitation of the anisotropic apparent diffusion tensor, this study shows significant differences in the E-field profiles of models I2 and I4. These variations support the findings of Goto et al. (2010) and highlight the need for additional improvements in the conductivity estimation profile to better understand the behaviour of the E-field in cortical modulation. Improvement can be made in field assessment across brain regions suffering from Partial Volume Effect (PVE) utilizing some advance DTI processing algorithms such as those discussed by Kun et al. (2008). Similarly, ambiguity in the GM and WM regions can be further resolved by incorporating the Diffusion Spectrum Imaging (DSI) scheme (Wedeen et al. 2008) in the pre-processing. The additional enhancement would resolve the issue of fibre crossing and provide further refinement in the conductivity estimation in the regions of low *FA*. Such an improvement would be immensely valuable in studying new protocols specifically designed for superficial cortical regions, such as High-Definition-tDCS (Datta et al. 2009). Improvement in conductivity estimation would give clinicians a deeper understanding of the field behaviour across the target regions, thus enabling them to devise safer and more effective protocols for electrotherapies.

7.5. Conclusion

The focus of this chapter was to underline the contribution of regional anisotropic conductivity of brain on the spatial distribution of an induced electric field across the grey matter, white matter and sub-cortical regions under transcranial direct current stimulation. The assessment was conducted using a passive high-resolution finite element head model with inhomogeneous and variable anisotropic conductivities de-

rived from the diffusion tensor data. The electric field distribution was evaluated across different cortical as well as sub-cortical regions under four different electrode configurations. Results indicated that regional tissue heterogeneity and anisotropy caused the pattern of induced field to vary in orientation and strength when compared to the isotropic scenario. Different electrode montages resulted in distinct distribution patterns with noticeable variations in field strengths. The effect of anisotropy was highly sensitive to the montage, and directional conductivity had a more profound effect in defining the strength of the induced field. The inclusion of anisotropy in the GM and sub-cortical regions had a significant effect on the strength and spatial distribution of the induced electric field. Under the (C3–Fp2) montage, the inclusion of GM and sub-cortical anisotropy increased the average percentage difference in the brain field strength from 5% (WM anisotropy only) to 34%. In terms of pattern distribution, the topographic errors increased from 9.9% (WM anisotropy only) to 40% across the brain.

8. EFFECT OF TISSUE ANISOTROPIC CONDUCTIVITY AND FIBRE TRACTS IN NEUROMODULATION

8.1. Introduction

Current forward models of TES and TMS only provide the scalar spatial distribution maps of field parameters (*E/J*) across volume conductor domains. These scalar maps are not sufficient for identifying the intricate volume conductor current pattern and neural membrane polarisation, which is the first step towards predicting neuromodulation. In this part of the research a high-resolution finite element head model with twenty anatomically distinct regions was used. Three electrode montages (two 4x1 High-Definition and one bi-cephalic C3–Fp2 montage) were used and assessment was conducted under the influence of directional conductivities of the skull, muscle of mastication, eye muscles and brain. Anisotropic conductivity in the non-cortical regions was introduced using the eigenvalue decomposition (eq. 4.5–4.9), whereas, the Equivalent Isotropic Trace algorithm (eq. 4.32) was used to estimate the conductivity profile of the entire brain region.

Inter- and intra-montage differences, due to variations in electrode configurations and conductivity profiles respectively, were quantified on the basis of magnitude and distribution variations. Statistical indices such as Residual Error and Relative Differ-

ence Measure were used to estimate these variations. Fibre architecture of five white matter regions were traced by applying streamline based tractography (FACT) to the measured tensor data. Three mechanisms of neural/axonal polarisation were used (Section 4.5) to investigate the orientation specificity of the three considered montages on regulating the neural activities.

8.2. Material and methods

The detailed description about the head model design and scalar conductivity assignment is provided in Chapter 4, Section 4.1. The isotropic electric conductivities of different tissues used in this chapter are listed in Table 4.1. The measured diffusion tensor was extracted from the ICBM-DTI-81 atlas and the Equivalent Isotropic Trace scheme was used to translate the directional conductivity estimate from the measured diffusion tensor (section 4.4.6). Anisotropic conductivity in the skull, muscle of mastication and eye-muscles was introduced using the scheme developed in the Section 4.2 of Chapter 4. The scheme proposed in Section 4.5 of Chapter 4 was used to perform the assessment of stimulation/modulation mechanisms along the fibre pathways of five selected regions of interest.

8.2.1. Electrode configurations and field calculations

The efficacy of three electrode configurations was assessed according to their capability to modulate the selected ROIs. Montage m1, was based on a high definition (five electrode) configuration (Datta et al. 2009). The location C3 was selected for the anode and C1, FC3, CP3 and C5 were considered as cathodes (Figure 3.4c). In montage m2, the anode was placed at C1 and cathodes were placed at Cz, C3, FC1 and CP1 (Figure 3.4d and Figure 8.1a). Each electrode had a radius of 6mm and the conductivity of copper. Electrode gel with the conductivity of 0.43 S/m, an approximate thickness of 2mm and a radius of 6mm was emplaced between the scalp and the electrodes. In the third montage m3, 5x5 cm^2 electrode pads of conductivity 1.4 S/m were placed at the approximate locations of C3 (anode) and Fp2 (cathode) (Figure 3.3a and Figure 8.1a).

Assuming that the spongy pads and gel had their exposed surfaces connected to a constant current stimulator by conductive rubber and copper electrodes, respectively, the conductivity of the conductive surfaces could be considered much higher than that of a volume conductor, spongy pads or conductive gel. Therefore, the Dirichlet boundary condition ($V=V_0$) was applied at the exposed surfaces of the sponge electrode (anode) and the conductive gel (anode). Similarly, the Dirichlet boundary condition ($V=0$) was applied at the exposed surfaces of the spongy cathode and the gel (cathode). Remaining external boundaries were considered electrically insulated ($n \cdot J=0$) and the continuity of the normal component of J was maintained across all the inner boundaries ($n \cdot J_1 = n \cdot J_2$).

In clinical practice, a constant current stimulator is used. Therefore, to achieve the desired electric current ($1mA$) through the anode (in all three cases), the voltage across the anode surfaces must be re-adjusted. Based on the initial estimate, the voltage was readjusted and, to confirm the injected current of $1mA$ through the active surface, the integral of J was determined under each electrode. The difference between the injected and return current were estimated to be around 7% in m1 and m2 and 5 % in m3 configurations. It was observed that these errors could be further reduced by selectively increasing the mesh density in specific regions, such as the electrodes, gel, and scalp. However, further refinement was deemed unnecessary to keep computational cost manageable.

In each case, the resistance between the electrodes and current distribution from anodes to cathodes were estimated. Further details are discussed in the Results and Discussion sections. The models considered in this chapter were electrically passive i.e. there were no active sources inside the volume conductor. However, the effects of brain fibre architecture were incorporated. Under the quasi-static approximation, Laplace's equation was used to solve the models in a commercial finite element package "COMSOL".

8.3. Results

8.3.1. HD vs. conventional tDCS electrode configurations

In both High-Definition montages, it was observed that the current distributions between four electrodes were not identical. The major proportion of the current was confined in the scalp region, therefore, the effect of brain anisotropy on scalp current distribution was less than 0.1%. On the other hand, incorporation of the skull and muscle anisotropy contributed to an increase of 1.5% in the input power through the stimulating electrodes. Owing to the relative distance between the electrodes, in the C3-Fp2 configuration, the increase was around 28%. Table 8.1 lists the proportion of return currents to individual cathodes in HD-montages.

Table 8-1: Return current distribution among cathodes in HD-montages

Electrode location	Montage m1 (skull, muscle and brain anisotropic)	Electrode locations	Montage m2 (skull, muscle and brain anisotropic)
C1	21%	Cz	29.1%
C5	26.7%	C3	18.2%
FC3	29.9%	FC1	26.2%
CP3	21%	CP1	26.5%

In m1, the maximum return current was attributed to FC3 and in montage m2, Cz received the highest proportion of the return current. This uneven distribution reflects the important role of superficial layers, such as the scalp and skull, in defining the current distribution across a volume conductor.

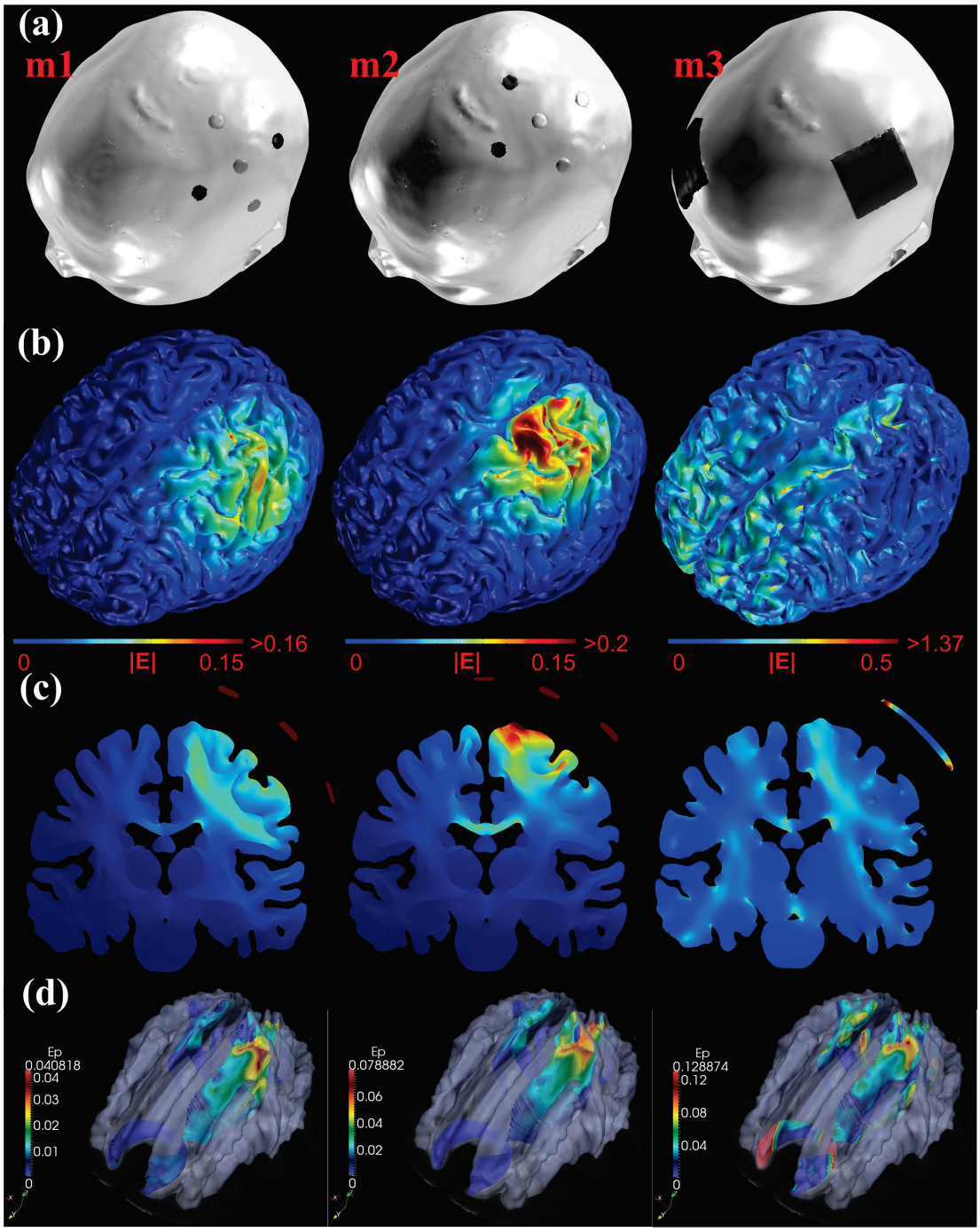

Figure 8.1: Role of electrode montage on the site and strength of induced electric field under anisotropic (skull, muscles, and brain) tissue conductivities. (a) Two High-Definition (4x1) and one conventional montage. In m1, anode is located at C3, whereas, in m2, anode is positioned at C1. Montage m3 is based on conventional 5x5 cm^2 electrode pads. In m3 anode is approximately positioned at C3 and cathode is placed at the approximate location of Fp2. (b) The depiction of induced electric field strength and distribution pattern across anisotropic brain under considered montages. (c) Anterior view of an arbitrary coronal slice, highlighting the changes in electric field strength and distribution pattern due to different electrode

configurations. (d) Effect of electrode configuration on the magnitude of the component of induced electric field parallel to the fibre pathways (*Ep*) across the selected ROIs.

The skull, being anisotropic and exhibiting the lowest electrical conductivity in the volume conductor model, played a crucial role in defining the strength of the induced E/J fields in the brain region. From Figure 8.1, it can be seen that the montage m2 caused E-field enhancement in the vicinity of the anode (C1), compared to montage m1 (C3). In the case of m3, high E-field regions were mainly confined in the deeper portions of the cortical sulci, mostly between and under the stimulating electrodes.

The skull thickness underneath C1 was lower compared to C3. This anatomical variation in skull thickness was the main reason for field enhancement in m2 configuration. From Figure 8.1(b and c), it can be seen that different electrode configurations resulted in distinct E-field distributions in the brain. Montages m1 and m2 resulted in a more confined distribution. The pattern of m1 was concentrated in the proximity of the C3 electrode and in WM, the fibre architecture (pyramidal tracts) enhanced the field in the top left hemisphere (PA–posterior anterior). In montage m2, the effect was more prominent across precentral and superior frontal gyrus. The WM fibres selectively enhanced the E-field in the vicinity of the superior frontal gyrus. The location of the anode and its proximity to the superior sagittal sinus caused the current to flow through the CSF (path of least resistance), generating high E-field strength in the corpus callosum of montage m2 compared to montage m1.

In general, both HD-configurations restricted the field pattern in the left hemisphere (PA). In the C3-Fp2 configuration, the large size and greater distance between electrodes resulted in a wider and dispersed field pattern. From Figure 8.1(b and c), it can be seen that current flow attributed to montage m3 caused field enhancement in the WM. The field strength was comparatively stronger across the left corticospinal tracts (PA), whereas, in the right hemisphere (PA), the field strength was selectively enhanced in regions where the current flow was orthogonal to the fibre pathways. In Figure 8.1(d), the component of the induced E-field parallel to the fibres (E_P) has been projected along the five selected fibre tracts. It can be seen that in montages m1

and m2, the left-CST had the highest strength in E_P, whereas, in m3, the high strength regions were located across the Left-CST, M-CC and G-CC.

Overall, montages m1 and m2 produced more regional enhancement in E-field strength whereas, in m3, the E-field showed a wider distribution pattern. On average, the strength of the E-field in the GM and WM under m3 was approximately 8 times stronger than the average value of the E-field in the respective regions under the m1 and m2 configurations. From Table 8.2, it can be seen that montage m3 generated the strongest E-field in all the regions of interest. Compared to m3, the GMs (*ISO/ANISO*) of m1 and m2 recorded the difference of ≈ 170/160 and 168/154%, respectively. Similarly, the highest variations were recorded for the hippocampus (m1 ≈ 179/172 and m2 ≈ 179/169 %), and minimum differences were recorded for the fornix crura (m1 ≈ 153/148 and m2 ≈ 149/141 %).

Table 8-2: Strength of E-field (median values) in various regions for each electrode configuration

Regions	E_{median} (mV/m)					
	Isotropic			Anisotropic (skull, muscles and brain)		
	m1	**m2**	**m3**	**m1**	**m2**	**m3**
GM	8.0	8.5	98.2	7.0	8.2	64.1
WM	12.7	13.8	147.0	10.8	11.8	98.2
Hindbrain	3.3	3.3	45.2	3.9	4.4	41.2
Fornix crura	11.7	12.9	89.2	9.0	10.7	61.1
Hippocampus	4.6	4.6	83.3	4.3	4.8	57.2
Thalamus	9.0	10.2	109.5	6.6	7.9	51.7
Putamen	7.9	7.3	111.8	7.1	6.4	75.4
Caudate nucleus	8.4	10.0	106.8	6.5	7.9	74.0

8.3.2. Effect of anisotropic conductivity

In this chapter the skull, muscles of mastication, eye muscles and the brain were assigned the directional electrical conductivities. Figure 8.2(l and m) illustrate the anisotropic conductivity distribution in terms of conductivity ellipsoids. In Figure 8.2(l),

the volume of ellipsoids represents the magnitude of the local conductivity and its direction highlights the orientation of the local conductivity tensor. Skull tensors are quite small to be visible in Figure 8.2(l) therefore, Figure 8.2(m) shows the same distribution in the normalized form. Parts a, b and c of Figure 8.2 illustrate the current density distribution (arrows) under three electrode configurations in conjunction with tissue anisotropy. In the isotropic scenario, current flowing from the high to low conductivity regions (CSF-GM or GM-WM) would enhance the E-field strength at the boundary/interface.

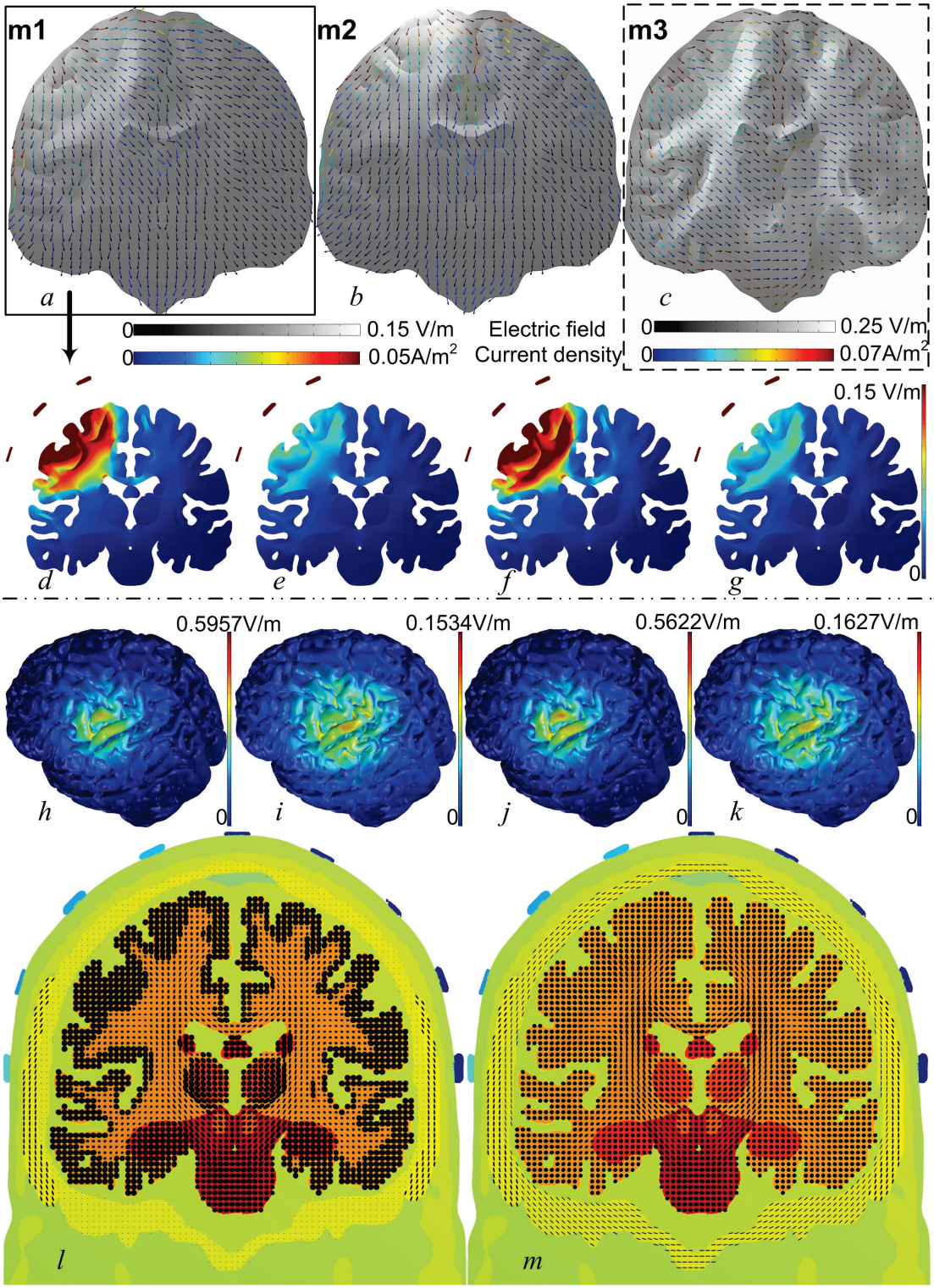

Figure 8.2: (a, b and c) Posterior view of an arbitrary coronal slice depicting E-field strength and distribution pattern in grayscale colours. Current distribution is highlighted by arrows, the orientation of arrows illustrates the direction of induced current and colour (RGB) signifies the strength of current density. Montage m1 and m2 are based on 4x1 HD-electrode configurations and in (a and b) field parameters (*E/J*) are highlighted using a common scale.

Montage m3 is based on conventional C3-Fp2 configuration and its field parameters are illustrated by separate legends. In (a, b and c) the field parameters (*E/J*) are depicted under the influence of anisotropic skull, muscles and brain anisotropic conductivities. The coronal slices include CSF, GM, WM and sub-cortical regions. In (d–g) a single scale has been selected to indicate the changes in E-field strength and distribution pattern associated with various anisotropic regions under m1 configuration. In (h–k) each model is represented by its individual E_{max} scale under m1 configuration. Slice (d) and 3 D brain (h) illustrate E-field distribution under m1 montage using isotropic conductivities. (e and i) illustrate field distribution under the influence of skull and muscles anisotropic conductivities. (f and j) depict distribution under brain anisotropy. (g and k) projects the combined influence of skull, muscles and brain anisotropy. Posterior view of an arbitrary coronal slice, illustrating anisotropic conductivity distribution in the form of conductivity ellipsoids, (l) non-normalized, (m) normalized. In (l and m) electrode locations are marked on the scalp using international 10-10 EEG electrode system.

From Figure 8.2 (a, b and c), it can be seen that the flow of the induced current is dictated by the size and location of electrodes. The highly conductive CSF also tends to channel current flow. As evident from Figure 8.2 (a, b and c), when the induced current was orthogonal to fibre pathways, the drop in the local conductivity along the current path increased the induced E-field. On the other hand, current flowing longitudinal to well-aligned fibre tracts, resulted in a significant attenuation in the strength of the E-field. Since current follows the path of least resistance, in WM fibres, local conductivity distribution tended to realign the current direction along the fibre pathways. However, electrode location played a more crucial role in tDCS paradigm.

Further extending the m1 configuration, (rows two and three of Figure 8.2) it can be seen that the inclusion of skull and muscle anisotropy had a strong effect on the strength and distribution of the induced E-field in the brain region (Figure 8.2e and Figure 8.2i). Similarly, the impact of brain anisotropy is highlighted in Figure 8.2(f) and Figure 8.2(j), where, a clear cut E-field redistribution is observable across the left pyramidal tracts (AP), and a drop in E strength is observable across the GM. Figure 8.2(g and k) highlight the collective effects of anisotropic conductivity. The result is selective E-field enhancement in the corticospinal tracts and diffused E-field distribution across the cortex.

To complement the analysis, statistical measures such as the percentage difference, residual error (RE) and the relative difference measure (RDM) were also employed

(Figure 8.3, Table 8.3, Table 8.4 and Table 8.5). For montages m1 and m2, in terms of magnitude and topographic variations, the maximum differences were observed for the GM followed by WM regions. Sub-cortical regions also showed magnitude variations in the range of ≈ 10 to 40%, whereas, topographic errors were in the range of 5-20 %. In the case of montage m3, the highest variation (RE=55 & RDM=16%) was recorded for the WM region.

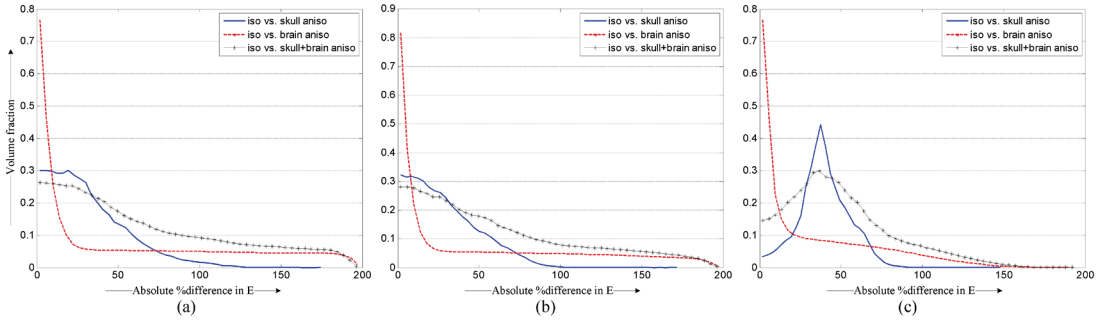

Figure 8.3: Absolute percentage difference in electric field magnitude across the brain due to the inclusion of skull, muscle of mastication, eye muscle anisotropy, brain directional conductivity and the overall influence of anisotropy under (a) 4×1 HD montage; m1, (2) 4×1 HD montage; m2, and (c) conventional montage (C3-Fp2) m3.

Table 8-3: Magnitude (RE) and topographic (RDM) errors in the induced electric field of the volume conductor model due to the inclusion of skull, eye muscles, muscle of mastication and brain directional electric conductivity. Electrode configuration is 4×1 high-definition with anode at C3 and four cathodes around C1, C5, FC3 and CP3

	m1: 4x1 HD-montage with anode at C3					
Regions	iso vs. skull and muscle anisotropy		iso vs. brain anisotropy		iso vs. skull, muscles and brain anisotropy	
	RE	RDM	RE	RDM	RE	RDM
GM	147.20	34.48	5.00	4.97	146.09	36.03
WM	121.28	31.14	9.97	8.71	111.57	34.16
Hind brain	23.36	23.44	6.71	6.30	23.34	23.50
Fornix crura	44.35	9.98	4.28	4.08	42.69	11.09
Hippocampus	20.04	11.71	4.37	4.09	21.58	13.07
Thalamus	42.97	7.05	4.12	4.08	45.34	8.14
Putamen	34.63	10.87	7.73	6.70	29.18	14.01
Caudate nucleus	43.93	16.07	9.34	7.95	37.69	15.78

Table 8-4: Magnitude (RE) and topographic (RDM) errors in the induced electric field of the volume conductor model due to the inclusion of skull, eye muscles, muscle of mastication and brain directional electric conductivity. Electrode configuration is 4×1 high-definition with anode at C1 and four cathodes around Cz, C3, FC1 and CP1

m2: 4x1 HD-montage with anode at C1						
Regions	Iso vs. skull and muscle anisotropy		Iso vs. brain anisotropy		Iso vs. skull, muscles and brain anisotropy	
	RE	RDM	RE	RDM	RE	RDM
GM	100.87	24.86	4.62	4.62	101.27	26.35
WM	94.93	22.66	8.04	7.31	88.95	25.32
Hind brain	21.54	21.49	6.17	5.08	23.04	21.95
Fornix crura	24.54	8.27	5.98	5.48	21.15	9.84
Hippocampus	13.27	11.93	3.99	3.99	13.75	13.38
Thalamus	28.13	5.14	4.61	3.96	30.23	7.12
Putamen	28.63	15.20	10.12	8.95	30.18	21.34
Caudate nucleus	28.73	12.93	6.45	6.13	27.04	16.61

Table 8-5: Magnitude (RE) and topographic (RDM) errors in the induced electric field of the volume conductor model due to the inclusion of skull, eye muscles, muscle of mastication and brain directional electric conductivity. Electrode configuration is conventional C3-Fp2

m3: C3-Fp2 conventional electrode montage						
Regions	Iso vs. skull and muscle anisotropy		Iso vs. brain anisotropy		Iso vs. skull, muscles and brain anisotropy	
	RE	RDM	RE	RDM	RE	RDM
GM	63.51	15.64	6.53	6.45	62.58	16.69
WM	64.75	13.36	12.22	10.23	55.16	16.28
Hind brain	24.90	11.62	5.45	5.22	23.54	12.32
Fornix crura	49.88	6.97	4.49	4.45	49.35	9.39
Hippocampus	39.72	4.30	6.31	5.64	43.20	6.93
Thalamus	45.27	3.11	6.60	6.23	49.50	7.35
Putamen	52.11	3.39	10.68	9.79	46.55	8.34
Caudate nucleus	51.97	7.82	7.93	6.99	46.93	9.77

From Tables 8.3, 8.4, and 8.5, it is also evident that the location and size of electrodes were equally important in defining the strength and distribution of field variables (*E/J*). Significant variations between montages m1 and m2 (GM-RE≈43% and WM-RE ≈20%) were observed and the distribution errors of ≈9% (GM-RDM) and 5% (WM-RDM) were also recorded. These observations indicate that the magnitude and distribution differences between the isotropic and anisotropic models depend upon the specific electrode configuration. These differences were higher in the case of

HD-montages (m1 & m2). For example, in case of WM regions under montages m1, m2 and m3, neglecting anisotropy resulted in the magnitude errors of 111%, 89% and 55%, respectively. On the other hand, distribution errors were 34, 25% and 16%, respectively. Relatively lower errors in C3-Fp2 (m3) electrode configuration were attributed to the use of large pads and larger distance (between the anode and the cathode). These factors caused the current to be more distributed and locally more aligned (iso vs. ansio).

Table 8-6: Qualitative ranking based on the selected regions of interest

Montage	Isotropic model	Model based on skull and muscle anisotro-py	Model based on brain anisotropy	Model based on skull, muscles and brain ani-sotropy
		E_{median} *(mV/m)*		
		ROI - M1		
m1	76.1	33.5	75.4	33.1
m2	70.4	36.9	69.3	36.8
m3	135.99	74.4	134.22	73.41
		ROI - Contralateral M1		
m1	9.1	7.5	8.7	7.4
m2	18.4	13.6	17.9	13.5
m3	110.6	71.3	112.4	72.4
		ROI - SMA		
m1	29.0	16.0	29.6	16.4
m2	41.2	23.4	41.4	23.5
m3	202.0	104.6	210.1	108.7

From Table 8.6, it can be seen that, in the isotropic case, shifting the montage from m1 to m2, caused a drop of 7.7% in the average electric field across the M1 region. For the brain anisotropic model, the drop was 8.4%. Similarly, the inclusion of skull and the muscle anisotropy attributed to the increase of 9.6% in the average electric field value. By comparing the M1 region under m1 and m3, the isotropic model produced a drop of 56.4% and brain anisotropic model produced a drop of 56.12%. On the other hand, the skull and the muscle anisotropy produced a drop of 75.8 % i.e. (≈20% variation). By comparing the other two ROIs, the inter-montage variations due to anisotropy were not more than 10%. These anisotropy-related variations would change the current flow pattern in the ROIs, however, these inter-montage dif-

ferences were not meaningful enough to influence clinical qualitative decisions for montage selection.

8.3.3.Assessment of electric field along fibre tracts

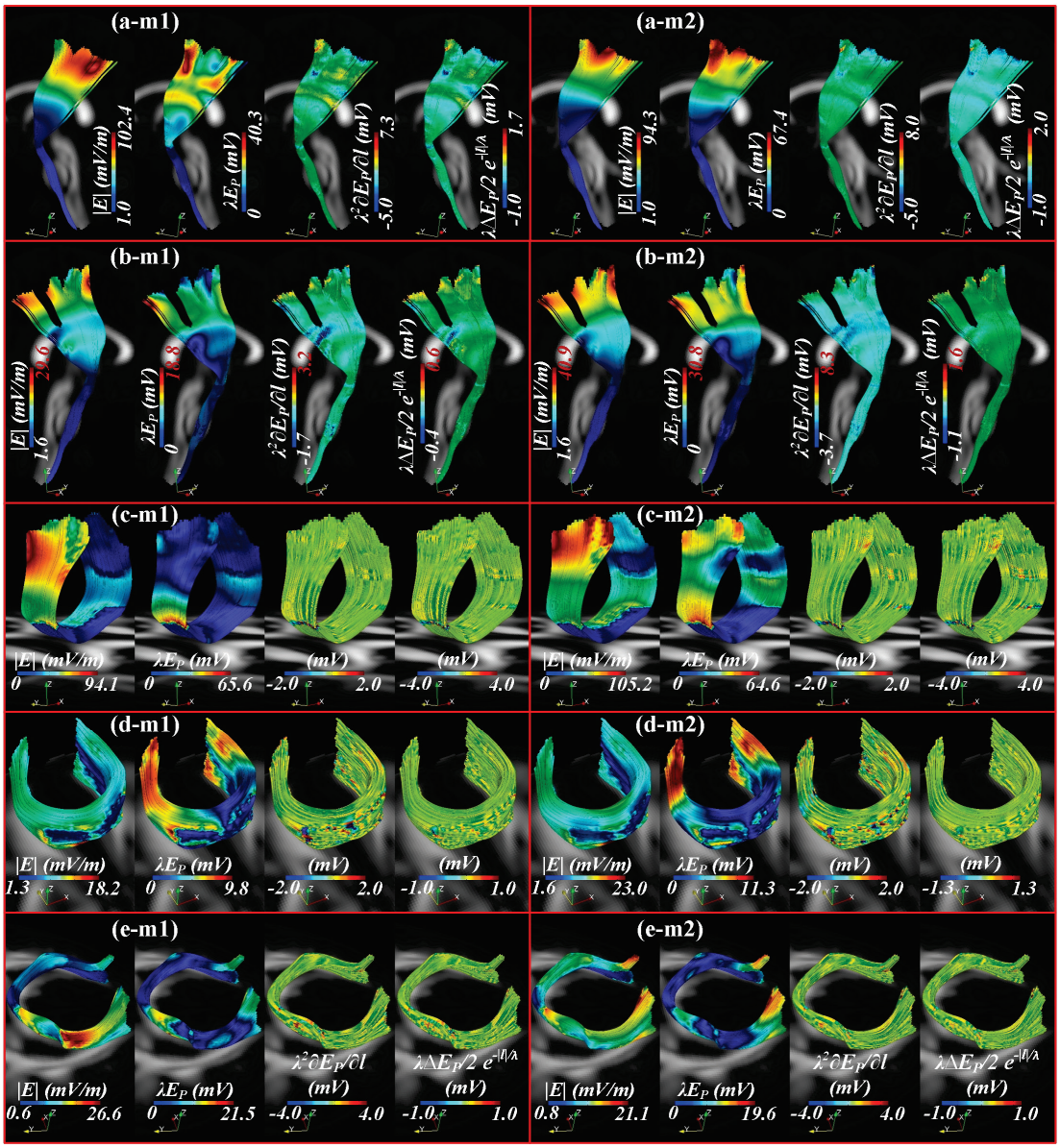

Figure 8.4: Montage specific behaviour of induced electric field *E* and stimulation parameters *Ep*, *∂Ep/∂l* and *ΔEp/2* across (a) left corticospinal tracts, (b) right corticospinal tracts, (c) medial of corpus callosum (d) genu of corpus callosum and (e) splenium of corpus callosum under HD montages m1 and m2, respectively (λ =1mm).

Figure 8.4 illustrates the induced E-field and three possible modulation mechanisms along the pathways of the selected fibre tracts under montages m1 and m2. The first and the fifth columns illustrate the E-field projection onto the fibres, whereas the second and the sixth column describes the E_P along the fibre pathways. By comparing Column 1 and 5, two types of differences can be observed. The first was the difference in the distribution pattern of the induced E-field and the second was related to its strength. E_P is the component of the induced electric field parallel to the local fibre pathway, therefore, E_P depends on the $\boldsymbol{E}$ and the orientation of the fibre tract. For example, under montage m3, E dropped along the fibre path (top to bottom), however, at a particular location if $\boldsymbol{E}$ was parallel to the local fibre path, E_P at that point would be high (Figure 8.5).

In the presence of a strong E-field an abrupt change in E_P strength can initiate excitation. In the L-CST of m1 and m2, the induced E-field targeted different portions of the fibre tract and overall field distribution was quite complex (Figure 8.4a). Mechanisms such as λE_P and ($\lambda^2 \partial E_P/\partial l$) can identify the possible sites of modulation. It can be seen that, even with these so-called targeted/focal montages, it was possible to induce excitation in other regions of the brain.

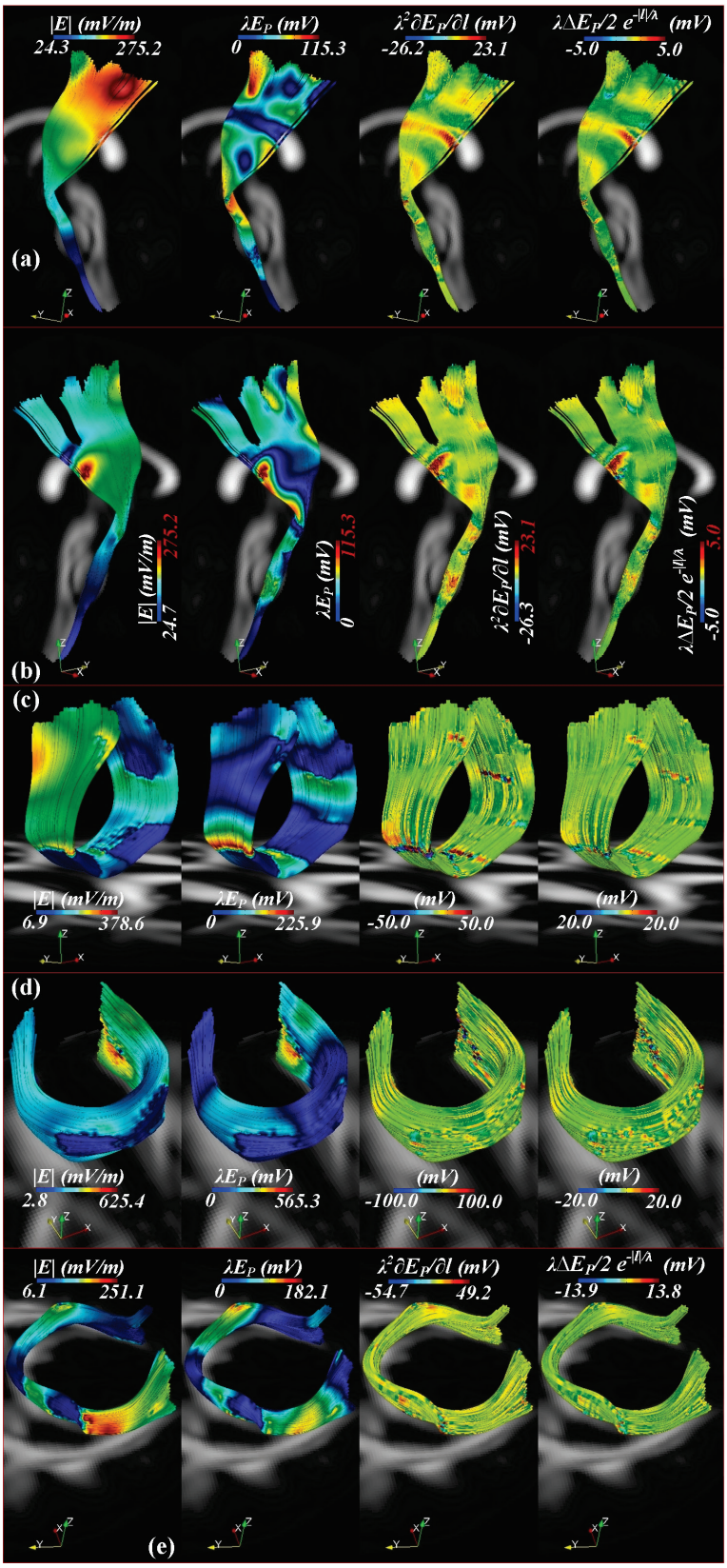

Figure 8.5: Montage specific behaviour of induced electric field ***E*** and stimulation parameters *Ep*, *∂Ep/∂l* and Δ*Ep/2* across (a) Left corticospinal tracts, (b) right corticospinal tracts,

(c) medial of corpus callosum (d) genu of corpus callosum and (e) splenium of corpus callosum under m3 (conventional) montage (λ =1mm).

The electric field along the fibre pathways depends on the location/proximity to the stimulating electrodes and the orientation of fibre tracts relative to the electrode/induced electric field. From Figure 8.6 (a-m1 and a-m2), it can be seen that the selected fibre in m1 had a lower magnitude of E_P compared to m2. This variation in the strength of E_P was attributed to the magnitude of the induced E and the local alignment of $\boldsymbol{E}$ with the fibre. For example, in m2 the $\boldsymbol{E}$ was more aligned to the fibre between 3-14 mm, whereas, in case of m1, even though E was weak compared to m2, the same fibre had high field alignment between 3-9 and 25-48 mm along the tract. These regions of high field alignment are shown along the fibre paths in the contrast of red. These regions are also displayed in the second and the sixth columns of Figure 8.4 (for montages m1 and m2) and for m3 in the second column of Figure 8.5. Under montage m3 the induced E-field showed a wider distribution pattern. Despite E_P under m3 (on average) been higher than m1 and m2, from Figure 8.6 (a-m3 and b-m3) it can be seen that, the maximum strength of E_P is located between 90-100 mm along the same fibre path. Because of the electrode size and location, the regions of high E_P strength were located in deeper parts across all the selected ROIs (Figure 8.5).

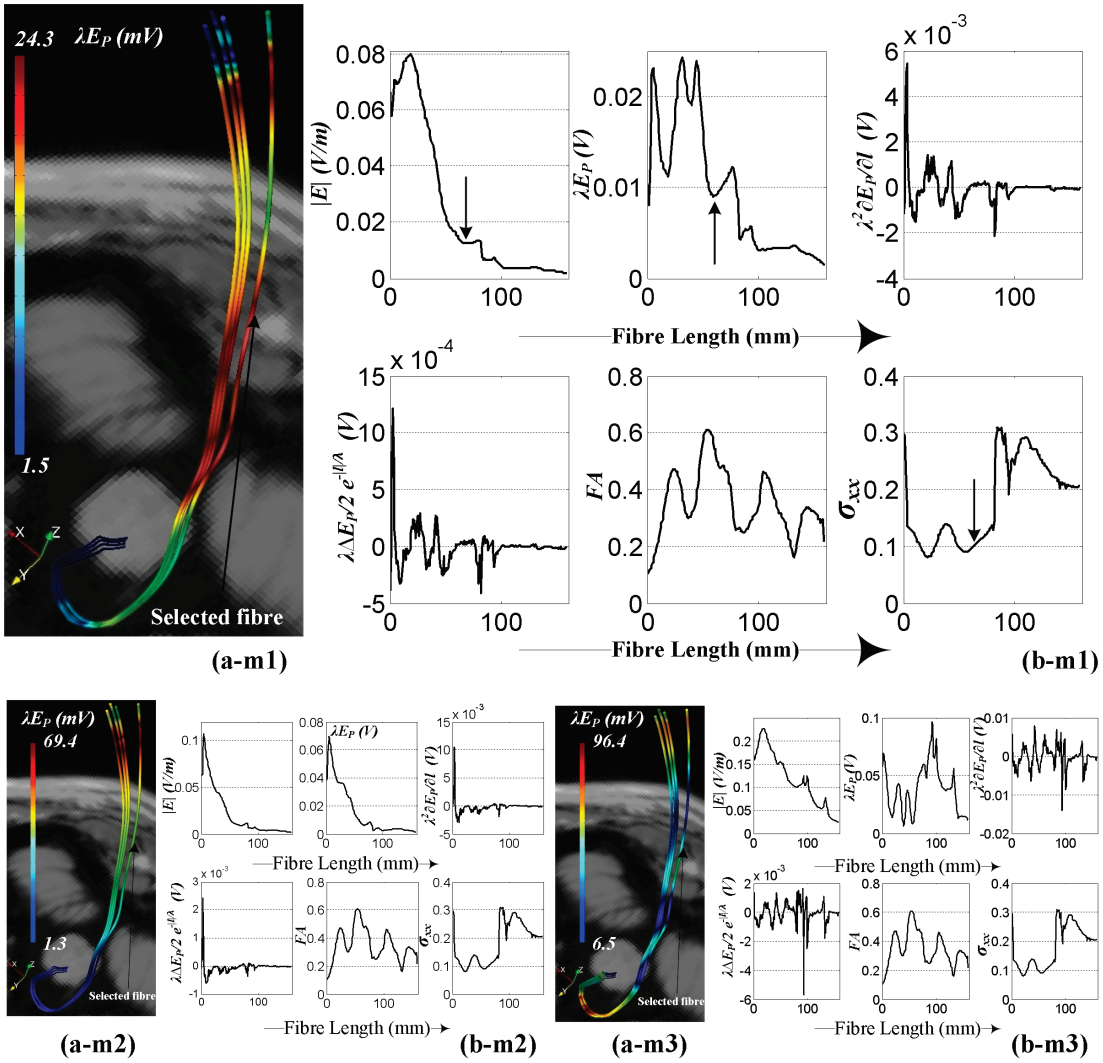

Figure 8.6: Single fibre level investigation using the projection of induced electric field '*E*', stimulation parameters E_P, $\partial E_P/\partial l$, $\Delta E_P/2$, fractional anisotropy index '*FA*" and conductivity distribution along the selected fibre (a-m1 and b-m1) under montage m1, (a-m2 and b-m2) under montage m2 and (a-m3 and b-m3) under montage m3. Sub-sections (a-m1, a-m2 and a-m3) illustrate E_P along the selected fibres of left corticospinal tract and (b-m1, b-m2 and b-m3) highlight the variations in electric field, stimulation mechanism, *FA* and anisotropic conductivity along the selected fibre (λ =1mm).

Abrupt changes in the orientation of fibre tracts in the presence of a strong E-field would cause high variations in the magnitude of E_P. These sudden changes in E_P, due to a bend, are illustrated in Figure 8.7(a) and Figure 8.7(c) for montage m1 and m2, respectively. E_P depends on the electric field vector and ***E*** depends on a number of parameters, such as the size and location of electrodes, tissue conductivity and ana-

tomical details of the cortical and non-cortical regions of the head. The gradient of E_P ($\lambda^2 \partial E_P / \partial l$) is illustrated in Figure 8.7(b and d). Since each fibre tract had a unique orientation with respect to the induced E-field, each fibre showed a distinctive strength and direction of $\lambda^2 \partial E_P / \partial l$, and this observation concurs with the findings of Kabakov et al. (2012). For example, the same fibres under montages m1 and m2 displayed different responses ($\lambda^2 \partial E_P / \partial l$) owing to the distinctive induced E-field distribution pattern.

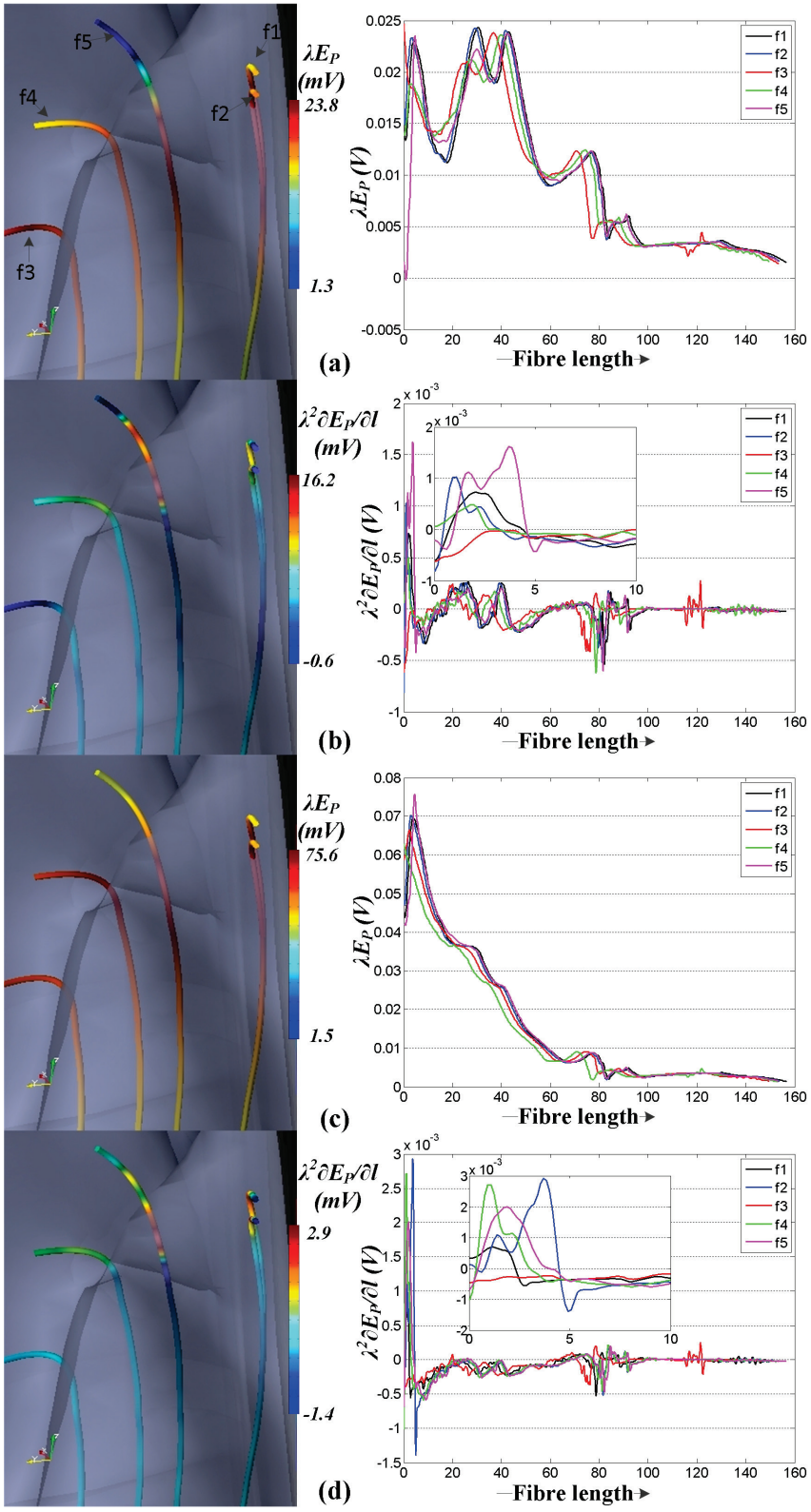

Figure 8.7: Behaviour of stimulation parameters E_P and $\partial E_P G/\partial l$ in the presence of artificial bends. (a and b) montage m1, (c and d) montage m2 (λ =1mm).

8.4. Discussion

Results of this chapter indicate that the site and strength of the induced E-field is highly sensitive to the electrode configurations, and tissue anisotropy further complicates these field distributions (*E & J*). The E-field generated by m1 was strongest in the left hemisphere (AP) in the proximity of the stimulating electrode. In montage m2, the peak of stimulation was located in the superior frontal gyrus with the second peak (lower amplitude) in the corpus callosum. Proximity of the anode to the medial longitudinal fissure and the superior sagittal sinus diverted more current to flow through the highly conductive CSF, thus increasing the current density in the vicinity of the corpus callosum. The field pattern produced by montage m3 was more dispersed with high field strengths observable between and under the electrodes. On average, the field strength (E_{median}) generated under montage m3 was approximately 8-10 times stronger than those of HD-configurations.

In one of the most recent studies, the analgesic effects of a weak E-field related to chronic migraine was analysed using the computational models (DaSilva et al. 2012). Similarly, another study by Parazzini, Fiocchi and Ravazzani (2012) analysed the efficacy of tDCS in the treatment of Tinnitus. Both studies used the isotropic computational models to estimate the spatial distribution of the induced E-field in the particular regions of interest. This chapter showed that bi-cephalic conventional montage m3 produced the highest E-field (compared to m1 and m2) in the sub-cortical structures, such as the thalamus, hippocampus and the putamen. These observations suggest that tDCS, under right electrode configuration, could induce changes in the excitability of the thalamus, hippocampus and other deep structures related to pain perception, attention, memory and learning.

The study conducted by Parazzini, Fiocchi and Ravazzani (2012) reported an insignificant influence of electrode position on the magnitude of $\boldsymbol{E}$ in different brain regions. However, comparing the two HD-electrode configurations used in this chapter, the percentage differences in E-field between the grey matter were 6.0_{ISO}, 15.8_{ANISO}, WM (11.65_{ISO}, 10.48_{ANISO}) and the highest difference was recorded for the caudate nucleus (17.4_{ISO}, 19.4_{ANISO}). These differences highlight the variations

caused by electrode placement along with tissue anisotropy. Other factors that might have contributed to this disparity (from Parazzini, Fiocchi and Ravazzani (2012) study) are the size and relative location of electrodes, tissue electrical properties and anatomical details of the volume conductor.

The study by Datta et al. (2009) reported the applicability of HD-montages to modulate limited regions, by confining the induced E-field in the close vicinity of the anode. Studies such as Borckardt et al. (2012) and Minhas et al. (2010) proposed the use of the HD-tDCS approach in the treatment of neuropsychiatric disorders due to its ability to deliver targeted dosage. However, the genesis of these studies is based on the assumption of brain being isotropic. As highlighted in this chapter, the role of anisotropy cannot be ignored as such a simplification can easily lead to an inaccurate assessment of dosage delivery and other field parameters. For instance, neglecting the role of anisotropic conductivity led the magnitude variation in the grey matter of m1, m2 and m3 to be around 146%, 101% and 62 %, respectively (intra-montage variation). Similarly, the topographic errors in the same regions were approximately 36%, 26% and 16%, respectively. These intra-montage variations in the magnitude and distribution of the induced E-field not only emphasise the importance of tissue anisotropy, but also the role of electrode configuration.

As demonstrated in the previous section, the spatial distribution of induced E-field is highly sensitive to electrode configuration and dielectric properties of the tissues. However, it is imperative to understand that the neural response to an induced E-field is not only dependent on the strength of the induced field, but also on the electrophysiological parameters, morphology and orientation of neurons with respect to the induced electric field. In order to estimate the impact of neural orientation on the site and strength of modulation, the DTI information used in the conductivity estimation was employed to perform fibre tracking on the selected ROIs. Such information is vital to understand the orientation specificity of different electrode montages. The incorporation of E_P to neural models can provide a deeper understanding of the connectivity estimation and field neural interaction, i.e. how an induced E-field acts on different neural structures of the brain.

By assessing E_P and its first derivative along fibre tracts of the selected ROIs under each electrode configuration, it was observed that each montage contributed in distinct distribution patterns. Depending on the orientation of fibres with respect to the induced electric field, localized enhancements in E_P strength at the GM-WM interface were observed in all the three montages. A change in the conductivity of regional volume would cause variations in the strength of the induced E-field, therefore, owing to the conductivity variation, the strength of E_P would also fluctuate. For example, in Figure 8.6(a-m1 and b-m1), at the location marked by the arrow in the conductivity plot, the x component of the directional conductivity is minimal, causing the E to increase/sustain. At the same time $\boldsymbol{E}$ is locally parallel to the fibre path, causing E_P to increase. The changes in the membrane potential across the selected fibre (Figure 8.6) associated with $\lambda\, E_P$ and $\lambda^2 \partial E_P / \partial l$ are in the range of $25\mu V$ (m1) to $100\ \mu V$ (m3) and $5.5\ \mu V$ (m1) to $15\ \mu V$ (m3), respectively. From these observations, it can be seen that tDCS cannot stimulate the resting neurons, and for long straight fibres, λE_P is the dominant modulation mechanism, whereas, $\lambda\ (\Delta E_P e^{-|l|/\lambda})/2$ is the lease effective mechanism. Similar behaviour was observed for fibres with artificially induced bends. These observations concur with the earlier findings of Miranda et al. (2007).

8.5. Conclusion

Electric field distributions characterised by two 4×1 High-Definition (m1=4×1 HD montage with anode at C3 and m2=4×1 HD montage with anode at C1) and a single bi-cephalic conventional (m3 = C3-Fp2) tDCS electrode montage were analysed under the influence of skull, muscles, and brain anisotropic conductivities. The electric field assessment was conducted using a high-resolution finite element head model derived from the structural Magnetic Resonance Imaging and Diffusion Tensor Imaging data. Distinct field patterns attributed to specific electrode montages were observed. Based on the statistical indices such as the Residual Error and Relative Difference Measure, it was observed that the effect of anisotropy was highly sensitive to the electrode configurations. In GM/WM, the inclusion of brain anisotropy resulted

in 5/10, 4/8 and 6/12 % and the inclusion of skull and muscle directional conductivity resulted in 147/121, 100/94 and 63/64 % variations (Residual Error) in the electric field strength under m1, m2 and m3 montages, respectively. Similarly, the topographic errors in electric field distributions were 5/8, 4/7 and 6/10 % for brain anisotropy and 34/31, 24/22 and 15/13 % for the skull and muscle anisotropic conductivity under m1, m2 and m3 montages, respectively. These indices highlight the importance of regional anisotropy and the role of electrode montage in defining the site and strength of stimulation. The role of individual doze optimization becomes quite significant in case of pathological abnormalities in brain regions, as general assumptions (based on clinical practices) might not hold. The highlighted indices were also well suited for addressing the variations caused by pathologies. To better understand the role of fibre tract stimulation on tDCS, multi-scale methods were used to predict the axon of passage polarization. The analysis showed that white matter anisotropy significantly affected the current flow along fibre tracks and that extension of electric field maps to membrane polarization further shaped predictions. Resulting predictions based on white matter polarization varied significantly from basic current flow maps.

9. CONCLUSION AND FUTURE DIRECTION

The focus of this thesis was to develop a realistic finite element based human head model to address the issues involved in the forward modelling of transcranial direct current stimulation (tDCS). The schemes proposed in this study are flexible enough to adapt to the requirements posed by the forward formulations of TMS, DBS and ECT.

In this thesis, an incremental approach was adopted to quantify and assess various modelling challenges, such as the role of additional non-cortical tissues and the influence of heterogeneously defined anisotropic electrical conductivity on field variables. Field sensitivity to such complexities were analysed step by step. Using the averaged and the subject specific MRI and DTI data, the head models with detailed anatomical features and realistic material (tissue) properties were developed to specifically address the role of morphological variations, structural details, tissue behaviour, inter-subject variations, electrode montages and neural fibre pathways in defining the site and strength of modulation/stimulation.

9.1. Main contributions

1. A framework to construct a morphologically accurate high-resolution finite element head model was developed:

a. High-resolution isotropic head models with increasing model complexities (ranging from 5 regions to 20 anatomically distinct regions) were developed using high-resolution scalar MRI modalities. The importance of considering additional non-cortical and deep brain regions in field assessment was investigated using multiple bi-cephalic and High-Definition electrode montages

b. Using subject specific MRI datasets the individualised high-resolution head models were developed and compared with averaged head models. The impacts of inter-subject anatomical variations were assessed across the GM, WM and multiple regions of interest. The effect of subject specific anatomical variations on dose parameters was also investigated

2. A method to incorporate tissue anisotropic behaviour in finite element head models was developed:

a. The role of non-cortical tissue anisotropy on input impedance, scalp return current and cortical current distribution was analysed using conventional and high-definition electrode configurations. The role of WM anisotropy in shaping the cortical electric field was examined and justified by incorporating artificial WM anisotropy using the eigenvalue decomposition

b. A new scheme to process and translate measured diffusion tensor data to conductivity tensor data was implemented. The method was tested using both the averaged and the noisy subject specific datasets. Four algorithms were developed and analysed for their ability to represent realistic WM anisotropic conductivity distribution. Multiple head models with inter-subject variations were used to analyse the robustness of DTI processing and translational schemes

c. Using the same scheme of DTI processing, the conductivity tensor profile was expanded to include the GM and sub-cortical regions as well. The expanded conductivity profile was used to examine the in-

fluence of cortical and deep brain regional anisotropy on induced electric field under four conventional and two High-Definition montages

d. The sensitivity of field parameters (*E/J*) on brain tissue conductivity variations was estimated using three inhomogeneous anisotropic conductivity profiles

3. Neuro-navigation scheme based on white matter fibre architecture was proposed. The connectivity estimation based on the deterministic scheme was developed to incorporate five major white matter fibre tracts with the induced electric fields. Using four bi-cephalic and two high-definition montages, the important role of dose parameters (electrode location and size) in shaping the brain electric fields was analysed in conjunction with the underlying fibre architecture. Three mechanisms of neural/axonal stimulation were used to investigate the orientation specificity of electrode montages in regulating neural activities. Fibre tractography based neuro-navigation scheme provided the additional information to understand the role of fibre pathways in regulating the neural activities

9.2. Future work and direction

During the course of this study, many improvements in head model design were explored for their efficacy in improving the forward solution. Despite these attempts, much room for improvement across a number of fronts remain.

In this thesis, the head models were extended from the top of the scalp to the base of foramen magnum. As a result, the analysis did not consider the role of lower parts of the head and neck regions. In future studies, it would be imperative to study the effect of head truncation on field assessment as ignoring these regions would induce additional current into the brain region (reducing shunting through superficial regions such as the scalp or skin). Since, the data used in this study were obtained from public repositories, such a comparison was not possible. The issue of head truncation

is more relevant to the absolute values of field parameters, whereas in this thesis, the assessments were based on the comparative analysis (ISO vs. ANISO), therefore, the effect of truncation would not be significant.

Another important issue in forward modelling is the accurate representation of dielectric properties of cortical tissues. Efforts have been made in measuring or estimating the conductivities of different biological samples, however, large inter- and intra-subject variability in conductivity, even across the same tissue, has, so far, led to a lack of consensus in values reported in the literature. These uncertainties in dielectric values would have a strong influence on the strength and distribution of the induced electric field and current density distribution.

WM is composed of highly parallelized fibre bundles that are detectable at a macroscopic scale (voxel level) therefore, their diffusion profile can be satisfactorily represented by a symmetric second rank diffusion tensor. The GM, in contrast, is composed of multiple cell types, axons projections and dendritic fibres. At a sub-voxel level (microscopic scale), these axons and dendritic fibres project in specific directions however, such orientations are not detectable at voxel scales (≈1- 2 mm^3). Therefore, under Pulsed Gradient Spin Echo-based sequences, GM and regions of fibre crossing in WM appear close to isotropic.

The conductivity estimation in this study was carried out using the DTI data under the assumption that the diffusion tensor is second rank and symmetric. Such an assumption caused the regions of fibre crossing to appear close to isotropic. The convoluted and inter-crossing branches of cortical neurons made it impossible to estimate actual fibre paths in low *FA* regions. To improve the conductivity estimation, it would be imperative to overcome the limitation of fibre crossing by using, advance DTI processing algorithms such as Kun et al. (2008) or using the Diffusion Spectrum Imaging (DSI) scheme (Wedeen et al. 2012; Wedeen et al. 2008). Perhaps, the Orientation Distribution Function (ODF) can be incorporated to characterize the diffusion distribution (Yeh & Tseng 2011). Diffusion data may be acquired using High-Resolution Diffusion Imaging (HARDI) scheme (Tuch et al. 2002) or Diffusion Spectrum Imaging (DSI) (Wedeen et al. 2008). Alternatively, model-free reconstruction methods such as Q-ball (Tuch 2004) with DSI could be used to estimate the dif-

fusion probability and diffusion ODFs. Since the fibre tracking performed in this thesis was based on DTI data, it was only possible to track fibres in the regions of high *FA*. As a result, the fibre tracking was limited to the regions of $FA>0.2$. However, by employing probabilistic tracking rather than a deterministic scheme, it would possible to have reliable information in low *FA* regions (Behrens et al. 2003). Such a scheme could extend the scope of this study into low *FA* regions and would be able to provide the much-needed neural interaction information in the superficial regions of the brain.

In this thesis, the fibres were considered unmyelinated and their morphological response and neural activation dynamics, in the presence of external stimulus were not considered. At present, there are no computational models that can realistically simulate the neural response to a weak electric current. However, using a simplified cortical model, Salvador et al. (2011) reported the electrophysiological response of various cortical neurons in a uniform E-field. Therefore, the next logical step would be to incorporate the mathematical models of neural responses and membrane kinetics into FE models to identify possible sites of neural excitation.

REFERENCES

Abascal, J-FPJ, Arridge, SR, Atkinson, D, Horesh, R, Fabrizi, L, De Lucia, M, Horesh, L, Bayford, RH & Holder, DS (2008), 'Use of anisotropic modelling in electrical impedance tomography; Description of method and preliminary assessment of utility in imaging brain function in the adult human head', NeuroImage, vol. 43, no. 2, pp. 258-68.

Ahrens, ET, Laidlaw, DH, Readhead, C, Brosnan, CF, Fraser, SE & Jacobs, RE (1998), 'MR microscopy of transgenic mice that spontaneously acquire experimental allergic encephalomyelitis', Magnetic Resonance in Medicine, vol. 40, no. 1, pp. 119-32.

Akhtari, M, Bryant, H, Mamelak, A, Flynn, E, Heller, L, Shih, J, Mandelkem, M, Matlachov, A, Ranken, D & Best, E (2002), 'Conductivities of three-layer live human skull', Brain Topography, vol. 14, no. 3, pp. 151-67.

Alexander, AL, Tsuruda, JS & Parker, DL (1997), 'Elimination of eddy current artifacts in diffusion-weighted echo-planar images: The use of bipolar gradients', Magnetic Resonance in Medicine, vol. 38, no. 6, pp. 1016-21.

Alexander, DC, Pierpaoli, C, Basser, PJ & Gee, JC (2001), 'Spatial transformations of diffusion tensor magnetic resonance images', IEEE Transcations on Medical Imaging, vol. 20, no. 11, pp. 1131-9.

Alexandre F, DS, Magdalena Sarah, V, Marom, B & Felipe, F (2011), 'Electrode positioning and montage in transcranial direct current stimulation', Journal of Visualized Experiments, no. 51. pii: 2744. Doi: 10.379112744.

Allen Institute for Brain Science, 2011, 25-05-2011,
<http://www.alleninstitute.org/>.

Amassian, V, Maccabee, P, Cracco, R, Cracco, J, Somasundaram, M, Rothwell, J, Eberle, L, Henry, K & Rudell, A (1994), 'The polarity of the induced electric field influences magnetic coil inhibition of human visual cortex: implications for the site of excitation', Electroencephalography and Clinical Neurophysiology/Evoked Potentials Section, vol. 93, no. 1, pp. 21-6.

Anderson, AW & Gore, JC (1994), 'Analysis and correction of motion artifacts in diffusion weighted imaging', Magnetic Resonance in Medicine, vol. 32, no. 3, pp. 379-87.

Antal, A, Kincses, TZ, Nitsche, MA, Bartfai, O & Paulus, W (2004), 'Excitability changes induced in the human primary visual cortex by transcranial direct current stimulation: direct electrophysiological evidence', Investigative Ophthalmology & Visual Science, vol. 45, no. 2, pp. 702-7.

Antal, A, Polania, R, Schmidt-Samoa, C, Dechent, P & Paulus, W (2011), 'Transcranial direct current stimulation over the primary motor cortex during fMRI', NeuroImage, vol. 55, no. 2, pp. 590-6.

Ardolino, G, Bossi, B, Barbieri, S & Priori, A (2005), 'Non-synaptic mechanisms underlie the after-effects of cathodal transcutaneous direct current stimulation of the human brain', The Journal of Physiology, vol. 568, no. 2, pp. 653-63.

Ary, J, Klein, S & Fender, D (1981), 'Location of sources of evoked scalp potentials: corrections for skull and scalp thicknesses', IEEE Transactions on Biomedical Engineering, vol. 28, no. 6, pp. 447-52.

Aubert-Broche, B, Evans, AC & Collins, L (2006), 'A new improved version of the realistic digital brain phantom', NeuroImage, vol. 32, no. 1, pp. 138-45.

Bammer, R, Keeling, SL, Augustin, M, Pruessmann, KP, Wolf, R, Stollberger, R, Hartung, HP & Fazekas, F (2001), 'Improved diffusion-weighted single-shot echo-planar imaging (EPI) in stroke using sensitivity encoding (SENSE)', Magnetic Resonance in Medicine, vol. 46, no. 3, pp. 548-54.

Bangera, N, Schomer, D, Dehghani, N, Ulbert, I, Cash, S, Papavasiliou, S, Eisenberg, S, Dale, A & Halgren, E (2010), 'Experimental validation of the influence of white matter anisotropy on the intracranial EEG forward solution', Journal of Computational Neuroscience, vol. 29, no. 3, pp. 371-87.

Barmpoutis, A & Vemuri, BC (2010), 'A unified framework for estimating diffusion tensors of any order with symmetric positive-definite constraints', in Biomedical Imaging: From Nano to Macro, 2010 IEEE International Symposium on: Biomedical Imaging, pp. 1385-8.

Barmpoutis, A, Vemuri, BC, Shepherd, TM & Forder, JR (2007), 'Tensor splines for interpolation and approximation of DT-MRI with applications to segmentation of isolated rat hippocampi', IEEE Transactions on Medical Imaging, vol. 26, no. 11, pp. 1537-46.

Basser, P & Roth, B (1991), 'Stimulation of a myelinated nerve axon by electromagnetic induction', Medical and Biological Engineering and Computing, vol. 29, no. 3, pp. 261-8.

Basser, P, Mattiello, J & LeBihan, D (1994a), 'Estimation of the effective self-diffusion tensor from the NMR spin echo', Journal of Magnetic Resonance-Series B, vol. 103, no. 3, pp. 247-54.

Basser, P, Mattiello, J & LeBihan, D (1994b), 'MR diffusion tensor spectroscopy and imaging', Biophysical Journal, vol. 66, no. 1, pp. 259-67.

Basser, PJ (1995), 'Inferring microstructural features and the physiological state of tissues from diffusion-weighted images', NMR in Biomedicine, vol. 8, no. 7, pp. 333-44.

Basser, PJ & Roth, BJ (1990), 'Electromagnetic stimulation of a myelinated axon', in Bioengineering Conference, 1990., Proceedings of the 1990 Sixteenth Annual North-east: proceedings of the Bioengineering Conference, 1990., pp. 129-30.

Basser, PJ & Pierpaoli, C (1996), 'Microstructural and physiological features of tissues elucidated by quantitative-diffusion-tensor MRI', Journal of Magnetic Resonance. Series B, vol. 111, no. 3, pp. 209-19.

Basser, PJ & Pajevic, S (1999), 'Method to reduce eigenvalue sorting bias in DT-MRI', in Proceedings of the 7th Annual Meeting of ISMRM, Philadelphia, PA, USA, p. 1788.

Basser, PJ & Pajevic, S (2000), 'Statistical artifacts in diffusion tensor MRI (DT-MRI) caused by background noise', Magnetic Resonance in Medicine, vol. 44, no. 1, pp. 41-50.

Bastin, ME (1999), 'Correction of eddy current-induced artefacts in diffusion tensor imaging using iterative cross-correlation', Magnetic Resonance Imaging, vol. 17, no. 7, pp. 1011-24.

Bastin, ME, Armitage, PA & Marshall, I (1998), 'A theoretical study of the effect of experimental noise on the measurement of anisotropy in diffusion imaging', Magnetic Resonance Imaging, vol. 16, no. 7, pp. 773-85.

Bastos, JPA & Sadowski, N (2003), Electromagnetic modeling by finite element methods, Marcel Dekker, New York, USA.

Baumann, S, Wozny, D, Kelly, S & Meno, F (1997), 'The electrical conductivity of human cerebrospinal fluid at body temperature', IEEE Transactions on Biomedical Engineering, vol. 44, no. 3, pp. 220-3.

Beaulieu, C (2002), 'The basis of anisotropic water diffusion in the nervous system–a technical review', NMR in Biomedicine, vol. 15, no. 7-8, pp. 435-55.

Beaulieu, C & Allen, PS (1994), 'Water diffusion in the giant axon of the squid: Implications for diffusion-weighted MRI of the nervous system', Magnetic Resonance in Medicine, vol. 32, no. 5, pp. 579-83.

Beaulieu, C & Allen, PS (2005), 'Determinants of anisotropic water diffusion in nerves', Magnetic Resonance in Medicine, vol. 31, no. 4, pp. 394-400.

Behrens, TEJ, Woolrich, MW, Jenkinson, M, Johansen-Berg, H, Nunes, RG, Clare, S, Matthews, PM, Brady, JM & Smith, SM (2003), 'Characterization and propagation of uncertainty in diffusion-weighted MR imaging', Magnetic Resonance in Medicine, vol. 50, no. 5, pp. 1077-88.

Beutel, J & Sonka, M (2000), Volume 2: Medical Image Processing and Analysis, Society of Photo Optical.

Bikson, M 2011, Bonsai, viewed 28/12/2011, <www.neuralengr.com/bonsai>.

Bikson, M, Datta, A, Rahman, A & Scaturro, J (2010), 'Electrode montages for tDCS and weak transcranial electrical stimulation: Role of "return" electrode's position and size', Clinical Neurophysiology, vol. 121, no. 12, p. 1976.

Bikson, M, Inoue, M, Akiyama, H, Deans, JK, Fox, JE, Miyakawa, H & Jefferys, JGR (2004), 'Effects of uniform extracellular DC electric fields on excitability in rat hippocampal slices in vitro', The Journal of Physiology, vol. 557, no. 1, pp. 175-90.

Boggio, PS, Nunes, A, Rigonatti, SP, Nitsche, MA, Pascual-Leone, A & Fregni, F (2007), 'Repeated sessions of noninvasive brain DC stimulation is associated with motor function improvement in stroke patients', Restorative Neurology And Neuroscience, vol. 25, no. 2, pp. 123-9.

Borckardt, JJ, Bikson, M, Frohman, H, Reeves, ST, Datta, A, Bansal, V, Madan, A, Barth, K & George, MS (2012), 'A pilot study of the tolerability and effects of high-definition transcranial direct current stimulation (HD-tDCS) on pain perception', Journal of Pain, vol. 13, no. 2, pp. 112-20.

BrainWeb: Simulated Brain Database. McConnell Brain Imaging Centre Montreal Neurological Institute. McGill University, 25/07/2012, <http://www.bic.mni.mcgill.ca/brainweb/.>.

Brody, D, Terry, F & Ideker, R (1973), 'Eccentric dipole in a spherical medium: generalized expression for surface potentials', IEEE Transactions on Biomedical Engineering, vol. 20, no. 2, pp. 141-3.

Brown, LG (1992), 'A survey of image registration techniques', ACM computing surveys (CSUR), vol. 24, no. 4, pp. 325-76.

Chaturvedi, A, Butson, CR, Lempka, SF, Cooper, SE & McIntyre, CC (2010), 'Patient-specific models of deep brain stimulation: influence of field model complexity on neural activation predictions', Brain Stimulation, vol. 3, no. 2, p. 65.

Chefd'hotel, C, Tschumperlé, D, Deriche, R & Faugeras, O (2002), 'Constrained Flows of Matrix-Valued Functions: Application to Diffusion Tensor Regularization',

in A Heyden, et al. (eds), Computer Vision — ECCV 2002, Springer Berlin Heidelberg, vol. 2350, ch. 17, pp. 251-65.

Chen, B & Hsu, EW (2005), 'Noise removal in magnetic resonance diffusion tensor imaging', Magnetic Resonance in Medicine, vol. 54, no. 2, pp. 393-401.

Christ, A, Kainz, W, Hahn, EG, Honegger, K, Zefferer, M, Neufeld, E, Rascher, W, Janka, R, Bautz, W, Chen, J, Kiefer, B, Schmitt, P, Hollenbach, HP, Shen, J, Oberle, M, Szczerba, D, Kam, A, Guag, JW & Kuster, N (2010), 'The Virtual Family-development of surface-based anatomical models of two adults and two children for dosimetric simulations', Physics in Medicine and Biology, vol. 55, no. 2, pp. N23-38.

Clark, C, Barker, G & Tofts, P (1999), 'An in vivo Evaluation of the Effects of Local Magnetic Susceptibility-Induced Gradients on Water Diffusion Measurements in Human Brain', Journal of Magnetic Resonance, vol. 141, no. 1, pp. 52-61.

Coben, R & Evans, JR (2010), Neurofeedback and neuromodulation techniques and applications, first edition, Academic Press, UK.

Cocosco, C, Kollokian, V, Kwan, K & Pike, GB 1997, 'BrainWeb: Online interface to a 3D MRI simulated brain database', Proceedings of 3rd International Conference on Functional Mapping of the Human Brain , vol. 5, no. 4, p. S425

Cogiamanian, F, Marceglia, S, Ardolino, G, Barbieri, S & Priori, A (2007), 'Improved isometric force endurance after transcranial direct current stimulation over the human motor cortical areas', European Journal of Neuroscience, vol. 26, no. 1, pp. 242-9.

Cogiamanian, F, Vergari, M, Pulecchi, F, Marceglia, S & Priori, A (2008), 'Effect of spinal transcutaneous direct current stimulation on somatosensory evoked potentials in humans', Clinical Neurophysiology, vol. 119, no. 11, p. 2636-40.

Comsol Multiphysics 4.1Reference Guide, (2010), Burlington, USA: COMSOL.

Conturo, TE, McKinstry, RC, Akbudak, E & Robinson, BH (1996), 'Encoding of anisotropic diffusion with tetrahedral gradients: a general mathematical diffusion formalism and experimental results', Magnetic Resonance in Medicine, vol. 35, no. 3, pp. 399-412.

Conturo, TE, Lori, NF, Cull, TS, Akbudak, E, Snyder, AZ, Shimony, JS, McKinstry, RC, Burton, H & Raichle, ME (1999), 'Tracking neuronal fiber pathways in the living human brain', Proceedings of the National Academy of Sciences, vol. 96, no. 18, pp. 10422-7.

Coulon, O, Alexander, D & Arridge, S (2004), 'Diffusion tensor magnetic resonance image regularization', Medical Image Analysis, vol. 8, no. 1, pp. 47-67.

Crank, J (1998), The mathematics of diffusion, second edition, Oxford Clarendon Press, Oxford.

Cuffin, BN, Schomer, DL, Ives, JR & Blume, H (2001), 'Experimental tests of EEG source localization accuracy in realistically shaped head models', Clinical neurophysiology, vol. 112, no. 12, pp. 2288-92.

DaSilva, AF, Mendonca, ME, Zaghi, S, Lopes, M, DosSantos, MF, Spierings, EL, Bajwa, Z, Datta, A, Bikson, M & Fregni, F (2012), 'tDCS-Induced Analgesia and Electrical Fields in Pain-Related Neural Networks in Chronic Migraine', Headache: The Journal of Head and Face Pain, vol. 52, no. 8, pp. 1283-95.

Datta, A, Bikson, M & Fregni, F (2010), 'Transcranial direct current stimulation in patients with skull defects and skull plates: high-resolution computational FEM study of factors altering cortical current flow', NeuroImage, vol. 52, no. 4, pp. 1268-78.

Datta, A, Elwassif, M, Battaglia, F & Bikson, M (2008), 'Transcranial current stimulation focality using disc and ring electrode configurations: FEM analysis', Journal of Neural Engineering, vol. 5, no. 2, pp. 163-74.

Datta, A, Baker, JM, Bikson, M & Fridriksson, J (2011), 'Individualized model predicts brain current flow during transcranial direct-current stimulation treatment in responsive stroke patient', Brain Stimulation, vol. 3, no. 3, pp. 169-74

Datta, A, Bansal, V, Diaz, J, Patel, J, Reato, D & Bikson, M (2009), 'Gyri–precise head model of transcranial DC stimulation: Improved spatial focality using a ring electrode versus conventional rectangular pad', Brain Stimulation, vol. 2, no. 4, pp. 201-7.

De Lucia, M, Parker, G, Embleton, K, Newton, J & Walsh, V (2007), 'Diffusion tensor MRI-based estimation of the influence of brain tissue anisotropy on the effects of transcranial magnetic stimulation', NeuroImage, vol. 36, no. 4, pp. 1159-70.

De Munck, J (1988), 'The potential distribution in a layered anisotropic spheroidal volume conductor', Journal of Applied Physics, vol. 64, no. 2, pp. 464-70.

Deng, ZD, Lisanby, SH & Peterchev, AV (2011), 'Electric field strength and focality in electroconvulsive therapy and magnetic seizure therapy: a finite element simulation study', Journal of Neural Engineering, vol. 8, no. 1, p. 016007.

Dmochowski, JP, Datta, A, Bikson, M, Su, Y & Parra, LC (2011), 'Optimized multi-electrode stimulation increases focality and intensity at target', Journal of Neural Engineering, vol. 8, no. 4, p. 046011.

Eaton, H (1992), 'Electric field induced in a spherical volume conductor from arbitrary coils: application to magnetic stimulation and MEG', Medical and Biological Engineering and Computing, vol. 30, no. 4, pp. 433-40.

Faria, P (2010), 'The Importance of the Numerical Resolution of the Laplace Equation in the optimization of a Neuronal Stimulation Technique', in International Conference of Numerical Analysis and Applied Mathematics 2010, vol. 1281, pp. 1199-202.

Faria, P, Leal, A & Miranda, PC (2009), 'Comparing different electrode configurations using the 10-10 international system in tDCS: A finite element model analysis', in Engineering in Medicine and Biology Society, (EMBC) 2009 Annual International Conference of the IEEE pp. 1596-9.

Faria, P, Hallett, M & Miranda, PC (2011), 'A finite element analysis of the effect of electrode area and inter-electrode distance on the spatial distribution of the current density in tDCS', Journal of Neural Engineering, vol. 8, no. 6, p. 066017.

Farzaneh, F, Riederer, SJ & Pelc, NJ (1990), 'Analysis of T2 limitations and off-resonance effects on spatial resolution and artifacts in echo-planar imaging', Magnetic Resonance in Medicine, vol. 14, no. 1, pp. 123-39.

Ferdjallah, M, Bostick, F & Barr, R (1996), 'Potential and current density distributions of cranial electrotherapy stimulation (CES) in a four-concentric-spheres model', IEEE Transactions on Biomedical Engineering, vol. 43, no. 9, pp. 939-43.

Ferdjallah, M, Bostick, FX & Barr, RE (1996), 'Potential and current density distributions of cranial electrotherapy stimulation (CES) in a four-concentric-spheres model', IEEE Transactions on Biomedical Engineering, vol. 43, no. 9, pp. 939-43.

Ferrucci, R, Mameli, F, Guidi, I, Mrakic-Sposta, S, Vergari, M, Marceglia, S, Cogiamanian, F, Barbieri, S, Scarpini, E & Priori, A (2008), 'Transcranial direct current stimulation improves recognition memory in Alzheimer disease', Neurology, vol. 71, no. 7, pp. 493-8.

Fillard, P, Pennec, X, Arsigny, V & Ayache, N (2007), 'Clinical DT-MRI estimation, smoothing, and fiber tracking with log-Euclidean metrics', IEEE Transactions on Medical Imaging, vol. 26, no. 11, pp. 1472-82.

Frank, E (1952), 'Electric potential produced by two point current sources in a homogeneous conducting sphere', Journal of Applied Physics, vol. 23, p. 1225.

Fregni, F & Pascual-Leone, A ‘(2007), 'Technology insight: noninvasive brain stimulation in neurology—perspectives on the therapeutic potential of rTMS and tDCS', Nature Clinical Practice Neurology, vol. 3, no. 7, pp. 383-93.

Fregni, F, Freedman, S & Pascual-Leone, A ‘(2007), 'Recent advances in the treatment of chronic pain with non-invasive brain stimulation techniques', The Lancet Neurology, vol. 6, no. 2, pp. 188-91.

Fregni, F, Boggio, P, Nitsche, M & Pascual-Leone, A (2005), 'Transcranial direct current stimulation', The British Journal of Psychiatry, vol. 186, no. 5, pp. 446-7.

Fregni, F, Thome-Souza, S, Nitsche, MA, Freedman, SD, Valente, KD & Pascual-Leone, A (2006), 'A controlled clinical trial of cathodal DC polarization in patients with refractory epilepsy', Epilepsia, vol. 47, no. 2, pp. 335-42.

Fregni, F, Marcondes, R, Boggio, P, Marcolin, M, Rigonatti, S, Sanchez, T, Nitsche, M & Pascual-Leone, A (2006), 'Transient tinnitus suppression induced by repetitive transcranial magnetic stimulation and transcranial direct current stimulation', European Journal of Neurology, vol. 13, no. 9, pp. 996-1001.

Fregni, F, Boggio, PS, Lima, MC, Ferreira, MJL, Wagner, T, Rigonatti, SP, Castro, AW, Souza, DR, Riberto, M & Freedman, SD (2006), 'A sham-controlled, phase II trial of transcranial direct current stimulation for the treatment of central pain in traumatic spinal cord injury', Pain, vol. 122, no. 1, pp. 197-209.

Friston, KJ (2006), 'Statistical parametric mapping: The analysis of functional brain images', Academic Press, UK.

Gabriel, C, Gabriel, S & Corthout, E (1996), 'The dielectric properties of biological tissues: I. Literature survey', Physics in Medicine and Biology, vol. 41, no. 11, pp. 2231-49.

Gabriel, S, Lau, RW & Gabriel, C (1996), 'The dielectric properties of biological tissues: II. Measurements in the frequency range 10 Hz to 20 GHz', Physics in Medicine and Biology, vol. 41, no. 11, pp. 2251-69.

Geddes, L & Baker, L (1967), 'The specific resistance of biological material-a compendium of data for the biomedical engineer and physiologist', Medical and Biological Engineering and Computing, vol. 5, no. 3, pp. 271-93.

Goncalve, S, De Munck, J, Verbunt, J, Heethaar, R & da Silva, F (2003), 'In vivo measurement of the brain and skull resistivities using an EIT-based method and the combined analysis of SEF/SEP data', IEEE Transactions on Biomedical Engineering, vol. 50, no. 9, pp. 1124-7.

Goto, T, Hatanaka, R, Ogawa, T, Sumiyoshi, A, Riera, J & Kawashima, R (2010), 'An evaluation of the conductivity profile in the somatosensory barrel cortex of Wistar rats', Journal of Neurophysiology, vol. 104, no. 6, pp. 3388-412.

Gulani, V, Webb, A, Duncan, I & Lauterbur, P (2001), 'Apparent diffusion tensor measurements in myelin-deficient rat spinal cords', Magnetic Resonance in Medicine, vol. 45, no. 2, pp. 191-5.

Gullmar, D, Haueisen, J, Eiselt, M, Gießler, F, Flemming, L, Anwander, A, Knosche, T, Wolters, C, Dumpelmann, M & Tuch, D (2006), 'Influence of anisotropic conductivity on EEG source reconstruction: investigations in a rabbit model', IEEE Transactions on Biomedical Engineering, vol. 53, no. 9, pp. 1841-50.

Güllmar, D, Haueisen, J & Reichenbach, J (2010), 'Influence of anisotropic electrical conductivity in white matter tissue on the EEG/MEG forward and inverse solution. A

high-resolution whole head simulation study', NeuroImage, vol. 51, no. 1, pp. 145-63.

Hallez, H, Staelens, S & Lemahieu, I (2009), 'Dipole estimation errors due to not incorporating anisotropic conductivities in realistic head models for EEG source analysis', Physics in Medicine and Biology, vol. 54, no. 2, pp. 6079-93.

Hallez, H, Vanrumste, B, Van Hese, P, Delputte, S & Lemahieu, I (2008), 'Dipole estimation errors due to differences in modeling anisotropic conductivities in realistic head models for EEG source analysis', Physics in Medicine and Biology, vol. 53, no. 7, pp. 1877-94.

Hallez, H, Vanrumste, B, Hese, P, D'Asseler, Y, Lemahieu, I & Walle, R (2005), 'A finite difference method with reciprocity used to incorporate anisotropy in electroencephalogram dipole source localization', Physics in Medicine and Biology, vol. 50, p. 3787.

Hamalainen, MS & Sarvas, J (1989), 'Realistic conductivity geometry model of the human head for interpretation of neuromagnetic data', IEEE Transactions on Biomedical Engineering, vol. 36, no. 2, pp. 165-71.

Hans Hallez, BV, Peter Van Hese, Steven Deputte, Yves D'Asseller and Ignace Lemahieu (2007), 'Importance of including anisotropic conductivities of grey matter in EEG source localization', in International Journal of Bioelectromagnetism: proceedings of the International Journal of Bioelectromagnetism, vol. 9, no. 2, pp. 105-6.

Haueisen, J, Ramon, C, Eiselt, M, Brauer, H & Nowak, H (1997), 'Influence of tissue resistivities on neuromagnetic fields and electric potentials studied with a finite element model of the head', IEEE Transactions on Biomedical Engineering, vol. 44, no. 8, pp. 727-35.

Haueisen, J, Tuch, D, Ramon, C, Schimpf, P, Wedeen, V, George, J & Belliveau, J (2002), 'The influence of brain tissue anisotropy on human EEG and MEG', NeuroImage, vol. 15, no. 1, pp. 159-66.

Heller, L & van Hulsteyn, DB (1992), 'Brain stimulation using electromagnetic sources: theoretical aspects', Biophysical Journal, vol. 63, no. 1, pp. 129-38.

Hoeltzell, PB & Dykes, RW (1979), 'Conductivity in the somatosensory cortex of the cat--evidence for cortical anisotropy', Brain Research, vol. 177, no. 1, pp. 61-82.

Holdefer, R, Sadleir, R & Russell, M (2006), 'Predicted current densities in the brain during transcranial electrical stimulation', Clinical Neurophysiology, vol. 117, no. 6, pp. 1388-97.

Hummel, F, Celnik, P, Giraux, P, Floel, A, Wu, WH, Gerloff, C & Cohen, LG (2005), 'Effects of non-invasive cortical stimulation on skilled motor function in chronic stroke', Brain, vol. 128, no. Pt 3, pp. 490-9.

Hyun Sang, S, Sang Hyuk, K, Won Hee, L & Tae-Seong, K (2009), 'Realistic simulation of transcranial direct current stimulation via 3-d high-resolution finite element analysis: Effect of tissue anisotropy', in Engineering in Medicine and Biology Society (EMBC), 2009, Annual International Conference of the IEEE, pp. 638-41.

Hyun Sang, S, Won Hee, L, Young Sun, C, Ji-Hwan, K & Tae-Seong, K (2010), 'Reduced spatial focality of electrical field in tDCS with ring electrodes due to tissue anisotropy', in Engineering in Medicine and Biology Society (EMBC), 2010, Annual International Conference of the IEEE, pp. 2053-6.

ICBM: International Consortium for Brain Mapping, 2012, <http://www.loni.ucla.edu/ICBM/Databases/>.

Ida, N & Bastos, J (1997), Electromagnetics and calculation of fields, second edition, Springer Verlag.

Im, C, Jung, H, Choi, J, Lee, S & Jung, K (2008), 'Determination of optimal electrode positions for transcranial direct current stimulation (tDCS)', Physics in Medicine and Biology, vol. 53, no. 11, pp. N219-N25.

Im, CH, Park, JH, Shim, M, Chang, WH & Kim, YH (2012), 'Evaluation of local electric fields generated by transcranial direct current stimulation with an extracephalic reference electrode based on realistic 3D body modeling', Physics in Medicine and Biology, vol. 57, no. 8, pp. 2137-50.

Iyer, MB, Mattu, U, Grafman, J, Lomarev, M, Sato, S & Wassermann, EM (2005), 'Safety and cognitive effect of frontal DC brain polarization in healthy individuals', Neurology, vol. 64, no. 5, pp. 872-5.

Jenkinson, M, Bannister, P, Brady, M & Smith, S (2002), 'Improved optimization for the robust and accurate linear registration and motion correction of brain images', NeuroImage, vol. 17, no. 2, pp. 825-41.

Jiang, H, van Zijl, PCM, Kim, J, Pearlson, GD & Mori, S (2006), 'DtiStudio: Resource program for diffusion tensor computation and fiber bundle tracking', Computer Methods and Programs in Biomedicine, vol. 81, no. 2, pp. 106-16.

Jiansheng, Y & Zhanghong, T (2003), 'Finite-element simulation of human brain electric activity', IEEE Transactions on Magnetics, vol. 39, no. 3, pp. 1539-42.

Jin, J (2002), The finite element method in electromagnetics, John Wiley and Sons, New York.

Jones, D, Horsfield, M & Simmons, A (1999), 'Optimal strategies for measuring diffusion in anisotropic systems by magnetic resonance imaging', Magnetic Resonance in Medicine, vol. 42, pp. 515-25.

Kabakov, AY, Muller, PA, Pascual-Leone, A, Jensen, FE & Rotenberg, A (2012), 'Contribution of axonal orientation to pathway-dependent modulation of excitatory transmission by direct current stimulation in isolated rat hippocampus', Journal of Neurophysiology, vol. 107, no. 7, pp. 1881-9.

Kajikawa, Y & Schroeder, Charles E (2011), 'How Local Is the Local Field Potential?', Neuron, vol. 72, no. 5, pp. 847-58.

Kammer, T, Vorwerg, M & Herrnberger, B (2007), 'Anisotropy in the visual cortex investigated by neuronavigated transcranial magnetic stimulation', NeuroImage, vol. 36, no. 2, pp. 313-21.

Kim, S, Kim, T, Zhou, Y & Singh, M (2001), 'Influence of Conductivity Tensors in the Finite Element Model of the Head on the Forward Solution of EEG', IEEE, pp. 1892-6.

Komlosh, M, Horkay, F, Freidlin, R, Nevo, U, Assaf, Y & Basser, P (2007), 'Detection of microscopic anisotropy in gray matter and in a novel tissue phantom using double pulsed gradient spin echo MR', Journal of Magnetic Resonance, vol. 189, no. 1, pp. 38-45.

Korgaonkar, MS, Grieve, SM, Koslow, SH, Gabrieli, JDE, Gordon, E & Williams, LM (2011), 'Loss of white matter integrity in major depressive disorder: Evidence using tract-based spatial statistical analysis of diffusion tensor imaging', Human Brain Mapping, vol. 32, no. 12, pp. 2161-71.

Kun, W, Shanan, Z, Mueller, BA, Lim, KO, Zhongming, L & Bin, H (2008), 'A New Method to Derive White Matter Conductivity From Diffusion Tensor MRI', IEEE Transactions on Biomedical Engineering, vol. 55, no. 10, pp. 2481-6.

Kwon, YH, Ko, M-H, Ahn, SH, Kim, Y-H, Song, JC, Lee, C-H, Chang, MC & Jang, SH (2008), 'Primary motor cortex activation by transcranial direct current stimulation in the human brain', Neuroscience Letters, vol. 435, no. 1, pp. 56-9.

Landini, L, Positano, V & Santarelli, MF (2005), Advanced Image Processing In Magnetic Resonance Imaging, Taylor & Francis Group.

Lang, N, Siebner, HR, Ward, NS, Lee, L, Nitsche, MA, Paulus, W, Rothwell, JC, Lemon, RN & Frackowiak, RS (2005), 'How does transcranial DC stimulation of the primary motor cortex alter regional neuronal activity in the human brain?', European Journal of Neuroscience, vol. 22, no. 2, pp. 495-504.

Lazar, M & Alexander, AL (2003), 'An error analysis of white matter tractography methods: synthetic diffusion tensor field simulations', NeuroImage, vol. 20, no. 2, pp. 1140-53.

Lazar, M, Hasan, K & Alexander, A (2001), 'Bootstrap analysis of DT-MRI tractography techniques: streamlines and tensorlines', in Proceedings of the 9th Annual Meeting of ISMRM, Glasgow, Scotland, p. 1527.

Lazar, M, Weinstein, DM, Tsuruda, JS, Hasan, KM, Arfanakis, K, Meyerand, ME, Badie, B, Rowley, HA, Haughton, V & Field, A (2003), 'White matter tractography using diffusion tensor deflection', Human Brain Mapping, vol. 18, no. 4, pp. 306-21.

Le Bihan, D, Breton, E, Lallemand, D, Grenier, P, Cabanis, E & Laval-Jeantet, M (1986), 'MR imaging of intravoxel incoherent motions: application to diffusion and perfusion in neurologic disorders', Radiology, vol. 161, no. 2, p. 401.

Le Bihan, D, Mangin, JF, Poupon, C, Clark, CA, Pappata, S, Molko, N & Chabriat, H (2001), 'Diffusion tensor imaging: concepts and applications', Journal of Magnetic Resonance Imaging, vol. 13, no. 4, pp. 534-46.

Lee, W, Seo, H, Kim, S, Cho, M, Lee, S & Kim, T (2009), 'Influence of White Matter Anisotropy on the Effects of Transcranial Direct Current Stimulation: A Finite Element Study', in 13th International Conference on Biomedical Engineering IFMBE Proceedings Springer, pp. 460-4.

Lee, WH, Deng, ZD, Kim, TS, Laine, AF, Lisanby, SH & Peterchev, AV (2010), 'Regional electric field induced by electroconvulsive therapy: A finite element simulation study', in Engineering in Medicine and Biology Society (EMBC), 2010 Annual International Conference of the IEEE, pp. 2045-8.

Lee, WH, Deng, ZD, Kim, TS, Laine, AF, Lisanby, SH & Peterchev, AV (2011), 'Regional electric field induced by electroconvulsive therapy in a realistic finite element head model: Influence of white matter anisotropic conductivity', NeuroImage, vol. 59, no. 3, pp. 2110-23.

Liebetanz, D, Nitsche, MA, Tergau, F & Paulus, W (2002), 'Pharmacological approach to the mechanisms of transcranial DC-stimulation-induced after-effects of human motor cortex excitability', Brain, vol. 125, no. 10, pp. 2238-47.

Liebetanz, D, Koch, R, Mayenfels, S, König, F, Paulus, W & Nitsche, MA (2009), 'Safety limits of cathodal transcranial direct current stimulation in rats', Clinical Neurophysiology, vol. 120, no. 6, pp. 1161-7.

Logothetis, NK, Kayser, C & Oeltermann, A (2007), 'In vivo measurement of cortical impedance spectrum in monkeys: implications for signal propagation', Neuron, vol. 55, no. 5, pp. 809-23.

Maccabee, P, Amassian, V, Eberle, L & Cracco, R (1993), 'Magnetic coil stimulation of straight and bent amphibian and mammalian peripheral nerve in vitro: locus of excitation', The Journal of Physiology, vol. 460, no. 1, p. 201.

Malmivuo, J & Plonsey, R (1995), Bioelectromagnetism: principles and applications of bioelectric and biomagnetic fields, Oxford University Press, USA.

Mangin, JF, Poupon, C, Clark, C, Le Bihan, D & Bloch, I (2002), 'Distortion correction and robust tensor estimation for MR diffusion imaging', Medical Image Analysis, vol. 6, no. 3, pp. 191-8.

Mariana Lazar, DW & Khader Hasan, AL (2000), 'Axon Tractography with Tensorlines', Proceedings of International Socient of Magnetic Resonance in Medicine, vol. 8, p. 482.

Marin, G, Guerin, C, Baillet, S, Garnero, L & Meunier, G (1998), 'Influence of skull anisotropy for the forward and inverse problem in EEG: simulation studies using FEM on realistic head models', Human Brain Mapping, vol. 6, no. 4, pp. 250-69.

McNab JA, VN, Chance S, Douaud G, Jenkinson N, Aziz T, Miller KL. (2008), ' High Resolution DTI in Whole, Fixed, Human Brain Reveals Cortical Fibre Patterns That Correspond Well with Histological Stains', in Human Brain Mapping: proceedings of the Human Brain Mapping Melbourne, Australia.

Meijs, J, Weier, O, Peters, M & Van Oosterom, A (2002), 'On the numerical accuracy of the boundary element method (EEG application)', IEEE Transactions on Biomedical Engineering, vol. 36, no. 10, pp. 1038-49.

Mignon, A, Laudenbach, V, Guischard, F, Limoge, A, Desmonts, JM & Mantz, J (1996), 'Transcutaneous cranial electrical stimulation (Limoge's currents) decreases early buprenorphine analgesic requirements after abdominal surgery', Anesthesia & Analgesia, vol. 83, no. 4, pp. 771-5.

Miller, KL & Pauly, JM (2003), 'Nonlinear phase correction for navigated diffusion imaging', Magnetic Resonance in Medicine, vol. 50, no. 2, pp. 343-53.

Minhas, P, Datta, A & Bikson, M (2011), 'Cutaneous perception during tDCS: role of electrode shape and sponge salinity', Clinical Neurophysiology, vol. 122, no. 4, pp. 637-8.

Minhas, P, Bansal, V, Patel, J, Ho, JS, Diaz, J, Datta, A & Bikson, M (2010), 'Electrodes for high-definition transcutaneous DC stimulation for applications in drug delivery and electrotherapy, including tDCS', Journal of Neuroscience Methods, vol. 190, no. 2, pp. 188-97.

Miranda, P, Faria, P & Hallett, M (2009), 'What does the ratio of injected current to electrode area tell us about current density in the brain during tDCS?', Clinical Neurophysiology, vol. 120, no. 6, pp. 1183-7.

Miranda P. C, CL, Salvador. R and Basser. P. J (2007), 'Tissue heterogeneity as a mechanism for localized neural stimulation by applied electric fields', Physics in Medicine and Biology, vol. 52, no. 18, p. 5603.

Miranda, PC, Lomarev, M & Hallett, M (2006), 'Modeling the current distribution during transcranial direct current stimulation', Clinical Neurophysiology, vol. 117, no. 7, pp. 1623-9.

Miranda, PC, Correia, L, Salvador, R & Basser, P (2007), 'Tissue heterogeneity as a mechanism for localized neural stimulation by applied electric fields', Physics in Medicine and Biology, vol. 52, no. 18, pp. 5603-17.

Miranda, PC, Pajevic, S, Pierpoali, C, Hallett, M & Basser, P (2001), 'The distribution of currents induced in the brain by magnetic stimulation: A finite element analysis incorporating DT-MRI-derived conductivity data', in Proc. Intel. Soc. Mag. Reson: proceedings of the Proc. Intel. Soc. Mag. Reson, p. 1540.

Mohr, M (2003), 'Comparing Iterative Solvers for Linear Systems associated with the Finite Difference Discretisation of the Forward Problem in Electroencephalographic Source Analysis', Mathematical and Biological Engineering and Computing, vol. 41, no. 1, pp. 75-84.

Mori, S, Oishi, K, Jiang, H, Jiang, L, Li, X, Akhter, K, Hua, K, Faria, AV, Mahmood, A & Woods, R (2008), 'Stereotaxic white matter atlas based on diffusion tensor imaging in an ICBM template', NeuroImage, vol. 40, no. 2, pp. 570-82.

Munck, J & Peters, M (1993), 'A fast method to compute the potential in the multisphere model', IEEE Transactions on Biomedical Engineering, vol. 40, no. 11, pp. 1166-74.

Neil Cuffin, B & Cohen, D (1979), 'Comparison of the magnetoencephalogram and electroencephalogram', Electroencephalography and Clinical Neurophysiology, vol. 47, no. 2, pp. 132-46.

Nicholson, P (1965), 'Specific impedance of cerebral white matter', Experimental Neurology, vol. 13, no. 4, pp. 386-401.

Nielsen, JF, Ghugre, NR & Panigrahy, A (2004), 'Affine and polynomial mutual information coregistration for artifact elimination in diffusion tensor imaging of newborns', Magnetic Resonance Imaging, vol. 22, no. 9, pp. 1319-23.

Nilsson, J, Panizza, M, Roth, B, Basser, P, Cohen, L, Caruso, G & Hallett, M (1992), 'Determining the site of stimulation during magnetic stimulation of a peripheral nerve', Electroencephalography and Clinical Neurophysiology/Evoked Potentials Section, vol. 85, no. 4, pp. 253-64.

Nitsche, M (2002), 'Transcranial direct current stimulation: a new treatment for depression?', Bipolar Disorders, vol. 4, pp. 98-9.

Nitsche, M & Paulus, W (2000), 'Excitability changes induced in the human motor cortex by weak transcranial direct current stimulation', The Journal of Physiology, vol. 527, no. 3, pp. 633-39.

Nitsche, M, Fricke, K, Henschke, U, Schlitterlau, A, Liebetanz, D, Lang, N, Henning, S, Tergau, F & Paulus, W (2004), 'Pharmacological modulation of cortical ex-

citability shifts induced by transcranial direct current stimulation in humans', The Journal of Physiology, vol. 553, no. 1, pp. 293-301.

Nitsche, MA & Paulus, W (2001), 'Sustained excitability elevations induced by transcranial DC motor cortex stimulation in humans', Neurology, vol. 57, no. 10, pp. 1899-901.

Nitsche, MA, Boggio, PS, Fregni, F & Pascual-Leone, A (2009), 'Treatment of depression with transcranial direct current stimulation (tDCS): a review', Experimental Neurology, vol. 219, no. 1, pp. 14-9.

Nitsche, MA, Liebetanz, D, Antal, A, Lang, N, Tergau, F & Paulus, W (2003), 'Modulation of cortical excitability by weak direct current stimulation–technical, safety and functional aspects', Supplements to Clinical Neurophysiology, vol. 56, pp. 255-76.

Nitsche, MA, Doemkes, S, Karakoese, T, Antal, A, Liebetanz, D, Lang, N, Tergau, F & Paulus, W (2007), 'Shaping the effects of transcranial direct current stimulation of the human motor cortex', Journal of Neurophysiology, vol. 97, no. 4, pp. 3109-17.

Nitsche, MA, Liebetanz, D, Schlitterlau, A, Henschke, U, Fricke, K, Frommann, K, Lang, N, Henning, S, Paulus, W & Tergau, F (2004), 'GABAergic modulation of DC stimulation-induced motor cortex excitability shifts in humans', European Journal of Neuroscience, vol. 19, no. 10, pp. 2720-6.

Nitsche, MA, Seeber, A, Frommann, K, Klein, CC, Rochford, C, Nitsche, MS, Fricke, K, Liebetanz, D, Lang, N & Antal, A (2005), 'Modulating parameters of excitability during and after transcranial direct current stimulation of the human motor cortex', The Journal of Physiology, vol. 568, no. 1, pp. 291-303.

Nunez, P & Srinivasan, R (2006), Electric fields of the brain: the neurophysics of EEG, Oxford University Press New York.

Oishi, K, Zilles, K, Amunts, K, Faria, A, Jiang, H, Li, X, Akhter, K, Hua, K, Woods, R & Toga, AW (2008), 'Human brain white matter atlas: identification and assignment of common anatomical structures in superficial white matter', NeuroImage, vol. 43, no. 3, pp. 447-57.

Oostendorp, T, Delbeke, J & Stegeman, D (2002), 'The conductivity of the human skull: results of in vivo and in vitro measurements', IEEE Transactions on Biomedical Engineering, vol. 47, no. 11, pp. 1487-92.

Oostendorp, TF, Hengeveld, YA, Wolters, CH, Stinstra, J, van Elswijk, G & Stegeman, DF (2008), 'Modeling transcranial DC stimulation', in Engineering in Medicine and Biology Society, (EMBS) 2008, 30th Annual International Conference of the IEEE, pp. 4226-9.

Opitz, A, Windhoff, M, Heidemann, RM, Turner, R & Thielscher, A (2011), 'How the brain tissue shapes the electric field induced by transcranial magnetic stimulation', NeuroImage, vol. 58, no. 3, pp. 849-59.

Ordidge, R, Helpern, J, Qing, Z, Knight, R & Nagesh, V (1994), 'Correction of motional artifacts in diffusion-weighted MR images using navigator echoes', Magnetic Resonance Imaging, vol. 12, no. 3, pp. 455-60.

Pakkenberg, B & Gundersen, HJG (1997), 'Neocortical neuron number in humans: Effect of sex and age', The Journal of Comparative Neurology, vol. 384, no. 2, pp. 312-20.

Papadakis, NG, Martin, KM, Pickard, JD, Hall, LD, Carpenter, TA & Huang, CLH (2000), 'Gradient preemphasis calibration in diffusion-weighted echo-planar imaging', Magnetic Resonance in Medicine, vol. 44, no. 4, pp. 616-24.

Parazzini, M, Fiocchi, S & Ravazzani, P (2012), 'Electric field and current density distribution in an anatomical head model during transcranial direct current stimulation for tinnitus treatment', Bioelectromagnetics, vol. 33, no. 6, pp. 476-87.

Parazzini, M, Fiocchi, S, Rossi, E, Paglialonga, A & Ravazzani, P (2011), 'Transcranial direct current stimulation: estimation of the electric field and of the current density in an anatomical human head model', IEEE Transections on Biomedical Engineering, vol. 58, no. 6, pp. 1773-80.

Park, JH, Hong, SB, Kim, DW, Suh, M & Im, CH (2011), 'A novel array-type transcranial direct current stimulation (tDCS) system for accurate focusing on targeted brain areas', IEEE Transactions on Magnetics, vol. 47, no. 5, pp. 882-5.

Peterchev, AV, Wagner, TA, Miranda, PC, Nitsche, MA, Paulus, W, Lisanby, SH, Pascual-Leone, A & Bikson, M (2012), 'Fundamentals of transcranial electric and magnetic stimulation dose: definition, selection, and reporting practices', Brain Stimulation, vol. 5, no. 4, pp. 435-53.

Pierpaoli, C & Basser, PJ (1996), 'Toward a quantitative assessment of diffusion anisotropy', Magnetic Resonance in Medicine, vol. 36, no. 6, pp. 893-906.

Pierpaoli, C, Jezzard, P, Basser, PJ, Barnett, A & Di Chiro, G (1996), 'Diffusion tensor MR imaging of the human brain', Radiology, vol. 201, no. 3, pp. 637-48.

Pierpaoli, C, Marenco, S, Rohde, G, Jones, D & Barnett, A (2003), 'Analyzing the contribution of cardiac pulsation to the variability of quantities derived from the diffusion tensor', in Proceedings of the 11th Annual Meeting of ISMRM, Toronto, Canada, p. 70.

Plonsey, R & Heppner, DB (1967), 'Considerations of quasi-stationarity in electrophysiological systems', Bulletin of Mathematical Biology, vol. 29, no. 4, pp. 657-64.

Polania, R, Paulus, W & Nitsche, MA (2012), 'Modulating cortico-striatal and thalamo-cortical functional connectivity with transcranial direct current stimulation', Human Brain Mapping, vol. 33, no. 10, pp. 2499-508.

Poupon, C, Clark, C, Frouin, V, Regis, J, Bloch, I, Le Bihan, D & Mangin, J (2000), 'Regularization of diffusion-based direction maps for the tracking of brain white matter fascicles', NeuroImage, vol. 12, no. 2, pp. 184-95.

Poupon, C, Mangin, JF, Frouin, V, Régis, J, Poupon, F, Pachot-Clouard, M, Le Bihan, D & Bloch, I (1998), 'Regularization of MR diffusion tensor maps for tracking brain white matter bundles', Medical Image Computing and Computer-Assisted Interventation—MICCAI'98, pp. 489-98.

Purpura, DP & McMurtry, JG (1965), 'Intracellular activities and evoked potential changes during polarization of motor cortex', Journal of Neurophysiology, vol. 28, no. 1, pp. 166-85.

Radman, T, Ramos, RL, Brumberg, JC & Bikson, M (2009), 'Role of cortical cell type and morphology in sub-and suprathreshold uniform electric field stimulation', Brain Stimulation, vol. 2, no. 4, p. 215.

Ramon, C, Schimpf, P & Haueisen, J (2006), 'Influence of head models on EEG simulations and inverse source localizations', Biomedical Engineering On Line, vol. 5, no. 1, p. 10.

Ramon, C, Schimpf, PH, Haueisen, J (2004), 'Effect of Model Complexity on EEG Source Localizations', in Neurology and Clinical Neurophysiology: proceedings of the Neurology and Clinical Neurophysiology.

Rampersad, S, Stegeman, D & Oostendorp, T (2011), 'On handling the layered structure of the skull in transcranial direct current stimulation models', in Engineering in Medicine and Biology Society (EMBC), 2011 Annual International Conference of the IEEE, pp. 1989-92.

Rampersad, S, Stegeman, D & Oostendorp, T (2012), 'Single-Layer Skull Approximations Perform Well in Transcranial Direct Current Stimulation Modeling', IEEE Transections on Neural System and Rehabilitation Engineering, vol. PP, no. 99, pp. 1-, item: 22855232.

Ren, L & Ueno, S (2000), 'Calculating the activating function of nerve excitation in inhomogeneous volume conductor during magnetic stimulation using the finite element method', IEEE Transactions on Magnetics, vol. 36, no. 4, pp. 1796-9.

Rohde, GK, Barnett, AS, Basser, PJ, Marenco, S & Pierpaoli, C (2004), 'Comprehensive approach for correction of motion and distortion in diffusion-weighted MRI', Magnetic Resonance in Medicine, vol. 51, no. 1, pp. 103-14.

Rullmann, M, Anwander, A, Dannhauer, M, Warfield, SK, Duffy, FH & Wolters, CH (2009), 'EEG source analysis of epileptiform activity using a 1 mm anisotropic hexahedra finite element head model', NeuroImage, vol. 44, no. 2, pp. 399-410.

Rush, S & Driscoll, DA (1968), 'Current distribution in the brain from surface electrodes', Anesthesia & Analgesia, vol. 47, no. 6, p. 717.

Rush, S & Driscoll, D (1969), 'EEG electrode sensitivity-an application of reciprocity', IEEE Transactions on Biomedical Engineering, pp. 15-22.

S Gabriel, RWLaCG (1996), 'The dielectric properties of biological tissues: II. Measurements in the frequency range 10 Hz to 20 GHz ', Physics in Medicine and Biology, vol. 41, no. 11, pp. 2251-69.

Sadiku, MNO (2000), Numerical techniques in electromagnetics, second edition, CRC Press.

Sadleir, R & Argibay, A (2007), 'Modeling skull electrical properties', Annals of Biomedical Engineering, vol. 35, no. 10, pp. 1699-712.

Sadleir, RJ, Vannorsdall, TD, Schretlen, DJ & Gordon, B (2010), 'Transcranial direct current stimulation (tDCS) in a realistic head model', NeuroImage, vol. 51, no. 4, pp. 1310-8.

Salvador, R, Mekonnen, A, Ruffini, G & Miranda, PC (2010), 'Modeling the electric field induced in a high resolution realistic head model during transcranial current stimulation', in Engineering in Medicine and Biology Society (EMBC), 2010 Annual International Conference of the IEEE pp. 2073-6.

Salvador, R, Silva, S, Basser, P & Miranda, P (2011), 'Determining which mechanisms lead to activation in the motor cortex: A modeling study of transcranial magnetic stimulation using realistic stimulus waveforms and sulcal geometry', Clinical Neurophysiology, vol. 122, no. 4, pp. 748-58.

Saypol, J, Roth, B, Cohen, L & Hallett, M (1991), 'A theoretical comparison of electric and magnetic stimulation of the brain', Annals of Biomedical Engineering, vol. 19, no. 3, pp. 317-28.

Scheler, G, Fischer, MJM, Genow, A, Hummel, C, Rampp, S, Paulini, A, Hopfengärtner, R, Kaltenhäuser, M & Stefan, H (2007), 'Spatial relationship of source localizations in patients with focal epilepsy: comparison of MEG and EEG with a three spherical shells and a boundary element volume conductor model', Human Brain Mapping, vol. 28, no. 4, pp. 315-22.

Schlaug, G, Renga, V & Nair, D (2008), 'Transcranial direct current stimulation in stroke recovery', Archives of Neurology, vol. 65, no. 12, p. 1571.

Scivill, I, Barker, A & Freeston, I (1996), 'Finite element modelling of magnetic stimulation of the spine', IEEE Engineering in Medicine and Biology Society (EMBS), pp. 393-4.

Shimony, JS, McKinstry, RC, Akbudak, E, Aronovitz, JA, Snyder, AZ, Lori, NF, Cull, TS & Conturo, TE (1999), 'Quantitative Diffusion-Tensor Anisotropy Brain MR Imaging: Normative Human Data and Anatomic Analysis1', Radiology, vol. 212, no. 3, pp. 770-84.

Silva, S, Basser, P & Miranda, P (2008), 'Elucidating the mechanisms and loci of neuronal excitation by transcranial magnetic stimulation using a finite element model of a cortical sulcus', Clinical Neurophysiology, vol. 119, no. 10, p. 2405.

Simpleware Reference Guide, (2010), vol. 4.2, Simpleware converting 3D images into models, SIMPLEWARE LTD, Exeter UK.

Skare, S & Andersson, JLR (2001), 'On the effects of gating in diffusion imaging of the brain using single shot EPI', Magnetic Resonance Imaging, vol. 19, no. 8, pp. 1125-8.

Smith, SM, Jenkinson, M, Woolrich, MW, Beckmann, CF, Behrens, TEJ, Johansen-Berg, H, Bannister, PR, De Luca, M, Drobnjak, I & Flitney, DE (2004), 'Advances in functional and structural MR image analysis and implementation as FSL', NeuroImage, vol. 23, pp. S208-S19.

Sonka, M, Fitzpatrick, JM & Masters, BR (2002), 'Handbook of Medical Imaging, Volume 2: Medical image processing and analysis', Optics & Photonics News, vol. 13, pp. 50-1.

Sparing, R & Mottaghy, FM (2008), 'Noninvasive brain stimulation with transcranial magnetic or direct current stimulation (TMS/tDCS)—From insights into human memory to therapy of its dysfunction', Methods, vol. 44, no. 4, pp. 329-37.

Squillacote, AH (2007), The ParaView guide: a parallel visualization application, Kitware.

Stecker, MM (2005), 'Transcranial electric stimulation of motor pathways: a theoretical analysis', Computers in Biology and Medicine, vol. 35, no. 2, pp. 133-55.

Stejskal, EO & Tanner, J (1965), 'Spin diffusion measurements: Spin echoes in the presence of a time-dependent field gradient', The Journal of Chemical Physics, vol. 42, p. 288.

Stok, CJ (1986), Thesis (doctoral), The inverse problem in EEG and MEG with application to visual evoked responses, University of Twente, the Netherlands.

Tang, Y, Nyengaard, J, Pakkenberg, B & Gundersen, H (1997), 'Age-induced white matter changes in the human brain: a stereological investigation', Neurobiology of Aging, vol. 18, no. 6, pp. 609-15.

Tehovnik, EJ (1996), 'Electrical stimulation of neural tissue to evoke behavioral responses', Journal of Neuroscience Methods, vol. 65, no. 1, pp. 1-17.

Tensaouti, F, Lotterie, JA & Berry, I (2009), 'Fiber tracking on the phantom dataset by using Sisyphe software', in MICCAI workshop on Diffusion Modelling and the Fiber Cup (DMFC'09), London, United Kingdom: proceedings of the MICCAI workshop on Diffusion Modelling and the Fiber Cup (DMFC'09), London, United Kingdom.

Thielscher, A, Opitz, A & Windhoff, M (2011), 'Impact of the gyral geometry on the electric field induced by transcranial magnetic stimulation', NeuroImage, vol. 54, no. 1, pp. 234-43.

Tofts, Pe (2005), Quantitative MRI of the brain: measuring changes caused by disease, Wiley.

Tuch, D, Wedeen, V, Dale, A & Belliveau, J (1963), 'Electrical conductivity tensor map of the human brain using NMR diffusion imaging: An effective medium approach', Journal of Physiology, vol. 205, pp. 203-7.

Tuch, D, Wedeen, V, Dale, A, George, J & Belliveau, J (2001), 'Conductivity tensor mapping of the human brain using diffusion tensor MRI', Proceedings of the National Academy of Sciences of the United States of America, vol. 98, no. 20, p. 11697.

Tuch, DS (2004), 'Q-ball imaging', Magnetic Resonance in Medicine, vol. 52, no. 6, pp. 1358-72.

Tuch, DS, Wedeen, VJ, Dale, AM, George, JS & Belliveau, JW (1999), 'Conductivity Mapping of Biological Tissue Using Diffusion MRI', Annals of the New York Academy of Sciences, vol. 888, no. Occupational Electrical Injury: An International Symposium, pp. 314-6.

Tuch, DS, Reese, TG, Wiegell, MR, Makris, N, Belliveau, JW & Wedeen, VJ (2002), 'High angular resolution diffusion imaging reveals intravoxel white matter fiber heterogeneity', Magnetic Resonance in Medicine, vol. 48, no. 4, pp. 577-82.

Utz, KS, Dimova, V, Oppenlander, K & Kerkhoff, G (2010), 'Electrified minds: transcranial direct current stimulation (tDCS) and galvanic vestibular stimulation (GVS) as methods of non-invasive brain stimulation in neuropsychology--a review of current data and future implications', Neuropsychologia, vol. 48, no. 10, pp. 2789-810.

Van den Broek, S, Reinders, F, Donderwinkel, M & Peters, M (1998), 'Volume conduction effects in EEG and MEG', Electroencephalography and Clinical Neurophysiology, vol. 106, no. 6, pp. 522-34.

Vanneste, S, Plazier, M, Ost, J, Van Der Loo, E, Van de Heyning, P & De Ridder, D (2010), 'Bilateral dorsolateral prefrontal cortex modulation for tinnitus by transcrani-

al direct current stimulation: a preliminary clinical study', Experimental Brain Research, vol. 202, no. 4, pp. 779-85.

Wagner, T, Fregni, F, Fecteau, S, Grodzinsky, A, Zahn, M & Pascual-Leone, A (2007), 'Transcranial direct current stimulation: a computer-based human model study', NeuroImage, vol. 35, no. 3, pp. 1113-24.

Wakana, S, Caprihan, A, Panzenboeck, MM, Fallon, JH, Perry, M, Gollub, RL, Hua, K, Zhang, J, Jiang, H, Dubey, P, Blitz, A, van Zijl, P & Mori, S (2007), 'Reproducibility of quantitative tractography methods applied to cerebral white matter', NeuroImage, vol. 36, no. 3, pp. 630-44.

Wang, C, Ulbert, I, Schomer, DL, Marinkovic, K & Halgren, E (2005), 'Responses of human anterior cingulate cortex microdomains to error detection, conflict monitoring, stimulus-response mapping, familiarity, and orienting', The Journal of Neuroscience, vol. 25, no. 3, pp. 604-13.

Wang, JJ, Deichmann, R, Hsiao, IT, Liu, HL, Wai, YY, Wan, YL, Turner, R & Ordidge, R (2005), 'Selective averaging for the diffusion tensor measurement', Magnetic Resonance Imaging, vol. 23, no. 4, pp. 585-90.

Wang, Y, Haynor, D & Kim, Y (2001), 'An investigation of the importance of myocardial anisotropy in finite-element modeling of the heart: methodology and application to the estimation of defibrillation efficacy', IEEE Transactions on Biomedical Engineering, vol. 48, no. 12, pp. 1377-89.

Wang, Z, Vemuri, BC, Chen, Y & Mareci, TH (2004), 'A constrained variational principle for direct estimation and smoothing of the diffusion tensor field from complex DWI', IEEE Transactions on Medical Imaging, vol. 23, no. 8, pp. 930-9.

Webster, BR, Celnik, PA & Cohen, LG (2006), 'Noninvasive brain stimulation in stroke rehabilitation', NeuroRx, vol. 3, no. 4, pp. 474-81.

Webster, JG & Hughes, PD (1991), 'Electrical impedance tomography', Journal of Clinical Engineering, vol. 16, no. 4, p. 349.

Wedeen, VJ, Rosene, DL, Wang, R, Dai, G, Mortazavi, F, Hagmann, P, Kaas, JH & Tseng, WYI (2012), 'The geometric structure of the brain fiber pathways', Science, vol. 335, no. 6076, pp. 1628-34.

Wedeen, VJ, Wang, RP, Schmahmann, JD, Benner, T, Tseng, WYI, Dai, G, Pandya, DN, Hagmann, P, D'Arceuil, H & de Crespigny, AJ (2008), 'Diffusion spectrum magnetic resonance imaging (DSI) tractography of crossing fibers', NeuroImage, vol. 41, no. 4, pp. 1267-77.

Weinstein, D, Kindlmann, G & Lundberg, E (1999), 'Tensorlines: Advection-diffusion based propagation through diffusion tensor fields', in Proceedings of the conference on Visualization'99: celebrating ten years IEEE Computer Society Press, pp. 249-53.

Westin, CF, Peled, S, Gudbjartsson, H, Kikinis, R & Jolesz, FA (1997), 'Geometrical diffusion measures for MRI from tensor basis analysis', in Proceedings of ISMRM, p. 1742.

Westin, CF, Maier, S, Mamata, H, Nabavi, A, Jolesz, F & Kikinis, R (2002), 'Processing and visualization for diffusion tensor MRI', Medical Image Analysis, vol. 6, no. 2, pp. 93-108.

Williams, JA, Imamura, M & Fregni, F (2009), 'Updates on the use of non-invasive brain stimulation in physical and rehabilitation medicine', Journal of Rehabilitation Medicine, vol. 41, no. 5, pp. 305-11.

Wilson, F & Bayley, R (1950), 'The electric field of an eccentric dipole in a homogeneous spherical conducting medium', Circulation, vol. 1, no. 1, p. 84.

Wimberger, DM, Roberts, TP, Barkovich, AJ, Prayer, LM, Moseley, ME & Kucharczyk, J (1995), 'Identification of" premyelination" by diffusion-weighted MRI', Journal of Computer Assisted Tomography, vol. 19, no. 1, p. 28.

Wolters, C (2003), Thesis (doctoral), 'Influence of tissue conductivity inhomogeneity and anisotropy on EEG/MEG based source localization in the human brain', MPI of Cognitive Neuroscience Leipzig.

Wolters, C, Anwander, A, Tricoche, X, Lew, S & Johnson, C (2005), 'Influence of local and remote white matter conductivity anisotropy for a thalamic source on EEG/MEG field and return current computation', International Journal of Bioelectromagnetism, vol. 7, no. 1, pp. 203-6.

Wolters, C, Anwander, A, Tricoche, X, Weinstein, D, Koch, M & MacLeod, R (2006), 'Influence of tissue conductivity anisotropy on EEG/MEG field and return current computation in a realistic head model: a simulation and visualization study using high-resolution finite element modeling', NeuroImage, vol. 30, no. 3, pp. 813-26.

Woods, RP, Grafton, ST, Holmes, CJ, Cherry, SR & Mazziotta, JC (1998), 'Automated image registration: I. General methods and intrasubject, intramodality validation', Journal of Computer Assisted Tomography, vol. 22, no. 1, pp. 139-52.

Woolsey, TA, Hanaway, J & Gado, MH (2008), The brain atlas: a visual guide to the human central nervous system, Wiley Hoboken, NJ.

Yan, D, Xu, W & Li, J (2010), 'Anisotropic WM conductivity reconstruction based on diffusion tensor magnetic resonance imaging: a simulation study', Journal of Biomedical Science and Engineering, vol. 3, no. 8, pp. 776-84.

Yeh, FC & Tseng, WYI (2011), 'NTU-90: A high angular resolution brain atlas constructed by q-space diffeomorphic reconstruction', NeuroImage, vol. 58, no. 1, pp. 91-9.

Yvert, B, Bertrand, O, Thévenet, M, Echallier, JF & Pernier, J (1997), 'A systematic evaluation of the spherical model accuracy in EEG dipole localization', Electroencephalography and Clinical Neurophysiology, vol. 102, no. 5, pp. 452-9.

Zhang, Y, Zhu, S & He, B (2004), 'A second-order finite element algorithm for solving the three-dimensional EEG forward problem', Physics in Medicine and Biology, vol. 49, p. 2975.

Zheng, X, Alsop, DC & Schlaug, G (2011), 'Effects of transcranial direct current stimulation (tDCS) on human regional cerebral blood flow', NeuroImage, vol. 58, no. 1, pp. 26-33.

Zhou, H & Van Oosterom, A (1992), 'Computation of the potential distribution in a four-layer anisotropic concentric spherical volume conductor', IEEE transactions on Biomedical Engineering, vol. 39, no. 2, pp. 154-8.